Atmospheric Structure of Carbon Stars and its Effect on the Analysis of Elemental Abundances and Isotopic Ratios

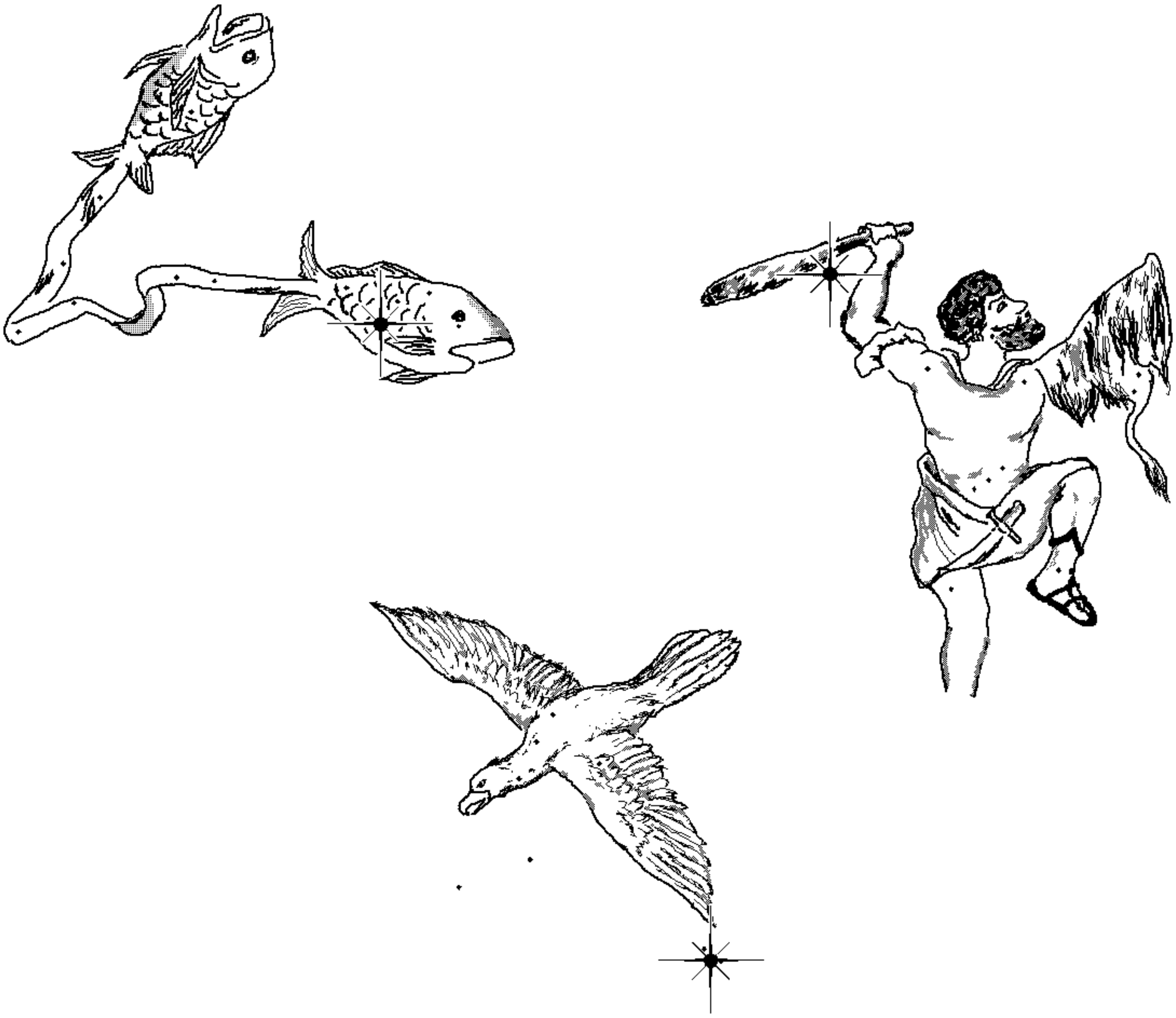

Keiichi Ohnaka

Institute of Astronomy, The University of Tokyo

学位論文

Atmospheric Structure of Carbon Stars and its Effect on the Analysis of Elemental Abundances and Isotopic Ratios

炭素星の大気構造と元素組成及び同位体比解析におけるその影響

平成8年12月 博士(理学)申請

東京大学大学院理学系研究科

天文学専攻

大仲 圭一

"All men have the stars," he answered, "but they are not the same things for different people. For some, who are travelers, the stars are guides. For others they are no more than little lights in the sky. For others, who are scholars, they are problems. For my businessman they were wealth. But all these stars are silent. You–you alone–will have the stars as no one else has them–"

— Antoine de Saint-Exupéry 'The Little Prince'

Preface

The late stage of the evolution of intermediate- and low-mass stars exhibits many phenomena of complicated nature. The material processed in the stellar interior is mixed into the stellar surface, and returned to the interstellar space by mass loss. Carbon stars are such objects of which evolution is still poorly understood. Spectroscopic observations serve as a diagnostic tool to derive information on the nuclear reactions operating in the stellar interior. Stellar spectra also bring us insight into physics and chemistry in the upper atmosphere, which in fact is the boundary condition to the circumstellar envelope.

However, the spectral analysis of carbon stars is one of the most challenging tasks for stellar spectroscopists. The predominance of molecular lines in the spectra of carbon stars is a major obstacle in constructing realistic model atmospheres which are indispensable for abundance analyses and hampers accurate analyses not only of elemental abundances but also of isotopic ratios. The lack of reliable model atmospheres as well as the heavily line blanketed spectra are responsible for the systematic differences in the results of abundance analyses of carbon stars.

I will report in this thesis the analysis of elemental abundances and isotopic ratios in carbon stars based on newly developed model atmospheres. The point is that the reliable model atmosphere is essential to reliable abundance analysis for carbon stars. Before the analysis of chemical composition in carbon stars, I will present the development of a new code of spherical model atmosphere of carbon stars, together with a test by observational data. It will be revealed that the atmospheric structure of carbon stars is very sensitive to the chemical composition which is exactly what is determined based on the model atmospheres. So the analysis of chemical composition in carbon stars will be done with the priority put on this interplay between the atmospheric structure and the chemical composition. I hope that this work will bring the controversy over the chemical composition in carbon stars to an end and that the result will be one of the reliable observational clues to unveil the mystery of carbon stars.

In addition to the abundance analysis, I will also report the analysis of the CO first overtone lines, by which the upper photosphere can be probed. The reliable model photospheres and the predicted spectra from them enable us to derive the physical properties in the upper photosphere or in the inner-circumstellar envelope. Such region is considered to play a crucial role in driving mass loss in cool luminous stars, but by the present observational technique the region cannot be observed with enough spatial resolution. Spectroscopic diagnosis is at present the only means to understand the physics and chemistry in the region close to the photosphere and the analysis done in this thesis has revealed new pictures of the outer atmosphere of carbon stars.

So, welcome to the world of carbon stars!

K. Ohnaka

Mitaka, Tokyo
March 1997

Contents

1 Introduction and Outline of the Thesis **9**
1.1 Recognition and classification of carbon stars 10
1.2 Atmospheric structure of carbon stars 12
1.2.1 Photosphere 12
1.2.2 Outer atmosphere 13
1.2.3 Circumstellar envelope 13
1.3 Evolution to carbon stars – where do they come from? 16
1.4 Chemical composition in carbon stars 18
1.5 Goal of the research and outline of the thesis 20

2 Quantitative Analysis of Carbon Isotopic Ratios in Carbon Stars I. 62 N-type and 15 SC-type carbon stars **25**
2.1 Introduction 27
2.2 Observation 30
2.3 Molecular Data 35
2.4 Model Atmosphere 37
2.5 Effective Temperature 40
2.5.1 Determination of Effective Temperatures 40
2.5.2 The C-classification 43
2.6 Analysis 44
2.7 Results 46
2.8 Discussion 50
2.8.1 Comparison with Previous Results 50
2.8.2 Model atmospheres 52
2.8.3 Carbon Star Formation 53
2.9 Concluding Remarks 55

3 Quantitative Analysis of Carbon Isotopic Ratios in Carbon Stars II. 26 J-type carbon stars including those with silicate emission **59**
3.1 Introduction 61
3.2 Observation 63
3.3 Model atmosphere 66
3.4 Effective temperature 67

3.5 Analysis 69
3.6 Results 71
3.7 Discussion 74
3.8 Concluding Remarks 76

4 Spherical Model Atmosphere of Carbon Stars 79
4.1 Introduction 81
4.2 Method of construction of spherical model 83
4.3 Results and Discussion 89
4.3.1 Does the code work correctly? 89
4.3.2 Effect of elemental abundance of oxygen 89
4.3.3 Effect of C/O ratio on the models 90
4.3.4 Spectral Energy Distribution 91
4.3.5 Comparison of SED with the observation by the ISO SWS 92
4.3.6 Synthetic spectra 92
4.4 Concluding remarks 96

5 Analysis of Elemental Abundances of Carbon and Oxygen in Carbon Stars 99
5.1 Introduction 101
5.2 Observational data 104
5.3 Molecular data 105
5.4 Stellar parameters 111
5.5 Analysis and results 113
5.5.1 Principle of the standard analysis 113
5.5.2 Self-consistent analysis with plane parallel models 114
5.5.3 Analysis with spherical models 116
5.5.4 Uncertainties of the results 118
5.5.5 Spectrum synthesis 119
5.6 Discussion on the result of the abundance analysis 121
5.6.1 Comparison with the result by Lambert et al. (1986) 121
5.6.2 Tests of model atmospheres 123
5.6.3 Carbon star formation 124
5.7 Concluding remarks 127

6 Analysis of the CO First Overtone Bands – Probing the Upper Photosphere of Carbon Stars 129
6.1 Introduction 131
6.2 Peculiar behavior of low excitation lines 133
6.2.1 Breakdown of the standard analysis 133
6.2.2 What is abnormal in the low excitation lines? 133
6.2.3 Line shift 134
6.3 Depth-dependent turbulent velocity hypothesis 136

6.4 Separation of the excess absorption 139
6.4.1 Physical properties of the CO absorption layer 139
6.4.2 Molecular hydrogen line 140
6.5 The more peculiar behavior of the CO bandhead 143
6.6 Concluding remarks 145

7 Conclusion 147

Chapter 1

Introduction and Outline of the Thesis

1.1 Recognition and classification of carbon stars

Studies on carbon stars date back to an Italian Jesuit in the 19th century. Angelo Secchi investigated about 4000 stars and classified them into four groups based on their spectra (Secchi 1868). It was the first spectral classification of stars. The stars classified into the groups III and IV were characterized by two distinct absorption features, which were later identified as due to TiO and C_2. The stars of the groups III and IV actually correspond to M-type stars and carbon stars, respectively.

The classification by Secchi was extended by Cannon & Pickering (1918), who made the spectral classification of nearly 300,000 stars. Their basis of the classification is called the Harvard classification and they published the result as the Henry Draper (HD) Catalogue. Carbon stars were divided into two subgroups, R- and N-type, in the Harvard classification. The basis of the classification was color: very red carbon stars were classified as N-type while less red ones as R-type. Shane (1928) later attempted to assign a temperature scale to the spectral classifications of R- and N-type carbon stars. He examined visual spectral energy distributions and concluded that N-type carbon stars, which exhibit remarkable depression in UV region, had lower surface temperatures. However, the UV spectra of N-type carbon stars are generally significantly depressed and would lead to the surface temperature less than 1000 K. The depression should be rather attributed to absorption due to some unidentified molecules and/or atoms.

It was found that a group of carbon stars exhibit very strong absorption due to ^{13}C-bearing molecules. Such stars were defined as J-type by Bouigue (1954). He measured the intensity ratio of ^{12}CN and ^{13}CN at 6210 Å and 6260 Å, respectively, and defined J-type stars as those exhibiting very conspicuous absorption at 6260 Å. Gordon (1971) defined J-type stars as those showing the (0,2) band of $^{12}C^{13}C$ with strengths equal to at least a half of the (1,3) band of $^{12}C^{12}C$.

Keenan & Morgan (1941) introduced two-dimensional classification of carbon stars so that it could better represent the physics and chemistry in the atmosphere of carbon stars. They employed Na I D lines as a major indicator of temperature of carbon star atmospheres. They also found that some carbon stars with almost the same temperature showed different strengths of C_2 absorption. They attributed such difference of the strengths of C_2 absorption to the variation of carbon abundance in the atmospheres and employed the strengths of C_2 absorption as the second parameter. Their classification is called the C-classification and applied to a number of carbon stars by Yamashita (1972, 1975).

A small group of peculiar cool stars, which were not classified into N-type nor into R-type, were left behind after Cannon & Pickering (1918) completed the Henry Draper Catalogue. Merrill (1922) realized such stars as a distinct group and named S stars. They are characterized by the strong absorption of ZrO. They also show strong absorption lines of Ba II and Sr I. Keenan (1954) classified S stars by two parameters, that is, the strengths of ZrO and TiO bands, and the relative strength of ZrO bands to TiO bands. The difference of the ratio of ZrO to TiO should be attributed to the difference of Zr abundance in S stars. Some S stars exhibit TiO bands and others exhibit weak absorption of CN and C_2. The former stars are called MS stars, while the latter ones SC or CS stars. These subgroups of stars can be considered to lie in a spectral sequence of M–MS–S–SC(or CS)–C(N).

1.2 Atmospheric structure of carbon stars

1.2.1 Photosphere

The spectral features of cool stars can be understood based on the chemical dissociation equilibrium. Russell (1934) showed that the molecular absorption such as due to TiO and VO in M stars can be explained by the chemical dissociation equilibrium in the atmosphere where oxygen is more abundant than carbon. On the other hand, he showed that the spectral features due to carbon-bearing molecules such as C_2, CN can be reproduced in the atmosphere with carbon more abundant than oxygen. Fujita (1939) found that the spectral features of S stars can be explained by the atmospheric composition characterized by C$\sim$O. Tsuji (1964) calculated the chemical dissociation equilibrium including more than 100 molecules and atoms. These works have been a basis to understand the spectral features as well as to construct model atmospheres of cool stars.

Constructing realistic model atmospheres of cool stars has lagged the case of hot stars because of a huge number of molecular lines which themselves are the major characteristics of cool stars. The gray approximation in which the absorption coefficient is independent of frequency is never valid in constructing model atmospheres of cool stars. At first, the strong frequency-dependence of the absorption coefficient was taken into account by the straight mean of opacity in a spectral mesh of an appropriate interval (Tsuji 1967). However, such approximation tends to overestimate the effect of molecular opacity and the predicted strengths of band absorption were stronger than observed. Auman (1967) reduced this problem by employing the harmonic mean opacity. The most sophisticated techniques used in computation of model atmospheres of cool stars at present are the Opacity Sampling (OS) and the Opacity Distribution Function (ODF) (e.g. Carbon 1984, Ekberg et al. 1986, Johnson 1986, Alexander et al. 1989). The OS method is the more consistent in treating the molecular line opacity, but it lacks flexibility because a huge table of opacity covering possible ranges of temperature, pressure, turbulent velocity, and chemical composition should be prepared prior to model computation.

Model atmospheres of carbon stars have been developed by several groups. Querci et al. (1974) and Querci & Querci (1975) constructed a grid of model atmospheres of carbon stars, including the effect of molecular opacity due to CO, CN, and C_2 by the Opacity Distribution Function. Johnson (1982) developed model atmospheres of carbon stars with more molecules included. He incorporated the molecular opacity due to CO, CN, C_2 TiO, NH, OH, and MgH by the Opacity Sampling. Scholz & Tsuji (1984) investigated the effect of sphericity in model atmospheres of carbon stars using the straight mean opacity. Jørgensen et al. (1992) recently developed a grid of spherical model atmospheres with the molecular opacity due to the polyatomics such as HCN and C_2H_2 as well as due to the diatomics incorporated by the OS method. Tsuji (1985) used the Band Model method to construct model atmospheres of carbon stars. Tsuji (1994) showed that the temperature stratification as well as the emergent flux calculated by the Band Model well reproduce those calculated by the OS method.

1.2.2 Outer atmosphere

Despite the considerable progress in modeling atmospheres of carbon stars, emergent fluxes predicted from those models have suffered from disagreements with observational data. The predicted strength of molecular band absorption tends to be stronger than observed. The models developed by Jørgensen et al. (1992) are considered to be state-of-the-art, but they do not offer comparison of emergent fluxes with observations. And modelers of atmospheres of cool stars still have a long way to reach a unified picture of the photosphere, outer atmosphere, chromosphere, and circumstellar envelope. Spectroscopic observations of high-resolution show that physical processes beyond the classical assumptions take place in the atmosphere of cool stars. For example, Hinkle et al. (1982) examined low excitation lines of the CO first overtone in an oxygen-rich Mira variable χ Cyg and found the existence of the layers kinematically distinct from the photosphere.

The physical properties of chromosphere of which existence is implied by the UV emission lines of Mg II and Ca II are not well known. Attempts to construct semi-empirical models of the chromosphere are under way including a self-consistent non-local thermodynamical equilibrium treatment both for carbon stars (Luttermoser et al. 1989) and for M giants (Luttermoser et al. 1994). Investigations are also being done to construct empirical models from the photosphere to chromosphere in carbon stars (e.g. Johnson 1991). However, in the case of the Sun, the observation of the CO fundamental bands revealed that the brightness temperature is below what semi-empirical models predict for the solar temperature minimum (Ayres 1981). The coexistence of cool components in the solar chromosphere has been confirmed by Solanski (1994), who did a high-resolution observation of the CO fundamental bands toward the solar limb. Therefore, such thermal bifurcation may occur in cool stars like carbon stars. In fact, intensity anomalies have been already reported in M giants by Tsuji (1988) based on high-resolution spectra of the CO first overtone bands. He attributed such anomalies to an extra component above the photosphere and extracted the physical properties of the cool component in the outer atmosphere. Jørgensen & Johnson (1991) suggested that the outer atmosphere of carbon stars might be inhomogeneous based on synthetic spectra of the CO fundamental bands. They combined a photospheric model of an N-type carbon star, TX Psc, with a semi-empirical chromospheric model and concluded that the CO fundamental lines would exhibit strong emission cores if there were not a cool component coexisting with the hot chromosphere.

On the other hand, Lambert et al. (1984) suggested a possibility that turbulent velocity might be dependent on the depth of atmosphere in order to explain the intensity anomalies of OH lines in red supergiants. Such possibility should be also examined to understand the structure of the outer atmosphere in cool stars.

1.2.3 Circumstellar envelope

Since the discovery of mass loss in an M giant, α Her, by Deutsch (1956), circumstellar envelopes around cool luminous stars have been extensively studied by observations not only in optical and infrared but also in radio domain. The first infrared sky survey carried out in 60's discovered a number of bright infrared objects (Neugebauer & Leighton 1969). Another infrared sky-survey project, AFGL survey (Price & Walker 1976), added further new infrared objects to the database. Many infrared observations have been carried out to study circumstellar envelopes of cool luminous stars. For example, Merrill & Stein (1976a, 1976b, 1976c) obtained spectrophotometric data not only for oxygen-rich and carbon-rich giants but also for more evolved objects such as proto-planetary nebulae. The impact brought about by the IRAS survey (IRAS science team 1985) was also huge for the researches on the circumstellar envelope of late-type stars. These observations have revealed the existence of dust grains in the circumstellar envelope of cool luminous stars. The presence of dust grains is obvious from the thermal emission which has its peak at around 10 μm. The infrared observations have revealed the hump at 11.3 μm due to silicon carbide grain for carbon stars while the feature due to silicate grain is significant in most of oxygen-rich stars.

Recent progress in infrared instrumentation has enabled us to obtain observational data of high spectral and spatial resolution for cool luminous stars. Especially, a dust-enshrouded carbon star IRC+10216 is one of the most extensively studied objects so far. Ridgway & Keady (1988) and Keady & Ridgway (1993) did an observation with high spectral resolution at 10 μm region and derived the detailed information on the kinematics and the molecular concentrations in the circumstellar envelope. The region close to the photosphere, where acceleration of matter is considered to take place, has been also investigated for IRC+10216 because of its proximity of about 120 pc. Sahai & Wannier (1985) employed an annular observing aperture to isolate the radiation from the inner circumstellar envelope. Bloemhof & McLaren (1988) obtained high spatial resolution images at 10 μm and found substantial deviation of density distribution from that expected from spherically symmetric outflow with constant velocity. However, such detailed observations of the inner circumstellar shell are in fact exceptional. For most of carbon stars as well as M giants, our understanding of the inner circumstellar shell or the outer atmosphere is still poor.

Molecular line observations in radio domain have also served to understand the physics and chemistry in the circumstellar envelope. Especially observations of the CO $J = 1-0$ transition have been extensively done because of the large abundance of CO in the circumstellar envelope as well as in the photosphere. Knapp & Morris (1985) observed the CO $J = 1-0$ line for 105 cool evolved objects and obtained the mass loss rates. The observations of molecules other than CO have been also done. The emission lines of CN and CS (Wilson et al. 1971), HCN (Morris et al. 1971), SiS, SiO, and HC_3N (Morris et al. 1975) were detected in IRC+10216. So far about 50 molecular species have been identified in the envelope of IRC+10216 by radio observations. The observations in radio domain can be also used to map the distribution of matter around cool luminous stars. Takano et al. (1992) obtained the distribution of SiC_2 around IRC+10216. The radio continuum emission from circumstellar dust was also detected for IRC+10216 and a proto-planetary nebula CRL 2688 by Knapp et al. (1994).

Theoretical studies have been also made to construct models of the circumstellar envelope around cool luminous stars. Bowen (1988) carried out numerical calculations of dynamical model atmospheres with the pulsation of Mira variables. Recent progress in theoretical formulation of grain formation processes, especially in carbon-rich mixture (e.g. Gail & Sedlmayr 1987, 1988), has led to the construction of hydrodynamical models of the circumstellar envelope around carbon-rich Mira variables (e.g. Fleischer et al. 1992, Feuchtinger et al. 1993, Winters et al. 1994). Further progress such as inclusion of the detailed formation of SiC grains has been made (Kozasa et al. 1996). However, those detailed models should be compared with various observations to establish their validity.

1.3 Evolution to carbon stars – where do they come from?

As the interstellar gas from which stars are born is oxygen-rich (C/O = 0.56 in the Sun), carbon abundance should be enhanced somewhere in stellar evolution in order to make carbon stars. Their high luminosities of 10^3 –10^4 $L_\odot$ and low effective temperatures about 3000 K imply that they should lie in the asymptotic giant branch (AGB). Stars at the AGB have the core of carbon and oxygen surrounded by the helium shell and the hydrogen envelope. Schwarzschild & Härm (1965, 1967) found that the helium-burning reaction at the bottom of the helium shell causes a runaway, which is so called the thermal pulse or the helium shell flash. Theoretical calculations by Iben (1974, 1975, 1976) showed that some of the freshly synthesized carbon can be dredged up into the stellar surface during the power-down phase of the thermal pulse. This dredge-up process, so-called the third dredge-up, is attractive to explain characteristics of carbon stars. The enhancement of the s-process elements in carbon stars (e.g. Utsumi 1985) can be also attributed to the thermal pulse and the third dredge-up, because enough supply of neutron is expected during the thermal pulse via the reaction $^{13}\mathrm{C}(\alpha, n)^{16}\mathrm{O}$.

However, the following calculations by Sugimoto & Nomoto (1975) and by Fujimoto et al. (1976) showed that the third dredge-up could operate in stars with core mass larger than 0.96 $M_\odot$, which corresponds to $M_{\mathrm{bol}} \sim -6.5$. This totally contradicts with the observational studies of carbon stars in the Magellanic Clouds. The observations have demonstrated that carbon stars should achieve their carbon-rich characteristics somewhere in the AGB not brighter than $M_{\mathrm{bol}} \sim -6.0$. Such discrepancy of luminosities of carbon stars between observations and theoretical works has been left unsolved till now as the *carbon star mystery* (Iben 1981). Even theoretical works including the effect of mass loss (e.g. Vassiliadis & Wood 1993) fail to reproduce the luminosity functions of carbon stars in the Magellanic Clouds.

What stars become carbon stars? In the solar neighborhood, carbon stars are in the minority, while M giants are in the majority. What stellar parameters turn a star born as oxygen-rich into a carbon star? A clue to this problem can come from the studies on the distribution of carbon stars in the Galaxy and in extra galaxies. Carbon stars have been also used as probes to investigate the Galactic structure or the stellar content in extra galaxies because of their high luminosities. The catalogues of carbon stars and S stars made by Stephenson (1973, 1976, 1989) are the bases of such studies. Blanco (1965) obtained the distributions of carbon stars and M giants in the Galaxy. He found that carbon stars are more populated in the direction of the anti-Galactic center while M giants are more populated in the direction of the Galactic center. Mavridis (1966) also obtained the apparent distributions of carbon stars and M giants along galactic longitude and found that the distributions of the two types of stars are anti-correlated.

These differences of distribution between carbon stars and M giants became better understood by the studies on the stellar contents in the Magellanic Clouds. Westerlund (1964) surveyed the Large Magellanic Cloud (LMC) and identified 400 carbon stars. It was discovered by this survey that carbon stars are located away from the central part of the system. Extensive studies on the stellar contents in the Magellanic Clouds done so far (e.g. Westerlund et al. 1978, Blanco et al. 1980, Blanco & McCarthy 1983) have revealed that carbon stars are not minority as compared with M giants in the Magellanic Clouds. Such studies on the stellar content have been also done for extra galaxies still farther (e.g. Cook et al. 1986).

What do these observational facts mean? Why are carbon stars located away from the center of the systems both in the Galaxy and in the LMC? Metallicity, probably. These observational facts imply that the carbon star formation may be favored in the environment of lower metallicity. The studies on the stellar content in various extragalactic sources have been done and the relation between the carbon star formation and metallicity has become rather clear (e.g. Pritchet 1987). However, theoretical calculations with the matallicities in the Magellanic Clouds cannot reproduce the luminosity functions of carbon stars, therefore, the carbon star mystery has been unsolved till now from theoretical point of view.

1.4 Chemical composition in carbon stars

Chemical composition at the stellar surface is crucial and fundamental information to understand nuclear reactions in the stellar interior. Given our poor understanding of the interior structure of AGB stars from theoretical point of view, the analysis of abundances in the stellar surface should be given a priority to clarify the evolution of AGB stars. However, accurate abundance analyses for carbon stars have been hampered by two major obstacles. Firstly, the predominance of molecular lines especially in visual spectra of carbon stars drives us to obtain spectroscopic data of high-resolution. Otherwise the measurement of equivalent widths of weak lines, which are essential to accurate determination of abundances, would be impossible because of blending of adjacent lines. And the true continuum level cannot be precisely determined by heavy line blanketing. To make matters worse, as line separations are often narrower than the intrinsic line widths, weak lines are obscured by the wings of strong lines even in very high resolution spectra. The other obstacle in accurate determination of abundances in carbon stars is the validity of model atmospheres. Model atmospheres play a critical role in determination of abundances. But as mentioned above, construction of model atmospheres of cool stars has been a tedious process. The development of realistic model atmospheres and the accurate determination of abundances should be regarded as both sides of a coin.

Chemical composition at the surface of carbon stars has been controversial till now by the reasons above. To derive abundances of C, N, O, and their isotopic ratios, which are in fact the most essential information to clarify the evolution to carbon stars, molecular lines of CO, C_2, CN, CH, etc. have been used. Lines of CN and C_2 in visual spectra have been used to derive isotopic ratios of carbon ($^{12}C/^{13}C$) and nitrogen ($^{14}N/^{15}N$) (e.g. Querci & Querci 1970). For determination of isotopic ratios, Fujita & Tsuji (1977) developed the iso-intensity method to avert the difficulty in defining the true continuum level in visual spectra. Ohnaka & Tsuji (1996, 1997) applied the iso-intensity method to determine $^{12}C/^{13}C$ ratios in more than 100 carbon stars from lines of CN around 8000 Å.

However, elemental abundances can be derived from infrared spectra where molecular line blanketing is less severe and the continuum level can be also relatively well defined. Lambert et al. (1986) determined the elemental abundances of C, N, O, and $^{12}C/^{13}C$ ratios based on high-resolution infrared spectra and the model atmospheres including the opacity due to CO, C_2, CN, HCN and C_2H_2. Their work is almost the only one to have analyzed the elemental abundances in a large sample of carbon stars and their result has been widely referred. Infrared spectra have been also used to derive oxygen isotopic ratios, $^{16}O/^{17}O$ and $^{16}O/^{18}O$, by Harris et al. (1987). But the chemical composition in carbon stars should never be regarded as well-established. The systematic disagreements can be found even in the results of isotopic ratios, of which determination has been believed to be easier than that of elemental abundances. In fact, the $^{12}C/^{13}C$ ratios derived by Ohnaka & Tsuji (1996) were by a factor of 2 to 3 smaller than those derived by Lambert et al. (1986). For elemental abundances, Goebel et al. (1993) analyzed the oxygen abundance of TX Psc based on high resolution spectra acquired with the Kuiper Airborne Observatory. Their result that the oxygen abundance is depleted by roughly two orders of magnitude than the solar value shows a marked contrast to the result by Lambert et al. (1986) who derived the oxygen abundance only slightly subsolar.

Chemical composition in the circumstellar envelope is also an important clue to understand the evolution of AGB stars. The abundance determination in the circumstellar envelope has been extensively done in the millimeter and submillimeter wavelengths. Kahane et al. (1988) derived carbon, nitrogen, sulfur, and silicon isotopic ratios in the envelope of IRC+10216 from the observations of optically thin lines of HCN, HNC, HC_3N, CS, SiO, SiS, and SiC_2. The studies of isotopic ratios in dusty circumstellar envelopes have been extended to objects such as proto-planetary nebulae (e.g. Wannier et al. 1991, Kahane et al. 1992). On the other hand, Olofsson et al. (1993) did an extensive study on molecular abundances in not so dusty circumstellar envelopes around bright carbon stars. They found that the $^{12}C/^{13}C$ ratios derived from CO and HCN lines in the millimeter wavelength were by a factor of about 2 smaller than the photospheric ratios derived by Lambert et al. (1986). However, their $^{12}C/^{13}C$ ratios in the circumstellar envelopes are in fact consistent with the photospheric ratios determined by Ohnaka & Tsuji (1996).

Despite its importance in understanding the evolution of AGB stars, chemical composition in carbon stars still suffers systematic uncertainties. Especially photospheric composition is by no means well-established as reviewed above. One should be very careful in analyzing the spectra of carbon stars because the quality of results of abundance analyses is dependent on the validity of model atmospheres as well as on the method of analyses.

1.5 Goal of the research and outline of the thesis

The story began from the analysis of carbon isotopic ratios in a large sample of carbon stars. In Ohnaka & Tsuji (1996, 1997) we have analyzed $^{12}C/^{13}C$ ratios in more than 100 stars from lines of the CN Red system around 8000 Å. The line blanketing is less severe around this spectral region than in the visual region for carbon stars. However, many lines of CN and C_2 almost obscure the true continuum and make it almost impossible to do the standard analysis using equivalent widths or the spectrum synthesis. We instead used the iso-intensity method, which will be described in Chapters 2 and 3. The resulting $^{12}C/^{13}C$ ratios in N-type carbon stars have turned out to be systematically smaller than the values derived by Lambert et al. (1986). The discrepancy could be more serious because the $^{12}C/^{13}C$ ratios we derived are by a factor of 2 to 3 smaller than those of Lambert et al. (1986) for the *same* stars. We found that the model atmospheres used in the analysis by Lambert et al. (1986) might have been by more than 500 K cooler than those we used. This could be seen in the emergent flux of their models: the 3 μm absorption feature predicted by their models is stronger than observed. But we could not specify firm reasons for the discrepancy of the $^{12}C/^{13}C$ ratios.

If the model atmospheres of Lambert et al. (1986) were not totally justified, their analysis of elemental abundances of carbon, nitrogen, and oxygen should be also again examined. The effect of atmospheric structure could be more considerable in the analysis of elemental abundances. To examine possible effects of the atmospheric structure on the analysis of chemical composition in carbon stars, the re-analysis of the spectra of Lambert et al. (1986) is undoubtedly the best and logical way. The goal of the research is to determine the elemental abundances of carbon and oxygen as accurately as possible by re-analyzing their spectra and to clarify the effect of atmospheric structure on the abundance analysis in carbon stars. The result of Lambert et al. (1986) could be characterized by C/O ratios rather close to unity. In fact, they concluded that about a half of their program stars have $C/O < 1.1$. The importance of C/O ratio in the chemical composition in the photosphere cannot be overemphasized. Chemistry not only in the photosphere but also in the circumstellar envelope is actually governed by C/O ratio, because the amount of carbon available to form molecules other than CO is given by $(C/O - 1) \times \varepsilon(O)$. Thus, accurate analysis of carbon and oxygen abundances is of prime importance to clarify the evolution of carbon stars as well as to understand various chemical processes, including the grain formation, in the circumstellar envelope.

The analysis of $^{12}C/^{13}C$ ratios in a large sample of carbon stars, which triggered the following works, is presented in Chapters 2 and 3. Chapter 2 includes the analysis for N- and SC-type carbon stars while Chapter 3 includes that for J-type carbon stars.

In Chapter 4, the development of a new code of spherical model atmosphere of carbon stars is presented. The effect of chemical composition on the atmospheric structure will be discussed. The effect of sphericity on synthetic spectra will be also investigated. The emergent fluxes of the new model atmospheres will be compared with the ISO observations to check the validity of the new models.

In Chapter 5, which is the heart of this thesis, a self-consistent analysis of the elemental abundances of carbon and oxygen is presented. The spectral data are those analyzed by Lambert et al. (1986). The analysis has been done in the way that has never been applied before, with the interplay between the atmospheric structure and the chemical composition fully taken into account. The resulting abundances of carbon and oxygen will be compared with those of Lambert et al. (1986) and the methods of both analyses will be discussed. In the final part of the Chapter, the results of C/O ratios and $^{12}C/^{13}C$ ratios will be discussed in view of the evolution of carbon stars.

The outer atmosphere of carbon stars will be investigated based on the high-resolution spectra in Chapter 6. We will present analysis of the CO first overtone lines in the carbon stars for which the abundances are determined. The intensity anomalies such as reported in M giants (Tsuji 1988) are also found in low excitation lines for the three carbon stars studied. The depth-dependent turbulent velocity hypothesis will be examined by numerical experiments. With the synthetic spectra from the model photospheres, we will extract information on the physical properties of extra components above the photosphere. Possible pictures of the outer atmosphere of carbon stars will be presented to explain the intensity anomalies of the CO low excitation lines.

References

Alexander D.R., Augason G.C., Johnson H.R., 1989, ApJ 345, 1014
Auman J.R., 1967, In: Colloquium on Late-type Stars, ed. Hack M., Astron. Obs. Trieste, p.313
Ayres T.R., 1981, ApJ 244, 1064
Blanco V.M., 1965, In: Galactic Structure, ed. Blaauw A., Schimidt M., Chicago, University of Chicago Press, p.241
Blanco V.M., McCarthy M.F., 1983, AJ 88, 1442
Blanco V.M., McCarthy M.F., Blanco B.M., 1980, ApJ 242, 938
Bloemhof E.E., McLaren R.A., 1988, ApJ 333, 300
Bouigue R., 1954, Ann. d'Astrophys. 17, 104
Bowen G.H., 1988, ApJ 329, 299
Cannon A.J., Pickering E.C., 1918, Ann. Harvard Coll. Obs. 91, 10
Carbon D.F., 1984, In: Methods in Radiative Transfer, ed. Kalkofen W., Cambridge, Cambridge Univ. Press, p.99
Cook K.H., Aaronson M., Norris J., 1986, ApJ 305, 634
Deutsch A., 1956, ApJ 123, 210
Ekberg U., Eriksson K., Gustafsson B., 1986, A&A 167, 304
Feuchtinger M.U., Dorfi E.A., Höfner S., 1993, A&A 273, 513
Fleischer A.J., Gauger A., Sedlmayr E., 1992, A&A 266, 321
Frogel J.A., Mould J., Blanco V.M., 1990, ApJ 352, 96
Fujimoto M.Y., Nomoto K., Sugimoto D., 1976, PASJ 28, 89
Fujita Y., 1939, Jap. Journ. Astr. and Geophys. 17, 17
Fujita Y., Tsuji T., 1977, PASJ 29, 711
Gail H.-P., Sedlmayr E., 1987, A&A 171, 197
Gail H.-P., Sedlmayr E., 1988, A&A 206, 153
Goebel J.H., Goorvitch D., Larson H.P., Alexander D.R., 1993, ApJ 402, 680
Gordon C.P., 1971, PASP 83, 667
Harris M.J., Lambert D.L., Hinkle K.H., Gustafsson B., Eriksson K., 1987, ApJ 316, 294
Hinkle K.H., Hall D.N.B., Ridgway S.T., 1982, ApJ 252, 687
Iben I.Jr., 1974, Bull. AAS 6, 316
Iben I.Jr., 1975, ApJ 196, 525
Iben I.Jr., 1976, ApJ 208, 165
Iben I.Jr., 1981, ApJ 246, 278
IRAS Catalogs and Atlases, Explanatory Supplement, 1985, ed. Beichman C.A., Neugebauer G., Habing H.J., Clegg P.E., Chester T.J., (Washington, DC:GPO)
Johnson H.R., 1982, ApJ 260, 254
Johnson H.R., 1986, In: The M-type Stars, eds. Johnson H.R., Querci F., NASA SP-492, p.323
Johnson H.R., 1991, A&A 249, 455
Jørgensen U.G., Johnson H.R., 1991, A&A 244, 462
Jørgensen U.G., Johnson H.R., Nordlund Å., 1992, A&A 261, 263
Kahane C., Cernicharo J., Gómez-González J., Guélin M., 1992, A&A 256, 235
Kahane C., Gomez-Gonzalez J., Cernicharo J., Guélin M., 1988, A&A 190, 167
Keady J.J., Ridgway S.T., ApJ 406, 199
Keenan P.C., 1954, ApJ 120, 484
Keenan P.C., Morgan W.W., 1941, ApJ 94, 501

Knapp G.R., Bowers P.F., Young K., Phillips T.G., 1994, ApJ 429, L33
Knapp G.R., Morris M., 1985, ApJ 292, 640
Kozasa T., Dorschner J., Henning T., Stognienko R., 1996, A&A 307, 551
Lambert D.L., Brown J.A., Hinkle K.H., Johnson H.R., 1984, ApJ 284, 223
Lambert D.L., Gustafsson B., Eriksson K., Hinkle K.H., 1986, ApJS 62, 373
Luttermoser D.G., Johnson H.R., Avrett E.A., Loeser R., 1989, ApJ 345, 54
Luttermoser D.G., Johnson H.R., Eaton J.A., 1994, ApJ 422, 351
Mavridis L.N., 1966, In: Colloquim on Late-Type Stars, ed. Hack M., Astron. Obs. Trieste, p.420
Merrill P.W., 1922, ApJ 56, 457
Merrill K.M., Stein W.A., 1976, PASP 88, 285
Merrill K.M., Stein W.A., 1976, PASP 88, 294
Merrill K.M., Stein W.A., 1976, PASP 88, 874
Morris M., Gilmore W., Palmer P., Turner B.E., Zuckerman B., 1975, ApJ 199, L47
Morris M., Zuckerman B., Palmer P., Turner B.E., 1971, ApJ 170, L109
Neugebauer G., Leighton R.B., 1969, Two Micron Sky Survey, NASA SP-3047, Washington
Ohnaka K., Tsuji T., 1996, A&A 310, 933
Ohnaka K., Tsuji T., 1997, A&A, submitted
Olofsson H., Eriksson K., Gutafsson B., Carlström U., 1993, ApJS 87, 305
Price S.D., Walker R.D., 1976, The AFGL Four Color Infrared Sky Survey, Air Force Geophys. Lab. Thec. Rep. No. AFGL TR-76-0208
Pritchet C.J., Richer H.B., Schade D., Crabtree D., Yee H.K.C., 1987, ApJ 323, 79
Querci M., Querci F., 1970, A&A 9, 1
Querci F., Querci M., 1975, A&A 39, 113
Querci F., Querci M., Tsuji T., 1974, A&A 31, 265
Ridgway S.T., Keady J.J., 1988, ApJ 326, 843
Russell H.N., 1934, ApJ 79, 317
Sahai R., Wannier P.G., 1985, ApJ 299, 424
Scholz M., Tsuji T., A&A 130, 11
Schwarzschild M., Härm R., 1965, ApJ 142, 855
Schwarzschild M., Härm R., 1967, ApJ 150, 961
Secchi A., 1868, Mem. Soc. Ital. Sienze (3) 2, 73
Shane C.D., 1928, Lick Bull. 13, 123
Solanski S.K., Livingston W., Ayres T., 1994, Science 263, 64
Stephenson C.B., 1973, Publ. Warner and Swasey Obs. 1., No.4
Stephenson C.B., 1976, Publ. Warner and Swasey Obs. 2., No.2
Stephenson C.B., 1989, Publ. Warner and Swasey Obs. 3., No.2
Sugimoto D., Nomoto K., 1975, PASJ 27, 197
Takano S., Saito S., Tsuji T., 1992, PASJ 44, 469
Tsuji T., 1964, Ann. Tokyo Astr. Obs. 2nd Ser. 9, 1
Tsuji T., 1967, In: Colloquium on Late-Type Stars, ed. Hack M., Astron. Obs. Trieste, p.260
Tsuji T., 1985, In: Cool Stars with Excesses of Heavy Elements, eds. Jaschek M., Keenan P.C., Reidel, Dordrecht, Holland, p.93
Tsuji T., 1994, In: Molecular Opacities in the Stellar Environment ed. Jørgensen U.G., Lecture Notes in Physics, Springer-Verlag, p.79
Tsuji T., 1988, A&A 197, 185

Utsumi K., 1985, In: Cool Stars with Excesses of Heavy Elements, eds. Jaschek M., Keenan P.C., Reidel, Dordrechet, Holland, p.243
Vassiliadis E., Wood P.R., 1993, ApJ 413, 641
Wannier P.G., Andersson B.-G., Olofsson H., Ukita N., Young K., 1991, ApJ 380, 593
Westerlund B.E., 1964, In: The Galaxy and the Magellanic Clouds, I.A.U. - U.R.S.I. Symp. No. 20, ed. Kerr F.J., Rodgers A.W., Canberra, Australian Academy of Science, p.239
Westerlund B.E., Olander N., Richer H.B., Crabtree D.R., 1978, A&AS 31, 61
Wilson R.W., Solomon P.M., Penzias A.A., Jefferts K.B., 1971, ApJ 169, L35
Winters J.M., Fleischer A.J., Gauger A., Sedlmayr E., 1994, A&A 290, 623
Yamashita Y., 1972, Ann. Tokyo Astr. Obs. 2nd Ser. 13, 169
Yamashita Y., 1975, Ann. Tokyo Astr. Obs. 2nd Ser. 15, 47

Chapter 2

Quantitative Analysis of Carbon Isotopic Ratios in Carbon Stars I. 62 N-type and 15 SC-type carbon stars

This chapter has been published in Astronomy and Astrophysics, 310, 933-951 (1996)
as
Quantitative analysis of carbon isotopic ratios in carbon stars
I. 62 N-type and 15 SC-type carbon stars
by
Keiichi Ohnaka,
Institute of Astronomy, The University of Tokyo
Takashi Tsuji,
Institute of Astronomy, The University of Tokyo

Abstract

We present a result of quantitative analysis of $^{12}C/^{13}C$ ratios in 62 N-type and 15 SC-type carbon stars. By the use of CCD as a detector we can obtain spectra of resolution $\sim 20{,}000$ with enough signal-to-noise ratios for a large number of carbon stars, for which $^{12}C/^{13}C$ ratios have not yet been derived. Carbon isotopic ratios are determined from lines of the CN red system around 8000 Å, based on the iso-intensity method and line-blanketed model atmospheres.

The average of $^{12}C/^{13}C$ ratios in 62 N-type carbon stars is found to be 27 ± 11 (standard deviation). The majority of the N-type carbon stars studied (about 85%) are found to have $^{12}C/^{13}C$ ratios less than 40, and the number of stars which have $^{12}C/^{13}C$ ratios larger than 40 is found to be relatively small. This result shows a marked contrast to some of the previous results that have shown the opposite distribution, namely, $^{12}C/^{13}C$ ratios mostly larger than 40 in N-type carbon stars.

The average of $^{12}C/^{13}C$ ratios in 15 SC-type carbon stars is found to be 22 ± 14 (standard deviation). Most of the SC-type carbon stars studied are found to have $^{12}C/^{13}C$ ratios larger than 10, while only three of them turn out to be ^{13}C-rich. This is in contrast with the earlier classification based on low resolution spectra which classified them as J-type, that is, ^{13}C-rich. The earlier temperature scale which classified SC-type carbon stars as the latest (C8 – 9) based on their strong Na I D lines can not be necessarily justified. The strong Na I D lines of SC stars should be attributed to the peculiar atmospheric structure due to C/O ratios very near to unity.

The resulting $^{12}C/^{13}C$ ratios are partly consistent with the scenario in which M giants evolve through SC-type to N-type carbon stars, as ^{12}C produced during the helium shell flash is added to the envelope.

2.1 Introduction

Carbon stars were first recognized by Secchi (1868) as a group of cool stars which show the distinct bands of possibly carbon-bearing molecules, instead of the bands seen in the spectra of another type of cool stars (now known as M stars). This peculiar spectral appearance was later attributed to the chemical composition of the stellar atmosphere in which carbon is more abundant than oxygen (Russell 1934). Carbon stars are, however, a heterogeneous group of stars, sharing only the photospheric composition C/O $>$ 1. They were classified into two groups, R and N, on the Harvard system (Cannon & Pickering 1918); the redder stars were N-type and the less red ones were R-type. Merrill (1922) introduced a new group of cool stars called S stars, which were characterized by the absence of strong molecular absorption and the presence of the distinct bands of ZrO and LaO replacing TiO bands found in M stars. The absence of strong molecular absorption was later attributed to the chemical composition of the atmosphere in which the abundances of carbon and oxygen are nearly equal (Fujita 1939). Since most of oxygen and carbon are locked into CO molecules, little of them are left behind to form other molecules. Later, some stars classified as S stars were found to show weak bands of TiO, others were found to show weak bands of C_2. These stars were classified as MS and SC stars, respectively. These groups of peculiar red giant stars, MS, S, and SC, are thought to be on the gradual spectral sequence from oxygen-rich to carbon-rich atmosphere. In addition to these peculiar stars, there exists another type of carbon stars called J-type. They are characterized by very strong features of ^{13}C-bearing molecules.

Keenan & Morgan (1941) introduced a new classification of carbon stars, which is now known as the C-classification. It was based on several spectroscopic features that were expected to be good indicators of fundamental parameters of stellar atmospheres such as effective temperature and C/O ratio. In fact, the C-classification employed the strength of Na I D lines as an indicator of temperature and the strength of C_2 bands as an indicator of carbon abundance. It has been, however, pointed out by Tsuji (1981) that the temperature scale of the C-classification is in poor correlation with effective temperatures derived by the InfraRed Flux Method, which will be described in Sect. 2.5.1. It has been suspected that the strength of D lines, the major criterion of the C-classification, may be affected by the C/O ratio of the stellar atmosphere as well as the effective temperature.

After we had a brief review of various types of carbon stars, a question arises: Why do carbon stars exist? How should we understand them, including various subclasses, from a point of view of stellar evolution? This problem has been controversial for a long time. Carbon stars, except for R-type carbon stars, have high luminosities of 10^3 – 10^4 $L_\odot$ and effective temperatures about 3000 K. These facts suggest that they lie on the asymptotic giant branch (AGB). Intermediate- and low-mass stars ($1M_\odot \lesssim M \lesssim 8M_\odot$) arrive at the AGB stage with the degenerated core of carbon and oxygen, the helium shell overlying it surrounded by the hydrogen envelope. AGB stars undergo the double shell burning, that is, the quiescent hydrogen shell burning and the unstable helium shell burning, which is called the helium shell flash or the thermal pulse. The ^{12}C produced via the triple-α process during the thermal pulse is dredged up into the surface, which is so-called the third dredge-up. If enough amount of carbon is dredged up into the surface, an oxygen-rich atmosphere becomes carbon-rich. The spectral sequence of M-MS-S-SC-C (N-type carbon stars) can be interpreted as an evolutionary sequence from an oxygen-rich star to a carbon star. The enhanced atomic lines of the s-process elements such as Zr, Ba, and Sr observed in N and SC stars and the bands of ZrO or LaO observed in S and MS stars lend a support to this scenario. Enhancements of the s-process elements can be attributed to the thermal pulse, during which enough neutron supply is expected via the reaction $^{13}C(\alpha,n)^{16}O$ or $^{22}Ne(\alpha,n)^{25}Mg$.

This scenario seems qualitatively correct, but it fails to account for observational facts quantitatively. For example, theoretical calculations (e.g. Iben 1981), even one including mass loss (e.g. Vassiliadis & Wood 1993), fail to predict the luminosity function of carbon stars observed in the Magellanic Clouds (e.g. Blanco, McCarthy, & Blanco 1980; Frogel & Cohen 1982). The result by Vassiliadis & Wood (1993) says that the third dredge-up is effective enough to turn oxygen-rich stars into carbon stars only in massive stars ($> 5\ M_{\odot}$), therefore, they cannot reproduce a large amount of low luminosity carbon stars observed in the Magellanic Clouds. And theoretical calculations had predicted a large amount of carbon stars of high luminosity ($M_{\rm BOL} < -6.0$), none of which is observed in the Magellanic Clouds. But Blöcker & Schönberner (1991) demonstrated that a 7 $M_{\odot}$ stellar model develops a deep convective envelope all the way down to the hydrogen burning shell and that any dredged-up ^{12}C is rapidly converted into ^{14}N, turning a carbon star back into a nitrogen-rich M giant.

It is unknown what parameters are decisive for an oxygen-rich star to become a carbon star: initial mass, metalicity or anything else? Since the ratios of carbon stars to M giants in the Magellanic Clouds are considerably higher than in the Galaxy, the carbon star formation is thought to be favored in lower metallicity. But theoretical evolutionary models cannot reproduce the luminosity function of carbon stars observed in the Magellanic Clouds, as mentioned above. The carbon isotopic ratio brings us important information about the nucleosynthesis and mixing in the stellar interior, because carbon is one of the elements involved in the nucleosynthesis in the thermal pulse and mixing into the surface. If the scenario mentioned above is correct, at least in a sense that ^{12}C synthesized in the thermal pulse is responsible for the formation of carbon stars, $^{12}C/^{13}C$ ratios of N and SC stars are expected to be enhanced as compared with those of their progenitors, and have a correlation with C/O ratios.

To demonstrate this correlation, we have carried out a quantitative analysis of carbon isotopic ratios from lines of CN located around 8000 Å, for a large sample of carbon stars, including N, SC, J, and R stars. Our main purpose is to find the distribution of $^{12}C/^{13}C$ ratios of each type of carbon stars based on a large sample, and to find some connections between carbon stars and G, K, and M giants, which are considered to be their progenitors. In this Paper I, we present an analysis of $^{12}C/^{13}C$ ratios in N and SC stars. Generally speaking, isotopic ratios are thought to be easier to determine than elemental abundances. It is true, however, that the previous results do not necessarily agree with one another. Disagreements among the previous results will be discussed. We will discuss the formation of N and SC stars, based on our result of $^{12}C/^{13}C$ ratios as well as the previous results of $^{12}C/^{13}C$ ratios and C/O ratios in G, K, and M giants. We will also discuss the tests of our model atmospheres by Na I D lines and H_2 1 - 0 S(0) line, because we find that the analysis of $^{12}C/^{13}C$ ratios is largely dependent on the adopted model atmospheres.

2.2 Observation

The program stars are summarized in Tables 1 and 2. The sample consists of 66 N and 19 SC stars, most of which were selected from lists of carbon stars with the C-classification (Yamashita 1972, 1975), those with comments on spectral peculiarities (Dean 1976), and those with the revised MK classification (Keenan & Boeshaar 1980). The IRAS database (NASA) and Stephenson (1973, 1976, and 1989) were also important references. We also emphasized such stars for which photometric data are available.

All observations were carried out using the 74-inch telescope of Okayama Astrophysical Observatory (OAO[1]), during the period between October 1987 and March 1994. The spectrograph was set at the coudé focus, equipped with a 640×1024 CCD (RCA) with pixel size of 15×15 μm. We used the F/10 camera with 1200 grooves/mm grating which is blazed to 7500 Å. The linear dispersion is 8 Å/mm and the 3 pixels resolution is 0.36 Å. The measured full width at half maximum of thorium comparison line appears to be about 0.4 Å, therefore, the spectral resolution is about 20,000. The signal-to-noise ratios are estimated by photon statistics. They are about 100, although somewhat lower for faint stars and much higher for some bright stars.

All spectra consist of two adjacent exposures, covering from 7800 to 8030 Å. Each exposure covers 120 Å with an overlap of 10 Å allowed. For TX Psc, in addition to these two exposures, three more exposures were taken to cover from 7680 to 8250 Å. The data reduction was done in the usual way by correcting pixel responses with uniformly illuminated exposures after we subtracted dark levels. The calibration of wavelength was done using the lines of Th-Ne listed by Palmer & Engleman (1983). We also observed spectra of hot stars, such as Vega, Sirius, and Regulus, in order to check the contamination of telluric lines. The contamination turned out to be not severe in winter, but rather remarkable in summer. The lines contaminated with telluric lines are not used in the analysis anyway.

[1] OAO is a branch of National Astronomical Observatory of Japan (NAOJ). This work was carried out under the common use program of OAO.

Table 1. Summary of observations for N-type carbon stars

GCCGCS	CCCS	Name	C-Class	m_V	Date Observed	S/N
32	10	ST Cas	C4,4	7.5 – 9.0	1992 Nov 17	80
					1992 Nov 17	100
65	16	AQ And	C5,4	7.92	1990 Dec 27	200
					1990 Dec 27	700
198	63	Z Psc	C7,2	7.4 – 8.1	1988 Oct 26	800
					1988 Oct 25	400
234	68	R Scl	C6,4	6.2 – 8.8	1993 Nov 27	220
					1993 Nov 24	260
238	70	WW Cas	C7,1e	9.1 – 11.7	1993 Nov 22	180
					1993 Nov 23	100
295	87	X Cas	C5,4e	8.4 – 13.1	1993 Nov 24	200
					1993 Nov 24	120
350	99	BS Per	C5,5	9.5	1993 Nov 28	320
					1993 Nov 28	180
461	134	HD19881	C7,4	9.2	1992 Nov 17	110
					1992 Nov 17	130
540	154	U Cam	C5,4	7.55	1991 Mar 2	480
					1991 Mar 1	1000
541	155	BD+51°762	C5,5	8.9	1992 Nov 17	160
					1992 Nov 17	260
556	157	AC Per	C6,3	9.5	1992 Nov 15	160
					1992 Nov 15	130
769	240	ST Cam	C5,4	7.0 – 8.3	1991 Mar 2	600
					1991 Mar 1	1000
794	254	TT Tau	C7,4	8.1 – 8.8	1990 Dec 27	400
					1990 Dec 26	120
853	284	W Ori	C5,4	5.9 – 7.7	1990 Dec 24	1100
					1990 Dec 26	500
860	288	TX Aur	C5,4	8.5 – 9.2	1993 Feb 5	60
					1993 Feb 5	80
875	297	SY Eri	C6,3	8.6	1993 Nov 24	160
					1993 Nov 24	60
904	313	HD34467	C6,3	9.1	1992 Nov 17	100
					1992 Nov 17	130
988	364	RT Ori	C6,4	7.5 – 8.5	1991 Mar 2	160
					1991 Mar 1	160
1004	373	HD37212	C6:,4	7.48	1991 Mar 6	140
					1991 Mar 3	140
1038	390	TU Tau	C5,4	8.7 – 9.5	1993 Feb 5	83
					1993 Feb 5	65

Table 1. — Continued

GCCGCS	CCCS	Name	C-Class	m_V	Date Observed	S/N
1042	393	Y Tau	C6,4	6.5 – 8.9	1992 Nov 14	190
					1992 Nov 15	400
1061	402	FU Aur	C7,2	9.0 – 9.3	1993 Feb 6	60
					1993 Feb 6	57
1179	461	TU Gem	C6,4	7.4 – 8.3	1992 Mar 21	100
					1992 Mar 18	160
1222	480	GK Ori	C5,4	9.5	1993 Feb 7	50
					1993 Feb 7	38
1251	501	ZZ Gem	C5,3e	8.9 – 9.9	1993 Feb 5	50
					1993 Feb 5	80
1264	508	BL Ori	C6,3	4.7 – 6.6	1990 Dec 24	100
					1990 Dec 26	180
1316	537	UU Aur	C6,4	5.1 – 6.8	1990 Dec 24	60
					1990 Dec 23	500
1355	558	VW Gem	C5,4	8.6 – 8.8	1993 Feb 2	180
					1993 Feb 1	150
1378	573	CZ Mon	C4,5	9.45	1993 Feb 6	61
					1993 Feb 6	37
1401	584	DF Mon		10.6	1993 Feb 5	53
					1993 Feb 5	120
1453	609	GY Mon	C6,3	8.07	1993 Feb 2	90
					1993 Feb 1	130
1465	615	CL Mon	C6,3e	9.0	1993 Nov 22	80
					1993 Nov 23	30
1489	632	RV Mon	C4,4	6.88	1991 Mar 6	80
					1991 Mar 3	200
1549	670	RY Mon	C5,5	8.09	1991 Mar 6	140
					1991 Mar 3	360
1565	676	W CMa	C6,3	6.59	1991 Mar 6	500
					1991 Mar 3	360
1616	695	BD+5°1606	C5,5	9.5	1993 Nov 22	300
					1993 Nov 23	80
1737	779	HD59643	C6,2	7.80	1991 Mar 6	100
					1991 Mar 3	90
1877	897	GO Pup		10.43	1993 Nov 24	140
					1993 Nov 25	140
2150	1123	RY Hya	C6,4e	8.3 – 9.6	1993 Feb 6	10
					1993 Feb 6	54
2177	1147	AC Pup	C5,4	9.15	1993 Nov 22	120
					1993 Nov 23	80
2378	1338	X Cnc	C5,4	5.9 – 7.5	1990 Apr 14	80
					1990 Apr 13	300

Table 1. — Continued

GCCGCS	CCCS	Name	C-Class	m_V	Date Observed	S/N
2384	1344	T Cnc	C5,5	7.89	1990 Dec 23	240
					1990 Dec 22	200
2641	1566	Y Hya	C4,5	6.5 – 8.0	1990 Dec 26	700
					1990 Dec 26	100
2803	1714	U Hya	C6,3	4.8 – 5.9	1990 Dec 22	1400
					1990 Dec 21	1000
2835	1736	VY UMa	C6,3	6.0 – 6.6	1990 Apr 15	400
					1990 Apr 15	100
2877	1766	V Hya	C6,5	6.7 – 12.0	1990 Dec 27	260
					1990 Dec 26	154
3236	1999	SS Vir	C5,3e	6.0 – 9.6	1990 Dec 27	212
					1990 Dec 26	136
3698	2334	V Oph	C7,3e	7.0 – 10.5	1994 Mar 23	100
					1994 Mar 24	140
3901	2499	V781 Sgr		9.7	1994 Mar 26	60
					1994 Mar 27	180
3921	2512	T Dra	C6,2e	7.2 – 14.0	1992 Mar 21	71
					1992 Mar 18	118
	2602	TY Oph	C5,5	9.5 – 10.1	1994 Mar 23	260
					1994 Mar 24	40
4052	2620	RX Sct	C5,5	8.99	1991 Mar 2	100
					1991 Mar 1	100
4089	2651	HK Lyr	C7,4	8.1	1993 Feb 2	140
					1993 Feb 4	130
4121	2666	S Sct	C6,4	7.0 – 8.0	1991 Mar 2	240
					1991 Mar 1	160
4164	2695	V Aql	C5,4	6.7 – 8.2	1991 Mar 2	560
					1991 Mar 3	240
4241	2724	U Lyr	C4,5e	8.3 – 13.5	1994 Mar 26	60
					1994 Mar 27	100
4307	2739	AW Cyg	C4,5	8.0 – 10.2	1993 Feb 4	120
					1993 Feb 4	130
4333	2744	AQ Sgr	C7,4	6.6 – 7.6	1994 Mar 26	400
					1994 Mar 27	260
4415	2773	TT Cyg	C5,4	7.3 – 8.4	1993 Feb 4	140
					1993 Feb 4	140
4581	2833	AX Cyg	C4,5	7.4 – 7.9	1994 Mar 26	400
					1994 Mar 27	400
4653	2853	X Sge	C6,4	8.7 – 9.7	1993 Nov 25	240
					1993 Nov 28	120
5418	3060	V460 Cyg	C6,3	6.05	1987 Nov 27	140
					1987 Nov 28	320

Table 1. — Continued

GCCGCS	CCCS	Name	C-Class	m_V	Date Observed	S/N
5425	3063	RV Cyg	C6,4	7.1 – 9.3	1993 Nov 27	240
					1993 Nov 28	320
5719	3152	DG Cep	C7,4	8.84	1993 Nov 22	140
					1993 Nov 23	140
5928	3202	TX Psc	C7,2	5.30	1993 Nov 27	200
					1993 Nov 27	200
					1993 Nov 25	60
					1993 Nov 28	400
					1993 Nov 28	340
5987	3219	SU And	C6,4	8.5	1993 Nov 24	120
					1993 Nov 24	200

2.3 Molecular Data

The line positions of the ^{12}CN red system are given in Davis & Phillips (1963). For ^{13}CN, Wyller (1966) analyzed (2,0) and (3,1) bands of the red system and listed the positions of 437 rotational lines. The line of ^{13}CN is located at the wavelength longer by about 40 Å than the corresponding line of ^{12}CN due to the isotope effect. The gf-value of individual line of ^{12}CN is calculated by

$$gf = f_{v'v''} S_{J'J''} \frac{\lambda_{v'v''}}{\lambda}$$

where λ is the wavelength of the individual line, $\lambda_{v'v''}$ is the wavelength of the band origin of the (v', v'') band, $f_{v'v''}$ is the band oscillator strength defined at $\lambda_{v'v''}$, and $S_{J'J''}$ is the Hönl-London factor, which is well determined for each line. The values of $f_{v'v''}$ are based on the result by Bauschlicher et al. (1988). The gf-values of lines of ^{13}CN are reasonably assumed to be identical with those of the corresponding lines of ^{12}CN.

The oscillator strengths of transitions of the CN red system have never been well determined. For example, $f_{20} = 9.1 \times 10^{-4}$, which is adopted in this work, by Bauschlicher et al. (1988), while the experimental value is 7.6×10^{-4} by Davis et al. (1986). But the uncertainty does not affect the resulting ^{12}C/^{13}C ratios as long as we assume that the gf-values of the corresponding lines of ^{12}CN and ^{13}CN are identical.

The dissociation energy of CN molecule has been also uncertain. We adopted the value 7.66 eV (Engleman & Rouse 1975). But this uncertainty cancels out in deriving the isotopic ratios as long as we assume that the dissociation energy is identical for ^{12}CN and ^{13}CN.

Table 2. Summary of observations for SC-type carbon stars. Numbers in parentheses are from A General Catalogue of S Stars (GCSS; Stephenson 1976)

GCCGCS	CCCS	Name	C-Class	m_V	Date Observed	S/N
136	38	W Cas	C7,1e	8.6 – 11.8	1992 Nov 14	130
					1992 Nov 13	120
579	166	V372 Mon		11.0	1993 Feb 4	70
					1993 Feb 4	80
797	257	BD+38°955	C8,1J	8.64	1990 Dec 22	160
					1990 Dec 21	200
	(87)	GP Ori	C8,0J	9.43	1991 Mar 2	260
					1991 Mar 1	80
911	318	UV Aur	C8,1Je	7.9 – 10.1	1990 Dec 24	66
					1990 Dec 26	74
998	370	S Cam	C7,2Je	7.8 – 10.8	1990 Dec 24	60
					1990 Dec 23	60
	(146)	FU Mon	C8,0J	9.06	1990 Dec 24	180
					1990 Dec 23	80
1561	675	R CMi	C7,1Je	9.41	1990 Dec 24	50
					1990 Dec 21	180
1595	688	VX Gem	C7,2e	10.8 – <14.9	1992 Nov 15	90
					1992 Nov 15	80
3286	2032	RU Vir	C8,1e	9.0 – 12.6	1991 Mar 6	64
					1991 Mar 3	72
3665	2306	RR Her	C8,1e	7.8 – 9.5	1990 Apr 15	20
					1990 Apr 15	120
4159	2692	BD+10°3764	C8,1	9.5	1992 Nov 14	160
					1992 Nov 15	140
4208	2711	MSB65	C8,2J	9.0	1991 Mar 6	20
					1991 Mar 3	60
4758	2880	RS Cyg	C8,2e	6.5 – 9.3	1993 Nov 27	220
					1993 Nov 27	520
4806	2892	WX Cyg	C9.2JLi	9.78	1990 Dec 24	120
					1990 Dec 24	40
4817	2894	U Cyg	C8,2e	6.7 – 11.4	1993 Nov 27	300
					1993 Nov 27	160
		LX Cyg		11.5	1992 Sep 3	138
					1992 Sep 2	119
5570	3107	RZ Peg	C9,1e	7.6 – 13.6	1992 Nov 14	160
					1992 Nov 13	100
5976	3214	WZ Cas	C9,2JLi	7.16	1987 Oct 1	200
					1987 Oct 1	200

2.4 Model Atmosphere

Model atmospheres used in the analysis are based on the code developed by Tsuji (1965). We assumed plane-parallel hydrostatic atmospheres in the local thermodynamical equilibrium (LTE) and the radiative equilibrium. We used 80 layers from $\log \tau_{1.04} = -6$ to 1.9, where $\tau_{1.04}$ is the optical depth of the continuum at 1.04 μm. The dissociation and ionization equilibria including more than 100 molecules and atoms were solved to obtain their abundances.

One of the obstacles in modeling atmospheres of cool stars is how to incorporate opacities due to a huge amount of molecular lines. In dealing with the line opacities of molecules, we used the Band Model Method. This method characterizes a run of opacity by two parameters, that is, the mean absorption coefficient and the mean line separation for each spectral mesh of appropriate interval. Once the spectral line shape is defined, it is straightforward to obtain the opacity distribution function (ODF) for this model. The case of the Voigt profile was formulated by Golden (1969), which is known as the Voigt-Analogue Elsasser Band Model (VAEBM), and applied to modeling of the atmospheres of red supergiants by Tsuji (1976). With the two parameters prepared for 194 spectral meshes from 0.2 to 45 μm, line opacities due to CO, CN, C_2, HCN, and C_2H_2 were incorporated by this method.

The continuous opacity sources incorporated are followings; bound-free and free-free transitions of H and H^-, free-free transitions of H_2^- and He^-, Rayleigh scattering of H and H_2, photo-ionization of neutral metals, Si, Mg, and Ca, and collision induced absorption of H_2-H_2 and H_2-He pairs. The opacity of H^- is updated based on the work by John (1988).

Though the Band Model may be regarded as a rather simplified method, the model atmospheres we have constructed fairly reproduce the models calculated by the Opacity Sampling (OS) method, which are regarded to be state-of-the-art models. Figure 2.1 shows a comparison of the P_g-T relations between Jørgensen et al. (1992) (OS) and ours (VAEBM). Both models are calculated with $T_{\rm eff} = 2800$ K, $\log g = 0.0$, and C/O = 1.02. Further, our models are calculated for two cases: one with the effect of turbulent pressure included in the hydrostatic equilibrium, and the other without it. Whether they include the effect of turbulent pressure or not is not explicitly mentioned in Jørgensen et al. (1992). Our model without turbulent pressure, which we think is presumably the case for Jørgensen et al. (1992), shows a fairly good agreement with their model. The difference is rather small, 100 – 200 K at most. Our model with turbulent pressure is warmer by 100 – 200 K, as compared with their model. This agreement lends a support that the Band Model is fairly appropriate, at least, for the construction of the temperature distribution throughout the atmosphere, which plays an important role in predicting equivalent widths of lines. It is to be noted that the difference between the models with and without turbulent pressure is still larger than the difference due to different treatments of molecular opacities.

However, we should remember that it is by no means guaranteed that even a model constructed by the OS method is a realistic one representing atmospheres of cool stars.

Some unidentified absorptions due to molecules and/or atoms might cause some effects on the atmospheric structure, and so do uncertain molecular data of molecules even if they are identified. And cool evolved stars have warm chromospheres and cool circumstellar dust shells, but no model atmosphere which reproduces the real stellar atmosphere from the photosphere up to the dust shell has been yet constructed, because of our poor understanding of the nature of chromosphere and the mechanism of mass loss. The contributions from the chromosphere and the dust shell are not dominant in the observed region (~8000 Å) for most of our program stars, but they could give some effects on the stellar atmospheric structure.

Table 5. Principal choices of fundamental parameters of the standard grid of model atmospheres

Parameter	Values
$T_{\rm eff}$ (K)	2200, 2400, 2600, 2800, 3000, 3200, 3400, 3600
$\log g$ (cm s^{-2})	0.0
$V_{\rm micro}$ (km s^{-1})	3.0
C/O	1.01, 1.1, 2.0

Our model atmospheres are specified by a set of four parameters, ($T_{\rm eff}$, $\log g$, $V_{\rm micro}$, A), where $T_{\rm eff}$ is effective temperature, g is surface gravity, $V_{\rm micro}$ is micro-turbulent velocity, and A is chemical composition, especially, of C, N, and O. Effective temperature is determined by the way described in the next section. Surface gravity is calculated by

$$\log g = \log(M/M_\odot) - \log(L/L_\odot) + 4\log(T_{\rm eff}/T_{\rm eff\odot}) + 4.44$$

A set of parameters – $M = 2\,M_\odot, L = 5000\,L_\odot$, and $T_{\rm eff} = 3000$ K – corresponds to $\log g = -0.1$. When we assume $M = 3\,M_\odot, L = 4000\,L_\odot$, and $T_{\rm eff} = 3200$ K, we obtain $\log g = 0.3$. This value is expected to be nearly the upper limit for the Galactic carbon stars, given the range of their masses and luminosities. We adopted $\log g = 0.0$ for the standard grid of our model atmospheres. We also calculated model atmospheres with $\log g = 0.3$ for some combinations of parameters. We set $V_{\rm micro}$ to 3 km s^{-1}, which is a typical value among giant stars, and the effect of turbulent pressure is taken into account. Chemical compositions of atmospheres were set to be the solar abundances (Anders & Grevesse 1989), except for C, N, and O abundances. We adopted $\log\varepsilon({\rm N}) = 8.05$ and $\log\varepsilon({\rm O}) = 8.93$. The adopted carbon abundances were $\log\varepsilon({\rm C}) = 8.970$ (C/O = 1.1), 8.934 (C/O = 1.01), and 9.230 (C/O = 2.0). We used the models with C/O = 1.1 for N stars, since this is the mean value of C/O ratios for 24 N stars analyzed by Lambert et al. (1986). We calculated model atmospheres with C/O = 2.0, in order to check the influence of the C/O ratio on the resulting carbon isotopic ratios. For SC stars, we tentatively set C/O ratio to 1.01, because C/O ratios of SC stars are thought to be nearer to unity than those of N stars. Lambert et al. (1986) analyzed the C/O ratio of an SC star, WZ Cas, which was found to be 1.01. The grid of model atmospheres we used is shown in Table 5.

We show some examples of our model atmospheres with different sets of parameters in Fig. 2.2.

2.5 Effective Temperature

2.5.1 Determination of Effective Temperatures

Effective temperatures are determined by the InfraRed Flux Method (IRFM, Blackwell et al. 1980). By this method, effective temperatures are determined from the ratio of the bolometric flux to an infrared flux. If a star is a blackbody, the ratio is proportional to ${T_{\rm eff}}^3$, because the bolometric flux is proportional to ${T_{\rm eff}}^4$, according to the Stefan-Boltzmann formula, while an infrared flux is proportional to $T_{\rm eff}$ in the Rayleigh-Jeans regime. Though a real star is not a blackbody, we can determine the effective temperature from the observed bolometric flux and infrared flux, once we calibrate the ratio $R = f_{\rm BOL}/f_{\rm IR}$ against $T_{\rm eff}$ by model atmospheres. The advantage of the IRFM is that we can determine effective temperatures accurately because the ratio is roughly proportional to ${T_{\rm eff}}^3$ and pretty sensitive to $T_{\rm eff}$.

But the predominance of molecular absorption in the spectra of carbon stars, which depends on parameters other than effective temperature, modifies the infrared flux. In order to determine effective temperatures as independently of other parameters as possible, we used the L' band (3.7 μm) flux. This band region is relatively free from molecular absorption and shows a quasi-continuum in the spectra of carbon stars. However, absorption due to polyatomic molecules such as HCN and C_2H_2 becomes somewhat significant in stars as cool as 2600 K. Our possible concerns are strong absorption due to HCN and C_2H_2 centered at around 3.07 μm, their weaker bands ($\nu_1 + \nu_2$ of HCN and $\nu_2 + \nu_5$ of C_2H_2) around 3.7 μm, and weak absorption due to CS around 3.9 μm. The emergent flux predicted by our model atmospheres tends to overestimate the line-blanketing effect as compared with the observed band strengths. This is a general difficulty encountered by the present model atmospheres. For this reason, the effect of the 3.07 μm polyatomic molecular absorption is corrected by an empirical method based on the observed spectra (Tsuji 1981). When the L' filter is used, that empirical correction due to polyatomic molecular absorption is minor, because the absorption centered at around 3.07 μm is at the edge of the filter response function. The weaker bands of HCN and C_2H_2 at around 3.7 μm are quite weak (e.g. Bregman et al. 1978), and do not cause any serious problem. The absorption due to CS at around 3.9 μm is somewhat significant in Mira variables (Bregman et al. 1978), but most of our program stars are not Mira variables. Therefore we concluded that the absorption due to CS also do not cause a serious problem in the determination of effective temperatures of our program stars. The calibrations predicted by our model atmospheres are shown in Fig. 2.3. The difference of $T_{\rm eff}$ induced by C/O ratios becomes about 100 K for stars as cool as 2600 K, but it is minor for stars warmer than 3000 K.

The infrared and bolometric fluxes are obtained from photometric data available in the literature. Photometric data from the literature on different photometric systems are transformed into absolute fluxes. The absolute calibration is done based on the direct comparison with a blackbody (Blackwell et al. 1983; Selby et al. 1983; Mountain et al. 1985). For 33 of our program stars, photometric data throughout the whole spectral region, from U or B band to L or L' band, can be collected from the literature (e.g. Mendoza & Johnson 1965, Bergeat et al. 1976, Walker 1979, Bergeat & Lunel 1980, Walker 1980, Noguchi et al. 1981, Noguchi et al. 1991). The interstellar extinctions are estimated based on the works by Fitzgerald (1968) and by Sharov (1964), combined with the distances of stars estimated by the assumption of $M_V = -2.5$ for N- and SC-type carbon stars (Walker 1980). The bolometric fluxes are obtained by integrating absolute fluxes throughout the whole spectral region after the data are de-reddened.

For the rest of our program stars, photometric data throughout the whole spectral region are not available in the literature, and we cannot determine effective temperatures directly by the IRFM. We calibrated $(J - L')_0$ against the effective temperatures determined by the IRFM. Photometric data of J, H, K, and L' bands are available for most of our program stars, thanks to the works by Noguchi et al. (1981), Noguchi et al. (1991), and Noguchi (1993). Figure 2.4 shows the $(J - L')_0$ – $T_{\rm eff}$ relation for 33 stars, including 27 N stars and 6 SC stars. No systematic difference between two types of stars can be seen in this figure, therefore, we used this relation for both of two types of carbon stars.

The effective temperatures determined are given in the third and the seventh columns of Table 7 for N-type carbon stars, and in the third column of Table 8 for SC-type carbon stars. The effective temperatures with asterisks (*) indicate that they were directly determined by the IRFM, while others by the $(J - L')_0$ – $T_{\rm eff}$ relation. For the stars indicated by daggers (†), the photometric data of L' band are not available. We extrapolated the L' band fluxes from the L band fluxes and determined $T_{\rm eff}$ by the IRFM based on those extrapolated L' band fluxes.

The uncertainty of $T_{\rm eff}$ determined directly by the IRFM is estimated to be about 5 %, or 150 K for $T_{\rm eff}$= 3000 K. This figure comes from the uncertainty of model atmospheres, that of the interstellar extinction, and that of the absolute calibration of photometric data. The error of $T_{\rm eff}$ caused by the uncertainty of continuous opacities of model atmospheres is discussed by Blackwell et al. (1991) and about 2%. The uncertainty of A_v results in about 2% error on $T_{\rm eff}$. The error of the absolute calibration can cause about 1% error on $T_{\rm eff}$. Thus, we estimate the error of the derived $T_{\rm eff}$ caused by these errors to be about 3%. The internal errors of photometric data are rather small, but most of our program stars are variable, as known by their names. Photometric data throughout the spectral region are not necessarily obtained at the same time, therefore, variabilities may cause some errors on $T_{\rm eff}$. We conclude that the total error of the derived $T_{\rm eff}$ is about 5%, or 150 K for $T_{\rm eff}$ 3000 K. The error of $T_{\rm eff}$ determined by the $(J - L')_0$ – $T_{\rm eff}$ relation is somewhat larger than 150 K, because of the scattering in the $(J - L')_0$ – $T_{\rm eff}$ relation, as seen in Fig. 2.4. We estimate that the error in this case is about 200 K.

Effective temperatures can be also determined when both of angular diameters and bolometric fluxes are available. Effective temperatures determined from angular diameters are independent of model atmospheres, therefore, allow us to test model atmospheres and see if the IRFM is valid to determine effective temperatures. Table 4. shows comparisons between effective temperatures by angular diameters and by the IRFM. Angular diameters have been measured for Y Tau, X Cnc, AQ Sgr, and TX Psc by the authors listed in Table 6, making use of the lunar occultations. A catalogue of angular diameters by

Table 6. Effective temperatures determined by angular diameters, T_{eff} (A.D.), and by the IRFM, T_{eff} (IRFM). The values with U.D. and L.D. are based on uniformly illuminated stellar disk and fully limb-darkened disk assumptions, respectively, in the reductions

Star	λ (μm)	θ (mas)	Reference	T_{eff} (K) (A.D.)	T_{eff} (K) (IRFM)
Y Tau	1.65	8.91 ± 0.37 (U.D.)	Schmidtke et al. (1986)	2540 ± 50	2880 ± 144
	2.17	8.68 ± 0.35 (U.D.)	Schmidtke et al. (1986)	2574 ± 50	
	2.17	6.94 ± 0.20 (U.D.)	Schmidtke et al. (1986)	2878 ± 40	
	1.64	8.80 ± 0.25 (L.D.)	Ridgway et al. (1977)	2556 ± 40	
	1.64	8.38 ± 0.24 (L.D.)	Ridgway et al. (1977)	2619 ± 50	
X Cnc	0.69	7.90 (U.D.)	Bartholdi (1972)	2653	2910 ± 146
	1.62	7.62 ± 0.56 (U.D.)	Ridgway et al. (1982)	2701 ± 100	
AQ Sgr	0.64	5.97 ± 0.49 (L.D.)	Walker et al. (1979)	2823 ± 120	3100 ± 200
TX Psc	0.71	8.90 ± 1.00 (L.D.)	de Vegt (1974)	3365 ± 210	3080 ± 154
	0.70	9.00 ± 1.00 (U.D.)	Lasker et al. (1973)	3172 ± 180	
	0.69	10.2 ± 2.5 (L.D.)	Dunham et al. (1975)	2980 ± 380	

White & Feierman (1987) is also an important reference. The bolometric fluxes of these stars can be obtained by integrating the photometric data as mentioned above. The errors of effective temperatures determined by angular diameters are estimated only from the internal errors of measurements of angular diameters. In the case of X Cnc and TX Psc, the two methods give consistent effective temperatures within errors of both methods. In the case of Y Tau, for which Schmidtke et al. (1986) suggest a possibility of time variation of the angular diameter, effective temperatures determined by the two methods are consistent if we adopt the smallest value, 6.94 ± 0.20 mas. In the case of AQ Sgr, effective temperatures determined by the two methods are marginally consistent within errors of both methods.

Significant infrared excesses are found in energy distributions of six of our program stars, V Hya, CL Mon, T Dra, UV Aur, RU Vir, and U Cyg. We show two examples of energy distributions of these stars in Fig. 2.5, together with that of X Cnc for comparison. The flux distributions are normalized by the J band flux of each star. A glance of Fig. 2.5 reveals that these stars have large excesses longward the L band. Effective temperatures determined by the IRFM or by the $(J - L')_0$ – T_{eff} relation turn out to be as low as 2000 K or cooler. These stars have rather thick circumstellar dust shells and the thermal emission from them increases the L band fluxes, leading to extremely low temperatures by the IRFM. We cannot determine effective temperatures for these stars, and give up analyzing $^{12}C/^{13}C$ ratios.

2.5.2 The C-classification

In Fig. 2.4 as well as in Tables 7 and 8, no systematic difference of effective temperatures is found between N and SC carbon stars. This is in contradiction with the fact that SC stars have been mostly classified to be the latest subtype (C8–9) in the C-classification. The classification is based on the observational fact that they show very strong Na I D lines. We interpret the strong Na I D lines of SC stars to be a product due to C/O ratios very near to unity. In an atmosphere with C/O ratio very near to unity, little amount of carbon or oxygen is left behind to form various molecules, with almost all carbon and oxygen locked into CO molecules. The strong absorption due to CO effectively cools down the temperature of the atmosphere, while the backwarming effect does not work, lacking molecules such as CN which have many weak lines over a large wavelength range. This effect can be seen in Fig. 2.2b, where three model atmospheres with the same parameters except for C/O ratio are shown. With ionization prevented in cooler atmosphere with C/O $\sim$ 1.01, the stronger Na I D lines are expected to be observed. Figure 2.6 shows the observed strengths of Na I D lines in SC stars and N stars, together with the predicted strengths by our model atmospheres with C/O = 1.1 and 1.01. This figure assures that Na I D lines are stronger in the models with C/O = 1.01 than in the models with C/O = 1.1 for the same effective temperature. The observed equivalent widths of D lines are taken from the works by Bouigue (1954) and by Buscombe (1955). The accuracy of the measured equivalent widths of Na I D lines is estimated to be 30 – 50%, given the blend of CN and C_2 lines and the uncertainty of the *true* continuum level. A glance of Fig. 2.6 shows that the observed strengths D lines of SC stars are stronger, except for one star, than the predicted ones. Given the uncertainties of measurement of Na I D lines noted above, it could be said that our model atmospheres roughly reproduce the observed values. The strengths of Na I D lines of N stars can be also roughly reproduced, given the error of the measurement of D lines as well as the uncertainties of $T_{\rm eff}$ and C/O ratio of each star. Besides, the predicted strengths of Na I D lines are calculated without taking into account lines of CN and C_2. These lines would depress the continuum level with which equivalent widths are measured. Though it is desirable to generate synthetic spectra taking into account all the relevant lines, it would be not so easy because the definition of the *true* continuum, which is necessary for the spectrum synthesis method, is very difficult in the heavily line-blanketed region. We conclude that the strong Na I D lines of SC stars are a product due to the C/O ratios very near to unity, rather than the low temperatures. The temperature scale assigned to SC stars by the C-classification cannot be necessarily justified.

2.6 Analysis

The observed region is very crowded with lines due to the red system of ^{12}CN and ^{13}CN, and the Phillips system of C_2, as can be seen in Figs. 2.7, 2.8, 2.9, and 2.10. Intervals between lines are often smaller than the intrinsic line widths, and it is inevitable that the adjacent lines blend each other and look like a single line. These blended lines are useless in our analysis and we have to find really single isolated lines. After we checked blend of lines due to C_2, we selected isolated lines, whose central depths are expected not to be affected by the adjacent lines. Some lines are blended with other lines at almost the same wavelength. We used them in the analysis only if the blending line is weak enough compared with the line, considering its gf-value and lower excitation potential (LEP). The lines from which we can derive the isotopic ratios are very limited in the region studied. We selected about 10 lines of ^{12}CN and 2 lines of ^{13}CN for each star. Central depths are normalized by the fictitious continuum level, which is drawn so that it should go through the highest point in the observed region and assumed to be constant over the region. This assumption is reasonable since there is no reason to suppose that the continuum level should change within only 230 Å interval.

We adopted the iso-intensity method for the analysis. It is similar to the curve-of-growth method, but we use central depths of lines, instead of equivalent widths, as the ordinate. For lines of ^{12}CN and ^{13}CN, logarithms of the observed central depths normalized by the fictitious continuum level are plotted against $\log(gf\Gamma)$, which is the line intensity predicted by the weighting function method (e.g. Cayrel & Jugaku 1963). The horizontal shift between the two curves gives the isotopic ratio, as shown in Figs. 2.11 and 2.12 as examples.

We have three reasons for using this method in the analysis.

The first reason is that we cannot measure an accurate equivalent width of a line, since lines are very crowded in the observed region. Central depths of lines are less susceptible to blending of the adjacent lines than equivalent widths. This fact helps us to use as many lines as possible in the analysis, and it is indispensable to use as many lines as possible in order to suppress the internal error.

The second reason is that the fictitious continuum level adopted, in fact, does not affect the resulting isotopic ratios in the iso-intensity method. It is very difficult to determine the *true* continuum level in the heavily line-blanketed regions, as shown in Figs. 2.7, 2.8, 2.9 and 2.10. But note that the horizontal shift between the curves for ^{12}CN and ^{13}CN (see Figs. 2.11 and 2.12) is measured at the same depth, hence, the continuum location does not affect the resulting isotopic ratio as long as the continuum is constant in the observed region. In other words, the absolute values of central depths, which should be measured with respect to the *true* continuum, do not matter. Since the carbon isotopic ratios are determined by lines of ^{12}CN and ^{13}CN of the *same* intensities, what really matters is that central depths normalized by the fictitious continuum are a kind of measure of line intensities which serve to recognize that the lines of ^{12}CN and ^{13}CN are *iso*-intensity. In other words, we simply recognize that two lines are *iso*-intensity if their fluxes at the line centers are the same. This should be valid if two lines are located within a spectral interval where the Planck function as well as the detector sensitivity show little change. The central depths normalized by the true continuum can better be interpreted by theoretical models but our empirical analysis is free from such an interpretation. By this very reason, we did not apply the spectral synthesis method, which is often used in analyses of complicated spectra. Such analyses, in fact, cannot be justified unless the true continuum is well defined, since the theoretical synthetic spectra are always normalized by the true continuum.

The third reason is that we can determine isotopic ratios without determining the micro-turbulent velocity, which is considered to represent some kind of non-thermal velocity field. But the micro-turbulent velocity is actually a parameter to be defined so that abundances derived from strong lines and weak lines should agree. The saturation effect which affects the traditional curve-of-growth method can be also taken into account fully empirically, and the iso-intensity method is free from any problem associated with that effect.

As can be seen in Figs. 2.11 and 2.12, ^{12}C/^{13}C ratios are actually determined by the horizontal shifts between two or three lines of ^{12}CN and two lines of ^{13}CN. The scarcity of lines used could cause a large internal error, or even a systematic error on the resulting ^{12}C/^{13}C ratios, if these lines are blended. We examined this possibility by observing the spectrum of TX Psc in a wider range, from 7680 to 8250 Å, to find more weak lines suitable for the analysis. Several lines of ^{12}CN as weak as those of ^{13}CN are identified in the wavelength region from 7680 to 7800 Å and one more weak line of ^{13}CN is identified at 8037 Å. In Fig. 2.13b, these additional lines of ^{12}CN and ^{13}CN are plotted together with the lines used in the analysis for the wavelength range from 7800 to 8030 Å. These additional lines, which are due to (7,4), (6,3), and (5,2) transitions, fairly reproduce the curve-of-growth plotted in the previous analysis shown in Fig. 2.13a. This result confirms that the weak lines of ^{12}CN used in the analysis are unlikely to be in a systematic error. The additional line of ^{13}CN, together with two lines previously plotted, forms a weak line part of the curve-of-growth. We concluded that the resulting ^{12}C/^{13}C ratios are not in a systematic error due to the use of blended lines.

The errors of the resulting ^{12}C/^{13}C ratios include internal errors, which are represented by the scatterings of lines plotted in the curves-of-growth, and external ones, which come from the uncertainties of the adopted model atmospheres. Internal errors are estimated to be about 0.05dex from Figs. 2.11 and 2.12. The uncertainties of model atmospheres need scrutiny, because the correction of excitation effect by model atmospheres is crucial, especially when ^{12}C/^{13}C ratios are actually determined from the horizontal shifts between high excitation lines of ^{12}CN (7,4) band and low excitation lines of ^{13}CN (2,0) band. In other words, wrong correction of excitation effect by model atmospheres can lead to a systematic error on the resulting ^{12}C/^{13}C ratios. This correction of excitation effect is included in the calculation of $\mathit{\Gamma}$, which is approximately written in the form of $\mathit{\Gamma}(\chi) = \mathit{\Gamma}(0) - \chi\langle\theta_{\rm ex}\rangle$, where χ is LEP (in eV), and $\langle\theta_{\rm ex}\rangle$ is a kind of weighted mean of the reciprocal excitation temperature in the line formation region. The uncertainties of model atmospheres include two factors; the parameters which specify a model atmosphere and the atmospheric structure itself of the adopted model. The former effect can be checked by changing the parameters, while the latter problem is more difficult to check, because model atmospheres of cool stars are by no means well-established as mentioned in the Sect. 2.4, and will be discussed in Sect. 2.8.2.

The effect on the resulting $^{12}C/^{13}C$ ratios by the adoption of different model parameters are summarized in Table 9. In the case of N-type carbon stars, an error of $T_{\rm eff}$ by 200 K leads to an error of 0.02dex in the resulting $^{12}C/^{13}C$ ratio. The uncertainty of $\log g$, which may be estimated as 0.5, leads to an error of 0.02dex. The adoption of micro-turbulent velocity 2 km s^{-1}, instead of 3 km s^{-1}, leads to the difference of 0.1dex. The use of model atmospheres with C/O = 2.0 and 1.05, instead of C/O = 1.1, leads to the difference about 0.04dex and 0.07dex, respectively. Thus, the error induced by the uncertainties of the model parameters is about ± 0.12dex. We conclude that the total error of the resulting $^{12}C/^{13}C$ ratio of an N-type carbon star, including internal and external ones, is about 0.13dex, which corresponds to $(+9.4, -7.0)$ for $^{12}C/^{13}C = 27$.

In the case of SC-type carbon stars, dependency of the resulting $^{12}C/^{13}C$ ratios on model atmospheres is larger than in the case of N-type carbon stars. An error of $T_{\rm eff}$ by 200 K leads to an error of 0.10dex in the resulting $^{12}C/^{13}C$ ratio. The use of model atmospheres with C/O = 1.02, instead of C/O = 1.01, increases the resulting $^{12}C/^{13}C$ ratio by 0.23dex. If we assume that the errors induced by the uncertainties of $\log g$ and $V_{\rm micro}$ are the same as in the case of N-type carbon stars, the error induced by the uncertainties of the model parameters is estimated about 0.27dex. Thus, the total error of the resulting $^{12}C/^{13}C$ ratio of an SC-type carbon star is about 0.28dex, which corresponds to $(+20, -10)$ for $^{12}C/^{13}C = 22$.

2.7 Results

The results of $^{12}C/^{13}C$ ratios are given in the fourth and the eighth columns of Table 7 for 62 N-type carbon stars, and in the fourth column of Table 8 for 15 SC-type carbon stars. The average of $^{12}C/^{13}C$ ratios is 27 ± 11 (standard deviation) for N-type carbon stars and 22 ± 14 (standard deviation) for SC-type carbon stars. For GP Ori and FU Mon, we can only give lower limits of $^{12}C/^{13}C$ ratios, because lines of ^{13}CN are very weak. These two stars are also included in the statistics, taking those lower limits of $^{12}C/^{13}C$ ratios. The distributions of the derived $^{12}C/^{13}C$ ratios of each type of stars are shown in Fig. 2.14.

Figure 2.14a clearly shows that the most frequent $^{12}C/^{13}C$ ratio among 62 N stars is from 20 to 30. Nearly half of our program stars have the ratios of this range. And about 85% of our program stars have the ratios smaller than 40. It should be noted that the number of stars which have the ratios larger than 40 is relatively small. It shows a marked contrast with the result of Lambert et al. (1986) who have concluded that the most frequent ratio among 24 N stars they studied is from 50 to 60. This disagreement, which amounts to a factor of 2 to 3, will be discussed in the next section.

The scarcity of SC stars studied makes it difficult to discuss about the most frequent ratio among SC stars from Fig. 2.14b. But it should be noted that our program stars, except for three stars, have ratios larger than 10, while most of SC stars have been

Table 7. Effective temperatures and $^{12}C/^{13}C$ ratios of N-type carbon stars

Star	$(J-L')_0$	$T_{\rm eff}$ (K)	$^{12}C/^{13}C$	Star	$(J-L')_0$	$T_{\rm eff}$ (K)	$^{12}C/^{13}C$
ST Cas	1.23	3306	18	RV Mon	1.32	3330*	35
AQ And	1.52	2970*	29	RY Mon	1.97	2860*	50
Z Psc	1.50	3145	23	W CMa	1.33	3290*	38
R Scl	1.76	2830*	9	BD+5°1606	1.98	2869	24
WW Cas	2.05	2826	21	HD59643	1.06	3401	9
X Cas	2.10	2794	19	GO Pup	2.35	2650*	22
BS Per	2.01	2846	13	RY Hya	2.33	2664	32
HD19881	1.33	3247	18	AC Pup	1.80	2990*	13
U Cam	2.09	2670*	33	X Cnc	2.00	2910*	22
BD+51°762	2.09	2801	30	T Cnc	2.22	2770*	29
AC Per	1.83	2955	28	Y Hya	1.57	3050*	25
ST Cam	1.61	3081	29	U Hya	1.59	3080*	17
TT Tau	1.66	3055	28	VY UMa	1.53	3240*	17
W Ori	1.88	2980*	26	TY Oph	2.16	2780*	44
TX Aur	1.85	2941	33	RX Sct		3250†	33
SY Eri	1.60	3090*	17	V Oph	1.93	2880*	11
HD34467	1.39	3207	22	V781 Sgr		3160†	38
RT Ori	1.60	3100*	46	HK Lyr	1.98	2866	33
HD37212	1.04	3416	20	S Sct	1.66	3110*	14
TU Tau	1.88	2922	30	V Aql	2.14	2790*	66
Y Tau	1.84	2880*	40	U Lyr	2.26	2702	23
FU Aur	1.41	3198	22	AW Cyg	2.16	2759	26
TU Gem	1.62	3078	26	AQ Sgr		3100†	35
GK Ori	2.21	2735	40	TT Cyg	1.67	3046	14
ZZ Gem	2.22	2725	11	AX Cyg	2.12	2783	35
BL Ori	1.42	3180*	26	X Sge	1.77	2991	20
UU Aur	1.83	3010*	19	V460 Cyg	1.43	3230*	21
VW Gem	1.34	3236	48	RV Cyg	2.25	2709	23
CZ Mon	2.16	2860*	55	DG Cep	1.50	3148	32
DF Mon	2.02	2880*	20	TX Psc	1.65	3080*	22
GY Mon	1.31	3255	28	SU And	1.65	3057	48

*: $T_{\rm eff}$ are determined directly by the IRFM.

†: $T_{\rm eff}$ are determined directly by the IRFM, but L' band fluxes are extrapolated from L band fluxes. See also the text.

Table 8. Effective temperatures and ^{12}C/^{13}C ratios of SC-type carbon stars

Star	$(J-L')_0$	$T_{\rm eff}$ (K)	^{12}C/^{13}C
W Cas	1.45	3180	25
V372 Mon	1.73	3011	25
BD+38°955	1.89	2918	32
GP Ori	1.85	2920*	> 59
S Cam	1.79	2975	14
BB Tau	1.08	3392	9
FU Mon	1.73	2910*	> 40
R CMi	1.61	3050*	11
VX Gem	1.67	3045	9
RR Her	1.29	3268	17
BD+10°3764	1.71	3021	29
MSB65	1.61	3079	19
WX Cyg	1.76	2990*	14
RZ Peg	2.09	2803	18
WZ Cas	1.43	3160*	4

*: $T_{\rm eff}$ are determined directly by the IRFM.
See also the text.

Table 9. Errors from the uncertainties of model parameters

Uncertainty of parameter	Error
N-type carbon star	
$\Delta T_{\rm eff} = 200$ (K)	0.02dex
$\Delta \log g = -0.5$ (cm s^{-2})	0.02dex
$\Delta V_{\rm micro} = -1$ (km s^{-1})	0.1dex
C/O = 1.1 $\rightarrow$ 2.0	0.04dex
C/O = 1.1 $\rightarrow$ 1.05	0.07dex
SC-type carbon star	
$\Delta T_{\rm eff} = 200$ (K)	0.10dex
C/O = 1.01 $\rightarrow$ 1.02	0.23dex

classified as J-type, that is, ^{13}C-rich. We refer to $^{12}C/^{13}C < 10$ as ^{13}C-rich. The earlier classification was based on the strength of band heads observed in low resolution spectra. Absorption of some atoms and/or molecules might have led such a classification.

Figure 2.15 shows the results of $^{12}C/^{13}C$ ratios plotted against $T_{\rm eff}$. It shows almost no correlation between $^{12}C/^{13}C$ ratios and $T_{\rm eff}$. If any correlation should be found, we cannot exclude a possibility that the results may suffer a systematic error due to, for example, increased blend of unidentified lines with decreased temperature. Figure 2.15 confirms that our results are probably free from such an error.

Spectra of the Mira variables in our sample show distinct characteristics as compared with other type of variables, that is, the semiregular (SR) or irregular (Irr) ones. The spectra of a Mira variable, SS Vir, and an SR variable, X Cnc, are shown for comparison in Fig. 2.16. A glance of Fig. 2.16 reveals that spectral lines in SS Vir are smeared out and measurements of weak lines of ^{13}CN is impossible. In such cases, we had no choice but to give up the analysis of $^{12}C/^{13}C$ ratio. It is not clear why lines in the Mira variables are smeared out. The Mira variables generally have thick circumstellar dust shell, therefore, contamination due to thermal emission of dust might be responsible for it. Or some dynamical effects due to pulsation might broaden spectral lines.

Our sample includes two carbon stars, S Sct and TT Cyg, which show 60μm-excesses in the IRAS observation. It is inferred that these stars have detached shells shed in the episodic mass loss rather than a continuous mass outflow. The derived $^{12}C/^{13}C$ ratios are 14 for both of them. They fall in the second most frequent range of $^{12}C/^{13}C$ ratios in N stars, and we can find no peculiarity of $^{12}C/^{13}C$ ratios which would be related to an evolutionary stage characterized by the presence of detached shells.

The super Li-rich carbon stars, WZ Cas and WX Cyg, are included in our sample. Both of stars are classified as SC-type, but they show distinctly different $^{12}C/^{13}C$ ratios: WZ Cas has a very low $^{12}C/^{13}C$ ratio, 4, while WX Cyg has a moderately enhanced $^{12}C/^{13}C$ ratio, 14. Our result for WX Cyg implies that the super Li-rich phenomenon seems not to be related to low $^{12}C/^{13}C$ ratios found in J-type carbon stars. It should be noted that all of the super Li-rich stars ever discovered by now are SC stars. As pointed out by Denn & Luck (1991), atmospheric structure of SC stars with C/O ratios very near to unity may be partly responsible for the strong Li I doublet, as in the case of the strong Na I D lines discussed in Sect. 2.5.2.

2.8 Discussion

2.8.1 Comparison with Previous Results

Carbon isotopic ratios of carbon stars have been analyzed by several authors. Table 10 shows the previous results and the molecular lines analyzed. Of our program stars, TX Psc and V460 Cyg have been repeatedly analyzed by several authors, since they are bright and their spectra are easy to obtain. Our results for V460 Cyg and TX Psc are $21(+7, -5)$ and $22(+8, -6)$, respectively. The previous results are divided into two ranges. One is the range from 20 to 30, which roughly agrees with our results, and the other is the range from 60 to 80, which is two or three times larger than ours. Dominy et al. (1978) analyzed the $^{12}C/^{13}C$ ratio of V460 Cyg by the curve-of-growth method, which was essentially the same method as we used, except that their analysis was based on the approximation of a single excitation temperature. They derived $^{12}C/^{13}C = 30 \pm 13$ from lines of the CN red system with the adoption of excitation temperature of 2850 K. This should be regarded as a good agreement with our result $^{12}C/^{13}C = 21(+7, -5)$, given their adoption of relatively low excitation temperature. Since they presented identifications and central depths of the lines they used, we re-analyzed the data using our model atmosphere, and derived $^{12}C/^{13}C = 20 \pm 6$. This value agrees with our result, $^{12}C/^{13}C = 21(+7, -5)$. This agreement again confirms that our results are not in a systematic error due to using blended lines, because 113 lines of ^{12}CN and 32 lines of ^{13}CN are listed in Dominy et al. (1978) and the $^{12}C/^{13}C$ ratio is derived from the horizontal shift between the weak line parts formed by about 40 and 10 lines of ^{12}CN and ^{13}CN, respectively (see Fig. 3 of Dominy et al. 1978). The $^{12}C/^{13}C$ ratios derived from the first- and second-overtone bands of CO are somewhat larger than that derived from lines of CN. Scarcity of weak lines of CO makes it difficult to derive an accurate isotopic ratio. But their result, $^{12}C/^{13}C = 35 \pm 12$, agrees with ours within the errors of both results.

The large $^{12}C/^{13}C$ ratio derived by Fujita & Tsuji (1977) may be attributed to their adoption of rather low excitation temperature, 2520 K for V460 Cyg. They also used the iso-intensity method, but determined the excitation temperature so that the plotted lines could form a curve-of-growth as smooth as possible. Such an empirical determination of excitation temperature may have suffered from a large error, especially if the number of lines used is rather limited. In fact, it was difficult to determine excitation temperature in this way, and the excitation temperature was assumed to be lower by several hundreds degrees than the effective temperature. However, it was recognized later that such an assumption could not be justified and the excitation temperature could even be higher than the effective temperature because of the strong backwarming effect due to the heavy line-blanketing in atmospheres of cool carbon stars (Tsuji 1985). For this reason, the excitation temperature as low as 2520 K for V460 Cyg is not necessarily correct and hence a $^{12}C/^{13}C$ ratio as high as 100 is not justified, either. Such an effect of atmospheric structure on excitation temperature is more properly taken into account in our present analysis by the use of Γ.

The disagreement between the result of Lambert et al. (1986) and ours should be

Table 10. Comparison with the results by other authors

Sources	$^{12}C/^{13}C$	Molecular System	Type of Analysis
		V460 Cyg	
Fujita & Tsuji 1977	100	CN Red, $\Delta v = 2, 3$	curve-of-growth
Dominy et al. 1978	30 ± 13	CN Red, $\Delta v = 2, 3$	curve-of-growth
	35 ± 12	CO, $\Delta v = 2, 3$	curve-of-growth
Johnson et al. 1982	24	CN Red, $\Delta v = 2, 3, 4$	spectral synthesis
Little-Marenin & Little 1984	22-29	CN Red, $\Delta v = 2, 3$	spectral synthesis
Lambert et al. 1986	63 ± 6	CN Red, $\Delta v = -2$	curve-of-growth
	52 ± 8	CO, $\Delta v = 3$	curve-of-growth
	62 ± 13	CO, $\Delta v = 2$	curve-of-growth
This work	$21(+7, -5)$	CN Red, $\Delta v = 2, 3$	curve-of-growth
		TX Psc	
Olson and Richer 1979	21	CN Red, $\Delta v = 2$	spectral synthesis
Johnson et al. 1982	27	CN Red, $\Delta v = 2, 3, 4$	spectral synthesis
Lambert et al. 1986	47 ± 8	CN Red, $\Delta v = -2$	curve-of-growth
	39 ± 6	CO, $\Delta v = 3$	curve-of-growth
	38 ± 8	CO, $\Delta v = 2$	curve-of-growth
This work	$22(+8, -6)$	CN Red, $\Delta v = 2, 3$	curve-of-growth

taken seriously and it is difficult to specify the reason for the disagreement. Figure 2.17 shows their results and ours for the same stars, and the distributions of $^{12}C/^{13}C$ ratios derived by them and by us are shown in Fig. 2.18 for comparison. Their results are by a factor of 2 to 3 larger than ours. They analyzed infrared spectra, which were acquired with the Fourier transform spectrometer (FTS), of resolution about 75,000 with sufficient signal-to-noise ratios. The $^{12}C/^{13}C$ ratios were derived from lines of the first- and second-overtone bands of CO and $\Delta v = -2$ sequence of the CN red system. They reported that they used enough number of weak lines, from which abundances can be determined almost independently of micro-turbulent velocities. We noticed that their model atmospheres are cooler by more than 500 K in the line forming region than our model atmospheres of the same effective temperature. Figure 2.19 shows a comparison of P_g-T relations between their model atmosphere and ours for the same set of parameters – $T_{\rm eff}$ = 3000 K, $\log g$ = 0.0, C/O = 1.1, and $V_{\rm micro}$= 3.0 km s^{-1} [2]. This cool model might have led to large carbon isotopic ratios, as the low excitation temperature might have led a large $^{12}C/^{13}C$ ratio in the case of Fujita & Tsuji (1977).

The difficulty that the determination of $^{12}C/^{13}C$ ratios depends rather critically on excitation temperatures or model atmospheres was well recognized at an earlier time. Later attempts to determine $^{12}C/^{13}C$ ratios can be regarded as efforts to overcome this difficulty. Because of the extreme complexity of atmospheres of cool carbon stars, however, this problem has remained formidable till now. This is still the major source of systematic errors in the determination of $^{12}C/^{13}C$ ratios as we have just surveyed above in this subsection. For this reason, further observational tests of our model atmospheres are needed before we interpret our results.

2.8.2 Model atmospheres

The resulting $^{12}C/^{13}C$ ratios largely depend on the model atmospheres used in the analysis. It is necessary that the emergent flux predicted by model atmospheres should match with the observed ones. However, model atmospheres ever calculated so far cannot always explain both of continuous spectra and strength of band features. Certainly, it is desirable to test the line forming region of model atmospheres by spectral lines themselves.

Lambert et al. (1986) claimed that their model atmospheres with appropriate effective temperature were successful in reproducing equivalent widths of Na I D lines of cool carbon stars observed by H. B. Richer (1985, unpublished observations). The equivalent widths are reportedly 20 Å (BL Ori), 25 Å (Z Psc and VY UMa), and 30 Å (X Cnc). These equivalent widths do not agree with the results by the earlier works (Bouigue 1954, Buscombe 1955). For example, the equivalent widths of D lines are 9.1 Å (Bouigue 1954) and 6.0 Å (Buscombe 1955) for BL Ori, and 7.9 Å for Z Psc (Bouigue 1954), and 6.4 Å for X Cnc (Bouigue 1954). We estimated the equivalent widths of D lines from the spectral atlas published by Barnbaum (1994). The lines are located in the midst of many lines

[2]Figures 10a – f of Lambert et al. (1986) do not give a whole set of parameters to each model. We inferred the parameters comparing Figs. 10a, 10b, and 10c. Their models were calculated with $V_{\rm micro}$= 2.0 km s^{-1}, instead of 3 km s^{-1}, but the subsequent changes in the models are reportedly minor.

due to CN and C_2, which makes it difficult to measure the accurate equivalent widths. We estimated the sum of the equivalent widths of D lines to be about 6 Å for U Hya, and 8 Å for TX Psc, both of which are typical N-type carbon stars. In the earlier works, the equivalent widths are 6.4 Å (Bouigue 1954) and 10.8 Å (Buscombe 1955) for TX Psc, and 8.3 Å (Bouigue 1954) for U Hya. Our estimates agree with the results of the earlier works, given the blend of lines due to CN and C_2, or the uncertainty of the *true* continuum location. Our model atmospheres are roughly successful in reproducing these estimates, as discussed in Sect. 2.5.2. The equivalent widths of Na I D lines predicted by our model atmosphere are 6.1 Å for TX Psc, with $T_{\rm eff}$ = 3200 K and C/O = 1.1. This result fairly agrees with the results by Bouigue (1954) and by Buscombe (1955) as well as with our estimate based on the spectral atlas of Barnbaum (1994).

Absorption lines of molecular hydrogen provide us with a good opportunity to test model atmospheres, because hydrogen abundance is expected not to vary in stars. We examined whether our model atmospheres could reproduce the observed strengths of H_2 1 - 0 S(0) line. The strengths of H_2 line predicted by our model atmospheres and the observed strengths of 24 N stars and 1 SC star are shown in Fig. 2.20. The observed strengths of H_2 line were read from Fig. 20 of Lambert et al. (1986). Our model atmospheres can marginally reproduce the observed strengths, adopting C/O ratio from 1.01 to 1.1 and $\log g$ from 0.0 to 0.3. But the strengths of H_2 line predicted by our model atmosphere with C/O = 1.1 tend to be weaker than the observed in N stars. This trend is not fully consistent with the result by Lambert et al. (1986), who concluded that the average of C/O ratios in N stars is around 1.1.

2.8.3 Carbon Star Formation

We now discuss how an oxygen-rich star evolves to a carbon star, in terms of chemical compositions. We consider the scenario, in which an M giant evolves to an N type carbon star as ^{12}C produced in the helium shell flash is dredged-up into the surface, and SC stars are transitional objects from oxygen-rich stars to carbon stars. We examine this scenario, based on the chemical compositions, especially C/O ratios and ^{12}C/^{13}C ratios of N stars, SC stars, and M giants. First, analyses of chemical compositions of M giants have been done by Smith & Lambert (1985, 1990), who have shown that C/O = 1/2 – 1/3, and ^{12}C/^{13}C = 10 – 20 in M giants. On the other hand, C/O ratios in N stars have been analyzed by Lambert et al. (1986), who have shown that the average of C/O ratios in 24 N stars is 1.1. In other words, if we assume that the oxygen abundance is not modified by the third dredge-up, the carbon abundance is doubled or tripled by the addition of ^{12}C in the process from an M giant to an N star. Therefore, ^{12}C/^{13}C ratio should be also doubled or tripled from 10 up to 20∼30, which is consistent with our result for N stars. Besides, C/O ratios of SC stars are considered to be nearer to unity, that is, less than 1.1 of N stars. It means that the amount of ^{12}C added to the surface of SC stars is almost equal to that added to the surface of N stars. It implies that ^{12}C/^{13}C ratios of SC stars should have the similar distribution with that of N stars. Our result, Fig. 2.14a and 2.14b show that the range of ^{12}C/^{13}C ratios of SC stars is not so different from that of ^{12}C/^{13}C ratios of N stars. But it is highly desirable to analyze C/O ratios of more SC stars to verify the correlation between C/O ratio and $^{12}C/^{13}C$ ratio in the process of M giants to N stars through SC stars.

We examined the scenario more quantitatively by the result by Smith & Lambert (1990), who analyzed $^{12}C/^{13}C$ ratios and C/O ratios of M, MS, and S giants. They concluded that C/O ratios and $^{12}C/^{13}C$ ratios of normal M giants, which show no enhancements of the *s*-process elements, were similar to those of G and K giants. The averages for the 13 stars are $C/O = 0.40$ and $^{12}C/^{13}C = 14 \pm 4$ (see Table 10 of Smith & Lambert 1990). These M giants are not considered to be thermally pulsing, since they do not show the enhancements of the *s*-process elements. Assuming that C/O ratios of N stars are 1.1, we estimated what $^{12}C/^{13}C$ ratios those normal M giants would have when they became carbon stars by the addition of ^{12}C. In Fig. 2.21 we show the estimated distribution of $^{12}C/^{13}C$ ratios of the *would-be* carbon stars. The histogram fairly reproduces the peak at 20 to 30 and the second peak at 10 to 20 shown in Fig. 2.14a, although the number of stars in the range of 30 to 40 is somewhat larger than that in Fig. 2.14a. This simple estimate lends a support to an idea that G, K, and M giants, which are inferred to be in the red giant branch (RGB) or the He-core burning phase from their surface abundances, may evolve to N stars by the addition of ^{12}C synthesized in the thermal pulse.

As we have shown above, a simple and clear picture of the formation of N- and SC-type carbon stars can be presented based on our $^{12}C/^{13}C$ ratios and the C/O ratios by Lambert et al. (1986). However, we must keep it in mind that these $^{12}C/^{13}C$ ratios and C/O ratios are based on model atmospheres that differ by as much as 500 K in the line forming region for the same object. This fact implies that we cannot be so optimistic on our apparently consistent picture noted above until more consistent analysis of C, N, O, and their isotopic abundances in cool evolved stars are done based on model atmospheres which could pass more stringent tests for their validity in the line forming region.

The third dredge-up is a complicated phenomenon, since the material produced by the helium shell flash as well as that processed during the quiescent hydrogen shell burning phase between the flashes is involved. In the above, we discussed the formation of carbon stars, considering only the mixing of the material produced by the helium shell flash. Strictly speaking, we have to discuss the modification of $^{12}C/^{13}C$ ratio and C/O ratio, considering the contribution from both of the helium shell flash and the quiescent hydrogen shell burning. If C/O ratios of N stars are near to unity, $\sim$1.1, as analyzed by Lambert et al. (1986), our result of $^{12}C/^{13}C$ ratios means that the contribution from the quiescent hydrogen shell burning is negligible. But as pointed out by Smith & Lambert (1990), the enhancement of nitrogen abundance of MS and S stars, which is higher by 0.13dex in MS stars and by 0.29dex in S stars than normal M giants, cannot be explained by this scenario, because the enrichment of nitrogen implies the consumption of ^{12}C via the CNO-cycle.

2.9 Concluding Remarks

The first of our conclusions is that the majority (85%) of $^{12}C/^{13}C$ ratios of N-type carbon stars are distributed between 20 and 30. This shows serious disagreements with some results as surveyed in Sect. 2.8.1. For example, the result by Lambert et al. (1986), which is widely referred, shows that the distribution of $^{12}C/^{13}C$ ratios of 24 N-type carbon stars has a peak at 50 to 60.

The second conclusion is that the $^{12}C/^{13}C$ ratios of SC stars are distributed in the range similar to that of N stars, though our sample of SC stars is rather small. Only three of 15 SC stars are found to have the $^{12}C/^{13}C$ ratio smaller than 10. We concluded that the low-resolution classification which describes them as J-type (^{13}C-rich) can not be necessarily justified. The fact that SC stars show very strong Na I D lines could be explained by the peculiar atmospheric structure induced by C/O ratios very near to unity. The temperature classes of C8 – 9 assigned to SC stars are not necessarily correct.

It is generally conceived that the determination of isotopic ratios depends less critically on model atmospheres than that of elemental abundances. Our analysis revealed, however, that the resulting $^{12}C/^{13}C$ ratios depend critically on model atmospheres, and we suspect that the major reason of inconsistencies of $^{12}C/^{13}C$ ratios in the literature might be due to different understanding on atmospheric structures of cool carbon stars. For this reason, we tested our model atmospheres not only by the infrared fluxes (IRFM) but also by the spectral lines sensitive to the thermal structure of the line forming region of stellar atmospheres. We confirmed that our model atmospheres can reproduce the observed strengths of Na I D lines reasonably well, and H_2 quadrupole line marginally. We hope that our model atmospheres also represent reasonably well the thermal structure of the region responsible for the formation of CN lines.

Our result of N and SC-type carbon stars is consistent with the scenario in which an M giant becomes an N star through an SC star by the addition of ^{12}C synthesized in the thermal pulse. The $^{12}C/^{13}C$ ratios are doubled or tripled in SC and N stars as compared with M giants, as C/O ratios are also doubled or tripled in SC and N stars from M giants. This simple picture could basically explain the formation of N- and SC-type carbon stars, but still deserves further quantitative analyses in view of the present difficulties in the abundance analysis of very cool stars. Further, it remains to be solved at what evolutionary stage the change from M giants to carbon stars takes place. And the parameters which draw a line between the stars turning to carbon stars and those remaining oxygen-rich should be also investigated.

To clarify the complicated evolution of carbon stars and the related objects, further analyses of elemental abundances of C, N, O, and their isotopes in carbon stars are indispensable. Besides, analyses of the abundances of the *s*-process elements are highly desirable. These analyses of the chemical compositions will bring us an insight into the nuclear reactions and mixing operating in the stellar interior. And we should also investigate the mechanism of mass loss, which no one doubts plays an important role in the stellar evolution at the final stage. It has been revealed, since the IRAS observation, that circumstellar envelopes have important information about the stellar mass loss as well as its history. Circumstellar envelopes mostly emit their fluxes in the infrared region, which is accessible from the ground only through several windows of the terrestrial atmosphere. The Infrared Space Observatory (ISO) will bring us spectra of the objects at the final stage of stellar evolution. These spectra are not accessible from the ground and will be indispensable to clarify the physics and chemistry in circumstellar shells. This kind of approach is expected to clarify how the mass loss during the evolution from the AGB to planetary nebulae is related to the formation of carbon stars and the related objects.

Acknowledgements. We thank K. Noguchi for providing us with the valuable photometric data, and T. Okada for his support in the observations throughout this work. We also thank H. Sato and I. Yamamura for participating in some observations. The OAO CCD system was established by M. Iye in collaboration with E. Watanabe and other staffs of OAO. We also thank an anonymous referee for a careful reading of our paper and valuable comments. The data reductions and analyses were done by the use of the facilities of the Astronomical Data Analysis Center of NAOJ.

References

Anders E., Grevesse N., 1989, Geochim. Cosmochim. Acta 53, 197
Barnbaum C., 1994, ApJS 90, 317
Bartholdi P., Evans D.S., Mitchell R.I., Silverberg E.C., Wells D.C., Wiant J.R., 1972, AJ 77, 756
Bauschlicher C.W.Jr., Langhoff S.R., Taylor P.R., 1988, ApJ 332, 531
Bergeat J., Lefevre J., Kandel R., Lunel M., Sibille F., 1976, A&A 52, 245
Bergeat J., Lunel M., 1980, A&A 87, 139
Blackwell D.E., Leggett S.K., Petford A.D., Mountain C.M., Selby M.J., 1983, MNRAS 205, 897
Blackwell D.E., Lynas-Gray A.E., Petford A.D., 1991, A&A 245, 567
Blackwell D.E., Petford A.D., Shallis M.J., 1980, A&A 82, 249
Blanco V.M., McCarthy M.F., Blanco B.M., 1980, ApJ 242, 938
Blöcker T., Schönberner D., 1991, A&A 244, L43
Bouigue R., 1954, Ann. d'Astrophys 17, 104
Bregman J.D., Goebel J.H., Strecker D.W., 1978, ApJ 223, L45
Buscombe W., 1955, ApJ 121, 312
Cannon A.J., Pickering E.C., 1918, Ann. Harvard Coll. Obs. 91, 10
Cayrel R., Jugaku J., 1963, Ann d'Astrophys 26, 495
Davis S.P., Phillips J.G., 1963, The Red System ($A^2\Pi - X^2\Sigma$) of the CN Molecule (Berkely: University of California Press)
Davis S.P., Shortenhaus D., Stark G., Engleman R.,Jr., Phillips J.G., Hubbard R.P., 1986, ApJ 303, 892
Dean C.A., 1976, AJ 81, 364
Denn G.R., Luck R.E., 1991, ApJ 377, 657
de Vegt Chr., 1974, A&A 34, 457
Dominy J.F., Hinkle K.H., Lambert D.L., Hall D.N., Ridgway S.T., 1978, ApJ 223, 949
Dunham D.W., Evans D.S., Silverberg E.C., Wiant J.R., 1975, MNRAS 173, 61P
Engleman R., Rouse P.E., 1975, J. Quantit. Spectrosc. Radiat. Transfer 15, 831
FitzGerald M.P., 1968, AJ 73, 983
Frogel J.A., Cohen J.G., 1982, ApJ 253, 580
Fujita Y., 1939, Jap. Journ. Astr. and Geophys. 17, 17
Fujita Y., Tsuji T., 1977, PASJ 29, 711
Golden S.A., 1969, J. Quantit. Spectrosc. Radiat. Transfer 9, 1067
Iben I.,Jr., 1981, ApJ 246, 278
John T.L., 1988, A&A 193, 189
Johnson H.R., O'Brien G.T., Climenhaga J.L., 1982, ApJ 254, 175
Jørgensen U.G., Johnson H.R., Nordlund Å., 1992, A&A 261, 263
Keenan P.C., Boeshaar P.C., 1980, ApJS 43, 379
Keenan P.C., Morgan W.W., 1941, ApJ 94, 501
Little-Marenin I.R., Little S.J., 1984, ApJ 283, 188
Lambert D.L., Gustafsson B., Eriksson K., Hinkle K.H., 1986, ApJS 62, 373
Lasker B.M., Bracker S.B., Kunkel W.E., 1973, PASP 85, 109
Mendoza V.E.E., Johnson H.L., 1965, ApJ 141, 161
Merrill P.W., 1922, ApJ 56, 457

Mountain C.M., Leggett S.K., Selby M.J., Blackwell D.E., Petford A.D., 1985, A&A 151, 399
Noguchi K., 1993, private communication
Noguchi K., Kawara K., Kobayashi Y., Okuda H., Sato S., Oishi M., 1981, PASJ 33, 373
Noguchi K., Sun J., Wang G., 1991, PASJ 43, 311
Olson B.I., Richer, A.P., 1979, ApJ 227, 534
Palmer B.A., Engleman R.,Jr., 1983, Atlas of the Thorium Spectrum, Los Alamos National Laboratory
Ridgway S.T., Jacoby G.H., Joyce R.R., Siegel M.J., Wells D.C., 1982, AJ 87, 808
Ridgway S.T., Wells D.C., Joyce R.R., 1977, AJ 82, 414
Russell H.N., 1934, ApJ 79, 317
Schmidtke P.C., Africano J.L., Jacoby G.H., Joyce R.R., Ridgway S.T., 1986, AJ 91, 961
Secchi A., 1868, Mem. Soc. Ital. Sienze (3) 2, 73
Selby M.J., Mountain C.M., Blackwell D.E., Petford A.D., Leggett S.K., 1983, MNRAS 203, 795
Sharov A.S., 1964, SvA 7, 689
Smith V.V., Lambert D.L., 1985, ApJ 294, 326
Smith V.V., Lambert D.L., 1990, ApJS 72, 387
Stephenson C.B., 1973, Publ. Warner and Swasey Obs. 1, No. 4
Stephenson C.B., 1976, Publ. Warner and Swasey Obs. 2, No. 2
Stephenson C.B., 1989, Publ. Warner and Swasey Obs. 3, No. 2
Tsuji T., 1965, PASJ 17, 152
Tsuji T., 1976, PASJ 28, 543
Tsuji T., 1981, JA&A 2, 95
Tsuji T., 1985, In: Cool Stars with Excesses of Heavy Elements, eds, Jaschek, M., and Keenan, P.C., Reidel, Dordrecht, Holland, p.93
Vassiliadis E., Wood P.R., 1993, ApJ 413, 641
Walker A.R., 1979, SAAO Circ. 1, 112
Walker A.R., 1980, MNRAS 190, 543
Walker A.R., Wild P.A.T., Byrne P.B., 1979, MNRAS 189, 455
White N.M., Feierman B.H., 1987, AJ 94, 751
Wyller A.A., 1966, ApJ 143, 828
Yamashita Y., 1972 Ann. Tokyo Astr. Obs. 2nd Ser. 13, 169
Yamashita Y., 1975 Ann. Tokyo Astr. Obs. 2nd Ser. 15, 47

Chapter 3

Quantitative Analysis of Carbon Isotopic Ratios in Carbon Stars II. 26 J-type carbon stars including those with silicate emission

This chapter has been submitted to Astronomy and Astrophysics, (1996)
as
Quantitative analysis of carbon isotopic ratios in carbon stars
II. 26 J-type carbon stars including those with silicate emission
by
Keiichi Ohnaka,
Institute of Astronomy, The University of Tokyo
Takashi Tsuji,
Institute of Astronomy, The University of Tokyo

Abstract

We present a result of quantitative analysis of $^{12}C/^{13}C$ ratios in 26 J-type carbon stars. Carbon isotopic ratios are determined from lines of the CN red system around 8000 Å, based on the iso-intensity method and line blanketed model atmospheres.

The average of $^{12}C/^{13}C$ ratios in the 26 J-type carbon stars is found to be 4.7 ± 2.8 (standard deviation). All the stars studied, except for VX And and HD 52432, are found to have $^{12}C/^{13}C$ ratios smaller than 10. The $^{12}C/^{13}C$ ratios less than 3.4, the value at the equilibrium of the CN-cycle, are found for a significant fraction of the stars studied. For several stars, our results are in good agreement with the results by the previous authors. The serious disagreement of $^{12}C/^{13}C$ ratios, which we reported for N- and SC-type carbon stars in our preceding paper, is not found for J-type carbon stars.

A rough correlation between galactic latitude and $^{12}C/^{13}C$ ratio is found: the stars at the higher latitude have the smaller $^{12}C/^{13}C$ ratios. On the other hand, the stars at low galactic latitude have various $^{12}C/^{13}C$ ratios from less than 2 to larger than 10.

Five silicate carbon stars in our sample, EU And, BM Gem, V 778 Cyg, GC-CCS 447, and NC 83, show no peculiar $^{12}C/^{13}C$ ratios among the 26 J-type carbon stars studied in the present work. This result implies that the mechanism responsible for the low $^{12}C/^{13}C$ ratios in the silicate carbon stars might be the same with that for other J-type carbon stars. However, the $^{12}C/^{13}C$ ratios for the silicate carbon stars turn out to have given little clue to specify the mechanism for their formation.

3.1 Introduction

It is known that a small group of carbon stars can be distinguished by their enormous strength of ^{13}C-features and they were designated as J-type by Bouigue (1954). Such enormous enhancements of ^{13}C-bearing molecules are not observed in N- and SC-type carbon stars. Though SC-type carbon stars had been mostly classified as J-type by the earlier classification, Ohnaka & Tsuji (1996, hereafter Paper I) found that ^{12}C/^{13}C ratios in 15 SC-type carbon stars are mostly larger than 10.

The discussion on the formation of N- and SC-type carbon stars basically revolves around the thermal pulse and the third dredge-up at the asymptotic giant branch (AGB) (e.g. Iben 1981, Vassiliadis & Wood 1993 with mass loss included). The thermal pulse followed by the third dredge-up primarily adds ^{12}C to the stellar surface, turning oxygen-rich atmospheres to carbon-rich. Ohnaka & Tsuji (1996) showed that their ^{12}C/^{13}C ratios and the C/O ratios in N-type carbon stars derived by Lambert et al. (1986) can be consistently explained by addition of ^{12}C to atmospheres of red giants. None of the present evolutionary calculations of the carbon star formation has been successful in accounting for the observational results, such as the luminosity functions observed in the Magellanic Clouds (e.g. Blanco et al. 1980, Frogel & Cohen 1982), but the thermal pulse and the third dredge-up no doubt play a primary role in the formation of N- and SC-type carbon stars. The enhancements of the *s*-process elements observed in these types of carbon stars (e.g. Utsumi 1985) also lends a support to the recent operation of the thermal pulse, since enough neutron are expected to be supplied via ^{13}C(α,n)^{16}O or ^{22}Ne(α,n)^{25}Mg.

The enormous strength of ^{13}C-features in J-type carbon stars implies very low ^{12}C/^{13}C ratios such as less than 10. Besides, unlike N- and SC-type carbon stars, J-type carbon stars do not exhibit the enhancement of the *s*-process elements (Utsumi 1985). Thus, the scenario applied to N- or SC-type carbon stars is inadequate for J-type carbon stars. The mixing of the CN-cycled material is one of the scenarios for the formation of J-type carbon stars, since ^{12}C/^{13}C ratio is lowered to 3.4 at the equilibrium of the CN-cycle. But this scenario also has a serious shortcoming, that is, the operation of the CN-cycle means that most of carbon might be converted to nitrogen, turning carbon stars to nitrogen-rich M giants.

Carbon stars with silicate emission, which were discovered by Willems & de Jong (1986) and Little-Marenin (1986) in the IRAS Low Resolution Spectra (LRS), are also associated with J-type. The detection of silicate emission feature suggests that the circumstellar envelopes should be oxygen-rich, on the contrary to the photospheric chemical composition characterized by C/O > 1. The detection of OH and H_2O masers (Nakada et al. 1987, 1988; Little-Marenin et al. 1988) also suggests the existence of oxygen-rich material in the circumstellar envelopes of these stars. Since their discovery in the IRAS LRS spectra, the silicate carbon stars have been identified as J-type by Willems & de Jong (1986), Lloyd-Evans (1990), Chan (1993), and Lambert et al. (1990). However, ^{12}C/^{13}C ratios in silicate carbon stars have not yet been determined quantitatively.

The carbon isotopic ratios in these peculiar J-type carbon stars shed a light on the nucleosynthesis and mixing in the stellar interior. The knowledge of how much ^{13}C is enhanced in J-type carbon stars gives us a clue to clarify the nuclear reaction operating in the formation of J-type carbon stars. As for the silicate carbon stars, some peculiar $^{12}C/^{13}C$ ratios which would be associated with the presence of silicate emission may be found. We have carried out a quantitative analysis of carbon isotopic ratios from lines of the CN red system located around 8000 Å for 26 J-type carbon stars, including five silicate carbon stars, EU And, BM Gem, V 778 Cyg, GCCCS 447[1], and NC 83. Our main purpose is to find the distribution of $^{12}C/^{13}C$ ratios in J-type carbon stars. We will also discuss the resulting $^{12}C/^{13}C$ ratios in comparison with the previous results. In Sect. 7, we will discuss the mechanism responsible for the small $^{12}C/^{13}C$ ratios in J-type carbon stars. A rough correlation between galactic latitude and $^{12}C/^{13}C$ ratio will be also presented.

[1]A General Catalogue of Cool Carbon Stars (Stephenson 1973). The 2nd edition, A General Catalogue of Cool Galactic Carbon Stars (Stephenson 1989), is designated as GCCGCS.

3.2 Observation

The program stars are summarized in Table 11. The sample consists of 26 J-type carbon stars, most of which were selected from lists of carbon stars with the C-classification (Yamashita 1972, 1975), and those with comments on spectral peculiarities (Dean 1976). The IRAS database (NASA) and Stephenson (1973, 1989) were also important references. The silicate carbon stars were selected from the literature which identified them as J-type (Willem & de Jong 1986, Little-Marenin 1986, Lloyd-Evans 1990, Chan 1993, and Lambert et al. 1990). Our sample includes five of them: EU And, BM Gem, V778 Cyg, NC 83, and GCCCS 447 (a probable candidate, Lloyd-Evans 1990). We also emphasized such stars for which photometric data are available.

All observations were carried out using the 74-inch reflector of Okayama Astrophysical Observatory (OAO[2]), during the period between December 1987 and February 1993. All spectra consist of two adjacent exposures, covering from 7800 to 8030 Å. Each exposure covers 120 Å with an overlap of 10 Å allowed. The measured full width at half maximum of thorium comparison line appears to be about 0.4 Å, therefore, the spectral resolution is about 20,000. The signal-to-noise ratios are about 100, although somewhat lower for faint stars and much higher for some bright stars. The descriptions of the spectrograph and the way of data reduction are found in Paper I.

[2]OAO is a branch of National Astronomical Observatory of Japan (NAOJ). This work was carried out under the common use program of OAO.

Table 11. Summary of observations for 26 J-type carbon stars

GCCGCS[a]	GCCCS[b]	Name	C-Class[c]	m_V	Date Observed	S/N
36	11	VX And	C4,5J	8.5	1990 Dec 22	700
					1990 Dec 21	200
53	14	NQ Cas	C4,5J	9.7	1990 Dec 27	140
					1990 Dec 25	90
378	110	HD 16115	C2,3J	8.2	1990 Dec 24	100
					1990 Dec 23	20
384	112	VZ Per	C4,5J	11.0	1992 Sep 3	50
					1992 Sep 4	60
608	177	UV Cam	C5,4J	7.9	1990 Dec 22	700
					1990 Dec 21	80
654	197	BO Tau	C4,5J	10.9	1992 Nov 17	60
					1992 Nov 13	120
1158	447			11.0	1992 Nov 15	120
					1992 Nov 13	100
1290	522	DH Gem	C4,5J	10.0	1991 Mar 6	140
					1991 Mar 3	140
1466	616	UW Aur	C4,5J	10.0	1993 Feb 4	130
					1993 Feb 3	80
1507	645	HD 52432	C4,5J	7.0	1987 Dec 3	100
					1987 Dec 2	100
1653	716	BM Gem	C5,4J	9.8	1990 Apr 14	120
					1990 Apr 13	100
1891	906	MSB 31	C5:,5J	9.0	1991 Mar 6	200
					1991 Mar 3	80
2153	1126	HD 70138	C5,5J	9.3	1991 Mar 6	80
					1991 Mar 3	40
2301	1260	Lee 99	C3,4J	10.0	1993 Feb 5	30
					1993 Feb 5	36
2331	1290	HD 75021	C5,5J	7.2	1990 Dec 22	60
					1990 Dec 21	300

[a] A General Catalogue of Cool Galactic Carbon Stars, Stephenson (1989)
[b] A General Catalogue of Cool Carbon Stars, Stephenson (1973)
[c] Yamashita (1972, 1975)

Table 11. — Continued

GCCGCS	GCCS	Name	C-Class	m_V	Date Observed	S/N
2449	1403	HD 79319	C4,4J	8.9	1990 Dec 22	160
					1990 Dec 21	300
3283	2030	Y CVn	C5,5J	4.9	1992 Mar 21	800
					1992 Mar 18	120
3313	2047	RY Dra	C4,5J	6.4	1992 Mar 19	240
					1992 Mar 18	600
3558	2208	HD 133332	C4,4J	10.5	1993 Feb 2	110
					1993 Feb 4	100
4217	2717	CG Vul		9.0	1992 Mar 23	160
					1992 Mar 18	50
4222		NC 83		12.5	1992 Sep 3	60
					1992 Sep 2	60
4923	2919	V 778 Cyg	C4,5J	9.0	1990 Dec 24	200
					1990 Dec 23	80
5496	3082	RX Peg	C4,4J	7.7 – 8.6	1992 Nov 14	180
					1992 Nov 13	160
5728	3156	TX Lac	C3:,4J	10.2	1992 Sep 5	43
					1992 Sep 6	35
5848	3184	EU And		10.0	1990 Dec 22	160
					1990 Dec 21	100
5865	3186	V 353 Cas	C4,5J	9.0	1992 Sep 3	79
					1992 Sep 4	64

3.3 Model atmosphere

Model atmospheres used in the analysis are based on the code developed by Tsuji (1965). The model atmospheres are constructed on four assumptions: plane-parallel geometry, hydrostatic equilibrium, local thermodynamical equilibrium (LTE), and radiative equilibrium. The code includes the effect of a huge number of molecular lines by the Band Model Method. The detailed discussion of our model atmospheres is found in Paper I.

Our model atmospheres are specified by a set of four parameters: effective temperature, surface gravity, micro-turbulent velocity, and chemical composition. The determination of effective temperatures will be described in the next section. Surface gravity and micro-turbulent velocity are estimated by the same way as in the case of N- and SC-type carbon stars (Paper I); we set $\log g = 0.0$ and $V_{\rm micro} = 3.0$ km s^{-1}. Chemical composition is assumed to be solar (Anders & Grevesse 1989), except for the abundance of carbon. Lambert et al. (1986) analyzed elemental abundances of carbon, nitrogen, and oxygen for four J-type carbon stars[3], and showed that the average of the C/O ratios in the four stars is 1.3. Therefore, with oxygen and nitrogen abundances set solar – $\log \varepsilon(\rm N) = 8.050$ and $\log \varepsilon(\rm O) = 8.930$, we set carbon abundance to $\log \varepsilon(\rm C) = 9.044$ so that C/O ratio should be 1.3. The model grid used in the analysis is shown in Table 12. Examples of the model atmospheres adopted are shown in Fig. 3.1, together with those with C/O = 1.1 and 2.0. These models with C/O = 1.1 and 2.0 are calculated to check the effect of C/O ratio on the resulting ^{12}C/^{13}C ratios.

Table 12. Principal choices of fundamental parameters of the grid of the model atmospheres

Parameter	Values
$T_{\rm eff}$ (K)	2500, 2600, 2800, 3000, 3200, 3400, 3600, 3800
$\log g$ (cm s^{-2})	0.0
$V_{\rm micro}$ (km s^{-1})	3.0
C/O	1.3

[3]Lambert et al. (1986) also analyzed WZ Cas. But since it is classified as SC-type with the C/O ratio very near to unity, we exclude this star from the present work. It has been already discussed in Paper I.

3.4 Effective temperature

To determine effective temperature of each star, we apply the InfraRed Flux Method (IRFM, Blackwell et al. 1980). We also applied it to the determination of effective temperatures of N- and SC-type carbon stars in Paper I. Effective temperature can be determined by the ratio of bolometric flux to infrared flux observed, once the ratio is calibrated by the model atmospheres. The L'-band (3.7 μm) flux is employed as infrared flux, because this band region is least disturbed by molecular absorption in the spectra of carbon stars. Molecular absorption features are dependent on other parameters such as chemical composition, surface gravity, and microturbulent velocity as well as effective temperature. With the L'-band flux employed, however, we can determine effective temperatures as independently of those parameters as possible. The calibration of the ratio $\log R_{L'} = \log(f_{\rm BOL}/f_{L'})$ is shown in Fig. 3.2, which is calculated based on the model atmospheres with C/O = 1.3. Also plotted are the calibrations based on the model atmospheres with C/O = 1.1 and 2.0, for comparison.

Though the L'-band flux is relatively free from molecular absorption, one concern is the effect of the 3 μm absorption due to polyatomic molecules such as HCN and C_2H_2. The effect of this absorption feature is corrected by the empirical way as mentioned in Paper I. Anyway, the 3 μm absorption is located almost at the edge of the response function of the L' filter, thus the effect of this absorption feature on the observed L'-band flux has turned out to be minor. As discussed in Paper I, other molecular absorption features such as $\nu_1 + \nu_2$ bands of HCN, $\nu_2 + \nu_5$ bands of C_2H_2 at 3.7 μm, and CS at 3.9 μm is unlikely to cause any serious effect on the observed L'-band flux.

Photometric data from U or B-band throughout to L or L'-band are available in the literature (Mendoza & Johnson 1965, Noguchi et al. 1981, and Walker 1979) for four of our program stars: RY Dra, BM Gem, HD75021, and VX And. The photometric data are dereddened by A_v estimated based on the works by Sharov (1964) and by FitzGerald (1968). The bolometric fluxes are obtained by integrating the monochromatic fluxes throughout the relevant spectral region. With the bolometric fluxes and infrared fluxes evaluated in this way, we determine the effective temperatures of the four stars above. The effective temperatures determined directly by the IRFM are indicated by asterisks(*) in the third and seventh columns of Table 13. The uncertainties of $T_{\rm eff}$ are about 5%, or about 150 K for $T_{\rm eff}$ = 3000 K. Details of the origins of the uncertainties are discussed in Paper I.

For stars for which photometric data throughout the whole spectral region are not available, we determine effective temperatures by the use of the $(J - L')_0$ – $T_{\rm eff}$ relation. The photometric data of J, H, K, and L'-band of our program stars were kindly obtained by Dr. K.Noguchi, except for those available in the literature (Noguchi et al. 1981, Noguchi et al. 1995). In Fig. 3.3, we plot the effective temperatures of the four stars determined directly by the IRFM against $(J - L')_0$. Also plotted are the effective temperatures of N- and SC-type carbon stars which were also determined directly by the IRFM in Paper I. The effective temperatures of the four J-type carbon stars (filled circles) seem to be marginally higher than N- and SC-type carbon stars (open squares and open triangles, respectively) of the same $(J - L')_0$ color. However, given the uncertainties of $T_{\rm eff}$, 150 K, it seems safer to use the $(J - L')_0$ – $T_{\rm eff}$ relation based on all the three types of carbon stars than to use that based on only four J-type carbon stars. Thus, we use the $(J - L')_0$ – $T_{\rm eff}$ relation including all three types of carbon stars to determine effective temperatures of the rest of our program stars. The effective temperatures determined are summarized in the third and seventh columns of Table 13. The uncertainties of effective temperatures determined by the $(J - L')_0$ – $T_{\rm eff}$ relation are $\pm$ 200 K, as mentioned in Paper I.

3.5 Analysis

Figure 3.4 shows examples of the observed spectra of J-type carbon stars. It reveals that the spectra are severely obscured by the absorption due to ^{12}CN together with enormously strong absorption due to ^{13}CN. The spectra in Fig. 3.4 are normalized by the fictitious continuum levels, which are drawn so that they should go through the highest point in the region observed and assumed to be constant over the region. This assumption is reasonable since there is no reason to suppose that the continuum level should change significantly within only 230 Å interval.

The line positions of the ^{12}CN red system are given in Davis & Phillips (1963). For ^{13}CN, Wyller (1966) analyzed (2,0) and (3,1) bands of the red system and listed the positions of 437 rotational lines. The line of ^{13}CN is located at the wavelength longer by about 40 Å than the corresponding line of ^{12}CN due to the isotope effect. The *gf* -value of individual line of ^{12}CN is calculated by the way described in Paper I. The *gf* -values of lines of ^{13}CN are reasonably assumed to be identical with those of the corresponding lines of ^{12}CN.

We determine carbon isotopic ratios by the iso-intensity method, which is similar to the curve-of-growth method in a sense. For lines due to ^{12}CN and ^{13}CN, logarithms of the central depths normalized by the fictitious continuum level are plotted against $\log{(gf\varGamma)}$, where g is statistical weight, f is oscillator strength, and $\varGamma$ is line intensity predicted by the weighting function method (e.g. Cayrel & Jugaku 1963). $\varGamma$ can be approximately written in the form of $\varGamma(\chi) = \varGamma(0) - \chi\langle\theta_{\rm ex}\rangle$, where χ is lower excitation potential (LEP) of the line, and $\langle\theta_{\rm ex}\rangle$ is a kind of weighted mean of the reciprocal excitation temperature in the line formation region. Figure 3.5 shows examples of the iso-intensity method. The horizontal shift between the two curves for ^{12}CN and ^{13}CN gives the ratio of the abundance of ^{12}CN to that of ^{13}CN, namely, ^{12}C/^{13}C ratio. The two curves of ^{12}CN and ^{13}CN are quite close each other, implying that ^{12}C/^{13}C ratios in J-type carbon stars are very low. As can be seen in Fig. 3.5, we selected about 10 lines of ^{12}CN and 2 lines of ^{13}CN which are expected not to have their central depths disturbed by the adjacent lines. However, only several of such lines can be found for the stars whose spectra show very strong ^{13}CN lines. Some lines are blended with other lines at almost the same wavelength. We used such lines only if the blending lines are weak enough, considering their *gf* -values and LEPs.

It is very difficult to determine the true continuum level in such heavily line blanketed spectra as shown in Fig. 3.4. It should be borne in mind, however, that the carbon isotopic ratios are derived from the horizontal shifts between the two curves of ^{12}CN and ^{13}CN, that is, the ratios are determined basically from the lines of ^{12}CN and ^{13}CN with the same intensity. In other words, the absolute values of central depths, which should be measured with respect to the *true* continuum, do not matter. What really matters is that central depths measured with respect to the *fictitious* continuum level is a kind of measure of line intensities and that they serve to recognize that the lines of ^{12}CN and ^{13}CN are *iso*-intensity. That is why the resulting carbon isotopic ratios are not affected by the location of the fictitious continuum levels, as long as they are assumed to be constant over the region observed. The spectral synthesis method, which is often used in the analyses of complicated spectra, is not applied in the present work. Such analysis, in fact, cannot be justified unless the true continuum is well defined, since the synthetic spectra are usually normalized by the true continuum. More detailed description of the iso-intensity method and the reasons why we use it can be found in Paper I.

Uncertainties of the resulting $^{12}C/^{13}C$ ratios amount to about 20 %. For several stars, the uncertainties are much larger, about 50 %. Internal errors, which come from scattering of the lines plotted in the curves-of-growth, dominate the total errors. The effect of changing the model parameters is quite minor. An increase or decrease of effective temperatures by 200 K gives no noticeable change in the resulting $^{12}C/^{13}C$ ratios. The adoption of the model series with C/O = 1.1 and 2.0 instead of C/O = 1.3 neither gives any noticeable change. It should be remembered here that the model atmospheres give an effect to the resulting $^{12}C/^{13}C$ ratios via Γ, correction for the differences of LEPs of individual lines. In the case of J-type carbon stars, the lines of ^{13}CN are strong enough to enable us to determine the $^{12}C/^{13}C$ ratios by the iso-intensity method almost from (2,0) lines of ^{12}CN and ^{13}CN. These lines with almost the same LEPs are expected to be formed in almost the same layer. As a result, the effect of excitation temperature are minor in the determination of $^{12}C/^{13}C$ ratios for J-type carbon stars. We will return to this point when we discuss comparison with the previous results in the next section.

3.6 Results

Table 13. Effective temperatures and $^{12}C/^{13}C$ ratios

Star	$(J-L')_0$	$T_{\rm eff}$ (K)	$^{12}C/^{13}C$	Star	$(J-L')_0$	$T_{\rm eff}$ (K)	$^{12}C/^{13}C$
VX And	1.95	2890*	12 ± 2	Lee 99	1.18	3360	1.9 ± 0.5
NQ Cas	1.62	3090	5.3 ± 0.9	HD 75021	1.53	3150*	1.7 ± 0.7
HD 16115	0.57	3720	4.4 ± 1.4	HD 79319	1.50	3160	3.0 ± 0.3
VZ Per	1.97	2880	4.8 ± 1.2	Y CVn	2.01	2860	2.0 ± 0.5
UV Cam	1.19	3350	2.9 ± 0.4	RY Dra	1.76	3010*	1.9 ± 0.2
BO Tau	1.07	3420	2.1 ± 0.7	HD 133332	1.66	3070	3.0 ± 0.5
GCCCS 447	2.40	2620	5.6 ± 1.4	CG Vul	2.48	2570	1.9 ± 1.1
DH Gem	1.87	2940	5.3 ± 0.9	NC 83	2.71	2490	3.0 ± 1.0
UW Aur	2.22	2730	3.6 ± 0.7	V 778 Cyg	1.92	2910	4.8 ± 0.8
HD 52432	2.07	2818	12 ± 2	RX Peg	1.96	2890	7.6 ± 2.4
BM Gem	2.18	3010*	4.8 ± 0.8	TX Lac	1.12	3390	4.8 ± 1.2
MSB 31	1.90	2920	9.1 ± 1.5	EU And	1.86	2950	5.3 ± 0.9
HD 70138	1.62	3090	2.8 ± 0.7	V 353 Cas	2.09	2810	6.9 ± 1.2

*: $T_{\rm eff}$ are determined directly by the IRFM.

†: $T_{\rm eff}$ are determined directly by the IRFM, but L' band fluxes are extrapolated from L band fluxes. See also the text.

The resulting $^{12}C/^{13}C$ ratios in the 26 J-type carbon stars studied are given in the fourth and eighth columns of Table 13. The histogram of $^{12}C/^{13}C$ ratios is shown in Fig. 3.6. It shows a somewhat broad peak from $^{12}C/^{13}C = 1$ to 6. The average of $^{12}C/^{13}C$ ratios in the 26 J-type carbon stars is 4.7 ± 2.8 (standard deviation). Two exceptions are VX And and HD 52432, both of which have the ratio of 12. Attention should be also paid to the stars which have the $^{12}C/^{13}C$ ratios less than 3.4, the value expected at the equilibrium of the CN-cycle. Especially, Lee 99, HD 75021, RY Dra, and CG Vul have the extremely low $^{12}C/^{13}C$ ratios less than 2. Though the uncertainties of the $^{12}C/^{13}C$ ratios are relatively large for some of those stars, such low $^{12}C/^{13}C$ ratios cannot be explained by the CN-cycle at the equilibrium, as discussed in the next section.

We now turn to the silicate carbon stars in our sample. Willems & de Jong (1986) proposed that all of the silicate carbon stars might have enhanced ^{13}C abundances, noting that at least two of the silicate carbon stars they identified are J-type. Later, Lloyd-Evans (1990) identified seven stars showing photospheric spectra of carbon stars together with 9.8 μm silicate emission feature. Lloyd-Evans (1990) showed that five of the seven stars were J-type and the classification of other two stars remained to be further examined. Lambert et al. (1990) identified the two questionable stars of Lloyd-Evans (1990) as J-type from the observations of the K-band spectra. We confirm these previous identifications more quantitatively. The ^{12}C/^{13}C ratios are 5.3 ± 0.9 for EU And, 4.8 ± 0.8 for BM Gem, 4.8 ± 0.8 for V 778 Cyg, 3.0 ± 1.0 for NC 83, and 5.6 ± 1.4 for GCCCS 447. These results are perfectly consistent with the previous identifications of these stars as J-type. And it is worth noting that the five silicate carbon stars have the ^{12}C/^{13}C ratios which are the most common value in our sample. In other words, these stars exhibit no peculiar ^{12}C/^{13}C ratios which would be associated with the presence of the silicate emission feature.

One might point out, however, that Lambert et al. (1990) estimated the ^{12}C/^{13}C ratios of the silicate carbon stars they observed (EU And, V 778 Cyg, NC 83, and BM Gem) might be similar to that of VX And (^{12}C/^{13}C $= 13$ by Lambert et al. 1986 and ^{12}C/^{13}C $= 12 \pm 2$ by the present work). But the estimations of Lambert et al. (1990) were based only on the mean equivalent widths of ^{12}CN and ^{13}CN lines located around 2 μm, while our analysis is done on a line-by-line basis using model atmospheres which take correction for the differences of LEPs of lines into account.

Our sample includes several stars previously analyzed by other authors. The comparison with the previous results is shown in Table 14. RX Peg and Y CVn were analyzed by Fujita & Tsuji (1977) and Fujita et al. (1969), and their results were ^{12}C/^{13}C $= 6$ for RX Peg and ^{12}C/^{13}C $= 8$ for Y CVn. The excitation temperatures adopted were 3150 K for RX Peg and 2520 K for Y CVn. The errors of ^{12}C/^{13}C ratios were reportedly about a factor of 2. Therefore, our results are in agreement with theirs, given the errors of the results and the difference of the determination of excitation temperature. Our sample also includes three stars analyzed by Lambert et al. (1986): RY Dra, Y CVn, and VX And. Our results for these stars show a fair agreement with their results.

These agreements show a marked contrast to the cases of N- and SC-type carbon stars discussed in Paper I, where our results were by a factor of 2 to 3 smaller than the results by Fujita & Tsuji (1977) or Lambert et al. (1986). As we pointed out in Paper I, the differences of excitation temperature adopted or of the model atmospheres adopted were a prime suspect of the disagreement. It should be remembered here again that the model atmospheres give an effect to the resulting ^{12}C/^{13}C ratios via Γ, correction for the differences of LEPs of individual lines. As mentioned in the previous section, the ^{12}C/^{13}C ratios are determined by the iso-intensity method primarily from (2,0) lines of ^{12}CN and ^{13}CN. This implies that the corrections for the LEPs by model atmospheres should not be so different for ^{12}CN and ^{13}CN. Therefore, as long as we are concerned with isotopic *ratios*, the effect of model atmospheres is minor in the case of J-type carbon stars. In the cases of N- and SC-type carbon stars, lines of ^{12}CN as weak as those of ^{13}CN (2,0) band were from (7,4) transition. Namely, the ^{12}C/^{13}C ratios were determined from ^{12}CN lines of high LEPs and ^{13}CN lines of low LEPs. These lines of ^{12}CN and ^{13}CN are thought to be formed in the different layers in the atmosphere, thus the correction for this effect by model atmospheres was crucial for the determination of ^{12}C/^{13}C ratios.

Table 14. Comparison with the results by the previous authors

Sources	$^{12}C/^{13}C$	Molecular System	Type of Analysis
		Y CVn	
Fujita et al. 1969	8	CN Red, $\Delta v = 2, 3$	curve-of-growth
Lambert et al. 1986	3.4 ± 0.4	CN Red, $\Delta v = -2$	curve-of-growth
	3.0 ± 0.3	CO, $\Delta v = 3$	curve-of-growth
	4.1 ± 0.8	CO, $\Delta v = 2$	curve-of-growth
This work	2.0 ± 0.5	CN Red, $\Delta v = 2, 3$	curve-of-growth
		RX Peg	
Fujita & Tsuji 1977	6	CN Red, $\Delta v = 2, 3$	curve-of-growth
This work	7.6 ± 0.4	CN Red, $\Delta v = 2, 3$	curve-of-growth
		RY Dra	
Lambert et al. 1986	3.7 ± 0.5	CN Red, $\Delta v = -2$	curve-of-growth
	2.7 ± 0.4	CO, $\Delta v = 3$	curve-of-growth
	4.0 ± 1.0	CO, $\Delta v = 2$	curve-of-growth
This work	1.9 ± 0.2	CN Red, $\Delta v = 2, 3$	curve-of-growth
		VX And	
Lambert et al. 1986	13 ± 3	CN Red, $\Delta v = -2$	curve-of-growth
	6.5 ± 1.5	CO, $\Delta v = 3$	curve-of-growth
	13 ± 3	CO, $\Delta v = 2$	curve-of-growth
This work	12 ± 2	CN Red, $\Delta v = 2, 3$	curve-of-growth

3.7 Discussion

The $^{12}C/^{13}C$ ratios in 26 J-type carbon stars have been derived and the mean value is 4.7. The thermal pulse and the third dredge-up cannot account for such low $^{12}C/^{13}C$ ratios. Besides, the lack of enhancements of the *s*-process elements in J-type carbon stars (e.g. Utsumi 1985) cannot be interpreted by this scenario. The low $^{12}C/^{13}C$ ratio in J-type carbon stars has been often attributed to the mixing of the CN-cycled material, since $^{12}C/^{13}C$ ratio is lowered to 3.4 at the equilibrium of the CN-cycle. In other words, $^{12}C/^{13}C$ ratios could be lowered to 3.4 if the photospheres of J-type carbon stars consist of the pure CN-cycled material. This is the case expected if the CN-cycle operates at the bottom of the convective envelope (Hot Bottom Convective Envelopes, HBCE). Massive stars, say about 5 $M_\odot$ or more, develop deep convective envelopes with very high base temperature, leading to the possible operation of the CN-cycle (Sugimoto 1971, Iben 1975, Scalo et al. 1975, Renzini & Voli 1981, Blöcker & Schönberner 1991). $^{12}C/^{13}C$ ratios larger than 3.4 are also expected if the the mixing of the CN-cycled material is moderate. Thus, of our program stars, the stars which have $^{12}C/^{13}C$ ratios larger than 3.4 could be explained by the HBCE. The observations of J-type carbon stars in the Magellanic Clouds (Richer et al. 1979, Cohen et al. 1981), which showed that J-type carbon stars are among the most luminous of the carbon stars, suggest that they might be relatively massive stars and that the HBCE might be possible.

However, in fact, a significant fraction of our sample shows $^{12}C/^{13}C$ ratios below the equilibrium value of 3.4. Though the errors of the $^{12}C/^{13}C$ ratios are relatively large for some of those stars, this result implies that those J-type carbon stars may have experienced non-equilibrium process or the hot CNO cycle on their way of evolution. And the HBCE scenario has a drawback that the operation of the CN-cycle, which converts ^{12}C to ^{14}N, leads to depletion of carbon and enhancement of nitrogen abundance, turning carbon stars to nitrogen-rich M-giants. However, Lambert et al. (1986) showed that the N abundances in four J-type carbon stars (RY Dra, T Lyr, VX And, and Y CVn) are sub-solar. They concluded that the CN-cycle is inadequate to explain the low $^{12}C/^{13}C$ ratios in J-type carbon stars, though they also mentioned that RY Dra and Y CVn are relatively nitrogen-rich, therefore, the operation of the CN-cycle might be possible. For our program stars, nitrogen abundances are not known except for the four stars analyzed by Lambert et al. (1986). It is highly desirable to determine nitrogen abundances to clarify the origin of the low $^{12}C/^{13}C$ ratios in J-type carbon stars and their evolutionary status.

In Fig. 3.7, we plot the galactic latitude $|\, b \,|$ of each star against the resulting $^{12}C/^{13}C$ ratio. Though the plot appears to be rather scattered, it seems that the stars at high galactic latitude tend to have smaller $^{12}C/^{13}C$ ratios. Our program stars are thought to have been formed in the Galactic disk and then have moved up or down to the present galactic latitude. Thus it is inferred that the stars at the higher galactic latitude might have lived the longer life. Therefore, roughly speaking, these stars should have lower mass. Figure 3.7 roughly implies that *stars with the lower mass might have the lower* $^{12}C/^{13}C$ *ratios.* On the other hand, it is expected that stars of various masses should be found at low galactic latitude, and that these stars should have various $^{12}C/^{13}C$ ratios. This is consistent with the result shown in Fig. 3.7, where the ^{12}C/^{13}C ratios are distributed from less than 2 to larger than 10 for the stars at low $|\, b \,|$. The discussion above is rather coarse, and of course, other factors such as metalicity should be taken into account. Since the number of our program stars at high galactic latitude is relatively small, it is also desirable to analyze more stars at high galactic latitude before establishing the correlation above. We should also admit that this correlation between ^{12}C/^{13}C ratios and $|\, b \,|$ does not specify the nuclear mechanism for the formation of J-type carbon stars. Nonetheless, our result that the less massive stars have the smaller ^{12}C/^{13}C ratios could give a constraint to theoretical calculations of stellar evolution which try to reproduce J-type carbon stars.

As for the progenitors of J-type carbon stars, R-type carbon stars are one of the candidates, since they also have small ^{12}C/^{13}C ratios, $8 \sim 9$ (Dominy 1984). A statistical parallax study (Vandervort 1958) showed that R-type carbon stars have $\sim 100\ L_{\odot}$, which is the luminosity achieved by the He-core burning (Scalo 1976). And their effective temperatures are as high as 4000 – 5000 K (Dominy 1984). Namely, their locations on the HR diagram correspond to those of the horizontal branch stars. In addition, R-type carbon stars are distributed up to high galactic latitude, while N-type carbon stars almost along the Galactic plane. Thus R-type carbon stars are inferred to be members of a generation which is older and less massive. Since R-type carbon stars lies far below the luminosities expected for the AGB, the change of the photospheric composition from oxygen-rich to carbon-rich should take place by the time they come to the horizontal branch. Dominy (1984) suggested that the mixing at the He-core flash could turn oxygen-rich atmospheres to carbon-rich. Supposing that it is responsible for the formation of R-type carbon stars and they are the progenitors of J-type carbon stars, it will be interesting to see whether theoretical calculations predict the smaller ^{12}C/^{13}C ratios in the less massive stars.

The formation of silicate carbon stars has been also controversial. At present, the most plausible scenario is the binary model proposed by Morris (1987), Morris (1990), Lloyd-Evans (1990), and Lambert et al. (1990). According to that scenario, material shed by an oxygen-rich primary star, possibly at the He-core flash, is stored in the accretion disk around a low mass companion until the primary becomes carbon-rich. Barnbaum et al. (1991) showed that the variations of radial velocities observed for EU And, BM Gem, and V 778 Cyg are consistent with motion in binary systems. However, as pointed out by Lambert et al. (1990), a critical issue for this model is the stability of the accretion disk. If it is formed when the primary star is on the horizontal branch, it must survive until the primary becomes a luminous carbon star. As mentioned in the previous section, the ^{12}C/^{13}C ratios in the five silicate carbon stars studied in the present work show no peculiar values as compared with those of other J-type carbon stars. This implies that the mechanism responsible for the low ^{12}C/^{13}C ratios in silicate carbon stars might be the same with that for other J-type carbon stars. It might be inferred that the progenitors of silicate carbon stars and other J-type carbon stars are the same, R-type carbon stars for example, and that some of these stars could be observed as silicate carbon stars when the conditions for the stability of the accretion disk, such as mass ratio of the primary to the companion, separation, etc are met.

3.8 Concluding Remarks

The major result of this work is that $^{12}C/^{13}C$ ratios are quantitatively determined for a large sample of J-type carbon stars. The distribution shows a rather broad peak from $^{12}C/^{13}C = 1$ to 6. A significant fraction of them have the $^{12}C/^{13}C$ ratios below the value of 3.4, which is expected at the equilibrium of the CN-cycle. Two stars, VX And and HD 52432, are found to have moderately enhanced $^{12}C/^{13}C$ ratios. Though the CN-cycle can seemingly explain the resulting $^{12}C/^{13}C$ ratios, it seems inadequate for the formation of J-type carbon stars. The CN-cycle primarily leads to depletion of carbon and enrichment of nitrogen, which were not found in the four J-type carbon stars analyzed by Lambert et al. (1986). The analyses of elemental abundances of carbon, nitrogen, and oxygen and their isotopic ratios are highly desirable to clarify the nuclear mechanism responsible for the formation of J-type carbon stars.

Other conclusion is, though it is quite rough, that J-type carbon stars at the higher galactic latitude, $| b |$, tend to have the smaller $^{12}C/^{13}C$ ratios. As it is inferred that the stars at high galactic latitude should be less massive, the mechanism responsible for the small $^{12}C/^{13}C$ ratios in J-type carbon stars might work favorably in less massive stars. If the mixing at the He-core flash is responsible for the formation of R-type carbon stars and they are the progenitors of J-type carbon stars, it will be interesting whether theoretical calculations of stellar interior can predict smaller $^{12}C/^{13}C$ ratios in less massive stars. It should be also borne in mind that R-type carbon stars, which are inferred to become carbon-rich before the horizontal branch, could follow evolutionary tracks different from those of the stars which remain oxygen-rich at the horizontal branch. Such theoretical calculations should be also carried out to clarify the relation between R- and J-type carbon stars.

Our last conclusion is that the five silicate carbon stars in our sample show no peculiar $^{12}C/^{13}C$ ratios as compared with other J-type carbon stars. This result implies that the mechanism which lowers $^{12}C/^{13}C$ ratios in silicate carbon stars might not be different from that in other J-type carbon stars. Though the scenario in which oxygen-rich material shed at the He-core flash is stored in the accretion disk around a companion has still some drawbacks, it might be possible that some of R-type carbon stars would evolve and be observed as silicate carbon stars only when the conditions for the survival of the accretion disk around the companion are met.

Acknowledgements. We thank K. Noguchi for observing some of our program stars and providing us with valuable photometric data. We also thank T. Okada for his support in the observations throughout this work. K. Tomioka also participated in the initial phase of this work. The OAO CCD system was established by M. Iye in collaboration with E. Watanabe and other staffs of OAO. The data reductions and analyses were done by the use of the facilities of the Astronomical Data Analysis Center of NAOJ.

References

Anders E., Grevesse N., 1989, Geochim. Cosmochim. Acta 53, 197
Barnbaum C., Morris M., Likkel L., Kastner J.H., 1991, A&A 251, 1991
Blackwell D.E., Petford A.D., Shallis M.J., 1980, A&A 82, 249
Blanco V.M., McCarthy M.F., Blanco B.M., 1980, ApJ 242, 938
Blöcker T., Schönberner D., 1991, A&A 244, L43
Bouigue R., 1954, Ann. d'Astrophys 17, 104
Cayrel R., Jugaku J., 1963, Ann d'Astrophys 26, 495
Chan S.J., 1993, AJ 106, 2126
Cohen J.G., Frogel J.A., Persson S.E., Elias J.H., 1981, ApJ 249, 481
Davis S.P., Phillips J.G., 1963, The Red System ($A^2\Pi - X^2\Sigma$) of the CN Molecule (Berkely: University of California Press)
Dean C.A., 1976, AJ 81, 364
Dominy J.F., 1984, ApJS 55, 27
FitzGerald M.P., 1968, AJ 73, 983
Frogel J.A., Cohen J.G., 1982, ApJ 253, 580
Fujita Y., Tsuji T., 1977, PASJ 29, 711
Fujita Y., Tsuji T., Maehara H., 1969, Proc. Japan. Acad. 45, 484
Iben I.,Jr., 1975, ApJ 196, 525
Iben I.,Jr., 1981, ApJ 246, 278
Little-Marenin I.R., 1986, ApJ 307, L15
Little-Marenin I,R., Benson P.J., Dickinson D.F., 1988, ApJ 330, 828
Lambert D.L., Gustafsson B., Eriksson K., Hinkle K.H., 1986, ApJS 62, 373
Lambert D.L., Hinkle K.H., Smith V.V., 1990, AJ 99, 1612
Lloyd-Evans T., 1990, MNRAS 243, 336
Mendoza V.E.E., Johnson H.L., 1965, ApJ 141, 161
Morris M., 1987, PASP 99, 1115
Morris M., 1990, In: From Miras to Planetary Nebulae: Which Path for Stellar Evolution? eds. Mennessier M.O., Omont A., Editions Frontieres, Gif sur Yvette, p.520
Nakada Y., Deguchi S., Forster J.R., 1988, A&A 193, L13
Nakada Y., Izumiura H., Onaka T., Hashimoto O., Ukita N., Deguchi S., Tanabe T., 1987, ApJ 323, L77
Noguchi K., Kawara K., Kobayashi Y., Okuda H., Sato S., Oishi M., 1981, PASJ 33, 373
Noguchi K., Qian Z., Sun J., Wang G., 1995, PASJ 47, 41
Ohnaka K., Tsuji T., 1996, A&A in press
Renzini A., Voli M., 1981, A&A 94, 175
Richer H.B., Olander N., Westerlund B.E., 1979, ApJ 230, 724
Scalo J.M., 1976, ApJ 206, 474
Scalo J.M., Despain K.H., Ulrich R.K., 1975, ApJ 196, 805
Sharov A.S., 1964, SvA 7, 689
Stephenson C.B., 1973, Publ. Warner and Swasey Obs. 1, No. 4
Stephenson C.B., 1989, Publ. Warner and Swasey Obs. 3, No. 2
Sugimoto D., 1971, Prog. Theor. Phys. 45, 761
Tsuji T., 1965, PASJ 17, 152
Utsumi K., 1985, In: Cool Stars with Excesses of Heavy Elements, eds, Jaschek M., Keenan

P.C., Reidel, Dordrecht, Holland, p.243
Vandervort G.L., 1958, AJ 63, 477
Vassiliadis E., Wood P.R., 1993, ApJ 413, 641
Walker A.R., 1979, SAAO Circ. 1, 112
Willems F.J., de Jong T., 1986, ApJ 309, L39
Wyller A.A., 1966, ApJ 143, 828
Yamashita Y., 1972 Ann. Tokyo Astr. Obs. 2nd Ser. 13, 169
Yamashita Y., 1975 Ann. Tokyo Astr. Obs. 2nd Ser. 15, 47

Chapter 4

Spherical Model Atmosphere of Carbon Stars

Abstract

A new code of spherical model atmosphere of carbon stars has been developed with molecular line opacity due to CO, C_2, CN, HCN, and C_2H_2 incorporated by the Band Model method. Though the Band Model might be considered to be rather simplified, the temperature stratification calculated by our code reproduces well that of the model constructed with the Opacity Sampling method. The sphericity effect becomes significant in models as cool as 2800 K, because of the interplay between the cooling by dilution of radiation field and the formation of polyatomic molecules. The emergent fluxes are compared with the observation by the ISO SWS, and the match is satisfactory for the 3 μm absorption feature due to HCN and C_2H_2. However, the observed strength of the absorption at 7 μm due to the same molecular species is far weaker than the predicted, and the observed flux longward 6 μm appears to be contaminated by the contribution from the circumstellar envelope.

The sphericity effect on synthetic spectra of the CO first overtone and fundamental bands has been also investigated by the use of the line radiative transfer code in spherical geometry. It has been shown that weak lines appear to be weaker and strong lines appear to be stronger in spherical models than in plane parallel models. This can be interpreted as combination of the effect due to the temperature stratification and that due to the spherical geometry.

4.1 Introduction

Intermediate- and low-mass stars evolve up on the HR diagram after the helium at the stellar center is exhausted and they are called asymptotic giant branch (AGB) stars. They achieve luminosities of 10^3 – 10^4 $L_\odot$, with effective temperatures as cool as 3000 K. The change of chemical composition at the stellar surface is expected to be brought about by mixing of the material processed in the stellar interior. Carbon stars are one of such objects. The carbon freshly synthesized in the thermal pulse is considered to be responsible for the enhancement of carbon in these stars. The atmosphere of these stars becomes extended somewhat significantly in comparison with the stellar radius, though the extension is of course dependent on stellar parameters. At the same time, one of the major characteristics of AGB stars is slow and massive mass loss. The radiation pressure on dust grains is one of the driving mechanism suggested, but it still remains to be clarified where and how dust grains form. In addition, emission lines observed in the UV region imply the existence of chromosphere, which may have inhomogeneous structure. But its heating mechanism and any connections with the onset of mass loss are not well understood, either.

To understand the physics and chemistry in the region from the upper photosphere to the circumstellar envelope, it is necessary to construct realistic models of the photosphere, especially of the upper photosphere, because it serves as the boundary condition to models of the circumstellar envelope. In the upper photosphere of AGB stars, the effect of sphericity may be significant and the approximation of plane parallel geometry may not be adequate. The relative extension of the stellar atmosphere, $\Delta r_{atm}/R_\star$, (the ratio of the thickness of the atmosphere to the radius of the star) can be estimated based on model photospheres in plane parallel geometry and the stellar radius predicted by the theory of stellar evolution. The estimated relative extension, $\Delta r_{atm}/R_\star$, is from 10 to 20 % in carbon stars, therefore, the plane parallel approximation may not be necessarily justified.

The effect of sphericity on the atmospheric structure of late-type stars has been investigated by several authors. For M-type stars, spherical model atmospheres developed by two groups. Bessel et al. (1989a, 1989b, 1991) computed model atmospheres employing mean opacities for CN, CO, OH, H_2O, TiO, and VO. On the other hand, Plez et al. (1992) computed model atmospheres of M (super) giants employing the Opacity Sampling method including H_2O, TiO, and VO as well as diatomic molecules and atomic lines. They also offered the comparisons of the computed fluxes and colors with some observations. The matches between the models and observations were fair in the spectral region longer than 1 μm, but the visual spectra were poorly reproduced.

As for carbon stars, the effect of sphericity was first investigated by Scholz & Tsuji (1984). They employed the straight mean opacities in incorporating a huge number of molecular lines. They found that the effect of sphericity in the atmosphere of carbon stars was much smaller than in the corresponding M-type stars. Jørgensen et al. (1992) computed more than 200 model atmospheres in spherical symmetry with the Opacity Sampling method for CO, CN, C_2, HCN, C_2H_2, and C_3. They also computed synthetic spectra of CN, CO, and HCN, and found that the effect of sphericity is measurable only in the strongest lines of CO and in lines of HCN.

Though the models constructed with the Opacity Sampling method are regarded as the state-of-the-art, the method lacks flexibility because huge opacity tables covering relevant temperature, pressure, turbulent pressure, and chemical composition must be prepared prior to model computation. On the other hand, the Band Model method, which was formulated by Golden (1969) and first applied to modeling of the atmosphere of red supergiants by Tsuji (1976), is more flexible. We present here the development of spherical model atmosphere of carbon stars employing the Band Model method in incorporating molecular line opacities. The motivations of the development of the code include not only the investigation of the sphericity effect in high-resolution spectra, especially in the strong lines of the CO first overtone bands, but also a possible inclusion of hydrodynamics and dust formation in the upper photosphere and inner-circumstellar envelope in the future. In plane parallel models, surface gravity remains constant throughout the atmosphere, therefore, the construction of spherical models is essential to model the complicated phenomena in the upper atmosphere such as dust formation and the onset of mass loss.

4.2 Method of construction of spherical model

A code of spherical model atmosphere was developed on the following assumptions: spherical symmetry, hydrostatic equilibrium, the local thermodynamical equilibrium (LTE), and radiative equilibrium. In the case of plane parallel geometry, model atmospheres are specified by a set of four parameters: effective temperature, surface gravity, micro-turbulent velocity, and chemical composition. On the other hand, in the case of model atmospheres in spherical symmetry, stellar radius is necessary to specify model atmospheres in addition to the four parameters above. Since stellar radius, mass, and luminosity are related by the following formulae,

$$g = \frac{GM}{R_\star^2} \tag{4.1}$$

$$L_\star = 4\pi R_\star^2 \sigma T_{\mathrm{eff}}^4, \tag{4.2}$$

where σ is the Stefan-Boltzmann constant, it is arbitrary to choose the fifth parameter among radius, mass, and luminosity. We employ stellar mass as the fifth parameter to specify model atmospheres. Now our spherical model atmospheres are specified by a set of five parameters, effective temperature T_{eff}, surface gravity g, micro-turbulent velocity V_{micro}, chemical composition, and stellar mass M.

With an initial guess of temperature stratification, the hydrostatic equations

$$\frac{d\log P_{\mathrm{total}}}{d\log\tau_0} = \frac{\tau_0}{\kappa_0(T,P_{\mathrm{gas}})P_{\mathrm{total}}}\frac{GM}{r^2} \tag{4.3}$$

$$\frac{d\log P_{\mathrm{rad}}}{d\log\tau_0} = \frac{\tau_0}{\kappa_0(T,P_{\mathrm{gas}})P_{\mathrm{rad}}}\frac{L_\star\langle\kappa_{\mathrm{F}}\rangle}{4\pi c r^2} \tag{4.4}$$

$$\frac{dr}{d\log\tau_0} = -\frac{\tau_0\ln 10}{\kappa_0(T,P_{\mathrm{gas}})}\frac{\mathcal{R}T}{\mu(T,P_{\mathrm{gas}})P_{\mathrm{gas}}} \tag{4.5}$$

$$P_{\mathrm{tur}} = \frac{1}{2}\rho(r)v_{\mathrm{tur}}^2 \tag{4.6}$$

$$P_{\mathrm{total}} = P_{\mathrm{gas}} + P_{\mathrm{rad}} + P_{\mathrm{tur}} \tag{4.7}$$

are solved. The atmosphere is divided into 80 layers, from $\log\tau_0 = -6.0$ to 1.9, where τ_0 is the optical depth of continuum at 1.04 μm. The continuous opacity at that wavelength is denoted by κ_0. P_{gas}, P_{rad}, P_{tur}, and P_{total} represent the gas pressure, radiation pressure, turbulent pressure, and total pressure, respectively. The flux-mean-opacity is denoted by $\langle\kappa_{\mathrm{F}}\rangle$. $\mu(T,P_{\mathrm{gas}})$ is the mean molecular weight and $\mathcal{R}$ is the gas constant. At each of these layers, source function, mean intensity, and luminosity are evaluated as described below. However, prior to the integration of the hydrostatic equations above, total pressure and radiation pressure at the boundary $\log\tau_0 = -6.0$ should be determined. To evaluate these starting values, we set another 30 layers from $\log\tau_0 = -9.0$ to -5.9 above the

80 layers. We start integration from the outermost layer, $\log \tau_0 = -9.0$ through the smallest relevant optical depth layer of $\log \tau_0 = -6.0$ to the bottom of the atmosphere. If the starting pressures at the outermost layer are chosen small enough, the pressures at the smallest relevant optical depth layer are independent of those values. In fact, if the starting pressures at $\log \tau_0 = -9.0$ are by two or three orders of magnitude smaller than the expected values at the layer $\log \tau_0 = -6.0$, the choice of the starting values does not give any changes to the pressures and radius at the layer of the smallest relevant optical depth. The temperature stratification in the upper 30 layers is assumed to be iso-thermal, that is, the temperature in these layers is assumed to equal to that in the layer of $\log \tau_0 = -6.0$. This assumption seems to be too simplified, but the solution of the hydrostatic equations deeper than the smallest relevant optical depth has turned out to be insensitive to the temperature stratification in the upper 30 layers. These uppermost 30 layers are set only for finding the starting values of pressure at the layer of the smallest relevant optical depth, and the radiative transfer equation is solved in the layers deeper than $\log \tau_0 = -6.0$.

After one integration of the hydrostatic equations, we obtain the radius of each layer. Now the radius of each layer is corrected so that the radius of the layer $\tau_0 = 1.0$ should be equal to the stellar radius defined by $R_\star = \sqrt{GM/g}$. We rescale the radius of each layer by $r(\tau_0(i))_{\rm new} = r(\tau_0(i))_{\rm old} R_\star / r(\tau_0 = 1)$. With the new starting value of radius at the outermost layer, the hydrostatic equations are solved until the correction at the layer $\tau_0 = 1.0$ vanishes.

In the process of the integrations of the hydrostatic equations, ionization and chemical dissociation equilibria including more than 100 atoms, ions, and molecules are simultaneously solved. Therefore, after the integrations of the hydrostatic equations above, the pressure stratification of each molecular and atomic species is obtained.

As the second step of construction of model atmospheres, absorption and scattering coefficients of each molecular and atomic species are evaluated. The molecular line opacities are incorporated by the Band Model method. The applications of the Band Model method to model atmospheres are summarized in Tsuji (1994). This method characterizes a run of opacity by two parameters, that is, mean cross section and mean line separation in each spectral mesh of appropriate interval. Once the spectral line shape is defined, it is straight forward to obtain the opacity distribution function (ODF). The case of the Voigt profile was formulated by Golden (1969), which is known as the Voigt-Analogue Elsasser Band Model (VAEBM). We applied this method to evaluate the opacities due to CO, CN, C_2, HCN, and C_2H_2. The mean cross section and the mean line separation are calculated by the method described in Tsuji (1994) from molecular constants. With the mean absorption coefficient $\overline{l_i}$ calculated from the mean cross section and the mean line separation d_i, the spectral absorption in the i-th spectral mesh by the VAEBM is given by

$$P_{\rm VAEBM} = \overline{l_i} \left(1 + 2 \sum_{k=1}^{\infty} \exp[-k^2 \left(\frac{\pi \Delta\omega_{\rm D}}{d_i} \right)^2 - k \left(\frac{2\pi\gamma_{\rm L}}{d_i} \right)] \cos(\pi k x) \right) \tag{4.8}$$

where $\Delta\omega_{\rm D}$ is Doppler half-width, $\gamma_{\rm L}$ is damping half width, and

$$x = \frac{2(\omega - \omega_0)}{d_i} \tag{4.9}$$

with ω_0 wavenumber of the band center (Golden 1969).

If the intervals of spectral meshes are small enough for the Planck function to be regarded as constant, we can replace the spectral absorption coefficient by a probability distribution function

$$l_i(p) = \overline{l_i} \frac{P_{\mathrm{VAEBM}}(p)}{\int_0^1 P_{\mathrm{VAEBM}}(x) dx} \tag{4.10}$$

where p is the probability that the absorption coefficient is larger than $l_i(p)$. This probability distribution function works equivalently with an array of lines in solving radiative transfer and is formally equivalent to the opacity distribution function (ODF). To discretize the opacity distribution function above, we divide each spectral mesh into 5 submeshes.

For CO, CN, and C_2, tables of the mean cross section and the mean line separation are prepared as functions of temperature for 194 spectral meshes from 0.2 to 45 μm. For HCN and C_2H_2, line separations are not used in the calculation of the absorption coefficients, because the line separations for these polyatomics are usually smaller than the Doppler widths. In such case the mean absorption coefficient represents well the real opacity.

It has been one of the obstacles in constructing realistic model atmospheres of cool stars how to incorporate the opacity due to a huge number of molecular lines. Though the Opacity Sampling method is regarded as state-of-the-art at present, it lacks flexibility especially when applied to construct models including complicated phenomena such as dust formation processes and hydrodynamics. The advantage of the Band Model method is its flexibility. The molecular line opacity in each spectral mesh can be easily evaluated for a given temperature, pressure, micro-turbulent velocity, and chemical composition.

As the third step, which is the heart of the code, the radiative transfer equation is solved in each spectral submesh. We employed the integral equation method described in Schimdt-Burgk (1975). Outward and inward intensities are evaluated along a ray of a given impact parameter p as shown in Fig. 4.1. In other words, the angular dependence of outward and inward intensities is handled by a set of parallel rays with various impact parameters. We divide the impact parameter space into two regions: *core* and *shell* regions. The core is the central source assumed to be totally opaque and to emit intensity $I_\nu^s(p)$ from its surface. The shell is the atmosphere that we are now constructing. In the shell region 8 rays are taken at every 10 layers, while in the core region 10 rays are set equidistantly in cosine of the angle toward the normal.

With an initial guess of source function given, inward intensity at each spectral submesh is calculated by

$$I_\nu^-(p, z) = \int_z^{\sqrt{r_{-6}^2 - p^2}} \kappa_\nu(\sqrt{p^2+\zeta^2}) \rho(\sqrt{p^2+\zeta^2}) S_\nu(\sqrt{p^2+\zeta^2}) \exp(-\tau_\nu(p;\zeta,z)) d\zeta, \tag{4.11}$$

where r_{-6} is the radius of the layer of $\log\tau_0 = -6$, and $\tau_\nu(p; a, b)$ is optical depth from the point $z = b$ to $z = a$ along a ray with an impact parameter p. In fact, it is defined as

$$\tau_\nu(p; a, b) = \int_b^a \kappa_\nu(\sqrt{p^2 + z^2})\rho(\sqrt{p^2 + z^2})dz. \tag{4.12}$$

On the other hand, outward intensity at each spectral submesh is calculated by

$$\begin{aligned} I_\nu^+(p, z) &= I_\nu^s(p)\exp(-\tau_\nu(p; z, z_0)) \\ &+ \int_{z_0}^z \kappa_\nu(\sqrt{p^2 + \zeta^2})\rho(\sqrt{p^2 + \zeta^2})S_\nu(\sqrt{p^2 + \zeta^2})\exp(-\tau_\nu(p; z, \zeta))d\zeta \end{aligned} \tag{4.13}$$

for the core region. For the shell region, it is calculated by

$$\begin{aligned} I_\nu^+(p, z) &= I_\nu^-(p)\exp(-\tau_\nu(p; z, z_0)) \\ &+ \int_{z_0}^z \kappa_\nu(\sqrt{p^2 + \zeta^2})\rho(\sqrt{p^2 + \zeta^2})S_\nu(\sqrt{p^2 + \zeta^2})\exp(-\tau_\nu(p; z, \zeta))d\zeta, \end{aligned} \tag{4.14}$$

where z_0 is zero in the shell region and equals to $\sqrt{r_0^2 - p^2}$ in the core region. The radius of the innermost layer is denoted by r_0.

These integrations are, though they are seemingly straightforward, admittedly messy. In optically thick layers, the inward and outward intensities are almost determined by the contribution from very close layers. In other words, the integrands of the equation (4.11) and (4.13) or (4.14) drop very rapidly along ζ. Therefore, the integration must be carried out with a very fine mesh of ζ, which would take much computing time. We instead perform the integrations by the monochromatic optical depth τ_ν. The integrations above are written as follows.

$$I_\nu^-(p, z) = \int_z^{\sqrt{r_{-6}^2 - p^2}} S_\nu(\tau_\nu)\exp(-\tau_\nu(p; \zeta, z))d\tau_\nu, \tag{4.15}$$

$$I_\nu^+(p, z) = I_\nu^s(p)\exp(-\tau_\nu(p; z, z_0)) + \int_{z_0}^z S_\nu(\tau_\nu)\exp(-\tau_\nu(p; z, \zeta))d\tau_\nu, \tag{4.16}$$

for the core region, and

$$I_\nu^+(p, z) = I_\nu^-(p)\exp(-\tau_\nu(p; z, z_0)) + \int_{z_0}^z S_\nu(\tau_\nu)\exp(-\tau_\nu(p; z, \zeta))d\tau_\nu \tag{4.17}$$

for the shell region. In performing the integrations above, the source function $S_\nu(\tau_\nu)$ is approximated by a polynomial of the first order, that is, $S_\nu = a_0 + a_1\tau_\nu$. The approximation by polynomials allows us to perform the integrations analytically and saves us much computing time.

As an initial guess, the source function at each layer is assumed to be the Planck function B_ν. With this initial value of the source function, inward and outward intensities are obtained by the integrations above at each layer and at each impact parameter. Once they are obtained, the mean intensity at each layer is evaluated by

$$J_\nu = \frac{1}{2}\int_{-1}^{1}(I_\nu^+ + I_\nu^-)d\mu. \tag{4.18}$$

The revised source function is then given by

$$S_\nu = \frac{\kappa_\nu}{\kappa_\nu + \sigma_\nu}B_\nu + \frac{\sigma_\nu}{\kappa_\nu + \sigma_\nu}J_\nu \tag{4.19}$$

With the new source function, inward and outward intensities, and mean intensity are calculated until the source function converges.

Once the inward and outward intensities are obtained with the converged source function, it is straightforward to evaluate flux and luminosity at each layer. Flux is calculated by

$$F_\nu = 2\pi\int_{-1}^{1}(I_\nu^+ - I_\nu^-)\mu d\mu, \tag{4.20}$$

and luminosity is defined by

$$L_\nu = 4\pi R_\star^2 F_\nu \tag{4.21}$$

After solving the radiative transfer equation at each spectral submesh, the bolometric luminosity at each layer can be evaluated. We now enforce the condition of radiative equilibrium, that is, the luminosity constancy at each layer, and carry out the correction for temperature stratification so that the deviation from the luminosity constancy should be decreased. In fact, we use two temperature correction procedures: the lambda iteration and the flux (luminosity) iteration.

By the lambda iteration, the correction for temperature at each layer is given by

$$\Delta T = \frac{\int \kappa_\nu (J_\nu - B_\nu)d\nu}{\int \kappa_\nu \frac{dB_\nu}{dT} d\nu} \tag{4.22}$$

However, the lambda iteration does not work in deep layers, because radiation field is almost isotropic in optically thick layers, therefore, the source function and the mean intensity are almost equal to the Planck function.

To obtain temperature correction in deep layers, we use the luminosity iteration, of which principle is basically the same with the flux iteration described in Tsuji (1965). In deep layers, flux and luminosity are determined by temperature gradient. For example, if the luminosity at some layer is more than the pre-given value $L_\star$, the temperature gradient should be decreased. So it is quite logical to correct the temperature stratification as follows.

$$\left(\frac{dT}{d\tau_0}\right)_{\text{new}} = \frac{L_\star}{L(\tau_0)}\left(\frac{dT}{d\tau_0}\right)_{\text{old}} \tag{4.23}$$

Besides the temperature gradient throughout the atmosphere, the surface temperature should be determined to obtain the revised temperature stratification. The way to find the revised surface temperature is as follows. If the luminosity at the surface layer is more than the pre-given value, we decrease the surface temperature by some amount, say, 50 K, otherwise we increase it by some amount, 100 K. The first trial temperature stratification is calculated with the decreased or increased surface temperature and the corrected temperature gradient mentioned above. With this temperature stratification, the monochromatic luminosity at each layer is calculated by the procedure already described, and the bolometric luminosity at each layer is evaluated. Again the surface temperature is decreased or increased according to the deviation of the surface luminosity from the pre-given value, and then the temperature stratification for the second trial is calculated with the increased/decreased surface temperature and the same temperature gradient with the first trial. The bolometric luminosity at each layer is again evaluated with the second trial temperature stratification. Now we have two sets of $(T_{\rm surf}, \Delta L)$, where $\Delta L = L_{\rm surf}/L_{\star}$. The revised surface temperature can be obtained by the linear interpolation so that the deviation from the luminosity constancy should be zero. With this surface temperature and the temperature gradient, the temperature stratification for the third trial is calculated. After the evaluation of bolometric luminosity at each layer with this temperature stratification, another set of $(T_{\rm surf}, \Delta L)$ is obtained. The revised surface temperature is finally obtained by interpolation from three sets of $(T_{\rm surf}, \Delta L)$ as the temperature at $\Delta L = 0$, and the corrected temperature stratification is calculated with the finally revised surface temperature and the temperature gradient.

It takes from 10 to 20 iterations to obtain a converged model, though it depends on the starting models. It takes about 1 hour for one iteration by Hewlett-Packard 735 machine. As mentioned before, each mesh is divided into 5 submeshes, therefore, the radiative transfer must be solved at 194×5 wavelengths.

4.3 Results and Discussion

4.3.1 Does the code work correctly?

Firstly, we compare the temperature stratifications of spherical models with those in plane parallel geometry. In Fig. 4.2, we show the temperature stratifications of the plane parallel limit models, together with those calculated by the plane parallel code of which details are described in Chapter 2. The plane parallel limit models are calculated with a very large mass, say, 100 $M_{\odot}$, with $\log g$ kept unchanged. This realizes the atmosphere with very small atmospheric extension, about 1 %, which is nearly plane parallel atmosphere. Though such models do not correspond to any kind of real stars, this procedure is just to see if spherical models calculated by the code described above agree with plane parallel models in the limiting case. In other words, it is a test to see if the code works correctly. A glance of Fig. 4.2 reveals that the models of the plane parallel limit agree well with those calculated by the plane parallel code. The difference of temperature is about 50 K at most, which should be regarded as a good agreement given the fact that the plane parallel limit models still have atmospheric extension of about 1 %. This agreement is one of the evidences that the code works correctly.

Jørgensen et al. (1992) constructed more than 200 model atmospheres in spherical symmetry with molecular line absorption incorporated by the Opacity Sampling method. Therefore, their models serve as a test for the validity of the Band Model method in the model computation. In Fig. 4.3 we show comparison of the models computed by Jørgensen et al. (1992) and by this work. The models are calculated with the same set of parameters – $T_{\mathrm{eff}} = 2800$ K, $\log g = -0.5$, C/O = 1.35, $M = 1.5\ M_{\odot}$. We take into account the effect of turbulent pressure assuming $V_{\mathrm{micro}} = 3.0$ km s^{-1}, while it is not explicitly mentioned in Jørgensen et al. (1992) whether they included the effect of turbulent pressure. A glance of Fig. 4.3 reveals that the temperature stratification of the model computed by our code is in good agreement with that of the model of Jørgensen et al. (1992). This agreement ensures the validity of the Band Model method in the model computation.

4.3.2 Effect of elemental abundance of oxygen

Figures 4.4, 4.5, and 4.6 show the temperature stratifications of models with different oxygen abundances calculated by the spherical code and the plane parallel code. The oxygen abundances are $\log \varepsilon(\mathrm{O}) = -3.07$, -3.27, and -3.37. These figures show that the effect of sphericity on the temperature stratification becomes significant in cooler atmospheres. For example, the difference of temperature between the spherical model and the plane parallel model is only about 100 K in the case of $T_{\mathrm{eff}} = 3200$ K (Fig. 4.4a), while the difference amounts up to several hundred Kelvin in the case of $T_{\mathrm{eff}} = 2800$ K (Fig. 4.6a). These figures also show that the difference of temperature stratification decreases with decreased oxygen abundance. In the case of $T_{\mathrm{eff}} = 2800$ K and $\log \varepsilon(\mathrm{O}) = -3.07$, the difference of temperature between the spherical model and the plane parallel model amounts to several hundred Kelvin, while the difference of temperature is only about 200 K in the case of $\log \varepsilon(\mathrm{O}) = -3.37$. It should be noted here that the models are specified by C/O ratio and elemental abundance of oxygen, instead of elemental abundances of carbon and oxygen. Even if the models shown in Figs. 4.4, 4.5 and 4.6 have the same C/O ratio, they have different elemental abundances of carbon and oxygen. Therefore, the models with higher oxygen abundance also have higher carbon abundance. Since the amount of carbon available to form molecules other than CO is given by $(\mathrm{C/O} - 1) \times \varepsilon(\mathrm{O})$, the more carbon is available to form molecules such as C_2, CN, HCN, and C_2H_2 in the models with the higher oxygen abundance. In Figs. 4.7, 4.8, 4.9, and 4.10 we show molecular concentrations of C_2, CN, HCN, and C_2H_2 in the model with C/O = 1.1 and $\log \varepsilon(\mathrm{O}) = -3.07$, together with those in the plane parallel models with the same C/O ratio and oxygen abundance. A glance of these figures reveals that diatomics like C_2 and CN are less abundant in the spherical models than in the plane parallel counterparts. In turn, the polyatomics like HCN and C_2H_2 become more abundant by more than an order of magnitude.

This anti-correlation between abundances of the diatomics (C_2, CN) and the polyatomics (HCN, C_2H_2) is quite natural. Since the temperatures at surface layers in the spherical models are cooler than in the corresponding plane parallel models, the formation of the polyatomics is promoted. The abundances of the diatomics decrease because carbon is locked up into the polyatomics. The enhanced abundances of HCN and C_2H_2 lead to effective cooling of surface layers, which can be clearly seen in Fig. 4.6. In the models with low oxygen abundance, the amount of carbon available to form molecules like HCN and C_2H_2 is relatively small, therefore, the cooling by the polyatomics does not work so effectively as in the models with higher oxygen abundance.

4.3.3 Effect of C/O ratio on the models

Figure 4.11 shows the temperature stratifications of 2800 K models with different C/O ratios, 1.1, 2.0, 3.0, and 4.0. Other parameters are $\log g = 0.0$, $M = 2\ M_{\odot}$, and $V_{\mathrm{micro}} = 3.0$ km s^{-1}, $\log \varepsilon(\mathrm{O})$ = -3.07. This figure clearly shows that the temperature stratifications are largely dependent on the C/O ratios adopted. The difference of temperature amounts up to nearly 800 K between the models with C/O = 1.1 and 4.0. It should be also noted that the difference of temperature is the largest between the models with C/O = 1.1 and 2.0. The differences between the models with higher C/O ratios are much smaller. In other words, the temperature stratification changes largely from C/O = 1.1 to 2.0. This effect can be explained by the fact that the molecular opacity, which largely governs the temperature stratification, changes with $\varepsilon(\mathrm{C}) - \varepsilon(\mathrm{O})$. With most of oxygen locked up into CO molecules in the carbon-rich atmosphere, the amount of molecules other than CO is dependent on $(\mathrm{C/O} - 1) \times \varepsilon(\mathrm{O})$. In fact, this quantity increases by a factor of 10 from 0.1 to 1 between the models with C/O = 1.1 and 2.0. Thus, it is quite natural that the difference of the temperature stratifications should be the largest between the models with C/O = 1.1 and 2.0. In the atmospheres with higher C/O ratios, larger amount of molecules other than CO is formed, therefore, the atmospheres become more opaque. It means that the temperature in such atmospheres must be raised so that the same energy should be transferred. Especially CN molecule has many weak lines over a wide spectral range, and causes such backwarming effect.

It should be noted here that the surface temperatures of the models with C/O = 2.0, 3.0, and 4.0 are almost the same, except for the uppermost layers of the model with C/O = 4.0. The sudden decline of temperature at around $\log \tau_0 = -4.0$ corresponds to the layers where HCN and C_2H_2 start to form as shown in Figs. 4.9 and 4.10. Actually about 90 % of carbon available to form molecules other than CO is locked up into C_2H_2, and about 10 % is locked up into HCN. These molecules formed in the upper layers are expected to lower the surface temperature effectively, on the contrary to the backwarming effect. As a result, it is expected that the surface temperature is kept almost constant.

4.3.4 Spectral Energy Distribution

We now discuss on the spectral energy distribution (SED) predicted by the spherical code. Firstly, the SED's from spherical models are compared with those from the corresponding plane parallel models. Figure 4.12 shows the SED's from a spherical model and its plane parallel counterpart. Both models have the same set of input parameters, that is, $T_{\rm eff}$ = 3000 K, $\log g$ = 0.0, $V_{\rm micro}$ = 3.0 km s^{-1}, $\log \varepsilon({\rm O}) = -3.07$, and C/O = 1.1. The stellar mass adopted for the spherical model is 2 $M_\odot$. As can be seen from the figure, the SED of the spherical model exhibits little effect of the sphericity. However, the case for models with lower effective temperature is quite different. We show the SED's of the models with $T_{\rm eff}$ = 2800 K in Fig. 4.13. Other parameters are identical with those given above. At this temperature, the absorption due to polyatomics such as HCN and C_2H_2 becomes significant as clearly seen in the features around 3, 7, and 14 μm. Those absorption features become even stronger in the spherical model. The cooling by dilution of radiation field in the spherical geometry promotes the formation of polyatomics near the surface. These molecules in turn effectively cool the surface layers and bring about further formation of the polyatomics.

The strength of the absorption features due to HCN and C_2H_2 is dependent on C/O ratio. The predictions of the absorption feature around 3 μm with different C/O ratios are shown in Fig. 4.14. The parameters of those models are $T_{\rm eff}$ = 2800 K, $\log g$ = 0.0, M = 2 $M_\odot$, $V_{\rm micro}$ = 3.0 km s^{-1}, and $\log \varepsilon({\rm O}) = -3.07$. The C/O ratios used are 1.1, 2.0, 3.0, and 4.0. The figure shows that the absorption is strongest in the model with C/O = 1.1. This is because the temperature is coolest in the model with C/O = 1.1 as described in the previous subsection. With increased C/O ratio, two processes can compete to form polyatomics. One is that more carbon becomes available to form molecules other than CO, and the other is that the backwarming effect caused by the molecule such as CN also becomes more significant. For example, the absorption feature in the model with C/O = 2.0 is weaker than that in the model with C/O = 1.1. In this case, the latter process is dominant as compared with the former one. The further increase of C/O ratio leads to slight increase of the strength of the absorption feature. This can be interpreted as that the increase of carbon available to form the polyatomics overcomes the backwarming effect. The effects of the two processes may be equal in the models with C/O = 2 to 3 from the figure.

4.3.5 Comparison of SED with the observation by the ISO SWS

The 3 μm absorption feature predicted by the spherical models shows a fair agreement with the observation. We show in Fig. 4.15 comparison between the observed and predicted spectra for SS Vir, a carbon-rich Mira variable. The spectrum was acquired by the Short Wavelength Spectrometer (SWS) on board the Infrared Space Observatory (ISO) launched by the European Space Agency (ESA)[1]. The observation was carried out with the fastest full grating scan speed (AOT1, speed 1), and the spectral resolution is about 200. The effective temperature of SS Vir can be estimated by the $(J - L')_0$ – $T_{\rm eff}$ relation determined in Ohnaka & Tsuji (1996). The color $(J - L')$, which is available in Noguchi et al. (1981), is 2.30. It corresponds to $T_{\rm eff}$ = 2800 K. The predicted spectra shown in Fig. 4.15 are calculated with $T_{\rm eff}$ = 2800 K. A glance of the figure reveals that the spectra with C/O = 2.0 or 3.0 show a fairly good agreement with the observed spectrum. The predicted spectra tend to be somewhat broader than the observed, but this agreement should be regarded fairly good, given the fact that the absorption coefficients of HCN and C_2H_2 are taken into account based the approximation of the Band Model, not on a line-by-line basis. It should be kept in mind that this comparison is just tentative one, because the elemental abundances of carbon and oxygen in SS Vir are not available in the literature at present.

Even the spherical models which are successful in reproducing the 3 μm feature observed by the SWS fail to fit the observation at longer wavelength range. Figure 4.16 shows comparison between the observed and predicted spectra for SS Vir from 2 to 13 μm. As shown above, the predicted spectrum calculated with C/O = 2.0 reproduces the 3 μm feature fairly well, but it completely fails to reproduce the 7 μm feature which is also due to HCN and C_2H_2. The feature observed around 7 μm is much weaker than predicted. The observed spectrum appears to be filled as compared with the predicted one. The emission from the circumstellar envelope may fill the absorption at longer wavelength. The absorption feature around 5 μm has not yet been identified, and it may be due to molecules which are not incorporated in the present model, for example, C_3.

4.3.6 Synthetic spectra

Synthetic spectra from spherical models can be calculated by almost the same manner as employed in the evaluation of emergent flux in the model construction, except that a much finer spectral mesh is used. Synthetic spectra within a given spectral range are predicted using the temperature and pressure stratifications calculated by the spherical code. With the given temperature and pressure stratifications, dissociation and ionization equilibria are solved to obtain the abundance of each molecular or atomic species. The absorption

[1]Based on observations with ISO, an ESA project with instruments funded by ESA Member States (especially the PI countries: France, Germany, the Netherlands and the United Kingdom) and with the participation of ISAS and NASA.

coefficient can be evaluated in each fine spectral mesh. To predict a profile, we use a mesh with an interval of 5 – 10 % of the Doppler width over the relevant spectral range. In each mesh, the radiative transfer is solved to obtain the source function, and then the flux can be evaluated. Once the synthetic spectrum is obtained, equivalent widths can be also evaluated by simply integrating the synthetic spectrum over the relevant spectral range.

Since the effect of sphericity is more significant in the upper photosphere, it is expected that strong lines formed in the upper layers can be affected. As described in the following Chapters, we will present analysis of the second and the first overtone bands of CO. Especially, low excitation lines of the first overtone bands are formed in the uppermost layers, therefore, we can expect some changes due to sphericity in predicted spectra.

The subsequent changes in synthetic spectra come from two aspects. One comes from the temperature and pressure stratifications which are used in the calculation of synthetic spectra. The temperature of the spherical models is cooler than the plane parallel models, while the density of the spherical models is usually higher in the upper layers than the plane parallel models. Thus, the differences in these stratifications can give some effect on synthetic spectra through the evaluation of absorption coefficients of the relevant spectral lines. For example, the abundance of the relevant molecular species can be different from that in the plane parallel atmosphere, and the population of lower state of the relevant line may be also different. The other comes from the spherical geometry itself. The emergent luminosity at each layer can be approximately given by $4\pi r^2 B_\nu(T)$. Thus the line strength can be approximately written as

$$\frac{4\pi r_\ell^2 B_\nu(T_\ell)}{4\pi r_c^2 B_\nu(T_c)} = \left(\frac{r_\ell}{r_c}\right)^2 \frac{B_\nu(T_\ell)}{B_\nu(T_c)}, \tag{4.24}$$

where r_ℓ and T_ℓ are radius and temperature of the line forming region, respectively, and r_c and T_c are those of the layers where the continuum is formed. Therefore it depends on the competition between the ratios of the square of radius and of the Planck functions whether the line becomes stronger or weaker in the spherical models.

In Fig. 4.17, we show two synthetic spectra in the region around the bandhead of the CO first overtone. The solid line represents the spectrum calculated by the spherical code based on the temperature and pressure stratifications of the spherical model with $T_{\rm eff}$ = 2800 K, $\log g = 0.0$, $V_{\rm micro} = 3.0$ km s^{-1}, $M = 2\ M_\odot$, $\log \varepsilon({\rm O}) = -3.27$, and C/O = 1.1. The dotted line represents the spectrum calculated by the plane parallel code based on the temperature and pressure stratifications of the plane parallel model with the same parameters above. The temperature stratifications of the two models used in generating the synthetic spectra are shown in Fig. 4.6b. Figure 4.17 shows that the lines predicted by the spherical model are stronger than those predicted by the plane parallel model. This can be even clearly seen in the ratio of the two spectra, namely, the spectrum of the spherical model divided by that of the plane parallel model. Given the result that the atmospheric relative extension in the spherical model with the parameters above is about 10 %, the effect by the spherical geometry may not be possibly so large. To separate the two effects, that is, the effect due to the spherical geometry and that due to the temperature and pressure stratifications, we investigated two cases: 1) two spectra are calculated by the spherical radiative transfer code and by the plane parallel code, with the identical temperature stratification of the spherical model 2) two spectra are calculated by the spherical radiative transfer code with the temperature stratification of a spherical model and its plane parallel counterpart.

In Fig. 4.18, we show synthetic spectra around the (2,0) bandhead of CO for the case 1). The solid line represents the spectrum calculated by the spherical radiative transfer code based on the temperature and pressure stratifications of the spherical model. The dotted line represents the spectrum calculated by the plane parallel radiative transfer code, but with the temperature and pressure stratifications of the spherical model. Thus the difference between the two spectra means the effect of geometry in the radiative transfer. It is obvious in Fig. 4.18 that this effect is quite small in the case presented here. It is consistent with what has been expected, because the relative atmospheric extension is not so large, about 10 %. Furthermore, it can be seen that the lines calculated by the spherical radiative transfer code are slightly weaker than those calculated by the plane parallel code. This can be understood as follows. Since the identical temperature and pressure stratifications are used in the calculation, the ratio of the Planck function in the equation (4.24) is expected not to differ between the two spectra. However, the ratio of square of radius becomes larger than unity, which is roughly estimated to be $(r_\ell/r_c)^2 = 1.1^2$, in this case. This ratio is unity in the case of the plane parallel radiative transfer code. Thus, it is quite natural that the lines predicted by the spherical code should become weaker than those predicted by the plane parallel code.

On the other hand, the comparison of spectra corresponding the case 2) is shown in Fig. 4.19. The solid line represents the spectrum calculated by the spherical radiative transfer code, based on the temperature and pressure stratifications of the spherical model. The dotted line represents the spectrum calculated by the spherical radiative transfer code, but based on the temperature and pressure stratifications of the plane parallel model. It clearly shows that the difference of the two spectra in Fig. 4.17 is due to the effect that comes from the difference of the temperature and pressure stratifications used in the calculation of the synthetic spectra.

It is expected that the effect of sphericity should be more significant in the fundamental bands of CO than in the first overtone bands. In Fig. 4.20 we show two synthetic spectra around the bandhead of CO fundamental band. The spectrum represented by the solid line is calculated by the spherical radiative transfer code based on the temperature and pressure stratifications of the spherical model, while that represented by the dotted line is calculated by the plane parallel code based on the stratifications of the plane parallel model. The models used in both calculations are identical with those used in the calculations of the first overtone band. It should be noted here that *not* all the lines predicted by the spherical model are weaker than those predicted by the plane parallel model, unlike the case of the CO first overtone band discussed above. We again calculate a spectrum by the spherical radiative transfer code, but based on the plane parallel model in order to separate the effect of the temperature stratifications from that of geometry. Figure 4.21 clearly shows that the difference of the temperature stratifications between the spherical model and the plane parallel model gives changes only in strong lines. The weak lines are little affected. The strong lines are formed in the uppermost layers, where the difference of temperature between the spherical model and its plane parallel counterpart amounts to more than 400 K. We show in Fig. 4.22 the contribution function over the wavenumber range covering one of those strong line, $v = 1 - 0$ $R(73)$. In plane parallel geometry contribution function is written as $S_\nu(\tau_\nu)E_2(\tau_\nu)$ where τ_ν is the monochromatic optical depth, $S_\nu(\tau_\nu)$ is the source function, and $E_2(\tau_\nu)$ is the integral exponential function. As can be seen in the figure, the line core is formed at the layer around $\log \tau_0 = -5.5$. Thus, these strong lines are subject to the change of temperature near the surface. On the other hand, the weak lines shown in Fig. 4.20 are formed in deeper layers. The contribution function over the wavenumber range covering one of those weak lines, $v = 1 - 0$ $R(108)$, is shown in Fig. 4.23. In this case, the line formation region is located at the layers around $\log \tau_0 = -3$. In such layers the difference of temperature stratifications between the spherical model and the plane parallel one is not so significant, about 100 to 200 K at most. As a result these lines are not affected as much as the strong lines.

To investigate the effect of geometry, we show in Fig. 4.24 a comparison between a spectrum calculated by the spherical radiative transfer code and that calculated by the plane parallel code. Both spectra are calculated based on the identical temperature stratification of the spherical model. It is again seen that the lines predicted by the spherical radiative transfer code are weaker than those predicted by the plane parallel code. To summarize, weak lines are primarily affected by the spherical geometry, while strong lines are largely affected by the temperature stratification. As a result, weak lines appear to be even weaker in the spherical model, while strong lines appear to be stronger.

4.4 Concluding remarks

A new code of spherical model atmosphere for carbon-rich mixture has been developed with the molecular line opacities of CO, CN, C_2, HCN, and C_2H_2 incorporated by the Band Model method. The test models calculated in the plane parallel limit case show a good agreement with the models calculated by the plane parallel code. It supports that the new code works correctly. Comparison with the model constructed based on the Opacity Sampling is also satisfactory.

The temperature in spherical models is generally cooler than in the corresponding plane parallel models as was expected. However, the effect of sphericity appears more significantly in the models as cool as $T_{\rm eff}$ = 2800 K than those with higher effective temperature. This can be interpreted as the interplay between the formation of polyatomics and the cooling by dilution of radiation field due to the spherical geometry itself. Consequently, the effect of sphericity can appear significantly in the absorption due to polyatomics such as HCN and C_2H_2 around 3, 7, and 14 μm. These absorption features appear much stronger than in the plane parallel models with the same effective temperature.

The temperature stratification in carbon stars is very sensitive to C/O ratio: the models with the higher C/O ratios are the warmer. This can be explained by increase of the backwarming effect due to molecules such as C_2 and CN with increase of carbon available to form molecules other than CO. The difference of temperature between the models with C/O = 1.1 and 4.0 amounts to several hundred Kelvin. This sensitive dependence of temperature stratification on C/O ratio can be crucial in the analysis of elemental abundances of carbon and oxygen as described in the next Chapter.

As an observational test of the spherical models, the predicted 3 μm feature due to HCN and C_2H_2 is compared with the observational data taken by the ISO SWS for SS Vir. The observed 3 μm feature can be fairly well reproduced by the spherical model with $T_{\rm eff}$ = 2800 K and C/O = 2 to 3. However such models fail to reproduce the observed feature around 7 μm. A glance of the observed spectra at the wavelength range longer than 6 μm reminds us that the spectra might be filled by the emission from the circumstellar envelope. In order to reproduce the observed spectra, it will be necessary to include the physics and chemistry in the upper photosphere or in the inner circumstellar envelope. The molecular line data for HCN and C_2H_2 at high temperature ($\sim$ 1000 K) are also required to obtain further fit between the predicted spectra and observations with higher spectral resolution.

The effect of sphericity on synthetic spectra of the first overtone and the fundamental bands of CO has been investigated by the line radiative transfer code in spherical geometry. To summarize the effect, weak lines are weaker than those calculated with plane parallel models, while strong lines are stronger. The spectra of strong lines such as those near the (2,0) bandhead become stronger in the spherical models by about 10 % than those in the plane parallel models. This is largely because of the cooler temperature stratification near the surface in the spherical models, and the effect due to the radiative transfer in spherical geometry turned out to be relatively minor in the case of strong lines. On the other hand, weak lines are not much affected by the surface cooling in the spherical models, therefore, the geometry effect appears somewhat remarkable. As a result, weak lines appear weaker in the spherical models than in the plane parallel counterparts.

References

Bessel M.S., Brett J.M., Scholz M., Wood P.R., 1989a, A&AS 77,1
Bessel M.S., Brett J.M., Scholz M., Wood P.R., 1989b, A&A 213, 209
Bessel M.S., Brett J.M., Scholz M., Wood P.R., 1991, A&AS 89, 335
Golden S.A., 1969, J. Quant. Spectrosc. Radiat. Transfer 9, 1067
Jørgensen U.G., Johnson H.R., Nordlund Å, 1992, A&A 261, 263
Noguchi K., Kawara K., Kobayashi Y., Okuda H., Sato S., Oishi M., 1981, PASJ 33, 373
Ohnaka K., Tsuji T., 1996, A&A 310, 933
Plez B., Brett J.M., Nordlund Å, 1992, A&A 31, 265
Schmidt-Burgk J., 1975, A&A 40, 249
Scholz M., Tsuji T., 1984, A&A 130, 11
Tsuji T., 1965, PASJ 17, 152
Tsuji T., 1976, PASJ 28, 543
Tsuji T., 1994, In: Molecular Opacities in the Stellar Environment ed. Jørgensen U.G., Lecture Notes in Physics, Springer-Verlag, p.79

Chapter 5

Analysis of Elemental Abundances of Carbon and Oxygen in Carbon Stars

Abstract

We present analysis of elemental abundances of carbon and oxygen in three carbon stars (TX Psc, BL Ori, and V Aql) from high-resolution infrared spectra (1.5 – 2.5 μm). The elemental abundances of oxygen and carbon were derived from lines due to the second overtone bands of CO and the Phillips system of C_2. With the interplay between the atmospheric structure and the chemical composition properly taken into account, we determined elemental carbon and oxygen abundances self-consistently.

The elemental oxygen abundances derived for the three stars are in fairly good agreement with the results derived by Lambert et al. (1986). The oxygen abundances are found to be by 0.1 – 0.2 dex subsolar. On the other hand, the elemental carbon abundances derived in the present work show marked disagreements with those derived by Lambert et al. (1986). Especially for V Aql, the carbon abundance is much higher than that derived by them, therefore, the C/O ratio is also as high as 2.48 in contrast to their result C/O = 1.25. For BL Ori, our result of C/O ratio, C/O = 1.31 is also significantly higher than that derived by Lambert et al. (1986), 1.039. The C/O ratio in TX Psc, 1.14, also shows a disagreement with their result, 1.027. Though the disagreements of C/O ratios seem to be minor for BL Ori and TX Psc as compared with the case of V Aql, the disagreements of (C/O -1) amount up to a factor of 8 to 10 for all the three stars. Given that the abundance of C_2 is approximately proportional to the square of (C/O $-$ 1), these disagreements can be attributed to the difference of the model atmospheres used in the analyses or to the difference of the treatments of the excitation effect.

The analysis was done based on model atmospheres in spherical symmetry as well as plane parallel models to investigate the effect of sphericity on the resulting elemental abundances. The use of the spherical models leads to slightly higher elemental abundances both of carbon and oxygen than those derived with the plane parallel models. The oxygen and carbon abundances determined with the spherical models are by about 0.1 to 0.2 dex higher than those with the plane parallel models.

The $^{12}C/^{13}C$ ratios and the derived C/O ratios in three stars, including the high value in V Aql, show a clear correlation, which strongly supports that K and M giants evolve to carbon stars by addition of ^{12}C synthesized in the thermal pulse.

5.1 Introduction

Spectra of carbon stars exhibit the predominance of absorption due to carbon-bearing molecules such as C_2, CN, HCN, and C_2H_2, replacing oxygen-bearing molecules such as TiO and H_2O in M giants. The spectra rich with carbon-bearing molecules mean that those stars should have atmospheric chemical compositions characterized by C/O ratio larger than unity. Since the C/O ratios in molecular clouds from which the stars were formed are considered to be smaller than unity like the cosmic abundance, some mechanisms to enrich carbon in the stellar atmosphere are required to explain the existence of carbon stars.

At the asymptotic giant branch (AGB), stars undergo the double shell burning. AGB stars have the core consisting of carbon and oxygen, with the helium shell overlying on it surrounded by the hydrogen envelope. The energy generation takes place both at the bottom of the hydrogen envelope and at the bottom of the helium shell. The nuclear burning at the helium shell is thermally unstable and causes a runaway reaction, which is so-called the thermal pulse or the helium shell flash, in the interval of about 1×10^5 yr (e.g. Iben 1981, Vassiliadis & Wood 1993). The thermal pulse is an attractive nuclear process to produce enhancement of various elements observed in the spectra of AGB stars. Especially, addition of ^{12}C synthesized via the 3α-process in the thermal pulse to the surface is expected to turn oxygen-rich atmospheres to carbon-rich. This phenomenon is called the third dredge-up. The thermal pulse and the third dredge-up can also explain, at least qualitatively, the enhancement of the s-process elements observed toward carbon stars (e.g. Utsumi 1985).

It has been left unsolved till now, however, what stellar parameters draw a line between the stars which become carbon stars and ones which evolve to planetary nebulae as oxygen-rich. The metallicity may be one of such parameters: the carbon star formation may be favored in lower metallicity. For example, the ratio of carbon stars to M giants is significantly higher in the Magellanic Clouds (C/M $\sim$ 1) than in the solar neighborhood (C/M $\sim$ 0.1). On the other hand, the ratio is considerably lower in the Galactic Bulge (C/M $\sim$ 0.003) than in the solar neighborhood. The C/M ratios in a variety of galaxies also indicate that the carbon star formation is favored in lower metalicity (e.g. Pritchet 1987). However, no theoretical work on the AGB stage of stellar evolution has been successful in reproducing the observed properties of AGB stars. For example, the work by Vassiliadis & Wood (1993) sees that the third dredge-up is effective enough only in stars with relatively large masses ($M > 5M_{\odot}$) to turn them carbon-rich. As a result, the luminosity functions calculated by theoretical works tend to be brighter than those observed in the Magellanic Clouds (e.g. Frogel & Cohen 1982, Frogel et al. 1990).

Chemical analysis of the surface composition is one of the powerful weapon to struggle with the evolution of these *pathological* stars. However, reliable abundance analyses have been hampered by various reasons for cool stars, especially for carbon stars. Firstly, visual spectra of carbon stars are dominated by heavily crowded lines due to C_2 and CN, which almost obscure the true continuum. Therefore it is quite difficult to determine elemental abundances accurately by applying the standard analysis which always requires the true continuum to be well defined. Secondly, construction of reliable model atmospheres of carbon stars has been a tedious process because a huge number of molecular lines should be included in the evaluation of opacity. The accurate molecular data of the relevant species are also required.

In the situation above, Lambert et al. (1986) determined C, N, and O elemental abundances and $^{12}C/^{13}C$ ratios in 30 Galactic carbon stars from high-resolution infrared spectra. Infrared spectra of carbon stars are less subject to heavy line blanketing, therefore, the true continuum level can be well defined. They derived oxygen elemental abundances from lines of the first and the second overtone bands of CO, carbon abundances from lines of the C_2 Phillips system, nitrogen abundances from lines of the CN Red system, and $^{12}C/^{13}C$ ratios from lines of CO and CN. Their analysis is based on the model atmospheres including molecular line opacities due to CO, CN, C_2, HCN, and C_2H_2. Though their results have been widely referred, serious disagreements with those results have been found for $^{12}C/^{13}C$ ratios by Ohnaka & Tsuji (1996). The $^{12}C/^{13}C$ ratios derived by Ohnaka & Tsuji (1996) are systematically smaller by a factor 2 to 3 than those derived by Lambert et al. (1986). The reason for such disagreements could not be specified, but it was pointed out as one of the possibilities that the difference of model atmospheres used in the analyses could affect the determination of $^{12}C/^{13}C$ ratios via the correction for the excitation effect of lines. The difference of model atmospheres could be a large factor responsible for uncertainties or systematic disagreements in the abundance analysis especially for carbon stars, because the atmospheric structure is very sensitive to elemental abundances of carbon and oxygen. Thus it can be expected that carbon, nitrogen, and oxygen abundances should be also re-analyzed in order to specify the reason of such systematic disagreements in $^{12}C/^{13}C$ ratios and to establish reliable elemental abundances of C, N, and O.

Therefore, analysis of elemental abundances of C, N, and O should never be regarded well-established for cool carbon stars. The reliable analysis of chemical composition in the photosphere of carbon stars, especially elemental abundances of carbon and oxygen, is essential to understand not only stellar evolution at the AGB stage but also chemical processes in the circumstellar envelope. Chemistry of the grain formation could be dependent on chemical composition of the photosphere, therefore, accurate analysis of photospheric chemical composition is also crucial to construct, in future, comprehensive models from the photosphere to the circumstellar envelope including detailed processes of grain formation, hydrodynamics, and radiative transfer. Thus chemical composition in the photosphere is a fundamental clue to understand the driving mechanism of mass loss.

To investigate further the reason for the disagreements of $^{12}C/^{13}C$ ratios and the effect of model atmospheres on determination of elemental abundances, we analyzed elemental C and O abundances in three carbon stars, using the identical spectra that Lambert et al. (1986) had analyzed, but based on the new grid of line blanketed model atmospheres discussed in the previous Chapter. With the interplay between the atmospheric structure and chemical composition properly taken into account, the carbon and oxygen abundances were self-consistently determined. We also investigated the effect of sphericity on the abundance analysis using the line radiative transfer code in spherical geometry. The effect of model atmospheres on the abundance analyses will be discussed based on the comparison of the resulting carbon and oxygen abundances with those by Lambert et al. (1986). We will also discuss evolution to carbon stars based on $^{12}C/^{13}C$ ratios and C/O ratios.

5.2 Observational data

The spectra analyzed in the present work were originally obtained by Lambert et al. (1986) with the Kitt Peak 4 m Mayall reflector and the Fourier transform spectrometer (FTS) (Hall et al. 1979). The archived data of all the 33 stars they had observed were kindly made us available by Dr. K. H. Hinkle. The spectral region observed is from 4000 to 6600 cm^{-1} (2.5 – 1.5 μm) with nominal spectral resolution 0.0412 cm^{-1}, which is determined by the path difference of the FTS. All the spectra were apodized by the apodizing function No.2 by Norton & Beer (1976), resulting in the actual spectral resolution 0.07 cm^{-1}, which corresponds to about from $R = 9.4 \times 10^4$ to 5.7×10^4. The spectral region from 5100 to 5500 cm^{-1} is severely disturbed by the atmospheric absorption, therefore, the regions actually analyzed correspond to the H-band (5500 – 6400 cm^{-1}) and the K-band (4200 – 5100 cm^{-1}).

We selected three stars from thirty stars analyzed by Lambert et al. (1986). The selected stars are TX Psc, BL Ori, and V Aql, of which observation summary is given in Table 15. The primary criterion of the selection is effective temperature. In order to investigate the effects of model atmospheres on the abundance analysis, these stars were selected along the effective temperature scale determined by Ohnaka & Tsuji (1996). TX Psc was selected just because it is one of the carbon stars well studied, and its photometric data are also abundant. BL Ori was selected since it is one of the stars with the highest effective temperatures in the sample. V Aql was selected since it is one of the coolest carbon stars *without* a significant circumstellar envelope.

Figure 5.1, 5.2, and 5.3 show a portion of the observed H-band spectra of TX Psc, BL Ori, and V Aql, respectively. The continuum level can be determined by drawing an envelope over the peaks in the spectral region studied. The continuum levels can be relatively well defined as compared with in the visual region. Some of the ^{12}CO lines used in the analysis are indicated by the ticks in the figures.

Figure 5.4, 5.5, and 5.6 show the observed spectra of the three stars in the K-band. The ticks in the figures indicate the C_2 Phillips system lines used in the analysis.

Table 15. Observation summary of the stars analyzed in the present work

Star	C-Class.	Var. Class.	K-mag	Date	Int. time (min)	S/N
BL Ori	C6,3	Lb	0.75	4 Jan. 1980	154	61
TX Psc	C7,2	Lb	−0.76	7 Jul. 1979	65	146
V Aql	C5,4	SRb	−0.14	28 Apr. 1980	81	103

5.3 Molecular data

The second and the first overtone bands of CO originate from vibration-rotation transitions in the ground electronic state $X^1\Sigma$. The evaluations of line positions and f-values are done as described in Tsuji (1986). Actually the line list produced in Tsuji (1986) is used in the present work to identify lines of CO in the spectra of carbon stars.

Line positions can be evaluated by the merged Dunham coefficients based on various experiments (Guelachvili et al. 1983) for various isotopic species. Our line list of CO includes $^{12}C^{16}O$, $^{13}C^{16}O$, $^{12}C^{17}O$, and $^{12}C^{18}O$.

The f-value of a transition $(v, J) \rightarrow (v+n, J')$ can be given by

$$f = \frac{8\pi^2 mc}{3he^2}\omega S_J < v, J|M|v+n, J' >^2, \tag{5.1}$$

where ω is wavenumber of the transition, S_J is the Hönl- London factor, and $< v, J|M|v+n, J' >$ is the dipole moment matrix element. Chackerian & Tipping (1983) expressed the square of the dipole moment matrix in analytic form as below.

$$< v, J|M|v+n, J' >^2 = \frac{M(n)^2(v+n)!}{v!n!}H_n(v)F_n(v,m), \tag{5.2}$$

where $M(n)$ is the rotationless matrix element, $H_n(v)$ represents the effect of the vibrational anharmonicity, and $F_n(v,m)$ is the Herman-Wallis factor representing the effect of interaction between vibration and rotation ($m = J+1$ for R-branch and $m = -J$ for P-branch). The least-square fitted coefficients for $H_n(v)$ and $F_n(v,m)$ are given in Chackerian & Tipping (1983) for the range of $J < 50$ and $v < 10$. In the spectra we analyzed, lines with J as high as about 100 are also observed. For such high excitation lines, more elaborate fitting coefficients were made available by Drs. R. H. Tipping and C. Chackerian, Jr. in Tsuji (1986).

The C_2 Phillips system originates from transitions $A\,^1\Pi - X\,^1\Sigma$. Because of the relative simplicity of the singlet sigma state, energy levels, therefore, line positions and lower excitation potentials, can be evaluated with accurate molecular constants. Douay et al. (1988) recorded infrared spectrum of C_2 and analyzed 12 bands: $0-0$, $3-3$, $4-4$, $5-5$, $0-1$, $1-2$, $2-3$, $0-2$, $1-3$, $2-4$, $3-5$, and $4-6$. They derived molecular constants such as T_v, B_v, and H_v up to $v = 6$ for the $X\,^1\Sigma$ state and $v = 5$ for the $A\,^1\Pi$ state. Energy level in each electronic state can be expressed as below,

$$T_v + B_vJ(J+1) - D_v[J(J+1)]^2 + H_v[J(J+1)]^3. \tag{5.3}$$

The gf-values of individual rotational lines are given by

$$gf = f_{v'v''}\frac{S_{J'J''}\omega}{2\omega_{v'v''}}, \tag{5.4}$$

where $f_{v'v''}$ is the band oscillator strength, $S_{J'J''}$ is the Hönl-London factor, ω is the wavenumber of the individual line, and $\omega_{v'v''}$ is the wavenumber of the band origin of (v', v'') band. The Hönl-London factors are $S_{J'J''} = 2J''+1$ for Q-branch, $S_{J'J''} = J''-1$

for P-branch, and $S_{J'J''} = J'' + 2$ for R-branch. For the band oscillator strength of (0,2) and (1,3) bands, we adopted $f_{02} = 2.5 \times 10^{-4}$ and $f_{13} = 3.8 \times 10^{-4}$, which are the same values adopted in the analysis by Lambert el al. (1986).

Though analysis of CN lines is not included in the present work, line positions of CN are also calculated since its line list is required not only to analyze CN lines in future but also to check blends to lines of CO and C_2. Line positions of the CN Red system are evaluated based on the work by Cerny et al. (1978). They recorded infrared spectrum of CN and analyzed fourteen bands of $\Delta v = +1$, 0, -1, and -2 sequences. Energy level of each rotational line is calculated using the formulae and molecular constants given by Cerny et al. (1978).

Telluric lines are identified by comparing the stellar spectra with those of the Sun. The program stars of Lambert et al. (1986) were observed principally during morning daylight hours over a course of a year, therefore, spectra of hot standard stars were not obtained for each observing session. No effort can be done in order to remove telluric lines by dividing the stellar spectra with those of the Sun or hot stars.

After checking blend of CN lines and telluric lines, we finally selected lines which can be used in the analysis by visual inspection. This process is indispensable, because we should not use such lines that are poorly fitted by the Gaussian profile. They might have blend of some unidentified lines. We give a list of CO and C_2 lines which are finally used in the analysis for each star in Table 16. The number of C_2 lines is quite small partly because the line list of C_2 is much shorter than that of CO.

Table 16. List of the lines used in the analysis

$\omega_{\rm lab}$	$\log gf$	L.E.P. (cm^{-1})	Identification			$\log(W/\omega)$
		TX Psc				
^{12}CO						
5638.523	−5.907	15275.761	8 - 5	P	51	−4.808
5687.107	−5.481	18765.170	12 - 9	R	15	−5.036
5710.900	−4.731	24403.104	11 - 8	R	67	−5.075
5713.094	−4.700	26702.920	10 - 7	R	83	−5.384
5713.599	−5.963	13746.350	8 - 5	P	42	−4.766
5721.447	−5.970	13594.018	8 - 5	P	41	−4.788
5744.398	−5.992	13158.308	8 - 5	P	38	−4.742
5751.850	−6.000	13020.187	8 - 5	P	37	−4.879
5752.324	−5.851	16568.918	11 - 8	R	9	−4.966
5756.158	−5.929	13642.582	9 - 6	P	25	−4.830
5766.906	−5.588	16892.938	11 - 8	R	16	−4.985
5767.474	−4.986	20398.848	11 - 8	R	47	−4.807
5770.641	−5.014	20072.211	11 - 8	R	45	−4.907
5785.691	−6.006	13226.055	9 - 6	P	20	−4.861
5794.457	−6.055	12266.553	8 - 5	P	31	−4.827
5806.188	−6.204	11436.174	7 - 4	P	40	−4.760
5807.482	−6.086	12957.687	9 - 6	P	16	−4.880
5807.863	−6.076	12044.069	8 - 5	P	29	−4.763
5829.963	−5.026	19935.352	10 - 7	R	55	−5.004
5836.334	−6.235	10871.188	7 - 4	P	36	−4.720
5838.585	−4.984	24760.523	8 - 5	R	89	−5.459
5846.130	−6.353	12594.601	9 - 6	P	8	−4.819
5881.386	−7.123	8590.822	4 - 1	P	58	−4.917
5903.762	−6.752	8487.232	5 - 2	P	47	−4.843
5908.691	−6.174	12627.299	9 - 6	R	9	−4.918
5910.203	−6.422	10694.341	8 - 5	P	11	−4.810
5919.522	−6.501	10617.327	8 - 5	P	9	−4.832
5923.756	−5.910	12957.687	9 - 6	R	16	−4.746
5930.003	−5.798	13226.055	9 - 6	R	20	−4.837
5934.522	−5.703	13552.088	9 - 6	R	24	−4.740
5972.568	−7.171	6590.108	4 - 1	P	48	−4.720
5994.419	−6.238	10738.339	8 - 5	R	12	−4.736
6004.670	−5.475	14734.414	8 - 5	R	48	−4.737
6008.272	−5.459	20623.514	6 - 3	R	88	−5.209
6030.567	−7.213	5405.607	4 - 1	P	41	−4.723
6041.411	−7.796	4673.539	3 - 0	P	49	−4.854
6062.447	−5.556	14682.344	7 - 4	R	58	−4.792
6069.885	−5.581	17362.152	6 - 3	R	77	−4.990
6296.521	−6.497	9260.835	4 - 1	R	61	−4.740
6312.072	−8.353	172.978	3 - 0	P	9	−4.668
6319.232	−6.618	7347.152	4 - 1	R	52	−4.657

Table 16. – Continued

$\omega_{\rm lab}$	$\log gf$	L.E.P. ($\rm cm^{-1}$)	Identification			$\log(W/\omega)$
C_2						
4591.294	−2.954	3821.775	0 - 2	P	10	−5.255
4615.792	−2.508	3903.308	0 - 2	Q	12	−4.940
4623.431	−2.583	3821.775	0 - 2	Q	10	−5.018
4639.301	−2.561	4370.653	0 - 2	R	20	−5.000
4645.861	−2.602	4232.677	0 - 2	R	18	−5.080

Table 16. – Continued

$\omega_{\rm lab}$	$\log gf$	L.E.P. (cm^{-1})	Identification			$\log(W/\omega)$
		BL Ori				
^{12}CO						
5587.948	−5.726	16704.805	9 - 6	P	48	−4.999
5638.523	−5.907	15275.761	8 - 5	P	51	−5.079
5721.447	−5.970	13594.018	8 - 5	P	41	−4.913
5751.850	−6.000	13020.187	8 - 5	P	37	−4.968
5770.641	−5.014	20072.211	11 - 8	R	45	−5.065
5902.309	−5.102	21528.371	8 - 5	R	78	−5.152
5908.691	−6.174	12627.299	9 - 6	R	9	−4.997
5924.026	−6.547	10584.314	8 - 5	P	8	−4.834
5925.479	−5.880	13019.363	9 - 6	R	17	−4.814
5958.594	−7.755	6507.444	3 - 0	P	58	−4.981
6062.447	−5.556	14682.344	7 - 4	R	58	−4.825
C_2						
4399.632	−2.159	5996.193	1 - 3	Q	18	−5.291
4437.681	−2.401	5589.696	1 - 3	Q	10	−5.167
4453.439	−2.379	6132.686	1 - 3	R	20	−5.338
4615.792	−2.508	3903.308	0 - 2	Q	12	−5.111
4623.431	−2.583	3821.775	0 - 2	Q	10	−5.077
4639.301	−2.561	4370.653	0 - 2	R	20	−5.243
4645.861	−2.602	4232.677	0 - 2	R	18	−5.245

Table 16. – Continued

$\omega_{\rm lab}$	$\log gf$	L.E.P. ($\rm cm^{-1}$)	Identification			$\log(W/\omega)$
		V Aql				
^{12}CO						
5687.107	−5.481	18765.170	12 - 9	R	15	−5.065
5749.619	−6.158	12562.677	7 - 4	P	47	−4.879
5751.850	−6.000	13020.187	8 - 5	P	37	−5.005
5770.641	−5.014	20072.211	11 - 8	R	45	−4.916
5778.848	−5.137	18902.707	11 - 8	R	37	−4.928
5806.188	−6.204	11436.174	7 - 4	P	40	−4.808
5807.482	−6.086	12957.687	9 - 6	P	16	−4.939
5881.386	−7.123	8590.822	4 - 1	P	58	−4.959
5934.522	−5.703	13552.088	9 - 6	R	24	−4.755
5983.794	−6.818	6901.839	5 - 2	P	37	−4.777
5989.984	−5.379	16046.187	8 - 5	R	55	−4.887
5994.419	−6.238	10738.339	8 - 5	R	12	−4.774
6041.411	−7.796	4673.539	3 - 0	P	49	−4.945
C_2						
4376.792	−2.615	5765.005	1 - 3	P	14	−4.634
4399.632	−2.159	5996.193	1 - 3	Q	18	−4.588
4437.681	−2.401	5589.696	1 - 3	Q	10	−4.603
4453.439	−2.379	6132.686	1 - 3	R	20	−4.656
4507.885	−2.637	4370.653	0 - 2	P	20	−4.605
4561.872	−2.797	3998.982	0 - 2	P	14	−4.588
4634.276	−3.904	3637.329	0 - 2	P	2	−5.007
4639.301	−2.561	4370.653	0 - 2	R	20	−4.609

5.4 Stellar parameters

We use model atmospheres both in plane parallel geometry and in spherical symmetry in the analysis. Details of model atmospheres have been already described in Chapter 2 for the plane parallel models and in Chapter 4 for the spherical models. In this section, we discuss stellar parameters necessary to specify model atmospheres used in the analysis of three stars. Model atmospheres we use have four parameters in the plane parallel case and five in the spherical case. They are effective temperature, surface gravity, micro-turbulent velocity, chemical composition for the plane parallel case, and stellar mass should be added as the fifth parameter in the spherical symmetry case.

The effective temperatures of TX Psc, BL Ori, and V Aql were determined by Ohnaka & Tsuji (1996) based on the InfraRed Flux Method (IRFM). The effective temperatures are $T_{\rm eff} = 3080$ K for TX Psc, 3180 K for BL Ori, and 2790 K for V Aql. The uncertainties of effective temperatures are, as mentioned in Ohnaka & Tsuji (1996), 150 – 200 K. We finally use model atmospheres with $T_{\rm eff}$ = 3000 K, 3200 K, and 2800 K for the analysis of TX Psc, BL Ori, and V Aql, respectively.

For micro-turbulent velocity, which affects models by broadening of lines and by turbulent pressure, $V_{\rm micro} = 3$ km s^{-1} is adopted. However, micro-turbulent velocity, which is thought to represent some kind of non-thermal velocity field in the stellar atmosphere, is actually a parameter determined simultaneously with abundances. Therefore, the adopted value 3 km s^{-1} is in principle a tentative one. If the micro-turbulent velocity determined in the abundance analysis is largely different from 3 km s^{-1}, models with different micro-turbulent velocities should be computed. However, as described below, the values of micro-turbulent velocity derived for the three stars are not so different from the adopted value, 3 km s^{-1}.

It requires the estimation of stellar mass and luminosity to determine surface gravity, as surface gravity is calculated by

$$g = \frac{4\pi\sigma G M T_{\rm eff}^4}{L_\star}, \tag{5.5}$$

where σ is the Stefan-Boltzmann constant. Masses and luminosities of the Galactic carbon stars are subject to large uncertainties. Dean (1976) studied the kinematic properties from radial velocities and estimated distances to 427 carbon stars. It was concluded that the non-Mira carbon stars later than C4 are dynamically similar to dwarf F5 stars, which approximately have the mass of 1.2 $M_\odot$(Allen 1973). Catchpole & Feast (1985) studied the kinematics of Galactic SC stars and suggested that they might have masses around 2.0 $M_\odot$.

Studies on carbon stars in the Magellanic Clouds provide with more information on masses and, especially, on luminosities of carbon stars. Frogel et al. (1990) studied carbon stars and M giants in 39 clusters of the Magellanic Clouds. They used the Searle, Willkinson, and Bagnuolo (SWB) classification as an indicator of cluster age. They found that carbon stars are found only in the clusters of SWB types IV-VI, which correspond to the age from 1×10^8 to 5×10^9yr. The age of the youngest clusters in which carbon stars are found is about 100 Myr, which implies a maximum initial mass of 3 – 5 $M_\odot$for carbon stars. However, carbon stars found in older clusters could be less massive than those in the youngest clusters.

Luminosities of carbon stars in the Magellanic Clouds have been also extensively investigated. Frogel & Cohen (1982) obtained luminosity functions of carbon stars in the clusters and in the field of the Magellanic Clouds. The luminosity function of carbon stars in the clusters has a range from $M_{\rm bol} = -4.0$ to -5.5, while that of carbon stars in the field has a range from $M_{\rm bol} = -4.5$ to -6.0. Both luminosity functions have a quite similar mean of $M_{\rm bol} = -4.76$. Frogel et al. (1990) confirmed this result based on a larger sample. The mean bolometric magnitude for carbon stars in the field or clusters in the Magellanic Clouds was found to be around -4.8, which corresponds to $\sim 6000 L_\odot$. A study on carbon stars in the Fornax dwarf spheroidal galaxy by Aaronson & Mould (1980) also showed that the luminosities of the carbon stars they observed range from -4.5 to -5.5 in $M_{\rm bol}$. A set of $T_{\rm eff} = 3000$ K, $M = 2M_\odot$, and $L_\star = 6000 L_\odot$ gives $\log g = -0.18$. With a possible upper limit of mass 5 $M_\odot$ and the lowest luminosity of carbon stars in the Magellanic Clouds, we obtain an upper limit of surface gravity, $\log g = 0.52$ for $T_{\rm eff} = 3000$ K. If we combine the upper limit of luminosity of carbon stars in the Magellanic Clouds with $T_{\rm eff} = 3000$ K and 2 $M_\odot$, surface gravity as low as $\log g = -0.7$ is obtained. Therefore it is expected that the surface gravity of carbon stars might range from about -0.7 to 0.5. We adopt the value $\log g = 0.0$ for surface gravity and 2 $M_\odot$ for stellar mass in making a grid of model atmospheres which is used in the analysis.

The last input parameter to specify model atmospheres is chemical composition. However, chemical composition, especially elemental abundances of carbon and oxygen, is also what we are trying to determine based on the model atmospheres. Thus we make a grid of model atmospheres with carbon and oxygen abundances covering possible ranges. We specify the models by elemental abundance of oxygen and C/O ratio, instead of a set of elemental abundances of carbon and oxygen. We calculate models with oxygen abundances of -3.37, -3.27, -3.07, and -2.87. The C/O ratios used in computation are 1.1, 1.2, 1.5, 2.0, 3.0, and 4.0. In Table 17, we give input parameters of model atmospheres assigned to the three program stars.

Table 17. Stellar parameters assigned to the program stars

Star	$T_{\rm eff}$ (K)	$\log g$ (dyn cm^{-2})	$V_{\rm micro}$(km s^{-1})	Mass ($M_\odot$)
TX Psc	3000	0.0	3.0	2.0
BL Ori	3200	0.0	3.0	2.0
V Aql	2800	0.0	3.0	2.0

5.5 Analysis and results

5.5.1 Principle of the standard analysis

If a model atmosphere with a set of input parameters is assigned to a program star, we can derive the correction of molecular abundance to the assumed value for each selected line by comparing the equivalent widths predicted from the model atmosphere with those observed. However, we must determine the correction to the molecular abundance and micro-turbulent velocity simultaneously. In fact, micro-turbulent velocity is a parameter determined so that all the lines, including weak and strong ones, should give a consistent correction of molecular abundance. The equivalent widths of weak lines are almost independent of micro-turbulent velocity, while those of strong lines are much dependent on it. Therefore, a consistent abundance correction can be obtained only when the assumed micro-turbulent velocity is correct. With isotropic and depth-independent Gaussian micro-turbulent velocity assumed, we can calculate equivalent widths of the selected lines with three micro-turbulent velocities, say, $V_{\rm micro}$ = 2, 3, and 4 km s^{-1}. Then we evaluate the corrections to the molecular abundance for each line. The micro-turbulent velocity can be determined by interpolation from the three values above so that the corrections for each line should be equal. To determine the correction to the molecular abundance accurately, it is crucial to use both of weak lines and medium strong lines.

As most of oxygen is locked up into CO molecules in the atmosphere of carbon stars, determining oxygen elemental abundance can be attributed to determination of abundance of CO. The CO second overtone bands provide with enough number of medium strong lines and a handful of weak lines. Therefore we determine abundance correction for CO from lines of the CO second overtone bands. The first overtone bands, on the other hand, provide with few weak lines, but low excitation lines bring about important information on the physical properties of the upper photosphere. Thus we primarily use lines of the CO second overtone bands to determine oxygen abundance, and after determining carbon and oxygen abundances, we will investigate in the next Chapter the physical properties of the upper photosphere by subtracting the photospheric contribution from the observed spectra. Determination of carbon abundances from lines of the C_2 Phillips system is a tougher work, because only several weak lines can be used in the analysis. It is mainly because the line list of the C_2 Phillips system is far shorter than that of CO. In addition, the C_2 lines observed are generally quite weak, therefore they are susceptible to blends of adjacent lines.

In Fig. 5.7, we show the analysis of the CO second overtone lines for TX Psc as an example of the analysis described above. We calculate equivalent widths of the selected lines assuming a standard value of oxygen abundance $\log\varepsilon(\mathrm{O}) = -3.07$. In the figure, logarithm of the correction to the molecular abundance, $\delta(\mathrm{CO})$, is plotted, for three different values of micro-turbulent velocity, against

$$X = \log(W/\omega) + 6.0,$$

where W is the observed equivalent width and ω is the wavenumber in cm^{-1}. The corrections to the molecular abundance, $\delta(\mathrm{CO})$, are fitted to a quadratic function below,

$$\delta(\mathrm{CO}) = A(V_{\mathrm{micro}}) + B(V_{\mathrm{micro}})X^2$$

by the least square method. The coefficients A and B are functions of micro-turbulent velocity. The micro-turbulent velocity which gives the consistent correction $\delta(\mathrm{CO})$ for all the lines can be interpolated so that $B(V_{\mathrm{micro}})$ should be zero. At the same time, the consistent correction $A(V_{\mathrm{micro}})$ can be also determined.

In Fig. 5.8, we show an example of the same analysis applied to the lines of C_2 in TX Psc. It turned out almost impossible to determine micro-turbulent velocity from the analysis of the lines of C_2 as accurately as in the case of the CO second overtone lines, because we can not find medium strong lines of C_2 in the spectral region studied. In fact, we can formally determine micro-turbulent velocity only from several weak lines. But the result would suffer large uncertainty, since the coefficients of the quadratic function above become very sensitive to the relative positions of the points plotted in the $X - \delta(\mathrm{C}_2)$ plane. In some cases, we cannot determine micro-turbulent velocity from the lines of C_2, as can be seen in Fig. 5.9 where the analysis of the C_2 lines for BL Ori is shown. In this case, the coefficient $B(V_{\mathrm{micro}})$ is determined almost by the relative positions of the points plotted in the figure. Thus we use the micro-turbulent velocity determined from the lines of the CO second overtone bands for the analysis of C_2 lines. The mean of the corrections to C_2 abundance is adopted as the final abundance correction, because it is expected to give a more reliable result.

It should be remembered here, however, that carbon and oxygen abundances are also input parameters of the model atmosphere used in the analysis. In general, carbon and oxygen abundances derived by the analysis above are different from those used as input parameters of the model atmosphere. Therefore it requires a kind of iteration to determine the abundances self-consistently. For example, we could compute a model atmosphere with the carbon and oxygen abundances derived by the analysis, then again the abundances could be determined using that model. However, this procedure is admittedly messy, because we must compute model atmospheres with a number of sets of carbon and oxygen abundances. Besides, when we analyze more stars, such procedure should be carried out for all the program star even if some of them have the same effective temperature.

5.5.2 Self-consistent analysis with plane parallel models

Instead of doing the iterative procedure, we determine carbon and oxygen abundances simultaneously by the use of a grid of model atmospheres. In this subsection we describe the analysis based on the plane parallel models which were used for the analysis of $^{12}\mathrm{C}/^{13}\mathrm{C}$ ratios by Ohnaka & Tsuji (1996, 1997), but the method can be also applied to the analysis based on spherical models.

With effective temperature, surface gravity, and micro-turbulent velocity assigned to a program star, the corrections to the molecular abundances, $\delta(\mathrm{CO})$ and $\delta(\mathrm{C}_2)$, are calculated for each model atmosphere with various sets of $(\log\varepsilon(\mathrm{O}), \mathrm{C/O})$. The corrections to the abundances of CO and C_2 can be interpreted as functions of $(\log\varepsilon(\mathrm{O}), \mathrm{C/O})$, and these functions form curved surfaces in the 3-dimensional space of $(\log\varepsilon(\mathrm{O}), \mathrm{C/O}, \delta(\mathrm{AB}))$, where the corrections to the abundance of molecule AB is denoted by $\delta(\mathrm{AB})$. Then the points $(\log\varepsilon(\mathrm{O}), \mathrm{C/O})$ where the correction to the molecular abundances of CO and C_2 should be zero can be determined by interpolation. As a matter of fact, such points can be regarded as the curves formed where the surfaces cross the $(\log\varepsilon(\mathrm{O}), \mathrm{C/O})$ plane, and two curves can be obtained for CO and C_2. The intersection of the two curves, $\delta(\mathrm{CO}) = 0$ and $\delta(\mathrm{C_2}) = 0$, gives the set of $(\log\varepsilon(\mathrm{O}), \mathrm{C/O})$ with which both of $\delta(\mathrm{CO})$ and $\delta(\mathrm{C_2})$ should be zero.

We show in Fig. 5.10 an example of such analysis for the case of TX Psc. We first start with evaluation of the correction to the abundance of CO and micro-turbulent velocity. The input parameters of the model atmospheres are $T_{\mathrm{eff}} = 3000$ K, $\log g = 0.0$, $V_{\mathrm{micro}} = 3.0$ km s^{-1}, $\log\varepsilon(\mathrm{O}) = (-3.27, -3.07, -2.87)$, and $\mathrm{C/O} = (1.1, 1.2, 1.5, 2.0)$. The crosses in the figure represent a grid of model atmospheres. The correction to CO abundance and micro-turbulent velocity are simultaneously determined at each grid point by the standard method described in the previous subsection. Then at a given C/O ratio, we interpolate $\log\varepsilon(\mathrm{O})$ where the correction should be zero. The open circles in Fig. 5.10 represent these interpolated points, and the line represents the curve on which $\delta(\mathrm{CO})$ is zero. As can be seen in Fig. 5.10, oxygen abundance with which the correction $\delta(\mathrm{CO})$ should be zero changes only slightly along the increase of C/O ratio. This is because the abundance of CO changes little in the model atmospheres with different C/O ratios due to the stability of CO at the relevant temperature and gas pressure. The micro-turbulent velocity is also regarded as a function of $(\log\varepsilon(\mathrm{O}), \mathrm{C/O})$, and cannot be uniquely determined at this step.

We next evaluate the correction to the abundance of C_2 at each grid point. However, as mentioned in the previous subsection, it is quite difficult to determine the correction to the molecular abundance and micro-turbulent velocity simultaneously for the C_2 lines. Therefore, with $V_{\mathrm{micro}} = 3.0$ km s^{-1} tentatively assumed, we use the mean of the corrections for all the lines. The final value of micro-turbulent velocity is determined by iteration as described below. Then at a given value of $\log\varepsilon(\mathrm{O})$, the C/O ratio at which the correction to the C_2 abundance should be zero can be determined by interpolation. The filled circles represent these interpolated points, and the line represents the curve on which $\delta(\mathrm{C_2})$ is zero. This line shows that the larger C/O ratio is required at the smaller $\log\varepsilon(\mathrm{O})$. Since the model atmospheres are specified by $\log\varepsilon(\mathrm{O})$ and C/O ratio, the models with the smaller $\log\varepsilon(\mathrm{O})$ have the smaller amount of carbon available to form C_2 molecules. Therefore, the larger C/O ratio is required to fit the observed equivalent widths.

Finally oxygen abundance and C/O ratio are simultaneously determined as the intersection of the two curves, $\delta(\mathrm{CO}) = 0$ and $\delta(\mathrm{C_2}) = 0$. However, such oxygen abundance and C/O ratio should not be regarded as the final result, because they are derived based on the micro-turbulent velocity tentatively assumed. Now we can determine micro-turbulent velocity by a kind of iteration. The micro-turbulent velocity determined from the CO lines at each grid point is a function of $(\log\varepsilon(\mathrm{O}), \mathrm{C/O})$. We can evaluate the micro-turbulent velocity at the intersection of the two curves, $\delta(\mathrm{CO}) = 0$ and $\delta(\mathrm{C_2}) = 0$, by

2-dimensional interpolation. The micro-turbulent velocity now derived is, in general, different from the tentatively assumed value $V_{\rm micro}$ = 3.0 km s^{-1}. Then the corrections to the C_2 abundance are re-evaluated, assuming the new value of micro-turbulent velocity. This procedure should be repeated until the micro-turbulent velocity converges. However, as the uncertainty of determination of micro-turbulent velocity from the CO lines is about $\pm$0.5 km s^{-1}, it would not make much sense to repeat the iteration until the perfect convergence is obtained. All we have to do is to repeat the process until the difference of micro-turbulent velocity between the successive iterations is within the uncertainty of $\pm$0.5 km s^{-1}. In the case of TX Psc, $\log \varepsilon(\mathrm{O}) = -3.176$ and C/O = 1.160 are derived and the micro-turbulent velocity is finally derived to be 3.29 km s^{-1}.

We apply the analysis described above to BL Ori and V Aql as well. In Fig. 5.11 we show the self-consistent analysis for BL Ori. The effective temperature adopted is 3200 K. The surface gravity and the micro-turbulent velocity of the models are $\log g$ = 0.0 and $V_{\rm micro}$ = 3.0 km s^{-1}. We use a grid of model atmospheres with $\log \varepsilon(\mathrm{O}) = (-3.37, -3.27, -3.07)$ and C/O = $(1.1, 1.2, 1.5, 2.0)$. The open circles represent the interpolated points where $\delta(\mathrm{CO})$ should be zero, while the filled circles represent such points for $\delta(\mathrm{C_2})$. The curve of $\delta(\mathrm{C_2}) = 0$ is drawn with $V_{\rm micro}$ = 3.5 km s^{-1} assumed. The intersection of the two curves gives $\log \varepsilon(\mathrm{O}) = -3.262$ and C/O = 1.394. The final value of micro-turbulent velocity for BL Ori is 3.404 km s^{-1}.

The analysis for V Aql is shown in Fig. 5.12. The effective temperature 2800 K is adopted for this star. The surface gravity and micro-turbulent velocity in the model computation are $\log g = 0.0$ and $V_{\rm micro}$ = 3.0 km s^{-1}. The grid of model atmospheres is computed for $\log \varepsilon(\mathrm{O}) = (-3.37, -3.27, -3.07, -2.87)$ and C/O = (1.1, 1.2, 1.5, 2.0, 3.0, 4.0). As shown by the crosses in Fig. 5.12, the model atmospheres with C/O = 3.0 and 4.0 are calculated only for $\log \varepsilon(\mathrm{O}) = -3.27$ and -3.07. The intersection of the two curves, $\delta(\mathrm{CO}) = 0$ and $\delta(\mathrm{C_2}) = 0$, gives the final values of oxygen abundance and C/O ratio, $\log \varepsilon(\mathrm{O}) = -3.232$ and C/O = 2.825. The curve of $\delta(\mathrm{C_2}) = 0$ shown in the figure is derived with the assumption of $V_{\rm micro}$ = 3.5 km s^{-1}. On the other hand, the final value of micro-turbulent velocity has turned out to be 3.6 km s^{-1}. This value is consistent with the assumed value within the uncertainty.

5.5.3 Analysis with spherical models

The analysis described in the previous subsection has been done with the plane parallel models. We also do the analysis of oxygen abundances and C/O ratios using the spherical model atmospheres. The method of analysis is the same with that based on the plane parallel models, except that we use the radiative transfer code in spherical geometry in computing equivalent widths of lines.

The analysis for TX Psc is shown in Fig. 5.13. The effective temperature, the surface gravity, and the micro-turbulent velocity used in the model computation are identical with those in the analysis with the plane parallel models. The stellar mass $M = 2\ M_\odot$ is adopted for all the three stars. The crosses in the figure indicate the grid points of the model atmospheres. The curve of $\delta(\mathrm{CO}) = 0$ is represented by the open circles, while the curve of $\delta(C_2) = 0$ is represented by the filled circles. Compared with Fig. 5.10, the curve of $\delta(CO) = 0$ is almost horizontally shifted by about +0.1 dex. It should be noted here that the correction to the molecular abundance is primarily derived from weak lines (see, Fig. 5.7). Therefore, the horizontal shift of the curve $\delta(CO) = 0$ means that equivalent widths of weak lines predicted from the spherical models are weaker than those predicted from the plane parallel models. This phenomenon has been already discussed in Chapter 4. These weak lines have lower excitation potential (LEP) from 10000 to 20000 cm^{-1} (1 – 2 eV) and are formed in the layers about $\log \tau_0 = -4$, where the temperature stratifications do not differ so much between the spherical and the plane parallel models. Therefore, because of the effect of spherical geometry in radiative transfer, these weak lines become weaker in the spherical models than in the plane parallel models. The final values of oxygen abundance and C/O ratio in TX Psc are $\log \varepsilon(O) = -3.086$ and C/O = 1.140. For the reason mentioned just above, the oxygen abundance derived with the spherical models is larger by about 0.1 dex than that derived with the plane parallel models. The micro-turbulent velocity is finally derived to be 3.269 km s^{-1}.

Figure 5.14 shows the analysis for BL Ori. The symbols in the figure have the same meanings as in Fig. 5.13. The curve of $\delta(CO) = 0$ is almost horizontally shifted by about 0.1 dex as compared with the analysis with the plane parallel models. As a result, the oxygen abundance finally derived, $\log \varepsilon(O) = -3.148$, is by about 0.1 dex larger than that derived based on the plane parallel model atmospheres. The C/O ratio is finally derived to be 1.311, which is slightly smaller than in the analysis with the plane parallel models. The micro-turbulent velocity is derived to be 3.602 km s^{-1}.

We show the analysis for V Aql in Fig. 5.15. As compared with Fig. 5.11, the curve of $\delta(CO) = 0$ is horizontally shifted by about +0.2 dex, which is larger than in the cases of TX Psc and BL Ori. The final values of oxygen abundance and C/O ratio are $\log \varepsilon(O) = -3.090$ and C/O = 2.479. The micro-turbulent velocity is finally derived to be 3.883 km s^{-1}. The assumed value of micro-turbulent velocity in evaluating the curve of $\delta(C_2) = 0$ is 3.5 km s^{-1}, which is in agreement with the final value 3.883 km s^{-1} within the uncertainty. The oxygen abundance derived here is by about 0.15 dex larger than that derived based on the plane parallel models. This trend is consistent with the cases of TX Psc and BL Ori.

To summarize the results mentioned above, the effects of sphericity on the analysis of elemental abundances of carbon and oxygen are as follows. Firstly, the oxygen abundances derived with the spherical models are by about 0.1 to 0.15 dex larger than those derived with the plane parallel models. The lines with high excitation potentials, which play a major role in determination of abundances, are formed in the relatively deep layers, $\log \tau_0 \sim -4$. The difference of temperature stratification is small between the spherical and the plane parallel models in these layers. Thus, the effect of spherical geometry in solving radiative transfer leads to larger oxygen abundances than in the analysis based on the plane parallel models.

The second point is that the C/O ratios are not so affected by the use of the spherical models instead of the plane parallel ones. However, this does not mean that the effect of sphericity is not significant in determination of the carbon abundances. The elemental abundances of carbon are also affected by the use of spherical models. Though the C/O ratios are not so affected, the carbon abundances, $\varepsilon(\mathrm{C}) = \mathrm{C/O} \times \varepsilon(\mathrm{O})$, are also affected via the increase of the oxygen abundances.

The final results of oxygen abundances and C/O ratios in the three stars are given in Tables 18 for the analyses with the plane parallel models (PP) and with the spherical models (SS).

Table 18. The resulting oxygen abundances and C/O ratios. 'PP' denotes the analysis based on the plane parallel models, and 'SS' denotes the analysis based on the spherical models

Star	$\log\varepsilon(\mathrm{O})$		C/O	
	PP	SS	PP	SS
TX Psc	−3.176	−3.086	1.160	1.140
BL Ori	−3.262	−3.148	1.394	1.311
V Aql	−3.232	−3.090	2.825	2.479

5.5.4 Uncertainties of the results

We discuss uncertainties of the carbon and oxygen abundances derived, in terms of internal and external errors. Internal errors can be interpreted as uncertainties of determination of the abundances based on models with a fixed set of parameters – T_{eff}, $\log g$, V_{micro}, and M. On the other hand, external errors come from the uncertainties of the input parameters of model atmospheres, and the model atmospheres themselves.

Internal errors can be estimated from the probable errors of $\delta(\mathrm{CO})$ and $\delta(\mathrm{C_2})$ at each grid point. In Fig. 5.16, we show the effect of the uncertainties of $\delta(\mathrm{CO})$ and $\delta(\mathrm{C_2})$ on the resulting oxygen abundance and C/O ratio in the case of TX Psc. We derived two additional curves of $\delta(\mathrm{CO}) = 0$, taking the plus and minus signs of the probable error of $\delta(\mathrm{CO})$. In the same way, we derived two additional curves of $\delta(\mathrm{C_2}) = 0$ for each sign of the probable error of $\delta(\mathrm{C_2})$. Therefore, the uncertainties of the oxygen abundance and the C/O ratio derived are interpreted as the hatched area in Fig. 5.16. The oxygen abundance ranges from $\log\varepsilon(\mathrm{O}) = -3.253$ to -3.130, and the C/O ratio ranges from 1.109 to 1.249. The internal errors can be regarded to be about ± 0.1 dex for the oxygen abundance and $\pm 5\%$ for the C/O ratio in the case of TX Psc.

The same analyses of internal errors for BL Ori and V Aql are shown in Figs. 5.17 and 5.18, respectively. The uncertainties of the oxygen abundances and the C/O ratios are also represented by the hatched areas in the figures. In the case of BL Ori, the internal error of the oxygen abundance is about ± 0.2 dex, and the uncertainty of the C/O ratio is (+28%,−14%). In the case of V Aql, the uncertainty of the oxygen abundance is also about ± 0.2 dex, and the uncertainty of the C/O ratio is about $\pm 30\%$.

In Figs. 5.19, 5.20, and 5.21, we show the analyses of internal errors in the case of the analysis with the spherical models. The internal errors of the oxygen abundances and the

C/O ratios are also shown by the hatched areas in the figures. The uncertainties of the oxygen abundances and the C/O ratios are of the same order of magnitude with those in the analysis based on the plane parallel models.

We also analyzed the external errors, which can be interpreted as the errors induced by the uncertainties of the model atmospheres. We computed plane parallel model atmospheres with different input parameters adopted, and investigated the effect of the uncertainties of the input parameters on the resulting oxygen abundance and C/O ratio in the case of TX Psc. The decrease of effective temperature by 100 K leads to decrease of the oxygen abundance by 0.029 dex and to decrease of the C/O ratio from 1.160 to 1.111. The uncertainty of effective temperature gives only small effect on the results of the abundance analysis. On the other hand, the uncertainty of surface gravity has turned out to give larger effect on the results. The analysis with the model atmospheres with $\log g = -0.3$ reveals that the resulting oxygen abundance is by 0.094 dex smaller than the value derived based on the models with $\log g = 0.0$. The resulting C/O ratio derived based on the models with $\log g = -0.3$ is 1.247 while C/O = 1.160 is derived based on the models with $\log g = 0.0$. We also computed a grid of spherical model atmospheres with $M = 5\ M_\odot$ to investigate the effect of the uncertainty of stellar mass. The resulting oxygen abundance and C/O ratio are -3.097 and 1.148, respectively and the analysis with the massive models has shown that the uncertainty of stellar mass gives only minor changes both on the oxygen abundance and on the C/O ratio. As the plane parallel models can be actually considered to be very massive spherical models, the effect of the uncertainty of stellar mass is at most the differences of the results between the plane parallel models and the spherical models.

5.5.5 Spectrum synthesis

We calculate a synthetic spectrum for each line used in the analysis in order to finally check the carbon and oxygen abundances derived by the interpolation from the grid of model atmospheres. For each star, we first compute a model atmosphere with the carbon and oxygen abundances derived by the method described above. In order to fit the observed spectra by synthetic ones, we determine macro-turbulent velocity for each star. For this purpose, we plot the observed full widths at the half maximum (FWHM) of the CO lines used in the analysis against their central depths in Fig. 5.22. The optically thin limit of the FWHM is determined by extrapolating the plots to zero central depth. Such limiting value $(\mathrm{FWHM})_0$ can be interpreted as the intrinsic line width except for the instrumental effect. Thus the Gaussian velocity dispersion V_0 corresponding to $(\mathrm{FWHM})_0$ can be written as follows:

$$V_0^2 = V_{\mathrm{th}}^2 + {V_{\mathrm{micro}}}^2 + {V_{\mathrm{macro}}}^2 + V_{\mathrm{instr}}^2,$$

where V_{th} is the dispersion of the thermal velocity, V_{micro} is the micro-turbulent velocity, V_{macro} is the macro-turbulent velocity, and V_{instr} is the Gaussian dispersion corresponding to the spectral resolution defined by the apodizing function. By correcting the instrumental effect and assuming the thermal velocity dispersion to be 1.1 km s^{-1}, we can derive the effect of the non-thermal velocity dispersion, ${V_{\rm micro}}^2 + {V_{\rm macro}}^2$. The macro-turbulent velocity is finally determined by subtracting the effect of the micro-turbulent velocity derived in the abundance analysis. The values of $({\rm FWHM})_0$, V_0, $V_{\rm tur} = \sqrt{{V_{\rm micro}}^2 + {V_{\rm macro}}^2}$, $V_{\rm micro}$, and $V_{\rm macro}$ are given in Table 19.

With the micro- and macro-turbulent velocities determined, a line profile over an appropriate spectral interval is calculated for each line based on the model adjusted to each program star. The synthetic line profiles of all the lines are shown in Figs. 5.23, 5.24, and 5.25, for TX Psc, BL Ori, and V Aql, respectively. The synthetic spectra are calculated over an interval of 2 cm^{-1} so that it can cover one line. Only lines of CO are included in the calculations, while lines of other molecular and/or atomic species might contribute more or less to the observed line profiles. We also show in the figures ratioed spectra, that is, the observed spectra divided by the synthetic spectra. A glimpse of Figs. 5.23, 5.24, and 5.25 shows that the observed line profiles are fairly well reproduced by the calculations. This agreement ensures that the carbon and oxygen abundances as well as the turbulent velocities derived by the interpolation from the grid of model atmospheres give self-consistent results.

Table 19. Turbulent velocities derived for the program stars

Star	$({\rm FWHM})_0({\rm cm}^{-1})$	V_0 (km s^{-1})	$V_{\rm tur}$ (km s^{-1})	$V_{\rm micro}$ (km s^{-1})	$V_{\rm macro}$ (km s^{-1})
TX Psc	0.186	5.59	4.92	3.29	3.66
BL Ori	0.194	4.77	4.09	3.40	2.26
V Aql	0.220	6.61	6.13	3.60	4.96

5.6 Discussion on the result of the abundance analysis

5.6.1 Comparison with the result by Lambert et al. (1986)

Ohnaka & Tsuji (1996) analyzed ^{12}C/^{13}C ratios in more than 100 carbon stars, and found that the ^{12}C/^{13}C ratios they derived were systematically smaller by a factor 2 to 3 than those derived by Lambert et al. (1986). This discrepancy could be more serious since the disagreements were found for the same stars. It was first suspected that the difference of model atmospheres used in the analyses could explain the discrepancy of the ^{12}C/^{13}C ratios, but this argument should be also further examined. For example, inclusion of the effect of turbulent pressure could affect the comparison of the temperature stratifications, since the temperature stratifications were compared on the $\log P_g - T$ plane. Ohnaka & Tsuji (1996) included the effect of turbulent pressure in the hydrostatic equation, while Lambert et al. (1986) probably did not. But the effect of turbulent pressure might not explain the difference of the temperature stratifications reported by Ohnaka & Tsuji (1996) (see Fig. 19 of Ohnaka & Tsuji 1996). In Fig. 5.26 we show a comparison of the temperature stratifications calculated by Lambert et al. (1986) and by our code. We calculated model atmospheres with the same set of parameters given in Lambert et al. (1986) for two cases: one with the effect of turbulent pressure, and the other without it. The figure shows that the effect of turbulent pressure is not responsible for the difference of the temperature stratifications mentioned in Ohnaka & Tsuji (1996). In fact, the difference of temperature stratifications is 100 K at most between the models with turbulent pressure and without it. The difference of temperature is about 500 K between the models of Lambert et al. (1986) and that of Ohnaka & Tsuji (1996). Such a difference of the model atmospheres could give some effects on the analysis elemental abundances of carbon and oxygen as well as carbon isotopic ratios. That is exactly why we analyzed the identical spectra that Lambert et al. (1986) had done.

We now discuss the comparison of the resulting carbon and oxygen abundances with those derived by Lambert et al. (1986). The oxygen abundances and the C/O ratios in TX Psc, BL Ori, and V Aql derived by the two authors are given in Table 20. We will finally adopt the values derived based on the spherical models, because we expect the spherical model atmospheres could be more realistic than the plane parallel atmospheres. However, as Lambert et al. (1986) analyzed the spectra based on the plane parallel model atmospheres, we discuss the comparison of the results derived with the plane parallel models.

Firstly, the oxygen abundances we derived are in good agreement with the results by Lambert et al. (1986) for all the three stars. The agreement is almost perfect for TX Psc. For BL Ori and V Aql, the agreements should be regarded fairly good, given the errors of the oxygen abundances derived in the present work. These agreements could be expected. Because CO is the most stable molecule at the relevant ranges of temperature and gas pressure, its abundance is not much affected by the difference of temperature and pressure stratifications.

The comparison of the C/O ratios derived by the two authors reveals serious disagreements. Especially in V Aql, the discrepancy amounts up to about a factor of 2. Though the disagreements look minor for TX Psc and BL Ori, the discrepancies of (C/O -1) are very severe. Since most of oxygen is locked up into CO molecules, (C/O -1) is considered to be relevant to the abundance of C_2, from which the carbon abundances are derived. The discrepancy of the (C/O -1) amounts up to a factor of 8 to 10 in the three stars analyzed in the present work.

The difference of the effective temperature scale cannot explain such discrepancies of the C/O ratios. For example, $T_{\rm eff}$ = 2800 K is assigned to V Aql in the present work, while $T_{\rm eff}$ = 2600 K in Lambert et al. (1986). We computed plane parallel models with $T_{\rm eff}$ = 2600 K and derived oxygen abundance and C/O ratio with these models. The oxygen abundance is derived as $\log \varepsilon({\rm O}) = -3.27$, which is in good agreement with that derived by Lambert et al. (1986). However, the C/O ratio is derived to be 2.0, which is still significantly higher than their result.

Table 20. Comparison of the oxygen abundances and the C/O ratios derived by Lambert et al. (1986) and by the present work. 'PP' denotes the analysis based on the plane parallel models

	[O/H]		C/O	
Star	This work (PP)	Lambert et al. (1986)	This work (PP)	Lambert et al. (1986)
TX Psc	−0.096	−0.10	1.160	1.027
BL Ori	−0.182	−0.29	1.394	1.039
V Aql	−0.152	−0.20	2.825	1.25

These discrepancies could be rather attributed to the differences of the model atmospheres used in the analyses, as already pointed out by Ohnaka & Tsuji (1996). Besides, such disagreements might come from the difference of the role of the model atmospheres in the analyses. In fact, the treatments of the excitation effect by the model atmospheres are different. Lambert et al. (1986) says that they set the excitation temperature as that of the layer $\log \tau_{\rm Ross} = -1.4$ for all the models, where $\tau_{\rm Ross}$ denotes the optical depth evaluated with the Rossland mean opacity. However, they do not give any reason for the use of the temperature of the layer $\log \tau_{\rm Ross} = -1.4$. We investigated the validity of using such temperature as the excitation temperature for the lines both of CO and C_2. We evaluated contribution functions, which can be written as $S_\nu(\tau_\nu)E_2(\tau_\nu)$ in the plane parallel case, for some of the lines of CO and C_2. We show the contribution function of a line of the CO second overtone band, $12-9$ $R(15)$, in Fig 5.27. The contribution function is plotted as a function of the wavenumber from the line center, $\omega - \omega_0$, and the depth of the atmosphere labeled by $\log \tau_0$. This line plays a major role in determination of the correction to the CO abundance in the analysis of V Aql, since it is one of the weakest lines. The contribution function was calculated based on the plane parallel model with $T_{\rm eff}$ = 2800 K, $\log g$ = 0.0, $V_{\rm micro}$ = 3.0 km s^{-1}, $\log \varepsilon({\rm O}) = -3.07$, and C/O = 1.1. It was evaluated over an interval of 2 cm^{-1}, but is shown over half of the interval for easier visual inspection. The interval along the $\log \tau_0$ axis corresponds to 0.2. The figure shows that this line is formed at the layers around $\log \tau_0 = -1.4$. On the other hand, the layer of $\log \tau_{\rm Ross} = -1.4$ corresponds approximately to the layer with $\log \tau_0 = -1.0$ in this model. Therefore, the assumption adopted by Lambert et al. (1986) is expected to work almost correctly for weak lines of the CO second overtone bands.

In Fig. 5.28, we show the contribution function for a line of the C_2 Phillips system, $0-2$ $P(2)$. This line is used in the analysis of V Aql, and plays a critical role in determining the correction to the abundance of C_2, since it is the weakest of the lines used. The contribution function was calculated based on the model with the parameters mentioned just above. The figure reveals that the line is formed in the relatively deep layers, that is, the layers of $\log \tau_0 \sim 0.0$, where the contribution function has the maximum. The temperature of that layer is 3600 K in this model. On the other hand, the layer of $\log \tau_{\rm Ross} = -1.4$ corresponds approximately to the layer of $\log \tau_0 = -1.0$ in this model. The temperature of this layer is 3100 K. Of course, as can be seen in Fig. 5.28, the line formation region should not be considered to be a single layer such as that at $\log \tau_0 = 0.0$. Actually the line is formed over a certain range of layers. However, as compared with the case for the CO second overtone line mentioned above, the assumption of excitation temperature adopted by Lambert et al. (1986) does not seem to be appropriate for the C_2 lines. With such an assumption, the excitation temperature might have been estimated to be lower than that in the actual line formation region. Such lower excitation temperature might have led to the lower abundance of C_2, which means lower carbon abundance. Such a simple assumption for excitation temperature might not work properly for all the lines of CO, C_2, CN, and their isotopic species. The atmospheric structure of carbon stars is so sensitive to C/O ratio that it seems logical to expect that the line formation region is different for different molecular lines and for different model atmospheres. In our calculation of equivalent widths, we take into account the excitation effect by solving radiative transfer for an appropriate interval covering an individual line, instead of using a single excitation temperature. Thus it is expected that the correction for the excitation effect is properly taken into account in our analysis.

5.6.2 Tests of model atmospheres

We discuss in this subsection tests of the model atmospheres in comparison with observational data. Since the reliability of the result of the abundance analysis is largely dependent on that of model atmospheres, it is indispensable for the final model of each program star to pass tests by observational data. Otherwise, the result of the analysis would be regarded with some suspision.

In Fig. 5.29, we show comparison between observed flux of TX Psc and emergnet flux from the final spherical model for this star. The observed flux was read from Johnson et al. (1985). A glance of the figure reveals that the observed flux can be fairly well reproduced. Especially the 3 μm absorption feature due to HCN and C_2H_2 is well reproduced, while the match is rather poor for the absorption features due to CN and C_2 around 1.4 and 1.8 μm. However, these absorption features can be also well reproduced by the synthetic spectra calculated from the final model. In Figs. 5.30 and 5.31, we show such synthetic spectra from 1 to 2.5 μm for TX Psc and V Aql, respectively. We also show spectrophotometric data acquired by Lazáro et al. (1994) for these stars. Lines of the CN Red system, C_2 Phillips system, and CO vibration-rotation transitions are inculded in the calculation of the synthetic spectra. As can be seen in the figures, the matches between the observed and the synthetic spectra are fairly good. The absorption at 1.8 μm is due to the C_2 Ballik-Ramsay system, of which lines are not included in the calculation. The very strong absorption at around 1.6 μm in the synthetic spectra may be an artifact due to inaccurate oscillator strengths of CN.

As already done by Ohnaka & Tsuji (1996), we again attempt to test the model atmospheres using absorption lines of molecular hydrogen. Lines of molecular hydrogen are adequate to test model atmospheres because the abundance of hydrogen is expected not to vary in stars. Especially, H_2 $1-0$ $S(0)$ line at 4497.84 cm^{-1} can be, at least in principle, identified in the observed spectra. In Fig. 5.32 we show a portion of the observed spectra around the H_2 line. As can be easily seen in the figure, it is almost impossible to measure the equivalent width of $S(0)$ line for TX Psc and BL Ori. Thus, for these stars, the molecular hydrogen line provides us with little opportunity to test the model atmospheres. For V Aql the equivalent width of $S(0)$ line is $\log(W/\omega) = -5.111$. On the other hand, the equivalent width predicted by the final model of V Aql is $\log(W/\omega) = -7.0$, which is far weaker than observed. However, the radial velocity of $S(0)$ line in V Aql has turned out to be by about 2 km s^{-1} red-shifted from those of high excitation lines of the CO second overtone bands. As will be discussed in the next Chapter, the radial velocities of low excitation lines of the CO first overtone bands also show such systematic shifts as compared with those of high excitation lines. In fact, the radial velocity of $S(0)$ line coincides with those of the CO low excitation lines for V Aql. This means that H_2 $S(0)$ line observed toward V Aql may be formed in an extra component above the photosphere, which will be discussed in the next Chapter. Thus, the apparent disagreement between the observed line intensity and the predicted does not necessarily mean that the model atmospheres used in the analysis are not correct. It can be said that H_2 lines may not serve to test model atmospheres at least for V Aql.

5.6.3 Carbon star formation

We discuss here the scenario of carbon star formation. We have already derived $^{12}C/^{13}C$ ratios for TX Psc, BL Ori, and V Aql in Ohnaka & Tsuji (1996). The number of the stars for which oxygen abundances and C/O ratios are derived in the present work is not statistically enough to confirm the scenario of the carbon star formation, but we discuss the change of chemical composition for each star in comparison with that in M giants. In Table 21, the $^{12}C/^{13}C$ ratios, oxygen abundances, and C/O ratios in TX Psc, BL Ori, and V Aql are given. We finally adopt the oxygen abundances and the C/O ratios derived based the spherical models with $M = 2\ M_{\odot}$.

In the scenario of carbon star formation, which is currently regarded the most plausible, oxygen-rich AGB stars (K and M giants) turn into N-type carbon stars by addition of ^{12}C produced via the 3α- process in the thermal pulse. One of the obstacles to confirm this scenario lies in the fact that we can not know the chemical compositions that carbon stars ever had when they were oxygen-rich. We assume that the chemical compositions of the progenitors of carbon stars are the same with that derived for K and M giants. Smith & Lambert (1985, 1990) analyzed near-infrared (7500 Å) and infrared (1.6 – 4.0 μm) spectra of M, MS, and S giants and derived elemental C, N, and O abundances together with their isotopic ratios. We here assume only M giants as the progenitors of N-type carbon stars. The scenario of carbon star formation sees MS and S stars as transitional objects from M giants to carbon stars, but as pointed out by Smith & Lambert (1990), the enhancement of nitrogen abundance in MS and S stars suggests that some nuclear reactions other than the thermal pulse might operate in these stars. For example, the hot bottom burning in relatively massive stars could turn carbon stars back to N-rich S or MS giants (e.g. Blöcker & Schönberner 1991). Smith & Lambert (1990) showed that the oxygen abundances in 14 M giants range from $[O/H] = -0.22$ to 0.12 with the mean $\overline{[O/H]} = -0.07$. The C/O ratios range from 0.31 to 0.66 with the mean $\overline{C/O} = 0.45$. The $^{12}C/^{13}C$ ratios were found to range from 11 to 23 with the mean $\overline{^{12}C/^{13}C} = 13$. We first assume that the progenitors of N-type carbon stars have $C/O = 0.45$ and $^{12}C/^{13}C = 13$, taking the averages of the result by Smith & Lambert (1990).

For TX Psc, BL Ori, and V Aql, we can calculate $^{12}C/^{13}C$ ratios which such progenitors would have when their C/O ratios were increased to the values derived in the present work. In Table 21, such $^{12}C/^{13}C$ ratios for the three stars are given together with the results by Ohnaka & Tsuji (1996). The agreements of the $^{12}C/^{13}C$ ratios between predicted and derived are fairly good. Especially, the agreement is pretty good for V Aql, for which the large discrepancy of C/O ratio between Lambert et al. (1986) and the present work is found. The agreements for TX Psc and BL Ori are also fair, given the assumption that the chemical compositions of the progenitors are identical for all the three stars.

The C/O ratios and the $^{12}C/^{13}C$ ratios of the progenitors could be different for each star. So we next examine possible effects of the assumption on the chemical composition of the progenitors. For two cases with different C/O ratios and $^{12}C/^{13}C$ ratios, we calculated the $^{12}C/^{13}C$ ratios which M giants would have after they became carbon-rich. In the Case *c*, $C/O = 0.3$ and $^{12}C/^{13}C = 20$ are assumed for the progenitors of N-type carbon stars, while $C/O = 0.5$ and $^{12}C/^{13}C = 10$ are assumed in the Case *d*. The predicted $^{12}C/^{13}C$ ratios are given in Table 21. In the Case *c*, the predicted $^{12}C/^{13}C$ ratios are far larger than those derived. However, this case may be regarded to be an extreme case, because only one M giant has such low C/O ratio and $^{12}C/^{13}C$ ratio larger than 20 in the sample of Smith & Lambert (1990). In the Case *d*, the agreements for TX Psc and BL Ori are much better than in the case where the average values are assumed, while the agreement for V Aql is somewhat poor. But it would make little sense to examine further different C/O ratios and $^{12}C/^{13}C$ ratios for the progenitors. The point is that the results of C/O ratios derived in the present work for the three stars are very consistent with the $^{12}C/^{13}C$ ratios derived by Ohnaka & Tsuji (1996) in view of the current scenario of carbon star formation.

The discussion above can be more clearly seen in Fig. 5.33, where C/O ratio is plotted against $^{12}C/^{13}C$ ratio for each program star. The filled circles represent the stars analyzed in the present work, while the open circles represent all the stars analyzed by Lambert et al. (1986). The differences of the results for the same stars between by the present work and by Lambert et al. (1986) are shown by arrows. The solid lines in the figure represent the relations between ^{12}C/^{13}C ratio and C/O ratio predicted by dredge-up of ^{12}C to the stellar surface of K and M giants. We assumed the ^{12}C/^{13}C ratios and C/O ratios of the Cases *b* and *d* as those of progenitors. As compared with the results by Lambert et al. (1986), our results are plotted in a rather narrow area of which width in fact corresponds to the scattering of ^{12}C/^{13}C ratios and C/O ratios in K and M giants. It is of course indispensable to analyze a larger number of stars in order to confirm the clear correlation between ^{12}C/^{13}C ratio and C/O ratio shown in Fig. 5.33.

Table 21. ^{12}C/^{13}C ratios predicted by the carbon star formation scenario

	TX Psc	BL Ori	V Aql
[O/H]	−0.006	−0.068	−0.010
C/O	1.140	1.311	2.479
^{12}C/^{13}C (obs.)^a	22	26	66
^{12}C/^{13}C (pred.)^b	33	38	72
^{12}C/^{13}C (pred.)^c	76	87	165
^{12}C/^{13}C (pred.)^d	23	26	50

a: ^{12}C/^{13}C ratios derived by Ohnaka & Tsuji (1996)
b: ^{12}C/^{13}C ratios predicted from C/O = 0.45 and ^{12}C/^{13}C = 13 in progenitors
c: ^{12}C/^{13}C ratios predicted from C/O = 0.30 and ^{12}C/^{13}C = 20 in progenitors
d: ^{12}C/^{13}C ratios predicted from C/O = 0.50 and ^{12}C/^{13}C = 10 in progenitors

5.7 Concluding remarks

We have done re-analysis of the spectra of Lambert et al. (1986) to investigate the effects of the discrepancy of model atmospheres found by Ohnaka & Tsuji (1996) on the determination of elemental carbon and oxygen abundances.

The first of our conclusion is that the oxygen abundances derived for three stars, TX Psc, BL Ori, and V Aql, are in agreement with those derived by Lambert et al. (1986) within the errors of the analyses. The second conclusion is that the C/O ratios derived in the present work are markedly higher than those by Lambert et al. (1986). The discrepancy of (C/O -1) amounts up to a factor of 8 to 10. One of the reasons for this disagreement could be the difference of the model atmospheres used in the analyses, as pointed out by Ohnaka & Tsuji (1996). And another possibility is validity of the assumption for the excitation temperature adopted by Lambert et al. (1986). The atmospheric structure of carbon stars is largely dependent on chemical composition, especially C/O ratio, and such a simple assumption for the excitation temperature that Lambert et al. (1986) adopted cannot be necessarily justified in chemical analyses of carbon stars. It might have led to the lower carbon abundances than they really are.

It has been also shown that the emergent flux from our model atmosphere reproduces well the spectrophotomeric observation for TX Psc. The synthetic spectra over a rather wide range in infrared also reproduce fairly well the spectrophotometric observations. These matches between the predicted flux and the observed support the validity of our model atmospheres. We have also attempted to test the model atmospheres by H_2 $1-0$ $S(0)$ line. The equivalent widths of the line are not measurable in TX Psc and BL Ori since they are too weak. For V Aql, the equivalent width predicted by the final model is by two orders of magnitude weaker than the observed. However, this disagreement does not necessarily jeopardize the results of the analysis in the present work, because the radial velocity of $S(0)$ line implies that the line may be formed in an extra component above the photosphere.

The C/O ratios derived for the three stars are pretty consistent with the scenario in which addition of ^{12}C synthesized in the thermal pulse turns K and M giants to N-type carbon stars. Even for V Aql, in which the largest discrepancy of the C/O ratio is found, the $^{12}C/^{13}C$ ratio and C/O ratio can be well understood by this simple picture of carbon star formation. As we have focused on the investigation of the effects of model atmospheres in the present work, the number of stars analyzed is never enough to discuss the scenario statistically. However, it has been shown that the re-analysis for rest of the program stars of Lambert et al. (1986) should be also done in order to obtain accurate information on the chemical composition of carbon stars. Nitrogen abundance, which is not derived in the present work, should be also determined, since its possible changes might mean the operation of nuclear processes other than the thermal pulse.

References

Aaronson M., Mould J., 1980, ApJ 240, 804

Allen C.W., 1973, Astrophysical Quantities, 3rd ed., Athlone London, p.209

Blöcker T., Schönberner D., 1991, A&A 244, L43

Catchpole R.M., Feast M.W., 1985, In: Cool Stars with Excess of Heavy Elements, eds, Jaschek M., and Keenan P.C., Reidel Dordrecht Holland, p.113

Cerny D., Bacis R., Guelachvili G., Roux F., 1978, J. Mol. Spectrosc. 73, 154

Chackerian C.,Jr., Tipping R.H., 1983, J. Mol. Spectrosc. 99, 431

Dean C.A., 1976, AJ 81, 364

Douay M., Nietmann R., Bernath P.F., 1988, J. Mol. Spectrosc. 131, 250

Guelachvili G., de Villeneuve D., Farranq R., Urban W., Verges J., 1983, J. Mol. Spectrosc. 98 64

Frogel J.A., Mould J., Blanco V.M., 1990, ApJ 352, 96

Frogel J.A., Cohen J.G., 1982, ApJ 253, 580

Hall D.N.B., Ridgway S.T., Bell E.A., Yarbrough J.M., 1979, Proc. Soc. Photo-Opt. Instrum. Engineers 172, 121

Iben I.,Jr., 1981, ApJ 246, 278

Johnson H.R., Bower C.D., Lemke D.A., Luttermoser D.G., Petrakis J.P., Reihart M.D., Welch K.A., Alexander D.R., Goebel J.H., 1985, ApJ 292, 228

Jørgensen U.G., Johnson H.R., Nordlund Å., 1992, A&A 261, 263

Lambert D.L., Gustafsson B., Eriksson K., Hinkle K.H., 1986, ApJS 62, 373

Lazáro C., Hammersley P.L., Clegg R.E.S., Lynas-Gray A.E., Mountain C.M., Zadrozny A., Selby M.J., 1994, MNRAS 269, 365

Norton R.H., Beer R., 1976, J. Opt. Soc. Am. 66, 259

Ohnaka K., Tsuji T., 1996, A&A 310, 933

Pritchet C.J., Richer H.B., Schade D., Crabtree D., Yee H.K.C., 1987, ApJ 323, 79

Smith V.V., Lambert D.L., 1985, ApJ 294, 326

Smith V.V., Lambert D.L., 1990, ApJS 72, 387

Tsuji T., 1986, A&A 156, 8

Utsumi K., 1985, In: Cool Stars with Excesses of Heavy Elements, eds, Jaschek M., Keenan P.C., Reidel, Dordrecht, Holland, p.243

Vassiliadis E., Wood P.R., 1993, ApJ 413, 641

Chapter 6

Analysis of the CO First Overtone Bands – Probing the Upper Photosphere of Carbon Stars

Abstract

We present analysis of the CO first overtone bands in three carbon stars, TX Psc, BL Ori, and V Aql, based on high-resolution spectra. We first examine whether the models with the abundances and micro-turbulent velocities derived from lines of the CO second overtone bands and the C_2 Phillips system can reproduce the lines of the CO first overtone bands. The moderately strong lines, which have relatively high excitation potentials, can be reproduced. But it has been revealed that the low excitation lines (χ < 5000 cm^{-1}) show excess of absorption for TX Psc and V Aql. The intensity anomalies of the low excitation lines should be attributed to the large width of these lines, not to the depths.

We have carried out numerical experiments of the depth-dependent turbulent velocity hypothesis to see if it can reproduce such intensity anomalies. The observed intensities of the anomalous lines can be well reproduced by introducing the micro-turbulent velocity about 10 km s^{-1} in several upper layers of the models. However, the hypothesis completely fails to reproduce the line profiles near the (2,0) bandhead. Therefore, this solution cannot be accepted to explain the absorption excess of the low excitation lines.

Such excess might suggest the existence of molecular formation zone above the photosphere, though it still remains unclear whether such region is well separated from the photosphere or not. In any case the region with excitation temperature between 1000 and 2000 K is required to explain the anomalous intensities of the low excitation lines. Besides, it has turned out that the bandhead of (2,0) transition observed in V Aql can not be reproduced even with the extra molecular zone considered. An extra component with excitation temperature more than 2000 K is required to reproduce the observation, while the surface temperature of the photospheric model is 1090 K. This implies that at least two components with different temperatures might coexist in the upper photosphere of V Aql.

6.1 Introduction

Mass loss is one of the major characteristics of stars at the asymptotic giant branch (AGB) and believed to be closely related to stellar evolution at the late stage. With the onset of mass loss, stars become surrounded by the circumstellar envelope. Many observations of the outer atmosphere and the circumstellar envelope of AGB stars have been done to derive mass loss rate, terminal outflow velocity, excitation temperature, column density, etc., in various spectral regions from ultraviolet to radio domain.

Infrared spectrophotometry for AGB stars (e.g. Merrill & Stein 1976a, 1976b, 1976c) revealed the existence of dust grains as well as gaseous molecules in circumstellar envelopes. The low resolution spectra (LRS) acquired by the IRAS also brought valuable information on the nature of circumstellar envelopes around AGB stars for a large sample. The emission feature of silicate dust at 9.8 μm is observed for oxygen-rich stars, while emission of silicon carbide dust at 11.3 μm is observed for carbon stars, except for peculiar carbon stars showing the silicate emission despite their carbon-rich photospheres (Willems & de Jong 1986, Little-Marenin 1986). The radio observations for various molecular lines have served to derive the kinematics in the circumstellar envelope. The terminal velocities range from 10 km s^{-1} to 30 km s^{-1}, while the mass loss rates range from 10^{-7} to 10^{-5} $M_{\odot}$/yr (e.g. Netzer & Elitzur 1993, and references cited therein). These observations have revealed that the stellar wind in cool luminous stars is slow and massive, and that dust formation is associated with the circumstellar envelope. The observations by the International Ultraviolet Explorer (IUE) revealed the variability of fluxes of the emission lines such as due to Mg II, C II, and Fe II by a factor of 5 to 8 (Querci & Querci 1985, Johnson et al. 1986), which implies that the real chromospheres might be spatially inhomogeneous and temporally variable.

Considerable progress has also been made in recent years in constructing models of the circumstellar envelope which well reproduce observational data such as spectral energy distribution (SED), terminal velocity, and mass loss rate. For example, Keady et al. (1988) and Ridgway & Keady (1988) constructed an empirical model of the circumstellar envelope of IRC+10216, which is so far the brightest carbon-rich object in infrared, based on the line profiles of molecular species in a high-resolution spectrum around 10 μm.

Despite the progress so far both in observations and in theoretical works, the mechanism of mass loss has been left unclear. The observed outflow velocities are smaller than the escape velocity at the stellar surface, which is roughly 50 – 60 km s^{-1} (Reimers 1977). Thus, though this can be said for all classes of cool luminous stars, the stellar wind in AGB stars should originate somewhere between the outer atmosphere and the circumstellar envelope. And where and how the stellar wind starts is the very problem which has kept us from understanding the mechanism of mass loss.

Radiation pressure on dust grains is currently considered to be the driving force of stellar wind in cool luminous stars. Especially for Mira variables, the levitation of atmosphere by the stellar pulsation with large amplitude can provide with a physical condition favorable for the grain formation. Recent theoretical works which include detailed processes of grain formation as well as hydrodynamics have shown that the radiation pressure on dust grains can reproduce the slow and massive outflow in C-rich Mira variables (Fleischer et al. 1992, Winters et al. 1994). However, it still remains to be clarified whether the pulsation can levitate the stellar atmosphere high enough for the grain formation to be possible in semi-regular or irregular variables, since the amplitudes are much smaller than in Mira variables. The dust formation may not initiate mass outflow, but only a result of mass loss.

To understand the mechanism of mass loss, it is indispensable to clarify the physical condition and chemistry in the outer atmosphere or in the inner-circumstellar envelope which serves as the boundary condition to the circumstellar envelope. Lines of the CO first overtone bands provide us with an opportunity to probe the upper photosphere, since these lines are formed in shallow layers because of their optical thickness. Especially, low excitation lines in M giants show intensity anomalies and served to recognize the extra component above the photosphere (Tsuji 1988). We analyze lines of the CO first overtone bands in the three stars for which elemental abundances of carbon and oxygen have been derived in the previous Chapter, together with micro- and macro-turbulent velocities.

6.2 Peculiar behavior of low excitation lines

6.2.1 Breakdown of the standard analysis

The spectra analyzed in this Chapter are identical with described in the previous Chapter. The line list of CO is also the same with used in the analysis described in the previous Chapter.

Since not all of the CO first overtone lines show intensity anomalies in the case of M giants (Tsuji 1988), we first apply the standard analysis (see 5.5.1) of abundance determination in order to see if the lines of the CO first overtone bands can be fitted by the parameters determined from the CO second overtone lines and the C_2 Phillips system lines. In Figs. 6.1, 6.2, and 6.3, the corrections to the abundance of CO, δ(CO), are plotted against $X = \log(W/\omega) + 6.0$ for the lines of the CO first overtone bands together with those of the CO second overtone bands. The corrections to CO abundance are calculated based on the final models which are computed with the abundances of carbon and oxygen derived in the previous Chapter. Though we show the case of the plane parallel models in the figures, the situation has turned out to be also the same in the case of the spherical models. The corrections for the second overtone lines are scattered around $\delta(\mathrm{CO}) = 0$, therefore, it is again confirmed that the oxygen abundances derived by the use of the grid of model atmospheres are self-consistent results. The first overtone lines of moderate strength are also fairly fitted by the final models for all the three stars. However, the strongest lines of the first overtone show marked deviations especially in TX Psc and V Aql. As can be seen in the figures, the deviations of the strongest lines cannot be accounted for by adopting different values of micro-turbulent velocity. In fact it is impossible to find a consistent value of micro-turbulent velocity with which the correction δ(CO) would be almost zero for all the lines. Figures 6.1 and 6.3 reveal that the strongest lines show excesses of absorption. This behavior of the strongest lines has been already reported by Tsuji (1986, 1988) in M giants.

The intensity anomalies mentioned above are found only for low excitation lines. In order to clarify the critical excitation potential, we plot the δ(CO) for each line against lower excitation potential (L.E.P.) of the line in Fig. 6.4. The figure clearly shows that the intensity anomalies are found only in the lines with L.E.P. less than about 5000 cm^{-1}(0.6 eV). The first overtone lines with excitation potentials higher than 10000 cm^{-1} do not show such anomalies even in TX Psc and V Aql. It is also clear that anomalies of low excitation lines are not found in BL Ori, which has relatively high effective temperature 3200 K. This might mean that intensity anomalies of the low excitation lines appear in carbon stars cooler than 3000 K, though the analysis should be done for a larger number of stars.

6.2.2 What is abnormal in the low excitation lines?

To investigate what makes the low excitation lines stronger than predicted by the photospheric models, we characterize strength of a line by two parameters, that is, the central depth and the full width at half maximum (FWHM). In Fig. 6.5, the observed full widths are plotted against their central depths for the lines of the first and second overtone bands. The open circles and squares represent the lines of the second and first overtone bands, respectively. We also calculate a synthetic line profile for each line, and plot the predicted full widths against the central depths in the figure. The filled circles and squares represent such predictions for the lines of the second and first overtone bands, respectively. The synthetic line profiles are computed based on the final model for each star. The differences between the observations and the predictions are shown in Fig. 6.6 as vectors with their tails at the points predicted by the models. Firstly, for the second overtone lines and the first overtone lines of moderate strength, the predicted plots show good agreements with the plots of the observational data. However, the strongest lines, which show the intensity anomalies, exhibit significant deviations from the predictions. It should be noted here that anomalies of the full widths of these lines are responsible for such deviations. The central depths of the strongest lines do not appear to be much larger than predicted. This can be more clearly seen in Fig. 6.6. The vectors representing the differences between the points of the observational data and the predictions run almost vertically upward for the strongest lines. In other words, the low excitation lines with the intensity anomalies have wider widths than predicted by the photospheric models.

6.2.3 Line shift

The intensity anomalies of the low excitation lines suggest that something not included in the present photospheric models exists in the line formation region of these lines. However, the problem lies in the origin of the intensity anomalies – photospheric origin or circumstellar origin. In the former case, the present photospheric models break down in the uppermost layers, where the low excitation lines are formed. If some mechanism to broaden the low excitation lines without giving any effects on the high excitation lines were introduced, all the lines would be consistently analyzed. On the other hand, in the latter case, the photospheric models are expected to be correct from the uppermost layer to the bottom. Some extra components above the photosphere would exist and give rise to the excesses of absorption for the low excitation lines. In this case, we could derive the physical conditions in the extra components from the excesses of absorption.

In the case of M giants, Tsuji (1988) concluded that the intensity anomalies in the low excitation lines of the CO first overtone bands could be attributed to the extra component well separated from the photosphere based on the radial velocities of the lines. He found that the radial velocities of the low excitation lines show significant deviations from those of the high excitation lines of the CO first and second overtone bands. The kinematics of the line formation region of the anomalous lines should be a key to clarify the nature of the absorption excess.

In Figs. 6.7, 6.8, and 6.9, we plot the radial velocities of all the lines, including the first and the second overtone bands, against lower excitation potentials. We have here two definitions of radial velocity: the radial velocity measured at the peak of a line is denoted as V_{P}, while that measured at the midpoint of the FWHM is denoted as V_{M}. We checked the zero point correction of the Fourier transform spectrometer (FTS), because there is a factor which can give slight shift to the recorded wavenumber as mentioned in Tsuji (1988). We measured line positions of several of the well-defined atmospheric lines in the region from 4360 to 4450 cm^{-1}, which is free from stellar CO absorption lines. The result is that the shifts of the atmospheric lines are within 0.2 km s^{-1}.

In the case of BL Ori, the radial velocities of the low excitation lines (L.E.P. < 5000 cm^{-1}) do not seem to be systematically different from those of the high excitation lines, though the scattering of the plots is also large. This is quite logical because the low excitation lines in BL Ori do not show intensity anomalies. In the case of TX Psc, the radial velocities of the low excitation lines do not show significant deviations from those of the high excitation lines. Therefore, we can not say whether the intensity anomalies can be attributed to the upper photosphere or to the circumstellar envelope. However, in the case of V Aql, significant shifts can be seen between the low and high excitation lines. The difference of radial velocities between the high and the low excitation lines amounts to more than 2 km s^{-1}. The negative gradient of radial velocity against L.E.P. such as shown in Fig. 6.9 for V Aql can be interpreted as the result of the granular convective motion at the stellar surface. High excitation lines are favorably formed in warm cells moving upward, resulting in the smaller radial velocity. On the other hand, low excitation lines are formed in cool regions falling downward, showing the larger radial velocity. However, the almost null gradient found in BL Ori and TX Psc cannot be explained by such a granular convection model. The gradient of radial velocity against L.E.P. could be associated with the stellar pulsation. It is necessary to observe possible time variation of radial velocities of the lines in order to clarify the kinematics in the upper photosphere.

6.3 Depth-dependent turbulent velocity hypothesis

In the previous section, it has been revealed that the large widths of the low excitation lines are responsible for the intensity anomalies. The most plausible candidate to broaden the lines is micro-turbulent velocity. In fact, large excess of absorption of strong OH lines was found in α Ori by Lambert et al. (1984), who suggested the possibility of depth-dependent turbulent velocity. In this section, we carry out numerical experiments of the depth-dependent turbulent velocity hypothesis to see if it can reproduce well the intensity anomalies of the low excitation lines.

Firstly, we examine the line formation regions of the low and the high excitation lines. In Fig. 6.10, we show the contribution functions for a high excitation line of the CO first overtone, $4-2$ $R(95)$, and for a low excitation line, $2-0$ $P(9)$. Both of the contribution functions are calculated based on the final model of TX Psc in plane parallel geometry. The figure clearly shows the difference of the line formation regions between the high and the low excitation lines. The high excitation line is formed at the layer about $\log \tau_0 = -3.0$, while the low excitation line at the uppermost layer, $\log \tau_0 = -6.0$. Therefore, if the micro-turbulent velocity is larger near the uppermost layers than in the deeper layers, it is possible to reproduce the large widths of the low excitation lines. However, such large turbulent velocity should be limited to the upper layers, otherwise it would give some effects on the high excitation lines as well. Therefore, we examine the depth-dependence of micro-turbulent velocity such that the values of micro-turbulent velocity is large only at the uppermost layers.

Table 22. Test cases of the depth-dependent micro-turbulent velocity

		$V_{\rm micro}$ in upper layers	Number of layers
TX Psc	Case I	13 km s^{-1}	10
	Case II	15 km s^{-1}	5
	Case III	8 km s^{-1}	20
V Aql	Case IV	8 km s^{-1}	10
	Case V	13 km s^{-1}	5
	Case VI	6 km s^{-1}	20

We characterize the depth-dependency of micro-turbulent velocity by two parameters: the value of the large turbulent velocity and the number of layers where the large turbulent velocity is introduced. We calculate line intensities for the test cases given in Table 22. The micro-turbulent velocity at deep layers is set to the value derived in the abundance analysis for each star, and other model parameters used in the calculations are those of the final model in plane parallel geometry for each star.

The plots of the corrections to the abundance of CO, δ(CO), against the observed equivalent widths are shown in Figs. 6.11 and 6.12 for TX Psc and V Aql, respectively. A glance of Fig. 6.11 reveals that all the lines give a fairly consistent abundance correction in the Case I, where turbulent velocity as large as 13 km s^{-1} is introduced in the uppermost layers from $\log \tau_0 = -6.0$ to -4.0. In the Case II, the strongest lines still show the deviations even with the micro-turbulent velocity as large as 15 km s^{-1}introduced. In this case, the number of layers where the large micro-turbulent velocity is introduced has turned out to be not enough to reproduce the large widths of the strong lines. On the other hand, in the Case III, the large micro-turbulent velocity gives an effect on the moderately strong lines as well as the strongest lines because it is introduced in the deeper layers than in the Case I. Figure 6.12 shows that a fairly consistent abundance correction can be obtained in the Case IV, where the micro-turbulent velocity as large as 8 km s^{-1} is introduced in the layers from $\log \tau_0 = -6.0$ to -4.0. As can be seen in the figure, the Cases V and VI have turned out to be inadequate to reproduce the intensity anomalies of the strongest lines.

We examine the depth-dependent turbulent velocity hypothesis in view of line profiles. In Fig. 6.13 we plot the full widths against the central depths calculated based on the depth-dependency of micro-turbulent velocity given in the Case I for TX Psc. A glimpse of the figure reveals that the anomalously large widths of the strongest lines are well reproduced without giving effects on the weak lines. For V Aql, the plot of the FWHM against the central depths is shown in Fig. 6.14, with the depth-dependency of the Case IV adopted. As can be seen in the figure, the plot of the observed widths against the depths is fairly well reproduced by the calculation based on the depth-dependent micro-turbulent velocity.

We further conduct a test of the depth-dependent turbulent velocity hypothesis using the bandhead of the CO first overtone. Especially, the bandhead of $v = 2 - 0$ transition at 4360 cm^{-1} is salient in the spectra of carbon stars. Therefore we calculate synthetic spectra with the depth-dependent micro-turbulent velocity to see if we can obtain a good match for the $2 - 0$ bandhead. The synthetic spectra predicted by the depth-dependent turbulent velocity are shown in Figs. 6.15 and 6.16 for TX Psc and V Aql, respectively, together with the observed spectra. The spectra are calculated with the depth-dependency of micro-turbulent velocity of the Case I for TX Psc and of the Case IV for V Aql. In both cases, it is clearly seen in the figures that the observed spectra are poorly reproduced. The synthetic spectra appear to be too broad to fit the observed spectra. It has turned out to be impossible to find a depth-dependency to reproduce the observed spectra of the bandhead. This is because the lines near the bandhead are formed in almost the same layers with the strong lines showing the intensity anomalies. In fact, the R-branch of the CO $2 - 0$ transition has the bandhead at $J \sim 50$, and the lines near the bandhead have excitation potentials about 3000 – 7000 cm^{-1}. In Fig. 6.17 we show the contribution functions for the lines near the bandhead. Comparison with Fig. 6.10, where the contribution function for an anomalous line $2-0$ $P(9)$ is shown, reveals that the line formation regions for the lines near the bandhead and for the anomalous line are almost identical. That is exactly why we cannot find a depth-dependency of micro-turbulent velocity which would reproduce the intensity anomalies without giving any effects on the lines near the bandhead.

The numerical tests for the depth-dependent turbulent velocity have shown that it completely fails to reproduce the line profiles near the bandhead at least for the two stars analyzed in the present work. As shown in the following sections, we will obtain a good match near the bandhead between the observed and the synthetic spectrum for TX Psc without introducing a large micro-turbulent velocity in the upper layers. Thus the depth-dependent turbulent velocity hypothesis can be ruled out for TX Psc to explain the intensity anomalies in the strong lines of the CO first overtone bands. On the other hand, for V Aql, we will find that the observed intensity around the $2-0$ bandhead cannot be reproduced by the final model with the standard depth-independent micro-turbulent velocity. However, the radial velocities of the anomalous lines in V Aql show systematic shifts from those of the high excitation lines. This seems to imply the existence of extra components which have the kinematics distinct from that of the photosphere. Therefore the depth-dependent turbulent velocity does not seem to be adequate to explain the anomalous strengths of the strong lines for V Aql, either.

6.4 Separation of the excess absorption

6.4.1 Physical properties of the CO absorption layer

We attempt to separate the contribution of the extra component in the observed absorption to derive their physical properties quantitatively. For M giants such an attempt has been already done by Tsuji (1988), who has derived the physical properties such as excitation temperature, turbulent velocity, and column density. The excess of absorption can be in principle separated if the contribution from the photosphere is well defined. The model atmospheres with the abundances determined from the high excitation lines actually serve to define the contribution from the photospheric component. Then the contribution from the extra component can be evaluated by taking a ratio between the observed spectrum and the photospheric spectrum predicted by the appropriate model atmosphere. In Figs. 6.18 and 6.19 we show such ratioed spectrum of each line for TX Psc and V Aql, respectively. The photospheric spectra are predicted based on the spherical models with the oxygen and carbon abundances derived from the CO second overtone lines and the C_2 Phillips system lines. The stellar mass of 2 $M_{\odot}$ is adopted both for TX Psc and for V Aql. Unlike the case of the M giants analyzed by Tsuji (1988), the profiles of the divided spectra show complicated shapes. It is partly because the observed line profiles are not well defined especially in the wings due to blend of the adjacent lines. In some cases, the divided spectra show emission-like features. Therefore, we cannot recognize systematic trend of radial velocity deviation in TX Psc and V Aql from these figures.

If the absorption excess is large enough, we can measure the equivalent widths by integrating the divided spectra over the relevant spectral interval. The measured equivalent widths are given in Table 23. The measurement of equivalent widths is possible only for six lines in TX Psc and five lines in V Aql. If the extra component above the photosphere is responsible for the absorption excess, we can derive the physical properties such as excitation temperature and column density of CO in the extra component.

Excitation temperature can be determined by plotting $\log(W/gf\omega)$ against L.E.P. as shown in Fig. 6.20. The gradient in the plot of $\log(W/gf\omega)$ against χ gives the reciprocal excitation temperature $\theta_{\rm ex}$, since the equivalent width can be approximately written as $\log(W/\omega) = \log N + \log gf - \chi\theta_{\rm ex} - \log u(T) - \log\omega + {\rm const.}$, where N is the column density of the absorbing gas, χ is the lower excitation potential in eV, and $u(T)$ is the partition function of the absorbing molecule. The excitation temperatures derived for TX Psc and V Aql are 1600 K and 950 K, respectively. The surface temperature of the photospheric model is 1170 K for TX Psc and 1090 K for V Aql. Thus, the extra component in V Aql is considered to lying rather closely to the photosphere. If the excitation temperature derived here were correct for TX Psc, it would mean the existence of temperature inversion above the photosphere. It should be noted here, however, that the determination of excitation temperature described above can be applied only to unsaturated lines. The effect of saturation can be examined by plotting curves-of-growth, which will be discussed in the next paragraph. As will be shown, the curve-of-growth of the absorption excess in TX Psc shows the effect of saturation. If the excitation temperature is determined from somewhat saturated lines, it could be possibly overestimated. Therefore, the excitation temperature in TX Psc does not necessarily mean the existence of temperature inversion.

Column density can be also derived from the equivalent widths by the use of the curve-of-growth. Empirical curves-of-growth are obtained by plotting the observed equivalent widths $\log(W/\omega)$ against $X = \log gf - \chi\theta_{\rm ex} - \log u(T) - \log \omega$. We show such empirical curves-of-growth in Fig. 6.21 for TX Psc and V Aql. As already mentioned, a glance of the curve-of-growth for TX Psc reveals the effect of saturation. The curve-of-growth for V Aql shows little effect of saturation though the scattering of the points plotted is rather large. We can derive column density of the gas causing the absorption excess by comparing these empirical curves-of-growth with the theoretical ones. The theoretical curves-of-growth are obtained by plotting the observed equivalent widths $\log(W/\omega)$ against $X_0 = \log(\pi^{1/2}e^2/mc) + \log N + \log gf - \chi\theta_{\rm ex} - \log u(T) - \log \omega$. Note that the excitation temperatures have been already derived in the previous paragraph. Then the column density can be determined by fitting the abscissa of the empirical and the theoretical curves-of-growth. The column densities derived for TX Psc and V Aql are given in Table 24, together with the excitation temperatures. In both cases, the column densities are as high as 10^{20} cm^{-2}. Such high column densities in extra components have been already recognized in M giants as well by Tsuji (1988). The excitation temperatures of the absorbing gas are also comparable to those derived for M giants. For example, the excitation temperatures of the extra components in SW Vir and RX Boo, both of which have almost the same effective temperatures with TX Psc, are 2163 K and 1151 K, respectively. No stars cooler than $T_{\rm eff}$ = 3000 K were analyzed by Tsuji (1988), but the excitation temperature 950 K for V Aql, can be regarded reasonable, given its effective temperature of 2800 K. However, it is necessary to do the analysis for more stars in order to discuss the physical properties of the CO absorption layer in carbon stars in comparison with M giants.

6.4.2 Molecular hydrogen line

It has been revealed that a huge amount of CO exists above the photosphere. Such a huge amount of molecular gas could give rise to observable effects on other molecular lines. We discuss here the strength of molecular hydrogen line $1-0$ $S(0)$ at 4497.84 cm^{-1}. As already mentioned in the previous Chapter, the molecular hydrogen lines have been used to test model atmospheres, but the equivalent width of $S(0)$ line predicted for V Aql by our model atmosphere has turned out to be by two orders of magnitude smaller than observed. However, the radial velocity of $S(0)$ line in V Aql is 43 km s^{-1} and is consistent with those of the strong CO lines. Thus it is implied that $S(0)$ line is also formed in the extra molecular component above the photosphere. It is quite logical that the origin of the molecular hydrogen line is also circumstellar, given the huge column density derived for CO. We estimate the equivalent width of $S(0)$ line by $\log(W/\omega) = \log(\pi^{1/2}e^2/mc) + \log N_{\rm H_2} + \log gf - \chi\theta_{\rm ex} - \log u(T) - \log \omega$. The gf-value of $1-0$ $S(0)$ line, $gf = 2.34 \times 10^{-14}$, was used by Lambert et al. (1986) based on the ab initio calculation by

Table 23. Equivalent widths of the absorption excesses

TX Psc			
Wavenumber (cm^{-1})	Transition	L.E.P. (cm^{-1})	$\log(W/\omega)$
4168.807	4 - 2 $R(3)$	4282.712	-4.92
4183.264	3 - 1 $P(6)$	2223.272	-4.56
4267.543	2 - 0 $R(1)$	3.845	-4.38
4278.235	2 - 0 $R(4)$	38.448	-4.23
4286.612	3 - 1 $R(28)$	3686.120	-4.42
4348.179	2 - 0 $R(33)$	2149.381	-4.21
V Aql			
Wavenumber (cm^{-1})	Transition	L.E.P. (cm^{-1})	$\log(W/\omega)$
4222.955	2 - 0 $P(9)$	172.978	-4.44
4328.879	2 - 0 $R(22)$	971.233	-4.59
4333.051	2 - 0 $R(24)$	1151.315	-4.78
4336.935	2 - 0 $R(26)$	1346.601	-4.51
4345.339	2 - 0 $R(31)$	1901.131	-4.97

Table 24. Physical properties of extra components

Star	T_{ex} (K)	$\log N_{CO}$ (cm^{-2})
TX Psc	1600	20.6
V Aql	950 $\pm$150	19.9

Turner et al. (1977). The excitation temperature of H_2 line is unknown. But as the L.E.P. of $S(0)$ line is 0 eV, it is not necessary to obtain the excitation temperature to estimate the equivalent width. The partition function $\log u(T)$ does not show a strong temperature dependence. For example, $\log u(T = 1000\mathrm{K}) = 0.7$ and $\log u(T = 1500\mathrm{K}) = 0.9$. Since the discrepancy of the equivalent width between the observation and the prediction is about two orders of magnitude, such temperature dependence of the partition function does not cause serious effects on the discussion here. The column density of H_2 molecule can be estimated from that of CO. The ratio of the partial pressure of molecular hydrogen to that of CO is about $10^3 - 10^4$ at the relevant temperature and gas pressure, according to the chemical dissociation equilibrium. Therefore we tentatively adopt the column density $N(\mathrm{H_2}) = 10^{23}$ cm^{-2}. Then the predicted equivalent width is $\log(W/\omega) = -6.3$, which is still smaller than the observed value -5.111. However, with higher column density $N(\mathrm{H_2}) = 10^{24}$ adopted, we obtain $\log(W/\omega) = -5.3$. Though it is not clear whether such high H_2/CO ratio can be realized at the relevant temperature and the gas pressure, the rough estimate here suggests that the molecular hydrogen line can be formed in the extra component.

6.5 The more peculiar behavior of the CO bandhead

The absorption excesses of the strong CO lines can be attributed to the extra component with relatively low temperature and quite high column density. However, we have found that such a simple picture cannot necessarily explain all the spectral features observed. We have already discussed the spectrum synthesis around the CO $2-0$ bandhead at 4360 cm^{-1}, and we do it here again.

We show the synthetic spectra around the $2-0$ bandhead for TX Psc in Fig. 6.22. The synthetic spectrum is calculated by the final spherical model for the star. We also show the ratioed spectrum, that is, the observed spectrum divided by the predicted. A glance of Fig. 6.22 clearly shows that the observed spectrum of TX Psc is fairly well reproduced by the predicted one, except for the region where telluric lines are located. However, a close look at the divided spectrum reveals the absorption excesses at the line positions of CO indicated by the ticks. The R-branch of CO $2-0$ transition has a turning point at $J = 51$. So the absorption features seen in Fig. 6.22 consist of a pair of lines with high J and low J. The positions of the absorption excesses agree well with those of the low excitation lines, which is consistent with the discussion in the previous section.

On the other hand, the comparison between the predicted and the observed spectra of V Aql shows a quite different situation as can be seen in Fig. 6.23. The observed strength of absorption features is much weaker than predicted, which is clearly seen in the divided spectrum. However, this disagreement should not be taken as an evidence against the validity of the model atmospheres used in the analysis. In fact, no model atmosphere with the relevant effective temperature can reproduce such weak absorption features near the bandhead. For example, the synthetic spectrum predicted by the model with $T_{\rm eff}$ = 2600 K shows even stronger absorption, because the surface temperature is even cooler than the model with $T_{\rm eff}$ = 2800 K. Even with a model atmosphere with $T_{\rm eff}$ = 3000 K, the absorption of the bandhead cannot be reproduced. Therefore, Fig. 6.23 implies the existence of emission for the lines near the bandhead. Especially the peak of each emission-like feature in the divided spectrum is located at the position of the low excitation lines. This can be clearly seen in the features in which the separation between high J and low J lines is relatively large. Thus, it can be said that the absorption near the bandhead might be filled by the emission from an extra component. The temperature of such an extra component should be higher than that of the surface layer, which is 1090 K in the spherical model for V Aql. It should be more than 2000 K for the CO lines near the bandhead at 2.2 μm to be observed as emission. It shows a remarkable contrast to the existence of the cool component implied by the absorption excess of the low excitation lines. Therefore, a simple picture in which the cool molecular component is lying over the photosphere might not be justified at least for V Aql.

We have classified the low excitation lines as the lines of which excitation potentials are smaller than 5000 cm^{-1}. Of course the criterion between high and low excitation lines is somewhat arbitrary. In fact, the first overtone lines of which excitation potentials range from 3000 to 7000 cm^{-1} are not used in the analysis. Such lines are exactly the lines near the bandhead, therefore, they are not suitable for the line-by-line analysis.

The emission filling the absorption features near the bandhead implies that the extra component should be warm enough to excite the lines of which L.E.P. are about 5000 cm^{-1}. Such a component could also produce emission for the lines with L.E.P < 3000 cm^{-1}. As already shown in the previous section, however, the lines with L.E.P. less than 3000 cm^{-1} show the absorption excess. Therefore, the area of the warm component might be smaller than that of the cool component. Otherwise, the contribution of the warm component might be significant in the lines with L.E.P. < 3000 cm^{-1}, and the absorption excess would be filled by the emission from the warm component. However, it is possible that the low excitation lines might appear to be weaker in the warm component because of the decrease of level population. Therefore, the ratio of the areas of the two components should be further investigated. If the low excitation lines discussed in the previous section are somewhat filled by such emission from the warm component, the measured equivalent widths of the absorption excess might be underestimated. The column density of the absorbing CO might have been also underestimated. If the column density is somewhat higher than the derived in the previous section, the column density of H_2 might be also higher. With higher column density of H_2, the observed equivalent width of H_2 $1-0$ $S(0)$ line might be reproduced.

The warm component might be associated with the chromosphere. In the case of the Sun, it has been revealed that the chromosphere has inhomogeneous structure. Ayres (1986) showed that the CO lines originate in the cool component of inhomogeneities in the upper photosphere based on the observation of high-spatial resolution. Solanski et al. (1994) confirmed this by the high-resolution observation of the CO fundamental bands toward the solar limb: the absorption turns to the emission beyond the limb. Such inhomogeneities in the upper photosphere are also revealed for stars other than the Sun. The high spectral resolution observation of the CO fundamental bands in α Boo cannot be reproduced by the homogeneous chromospheric model which can explain Ca II H and K lines (Heasley et al. 1978). Inhomogeneities in the upper photosphere of carbon stars are also suggested by Jørgensen & Johnson (1991) based on the synthetic spectra of CO from photospheric and semi-empirical chromospheric models. The weakness of the low excitation lines has been already reported for V Hya by Lambert et al. (1986), who found that the low excitation lines of the CO first overtone bands give a markedly lower oxygen abundance. The emission filling the strong lines might be responsible for the lower abundance. The effective temperature of V Hya is also expected to be quite cool, maybe less than 2800 K. It is essential to do the same analysis for more stars to clarify whether the emission filling the absorption near the bandhead is a common phenomenon in stars cooler than 2800 K. And the CO fundamental bands will provide us with a good opportunity to investigate further the extra components above the photosphere.

6.6 Concluding remarks

We have analyzed the CO first overtone bands for three stars, BL Ori, TX Psc, and V Aql in order to investigate the physical conditions in the upper photosphere. The standard analysis used in the previous Chapter was applied, and we could not find a value of micro-turbulent velocity with which all the lines would give a consistent abundance of CO. The low excitation lines have been found to show intensity anomalies, that is, they are stronger than predicted by the model atmosphere with the parameters appropriate for each star. We have found that the widths of the strong lines are much larger than predicted, while the depths are fairly well reproduced by the model atmospheres.

The analysis of line shifts has revealed that the radial velocities of the low excitation lines are shifted by about 2 km s^{-1} from those of the high excitation lines in V Aql. Thus the intensity anomalies of the low excitation lines can be attributed to an extra component which has the kinematics distinct from the photosphere. In the case of TX Psc, we could not find any considerable dependence of radial velocity on excitation potential. We could not say at this step whether the intensity anomalies originated from the photosphere or an extra component.

To clarify the origin of the intensity anomalies, we have done tests for the depth-dependent turbulent velocity hypothesis. The micro-turbulent velocity as large as 13 km s^{-1} (TX Psc) or 8 km s^{-1} (V Aql) only in the upper layers has been successful in reproducing the intensity anomalies of the low excitation lines. However, it has turned out that such a hypothesis completely fails to reproduce the line profiles near the $2-0$ bandhead. Thus the depth-dependent turbulent velocity cannot be accepted to explain the intensity anomalies at least for the stars analyzed in the present work.

The intensity anomalies can be rather attributed to extra components lying above the photosphere. With the abundances determined from the CO second overtone lines and the C_2 Phillips system lines, we calculated the synthetic spectra which serve to define the photospheric contribution and separated the contribution from the extra component. The excitation temperatures and the column densities derived from the equivalent widths of the absorption excess imply the existence of cool component with CO column density as high as 10^{20} cm^{-2}. However, in the case of V Aql, the structure of the extra component might be more complicated. We have found the lines near the $2-0$ bandhead are filled by emission, which implies the existence of a warm component as well as the cool component.

To clarify the nature of the extra components, the analysis should be done for more stars. It will clarify the critical effective temperature for the absorption excess to become significant. The analysis of the stars even cooler than V Aql is essential to see if the emission is more remarkable in cooler stars. The analysis of lines of the CO fundamental bands is also promising to investigate the physical conditions in the upper atmosphere, since those lines are considered to be formed in even upper layers than the first overtone lines. Such analysis is important to construct comprehensive models from the photosphere to the circumstellar envelope, because the upper atmosphere actually serves as the boundary condition to the circumstellar envelope.

References

Ayres T.R., Testerman L., Brault J.W., 1986, ApJ 304, 542
Fleischer A.J., Gauger A., Sedlmayr E., 1992, A&A 266, 321
Heasley J.N., Ridgway S.T., Carbon D.F., Milkey R.W., Hall D.N.B., 1978, ApJ 219, 970
Keady J.J., Hall D.N.B., Ridgway S.T., 1988, ApJ 326, 832
Johnson H.R., Baumert J.H., Querci F., Querci M., 1986, ApJ 311, 960
Jørgensen U.G., Johnson H.R., 1991, A&A 244, 462
Lambert D.L., Brown J.A., Hinkle K.H., Johnson H.R., 1984, ApJ 284, 223
Lambert D.L., Gustafsson B., Eriksson K., Hinkle K.H., 1986, ApJS 62, 373
Little-Marenin I.R., 1986, ApJ 307, L15
Merrill K.M., Stein W.A., 1976, PASP 88, 285
Merrill K.M., Stein W.A., 1976, PASP 88, 294
Merrill K.M., Stein W.A., 1976, PASP 88, 874
Netzer N, Elitzur M., 1993, ApJ 410, 701
Querci M., Querci F., 1985, A&A 147, 121
Reimers D., 1977, A&A 57, 395
Ridgway S.T., Keady J.J., 1988, ApJ 326, 843
Tsuji T., 1986, A&A 156, 8
Tsuji T., 1988, A&A 197, 185
Turner J., Kirby-Docken K., Dalgarno A., 1977, ApJS 35, 281
Willems F.J., de Jong T., 1986, ApJ 309, L39
Winters J.M., Fleischer A.J, Gauger A., Sedlmayr E., 1994, A&A 290, 623

Chapter 7

Conclusion

The goal of the present work was to obtain the chemical composition in carbon stars as accurately as possible. The analyses presented in this thesis have been triggered by the discrepancy of $^{12}C/^{13}C$ ratios, which is discussed in Chapter 2. In fact, the disagreements of photospheric abundances have been reported especially for cool stars such as carbon stars and M giants. We have done re-analysis of the spectra of carbon stars from which the chemical composition widely referred was derived. We have also developed a new code of spherical model atmosphere of carbon stars and examined them in comparison with the observations.

The most remarkable result of the present work is that carbon stars are more carbon-rich than considered from the previous analysis. Our analysis has shown that the C/O ratios are 1.1, 1.4, and 2.4 in TX Psc, BL Ori, and V Aql, respectively. This result shows a marked contrast to what has been widely believed, that is, C/O ratios in majority of carbon stars are less than 1.1. The effect of atmospheric structure which brought about the discrepancy of $^{12}C/^{13}C$ ratios has been found to be considerable in the analysis of the elemental abundances as expected.

We have tested our model atmospheres in several ways, since the reliability of the results of the abundance analysis is dependent on the validity of the model atmospheres. Our model atmospheres are constructed with molecular line opacities incorporated by the Band Model method. It has turned out that our model atmospheres well reproduce the temperature stratifications of the models calculated with the OS method, which are actually the state-of-the-art models. Our model atmospheres can also reproduce the 3 μm absorption observed toward SS Vir with the ISO SWS. But the spectrum longward about 5 μm seems to be contaminated by the contribution from the circumstellar envelope. The final models of TX Psc and V Aql were examined using the spectrophotometric data, and the result of the test was fairly satisfactory. We also attempted to test the model atmospheres by the lines of H_2. It has been revealed, however, that $1-0$ $S(0)$ line of H_2 cannot serve to test model atmospheres, because it is probably formed in the extra component of which existence has been implied by the analysis of the CO first overtone bands.

The discrepancy of the $^{12}C/^{13}C$ ratios and C/O ratios should be attributed not only to the model atmospheres used in the analyses but also to the treatment of the excitation effect. Our analysis has been done in a self-consistent way with the excitation effect properly taken into account by solving radiative transfer for each spectral line. Coarse analyses employing a single excitation temperature cannot be applied to carbon stars because of the sensitive dependence of atmospheric structure of carbon stars on the chemical composition.

The C/O ratios derived in the present work can be very consistently interpreted by a simple picture of carbon star formation. We have shown, at least for the three carbon stars studied, that the C/O ratios and $^{12}C/^{13}C$ ratios we analyzed can be explained by the addition of the freshly synthesized ^{12}C into the stellar surface of K and M giants. To confirm the scenario of carbon star formation, it is necessary to re-analyze the spectra for a larger sample. The re-analysis for the rest of program stars should be done in the way described in the present work.

The analysis of the CO first overtone bands has revealed the existence of extra component(s) above the photosphere in two carbon stars, TX Psc and V Aql. Low excitation lines of CO show intensity anomalies: the observed absorption lines are stronger than predicted from the photospheric models which are calculated with the chemical compositions derived by the self-consistent analysis. We have shown that such anomalous lines are far wider than predicted while their depths are fairly reproduced by the photospheric models.

We have carried out numerical experiments of the depth-dependent turbulent velocity hypothesis to see if it can reproduce the intensity anomalies of the low excitation lines. We could find the depth-dependency of micro-turbulent velocity which can reproduce the intensity anomalies, but it totally fails to reproduce the line profiles near the bandhead. The depth-dependent turbulent velocity hypothesis was ruled out for TX Psc and V Aql. The intensity anomalies might be attributed to a cool component above the photosphere. Especially for V Aql, the radial velocities of the anomalous lines show deviations from those of high excitation lines, and this fact supports the existence of an extra component kinematically distinct from the photosphere. The excitation temperature of the extra component is derived to be 1000 – 2000 K and the column density of CO amounts up to 10^{20} cm^{-2}.

However, further analysis for V Aql has revealed that such a simple picture might not be justified for this star. The observed strength of the $2-0$ bandhead is weaker than predicted, which is the very opposite to the case of the low excitation lines. We have suggested that the outer atmosphere of V Aql might consist of two components with different temperatures – warm and cool components. But a comprehensive picture of the structure of the outer atmosphere could not be presented in the present work. To solve this problem, the analysis of other molecular lines will be indispensable. Especially, lines of the CO fundamental bands will be one of the best probes to obtain information on the even outer atmosphere. The analysis of lines of HCN and C_2H_2 at 14 μm is also of great interest, and such observations are already possible by the ISO. With such analyses and theoretical works put together, a unified picture from the photosphere to the circumstellar envelope in carbon stars is expected to be obtained in the future.

Acknowledgments

Firstly, I thank Prof. T. Tsuji for introducing me carbon stars and for leading my researches with continuous encouragement during the works over five years. Without his guide, this thesis could not have been completed and I could not have reached this final part of it. I would like to thank Dr. K. H. Hinkle at the Kitt Peak National Observatory, who kindly made me available the archived FTS data, without which this thesis could have been nonexistent. I am also grateful to Dr. K. Noguchi, who provided with his valuable photometric data of carbon stars and even did new observations for the stars of which photometric data had not been acquired. I thank Prof. M. Scholz for his precious advice on the code of spherical model atmosphere and for his kind help in checking the newly developed models. I also appreciate the hospitality of the people at the Institut für Theoretische Astrophysik, Universität Heidelberg, during my visit. It was realized by the kind help of Prof. M. Iye. Thanks should be also given to Profs. T. Onaka, H. Ando, T. Kajino, who gave me fruitful suggestions and comments.

I would like to appreciate the support by T. Okada during the observations at the Okayama Astrophysical Observatory. He really made the observing sessions done smoothly by his kind support for the operation of the telescope and the spectrograph. I am also grateful to Dr. I. Yamamura for having done the reduction of the ISO data at Groningen. Finally, I would like to thank my friends for giving me kind of fresh air from time to time.

Figures

Chapter 2

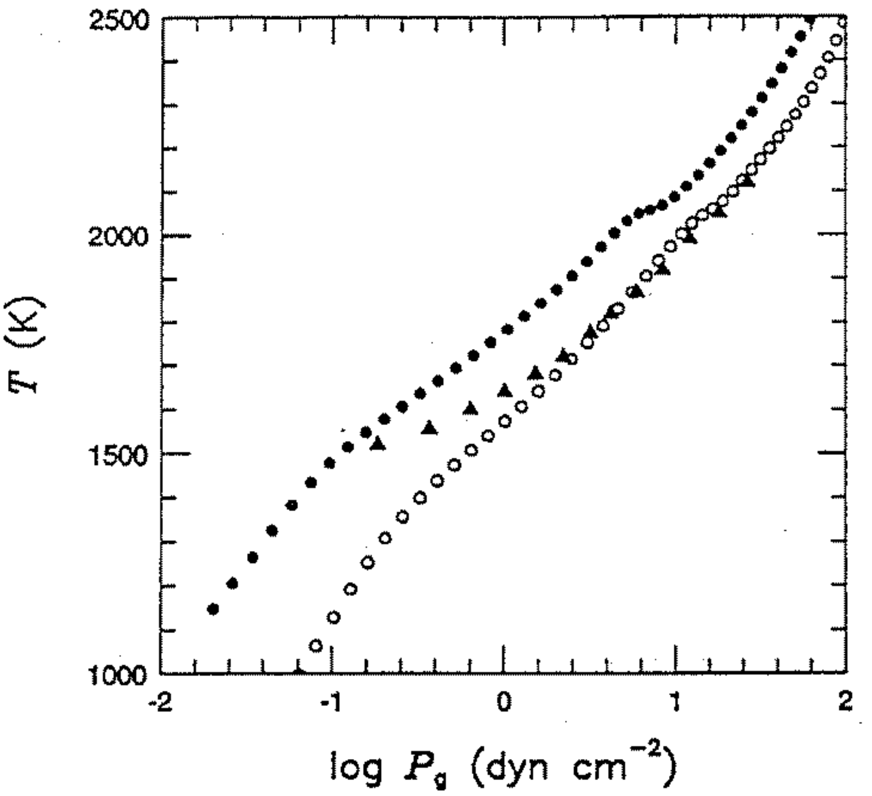

Fig. 2.1. Filled triangles represent a model of Jørgensen et al. (1992). Filled and open circles represent our model atmosphere with turbulent pressure and without it, respectively. Both models are calculated by the same set of parameters, $T_{\rm eff} = 2800$ K, $\log g = 0.0$, and C/O = 1.02

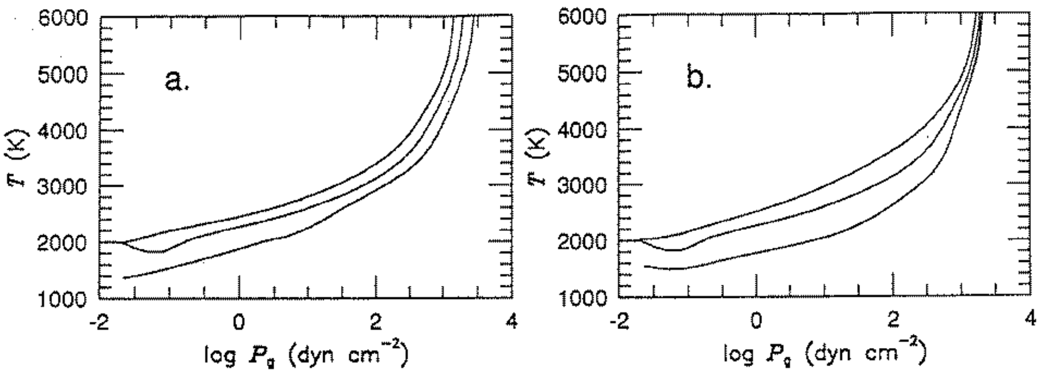

Fig. 2.2. **a** Model atmospheres with different effective temperatures, $T_{\rm eff}$ = 3400, 3000, and 2600 K, from top to bottom. Other parameters are the same for three models: C/O = 1.1, $\log g$ = 0.0, and $V_{\rm micro}$ = 3.0 km s^{-1}. **b** Model atmospheres with different C/O ratios, C/O = 2.0, 1.1, and 1.01, from top to bottom. Other parameters are the same for three models: $T_{\rm eff}$ = 3000 K, $\log g$ = 0.0, and $V_{\rm micro}$ = 3.0 km s^{-1}

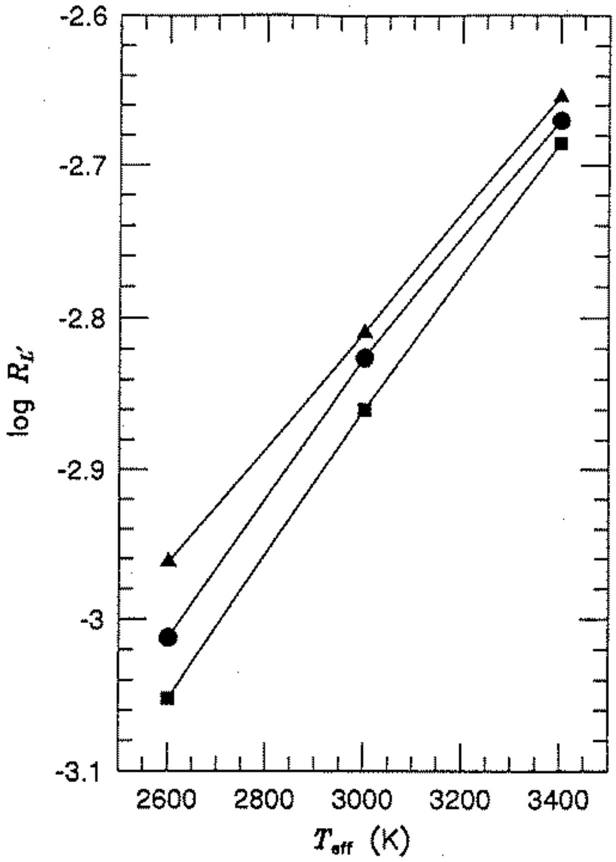

Fig. 2.3. The calibrations of $R_{L'}$ by model atmospheres with different C/O ratios. Filled triangles, filled circles, and filled squares correspond to the model with C/O = 1.01, 1.1, and 2.0, respectively

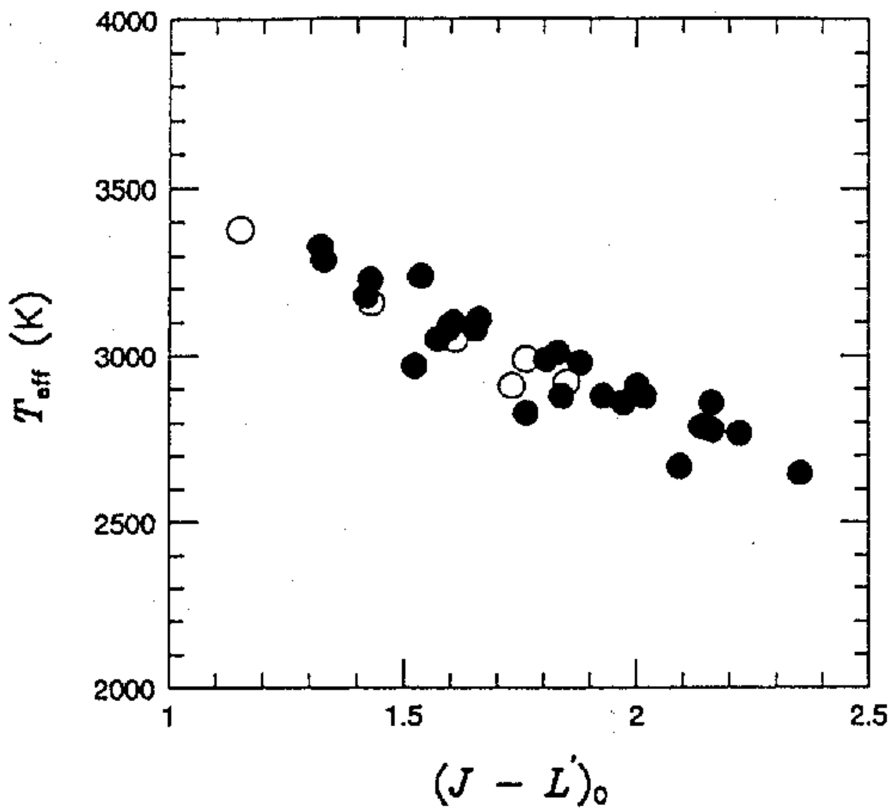

Fig. 2.4. $(J - L')_0 - T_{\rm eff}$ relation. Effective temperatures are determined by the IRFM. Filled circles and open circles represent N-type carbon stars and SC-type carbon stars, respectively

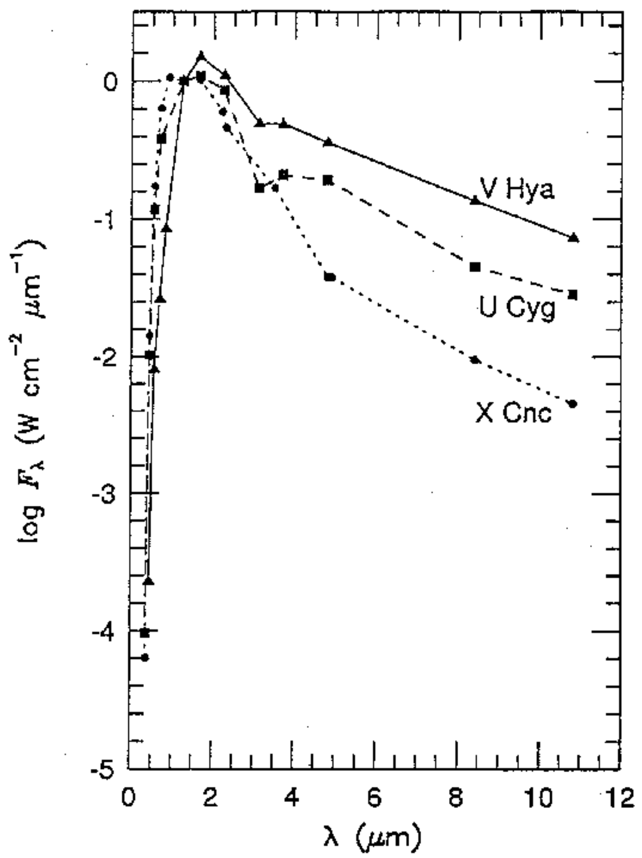

Fig. 2.5. Flux density distributions of V Hya and U Cyg which have excesses in the region longer than 3 μm, and X Cnc for comparison

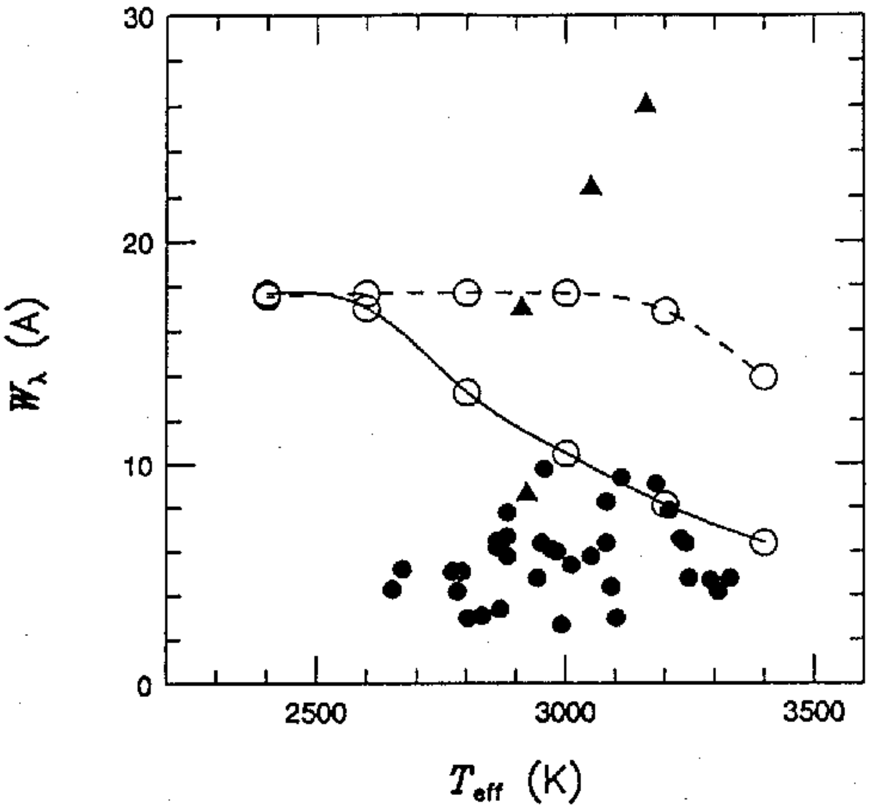

Fig. 2.6. Observed and predicted strengths of Na I D lines. Filled circles and filled triangles represent the strengths of Na I D lines observed in N-type carbon stars and SC-type carbon stars, respectively. Open circles represent the strengths predicted by our model atmospheres with C/O = 1.1 (solid line) and C/O = 1.01 (dashed line). Other parameters of model atmospheres are $\log g = 0.0$ and $V_{\rm micro} = 3.0$ km s^{-1}

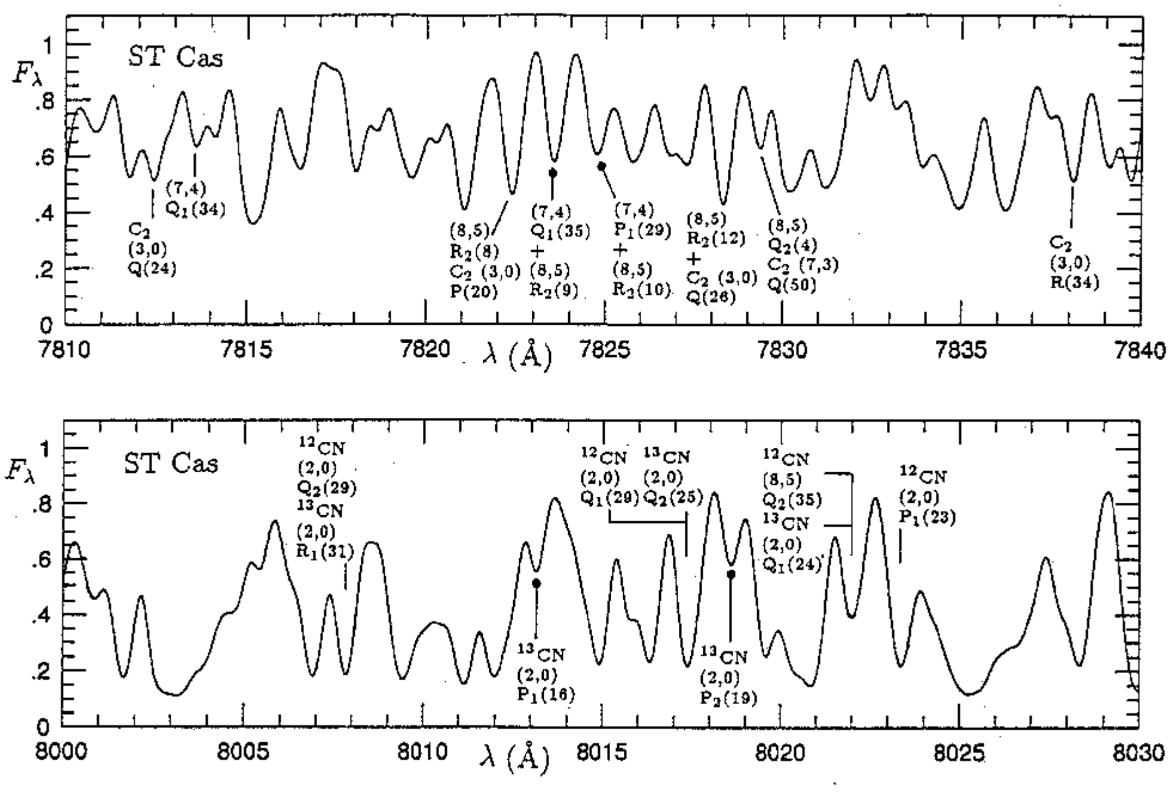

Fig. 2.7. The observed spectra of a normal N-type carbon star, ST Cas. The lines noted by filled circles are used in the analysis

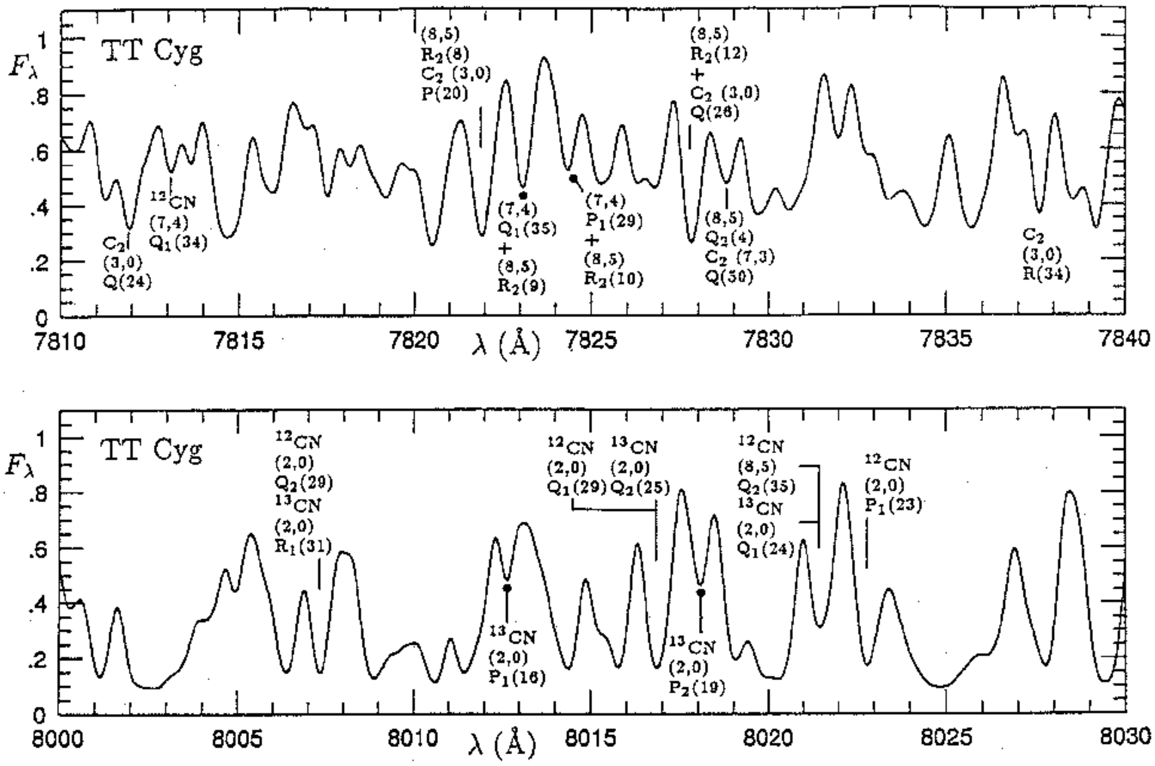

Fig. 2.8. The observed spectra of TT Cyg, which exhibits 60 μm excess. See also the legend to Fig. 2.7

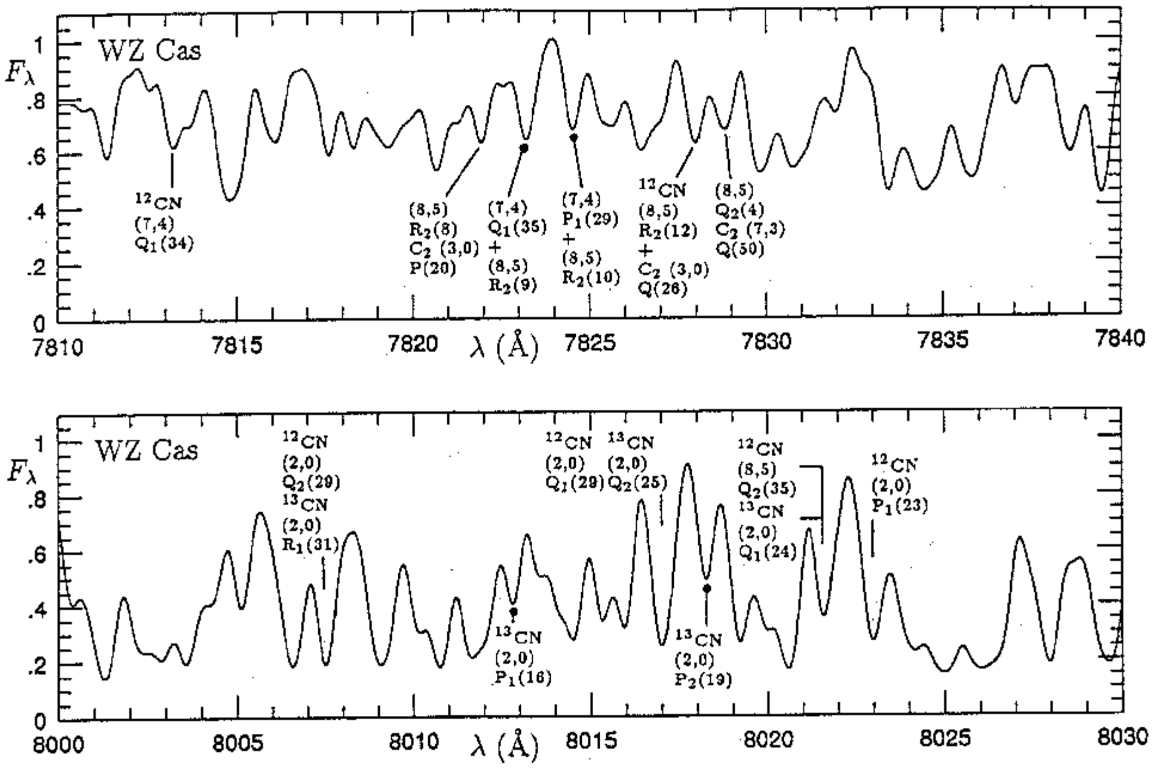

Fig. 2.9. The observed spectra of WZ Cas, which is classified as super Li-rich. See also the legend to Fig. 2.7

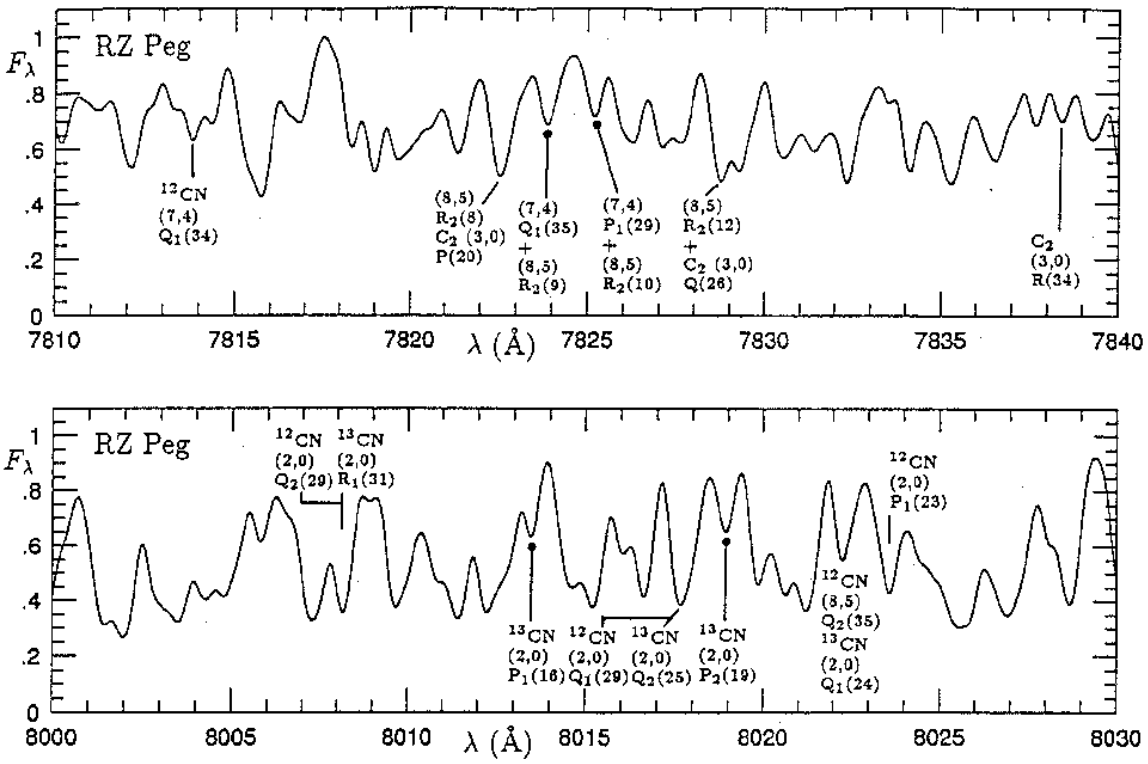

Fig. 2.10. The observed spectra of a normal SC-type carbon star, RZ Peg. See also the legend to Fig. 2.7

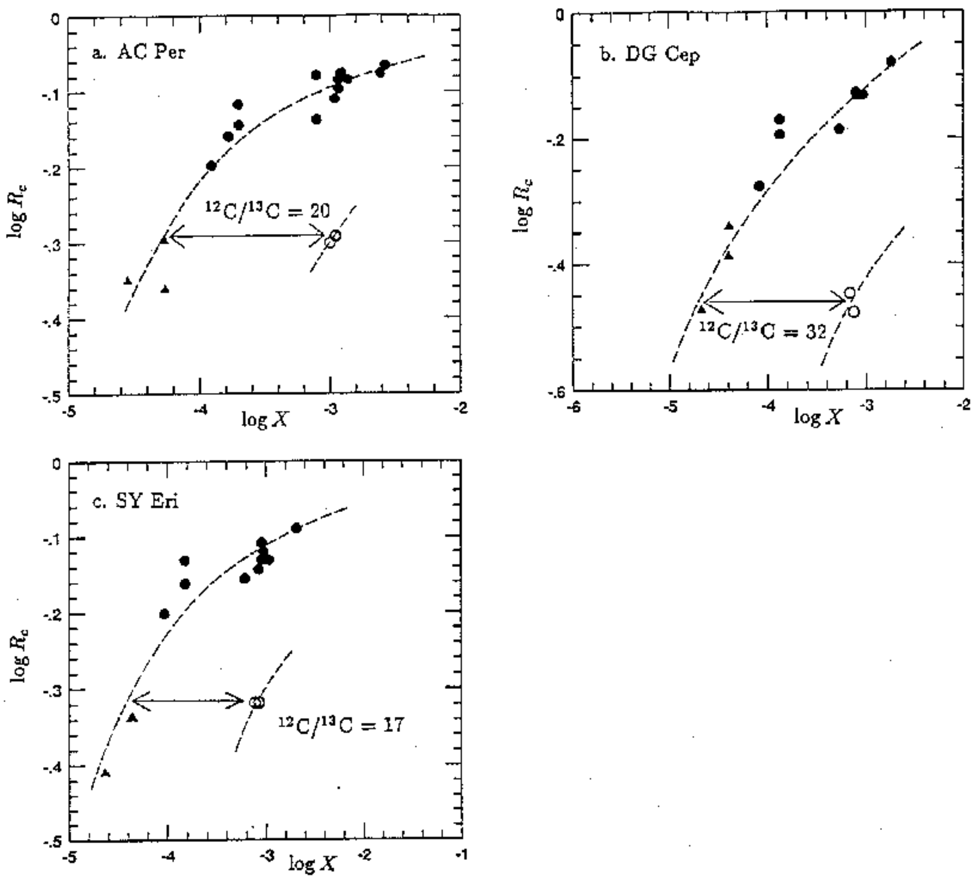

Fig. 2.11. Examples of curves-of-growth of N-type carbon stars. The ordinates are central depths normalized by the fictitious continuum level, and the abscissas are $\log X = \log(gf\Gamma)$. Filled circles represent (2,0) lines and filled triangles represent (7,4) lines of ^{12}CN. Open circles represent (2,0) lines of ^{13}CN: **a** AC Per. **b** DG Cep. **c** SY Eri

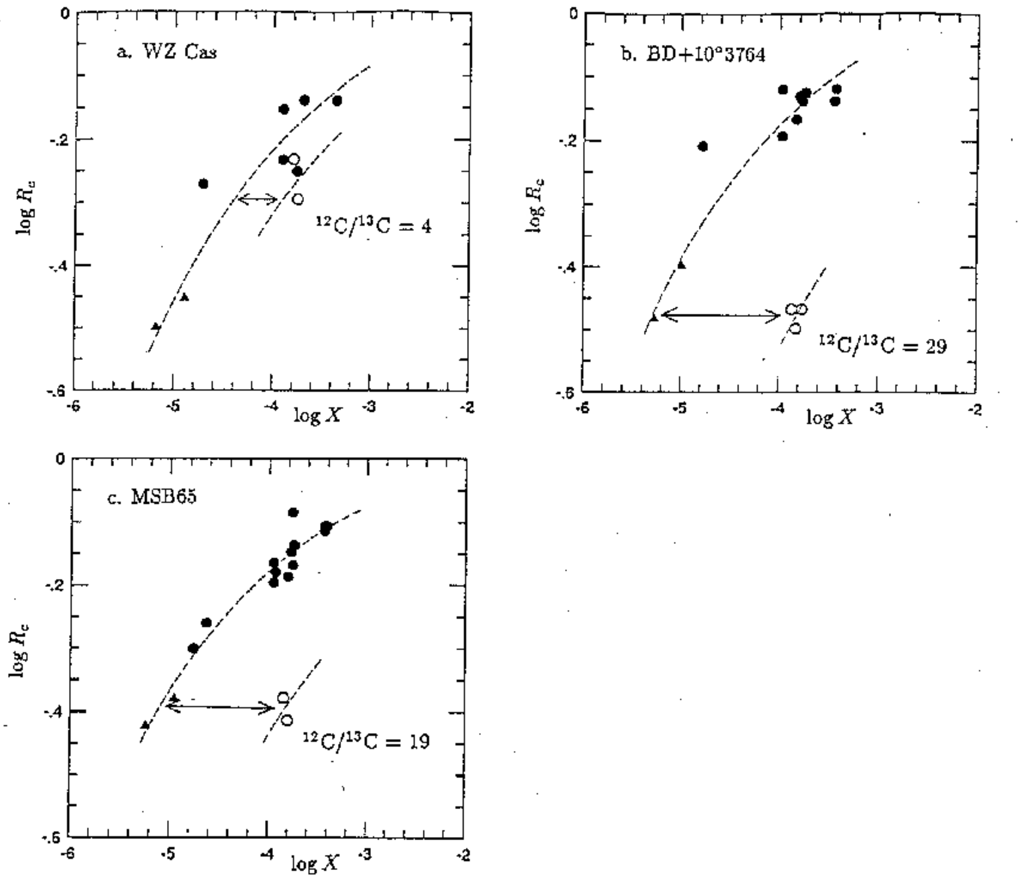

Fig. 2.12. Examples of curves-of-growth of SC-type carbon stars. **a** WZ Cas. **b** BD+10°3764. **c** MSB65. See also the legend to Fig. 2.11

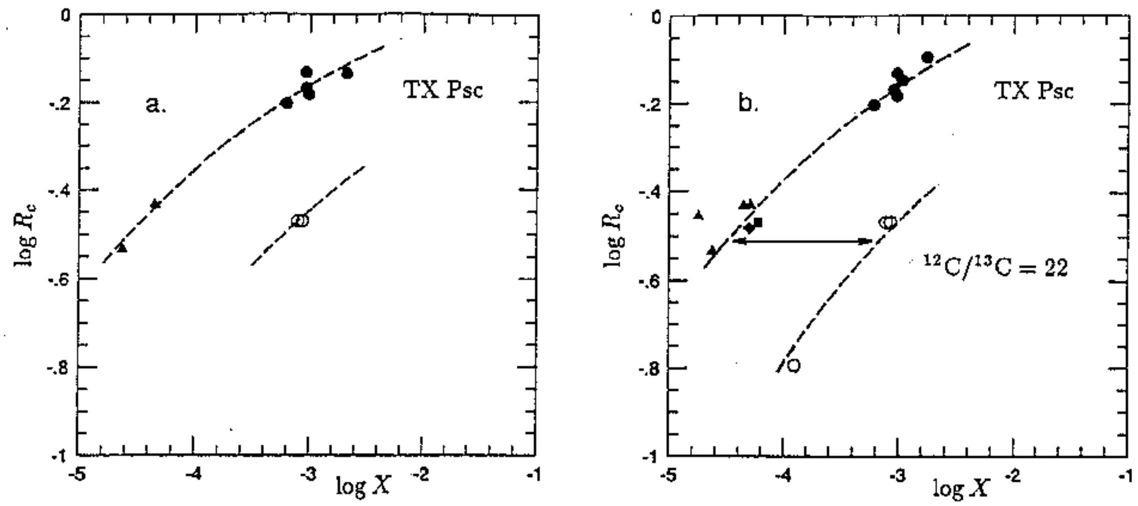

Fig. 2.13. Curves-of-growth for TX Psc. Filled symbols represent ^{12}CN lines and open symbols represent lines of ^{13}CN. Circle; (2,0) line, triangle; (7,4) line, square; (6,3) line, diamond; (5,2) line, triangle upside down; (3,1) line: **a** The standard case, using lines selected in the wavelength range from 7800 to 8030 Å. **b** A case of using additional lines in the wavelength range from 7680 to 8250 Å

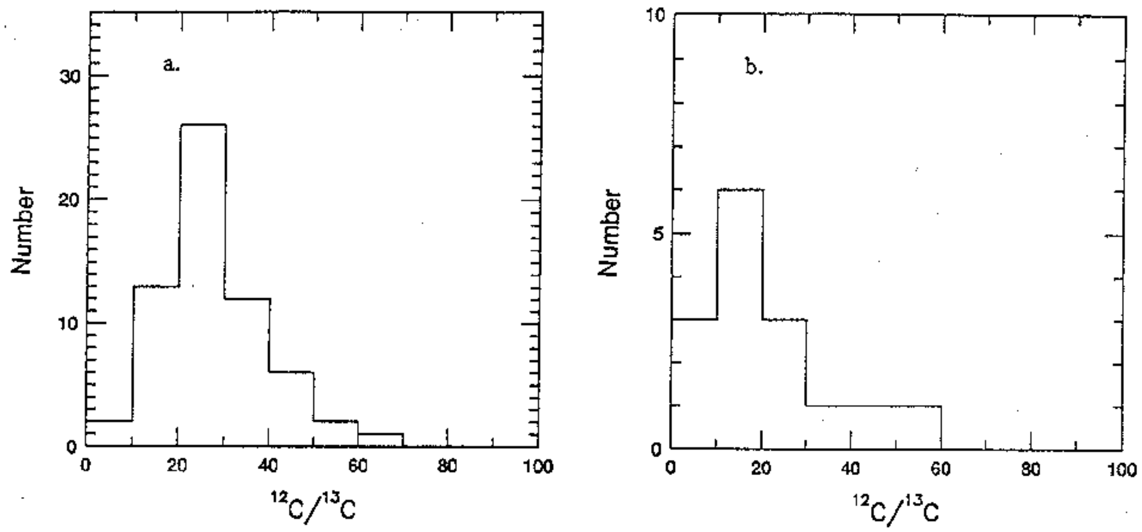

Fig. 2.14. Histograms of the $^{12}C/^{13}C$ ratios: **a** N-type carbon stars. **b** SC-type carbon stars

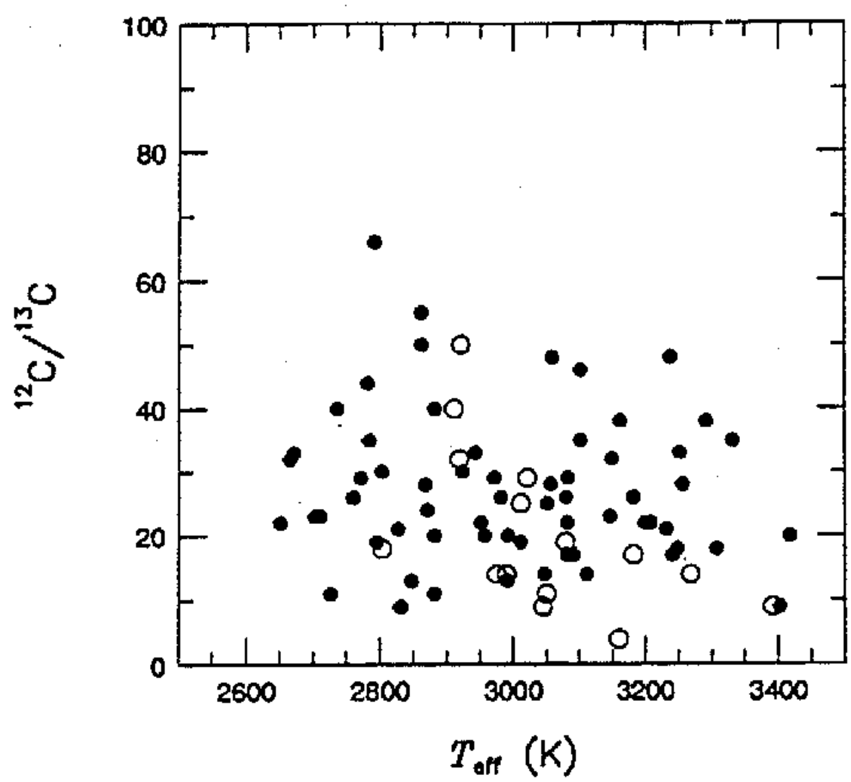

Fig. 2.15. The derived $^{12}C/^{13}C$ ratios are plotted against T_{eff}. Filled circles and open circles represent N-type carbon stars and SC-type carbon stars, respectively

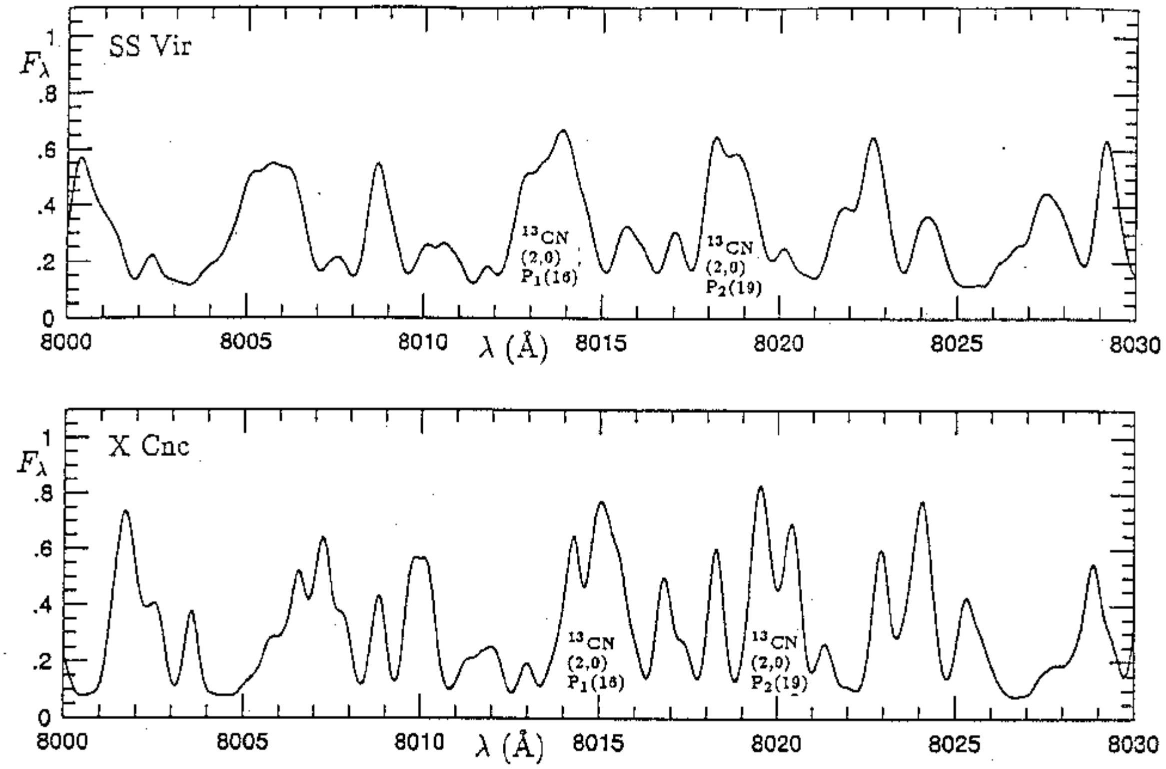

Fig. 2.16. The observed spectra of a Mira variable SS Vir (upper panel) and an SRb variable X Cnc (lower panel)

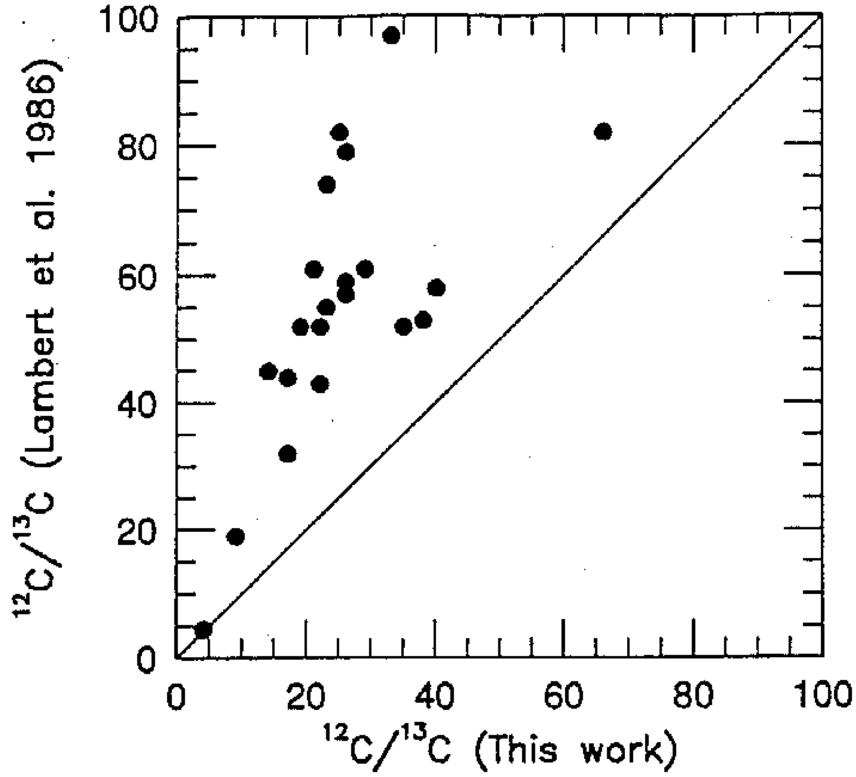

Fig. 2.17. Comparison between the $^{12}C/^{13}C$ ratios derived by Lambert et al. (1986) and this work

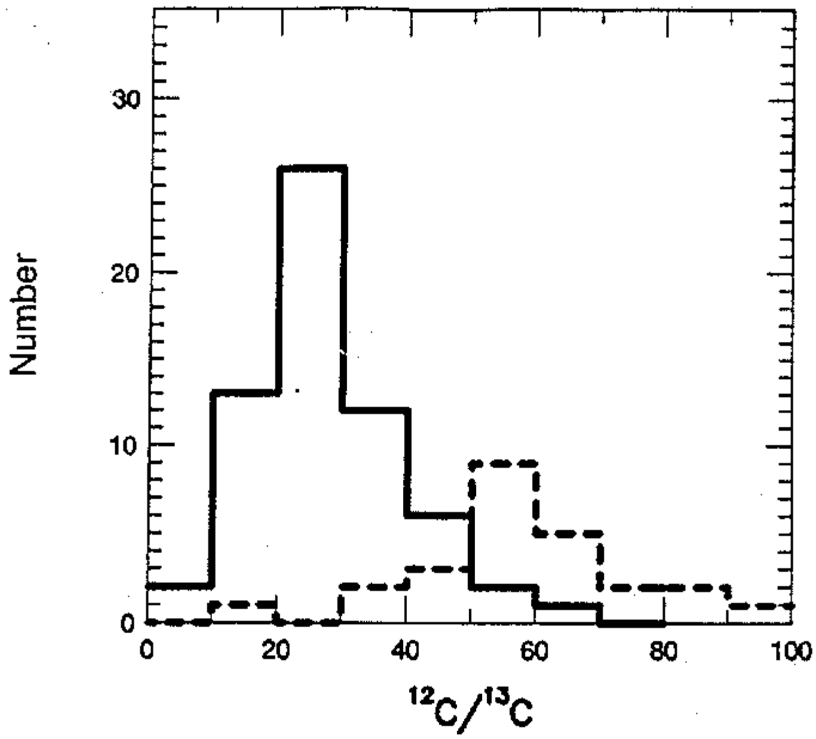

Fig. 2.18. Comparison between the histograms derived by Lambert et al. (1986) (dashed line) and this work (solid line)

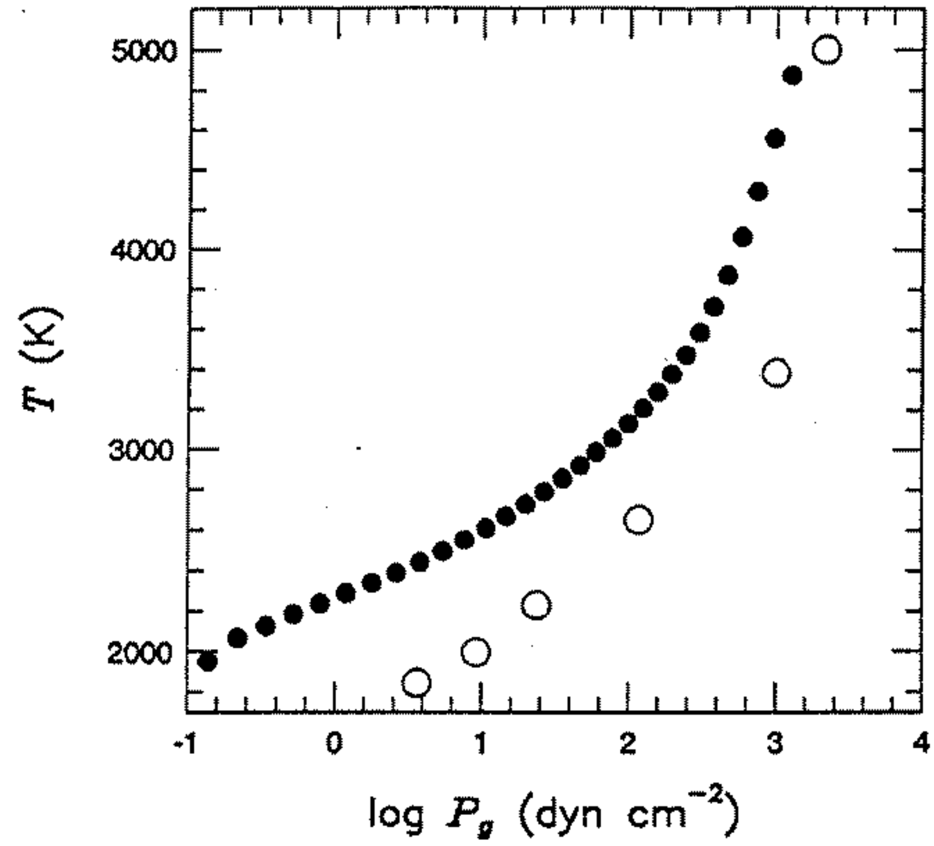

Fig. 2.19. Open circles represent a model atmosphere of Lambert et al .(1986). Filled circles represent our model. The parameters are $T_{\rm eff}$ = 3000 K, $\log g = 0.0$, C/O = 1.1, $V_{\rm micro}$ = 2.0 km s^{-1} (Lambert et al. 1986), and $V_{\rm micro}$ = 3.0 km s^{-1} (our model)

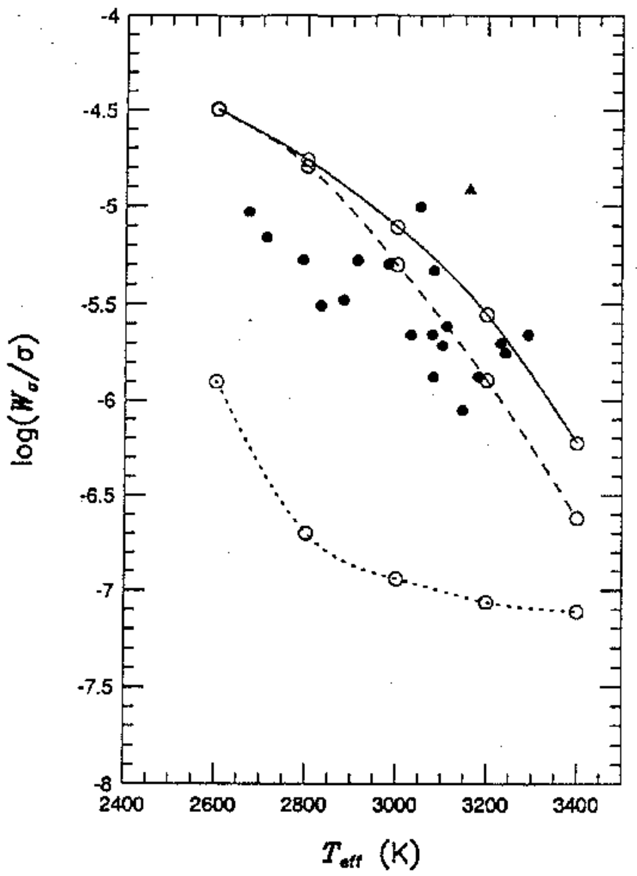

Fig. 2.20. The observed and predicted strengths of H_2 1 - 0 S(0) line. The observed strengths are from Lambert et al. (1986), and represented by filled circles (N-type carbon stars) and a filled triangle (SC-type carbon star, WZ Cas). Open circles represent the strengths predicted by our model atmospheres with (C/O, $\log g$) = (1.01, 0.3) (solid line), (1.01, 0.0) (dashed line), and (1.1, 0.0) (dotted line). $V_{\rm micro} = 3.0$ km s^{-1} for each calculation

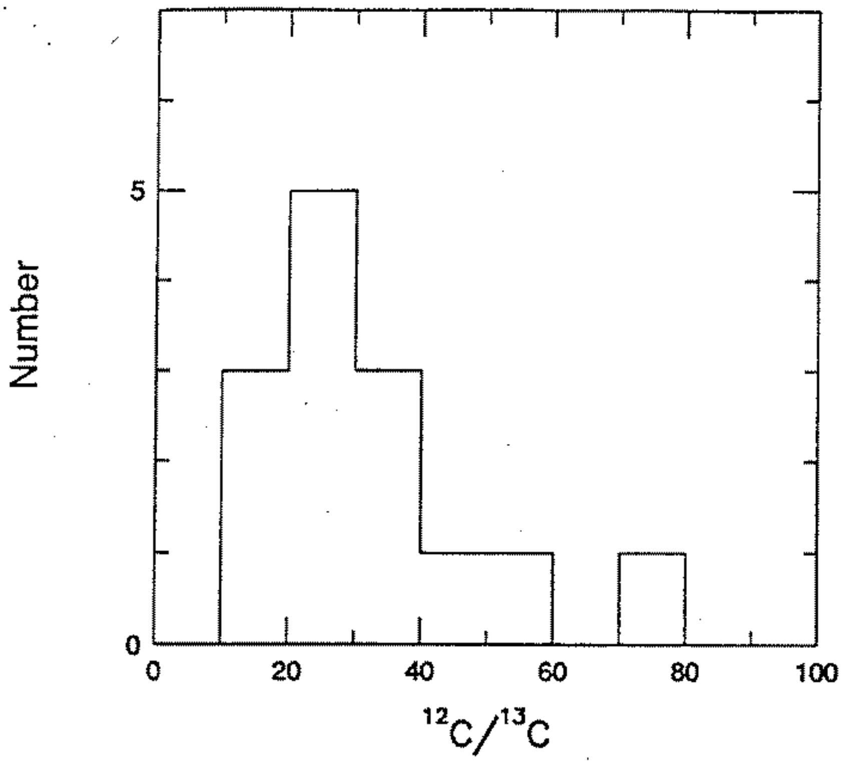

Fig. 2.21. Histogram of the $^{12}C/^{13}C$ ratios which M giants would have when they evolved into carbon stars

Chapter 3

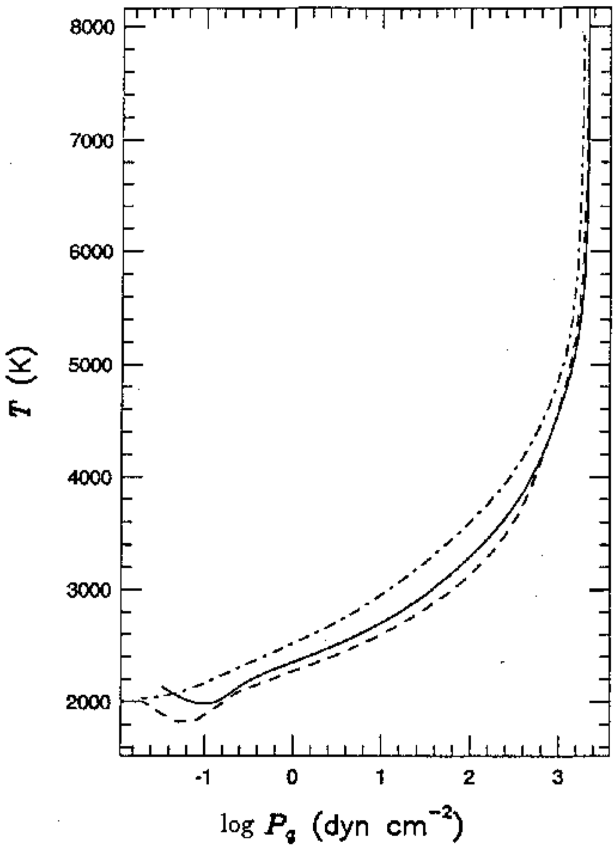

Fig. 3.1. Examples of the model atmospheres. The models calculated with C/O = 2.0, 1.3, and 1.1, are shown by the dashed-dotted, solid, and dashed lines, respectively. Other parameters are $T_{\rm eff}$ = 3000 K, $\log g = 0.0$, and $V_{\rm micro}$ = 3 km s^{-1}

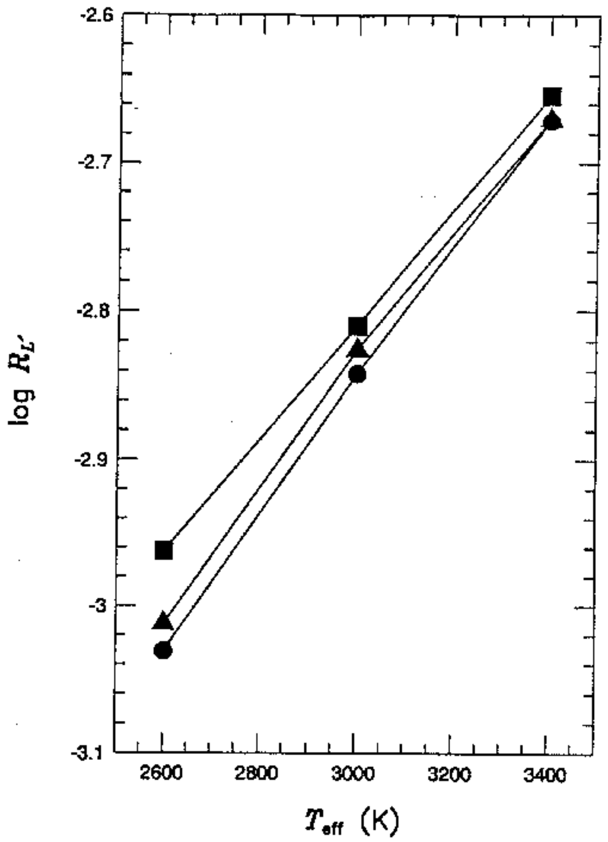

Fig. 3.2. The calibration of $R_{L'}$ against $T_{\rm eff}$ with different C/O ratios. Filled squares, triangles, and circles correspond to the models with C/O = 1.1, 1.3, and 2.0, respectively

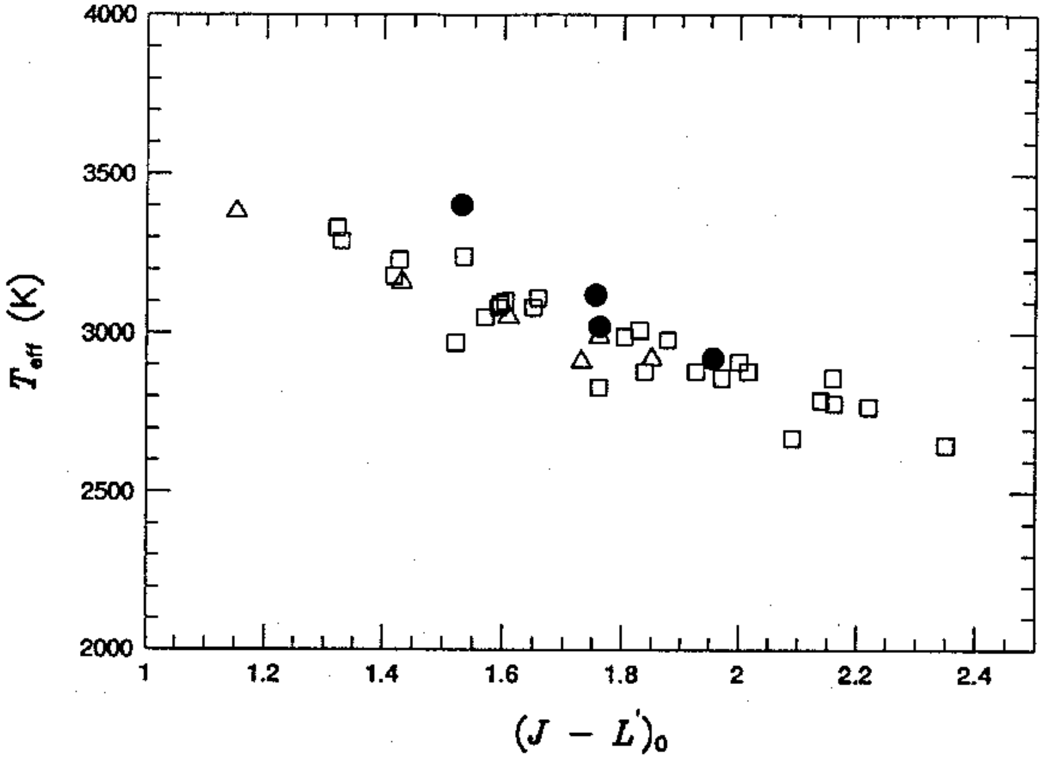

Fig. 3.3. $(J - L')_0$ – $T_{\rm eff}$ relation. Effective temperatures are determined by the IRFM. Filled circles represent J-type carbon stars. N- and SC-type carbon stars analyzed in Paper I are represented by open squares and triangles, respectively

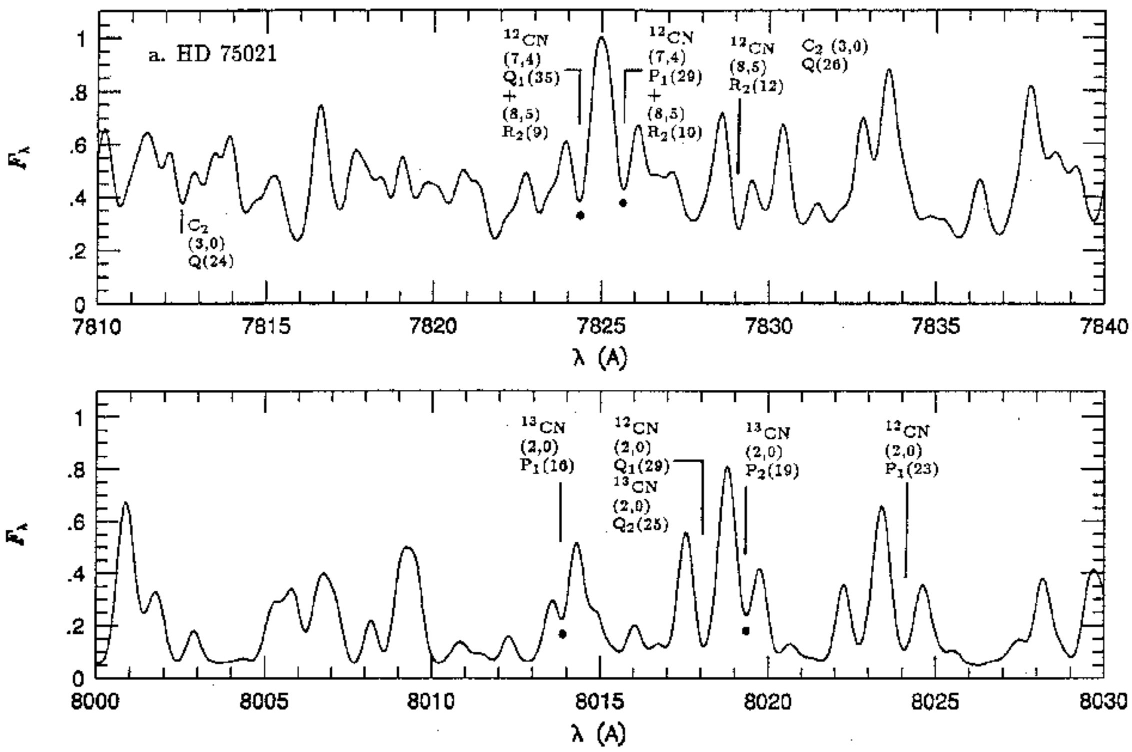

Fig. 3.4. a. The observed spectra of HD 75021. The lines indicated by filled circles are used in the analysis.

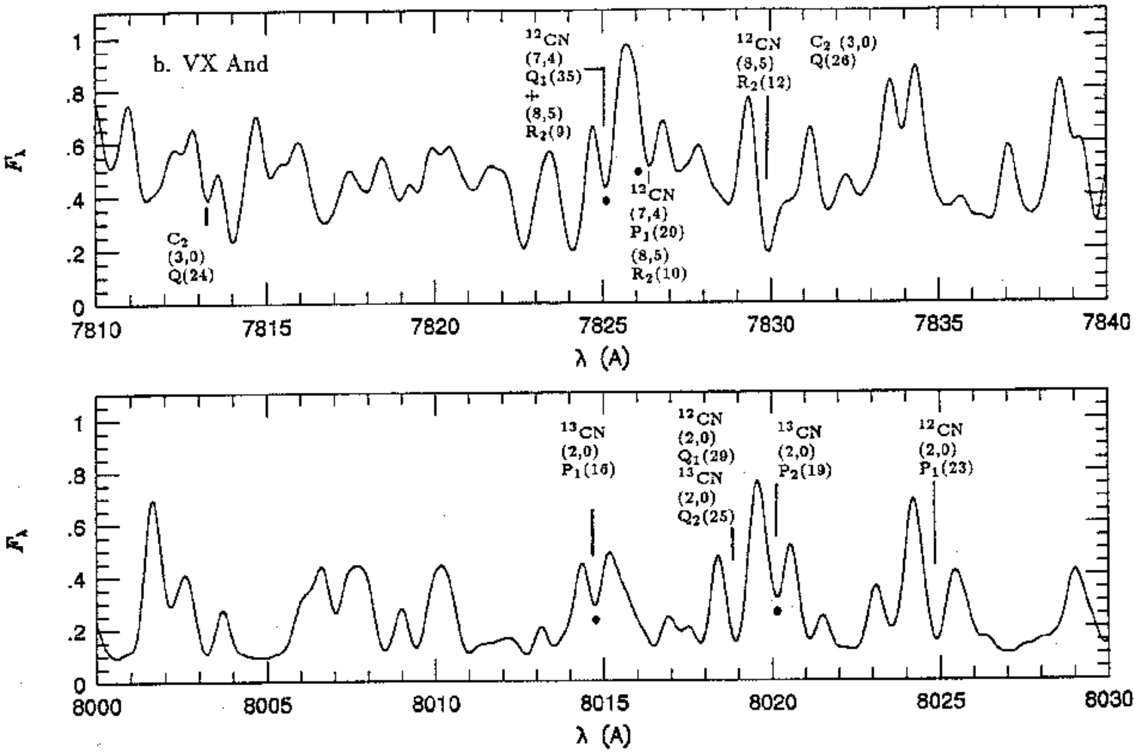

Fig. 3.4. b. The observed spectra of VX And. See also the legend to Fig. 3.4a

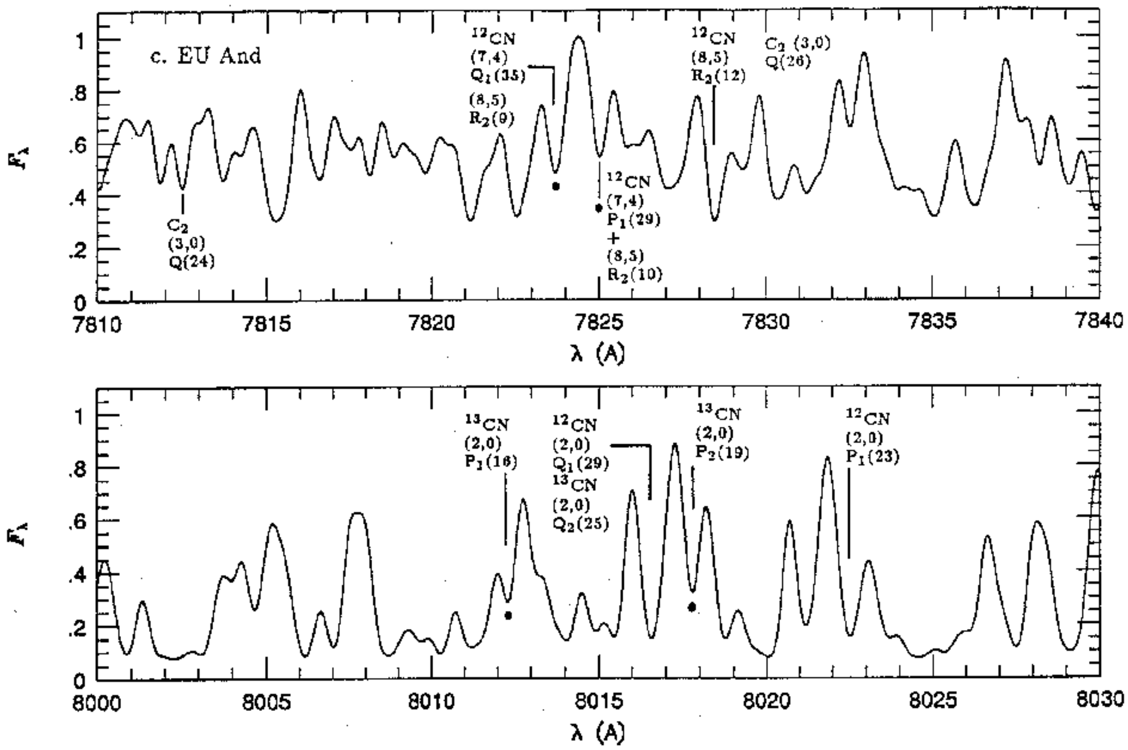

Fig. 3.4. c. The observed spectra of EU And. See also the legend to Fig. 3.4a

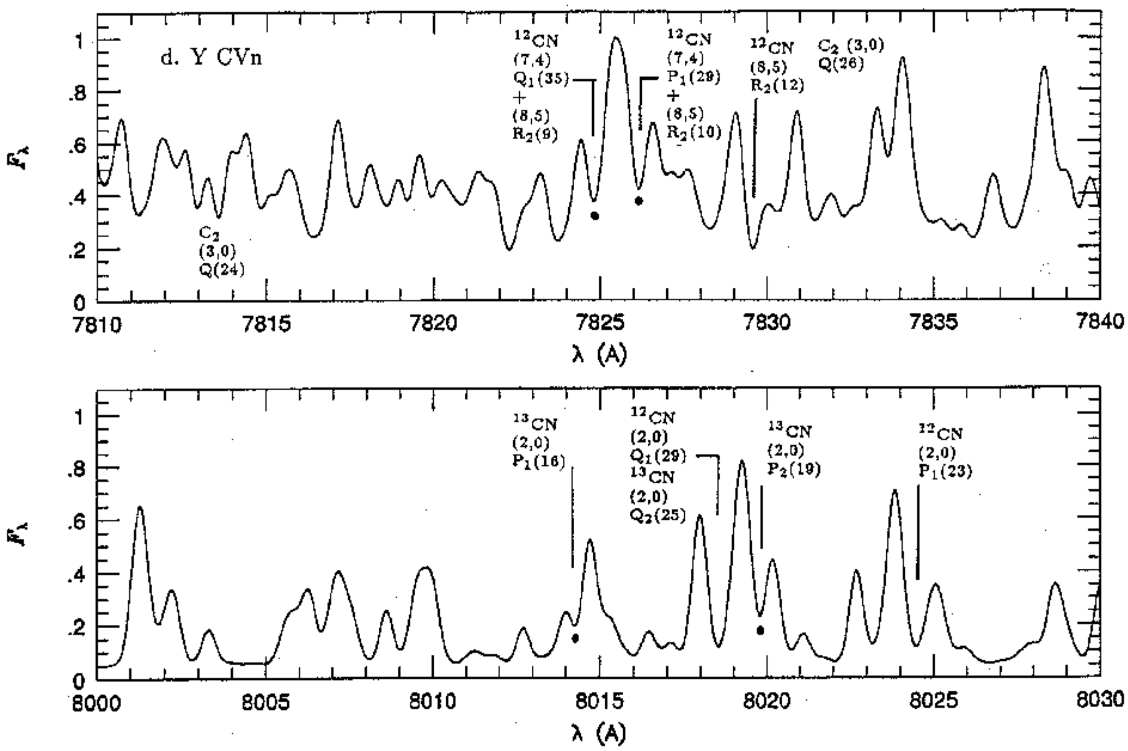

Fig. 3.4. d. The observed spectra of Y CVn. See also the legend to Fig. 3.4a

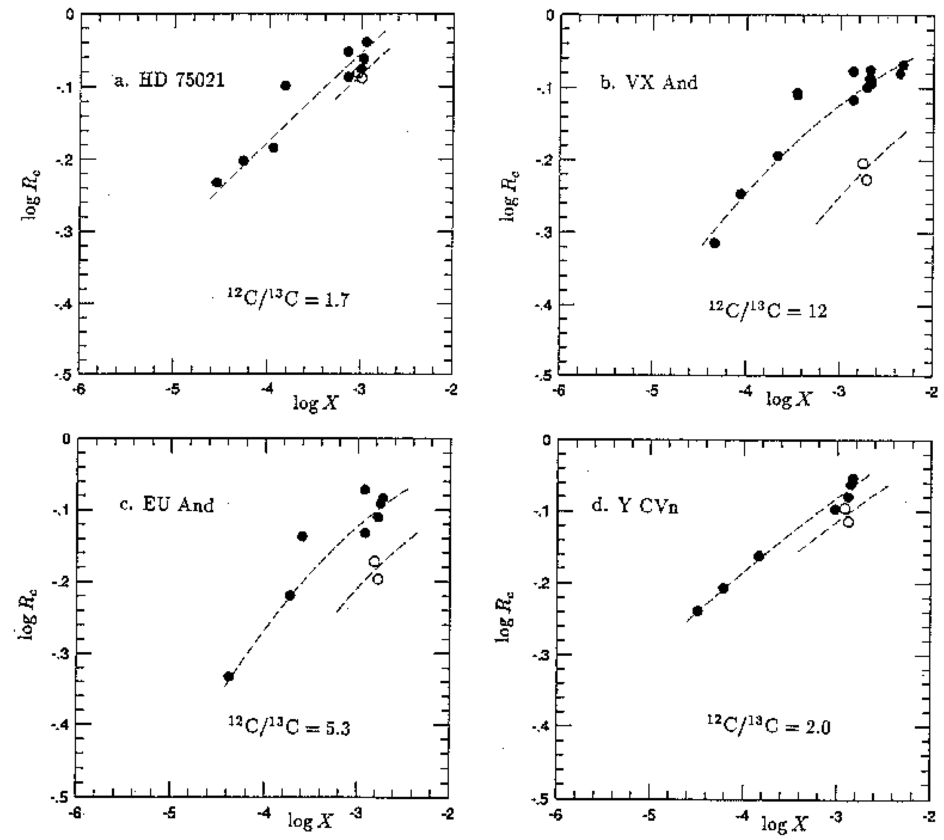

Fig. 3.5. Examples of the iso-intensity method for J-type carbon stars. The ordinates are logarithms of central depths normalized by the fictitious continuum level, and the abscissas are $\log X = \log(gf\Gamma)$. **a.** HD 75021. **b.** VX And. **c.** EU And. **d.** Y CVn

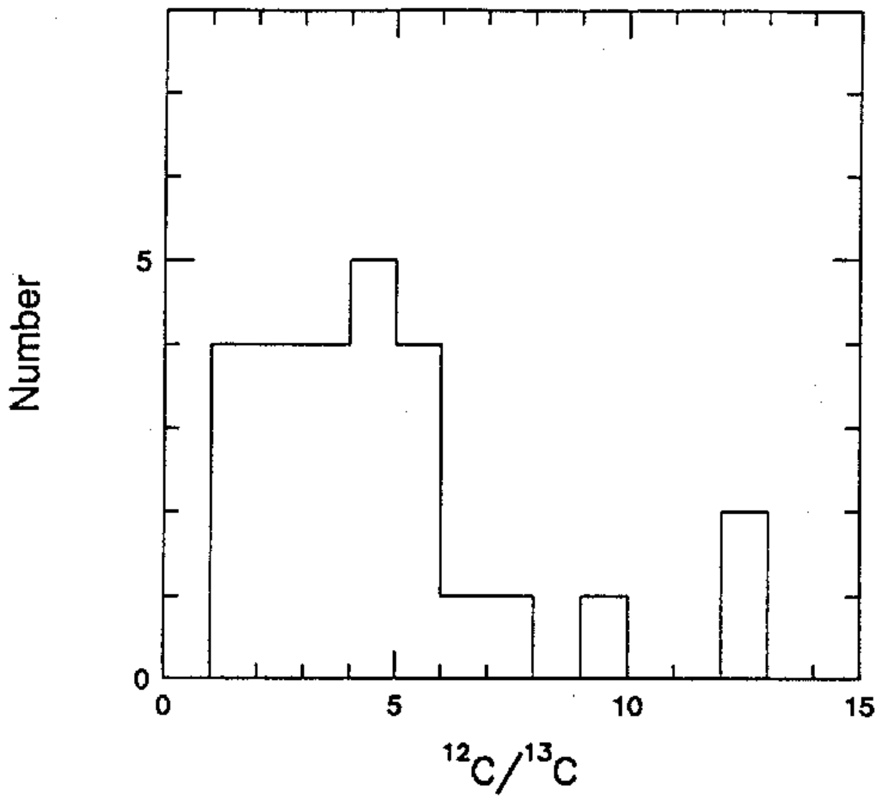

Fig. 3.6. Histogram of the resulting $^{12}C/^{13}C$ ratios

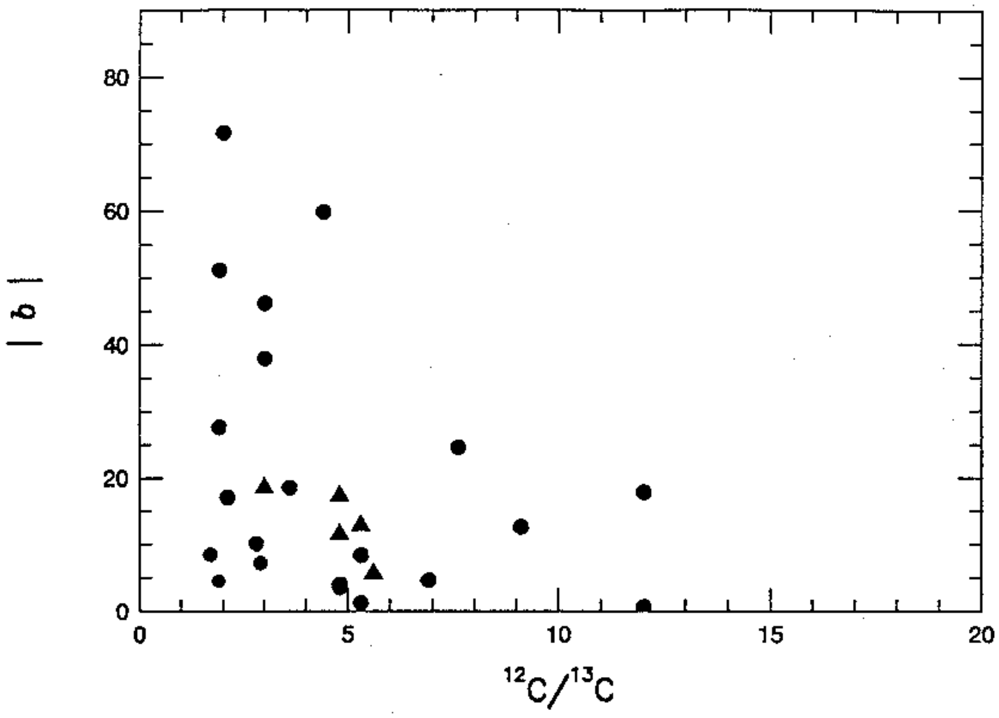

Fig. 3.7. Correlation between galactic latitude $|\, b \,|$ and $^{12}C/^{13}C$ ratio

Chapter 4

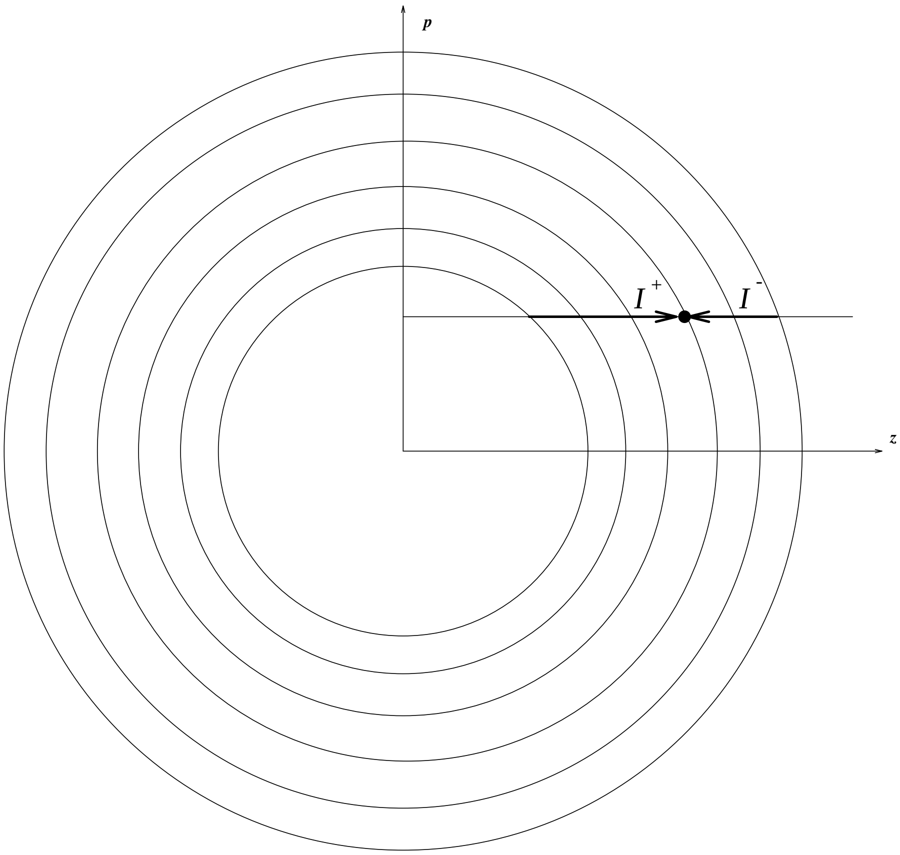

Fig. 4.1. The $p - z$ plane used in solving the radiative transfer equation. The outward and inward intensities are evaluated at points of given z and p

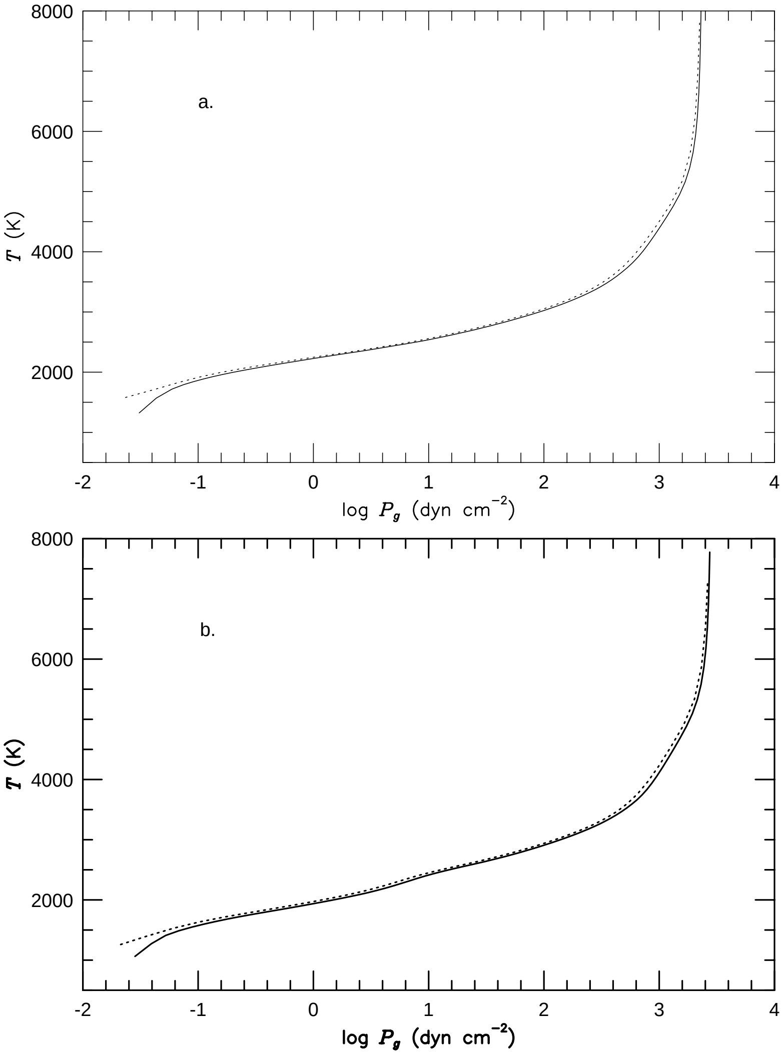

Fig. 4.2. The temperature stratifications of models in the plane parallel limit case. **a.** The solid line represents a spherical model with $T_{\rm eff}$ = 3000 K, $\log g$ = 0.0, $V_{\rm micro}$ = 3.0 km s^{-1}, $\log\varepsilon$(O) = -3.07, C/O = 1.1, and M = 2 $M_{\odot}$. The dotted line represents a plane parallel model with the same parameters except for the stellar mass. **b.** The case of $T_{\rm eff}$ = 2800 K

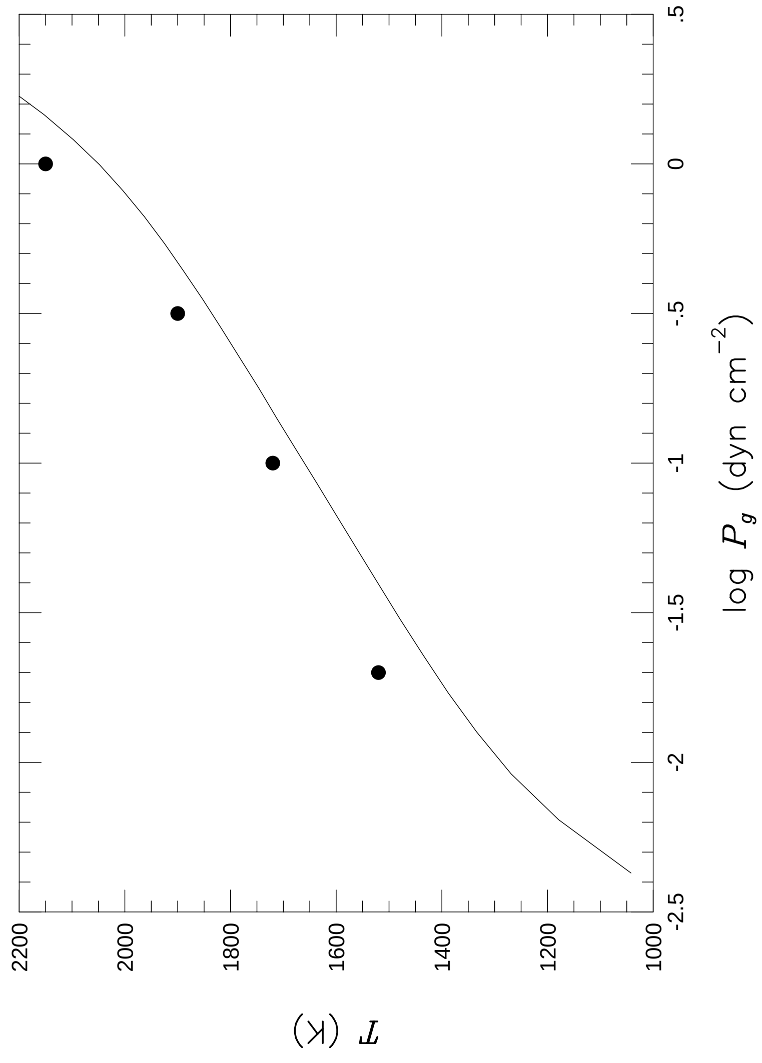

Fig. 4.3. Comparison of the temperature stratifications of the models by Jørgensen et al. (1992) (filled circles) and by this work (solid line). The parameters are $T_{\rm eff} = 2800$ K, $\log g = -0.5$, C/O = 1.35, and $M = 1.5\ M_\odot$

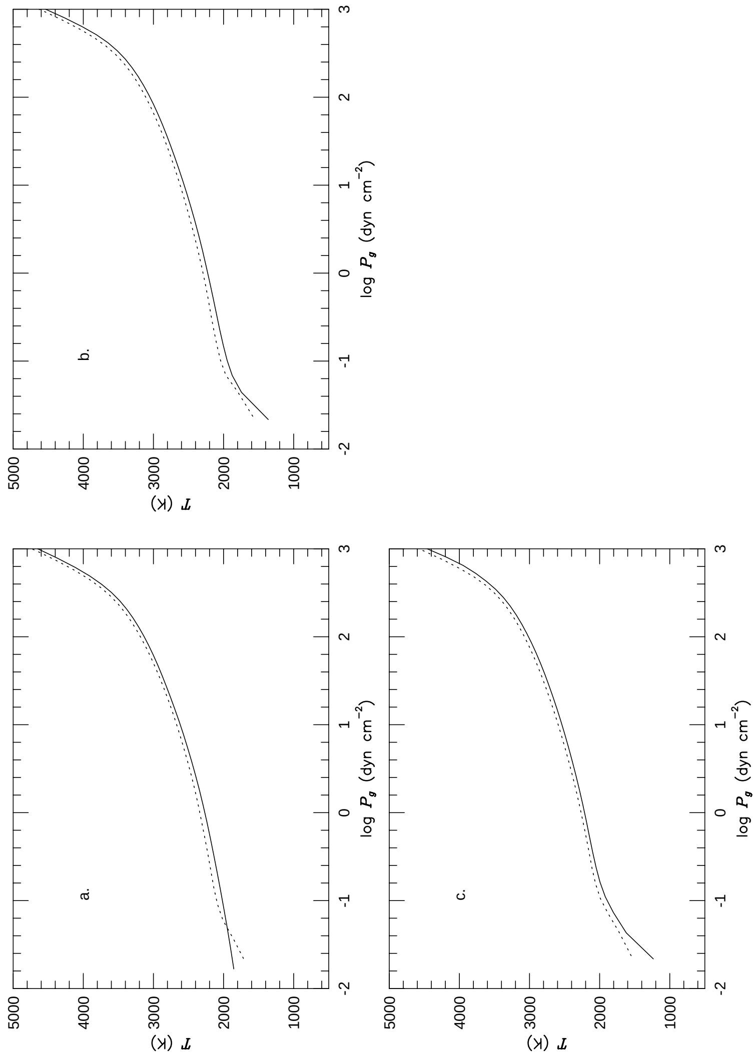

Fig. 4.4. The temperature stratifications of the models of $T_{\rm eff} = 3200$ K with different oxygen abundances are represented by the solid lines. The dotted lines represent the models with the same sets of parameters but in plane parallel geometry. The parameters are C/O = 1.1, $\log g = 0.0$, $V_{\rm micro} = 3.0$ km s^{-1}, and 2 $M_\odot$ (for the spherical models). The oxygen abundances are **a.** $\log \varepsilon(\rm O) = -3.07$, **b.** -3.27, and **c.** -3.37

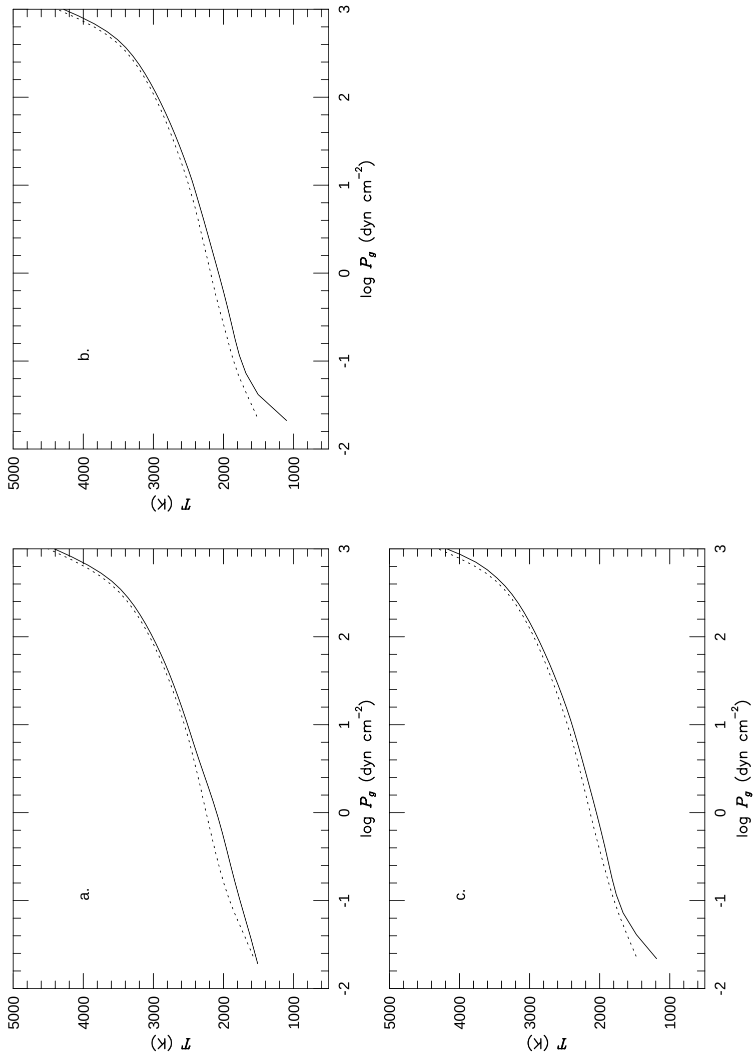

Fig. 4.5. The temperature stratifications of the models of $T_{\rm eff} = 3000$ K with different oxygen abundances are represented by the solid lines. The dotted lines represent the models with the same sets of parameters but in plane parallel geometry. The parameters are C/O = 1.1, $\log g = 0.0$, $V_{\rm micro} = 3.0$ km s^{-1}, and 2 $M_\odot$ (for the spherical models). The oxygen abundances are **a.** $\log \varepsilon(\mathrm{O}) = -3.07$, **b.** -3.27, and **c.** -3.37

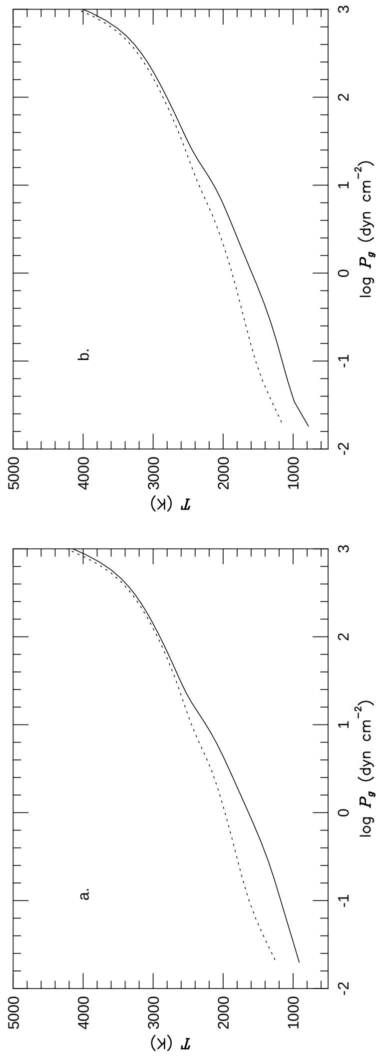

Fig. 4.6. The temperature stratifications of the models of $T_{\rm eff} = 2800$ K with different oxygen abundances are represented by the solid lines. The dotted lines represent the models with the same sets of parameters but in plane parallel geometry. The parameters are C/O = 1.1, $\log g = 0.0$, $V_{\rm micro} = 3.0$ km s^{-1}, and 2 $M_\odot$ (for the spherical models). The oxygen abundances are **a.** $\log \varepsilon({\rm O}) = -3.07$, **b.** -3.27, and **c.** -3.37

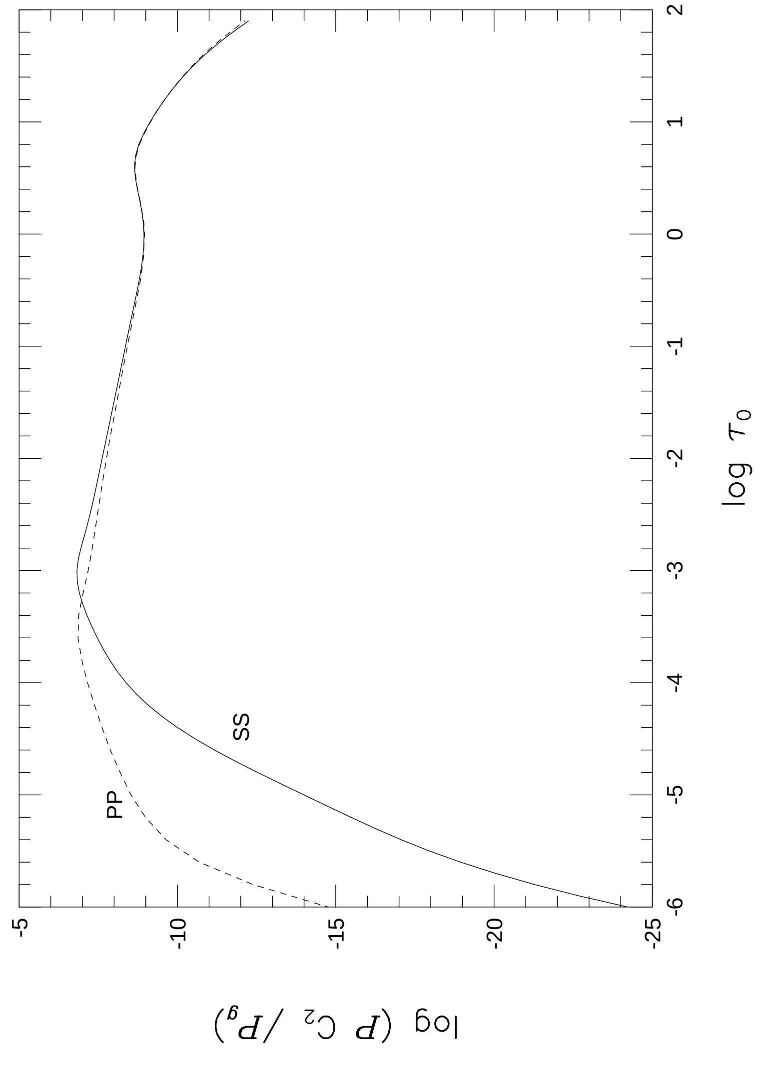

Fig. 4.7. The depth dependence of partial pressure of C_2 in the spherical and plane parallel models. The partial pressure is normalized by the gas pressure. The optical depth of continuum at 1.04 μm is denoted by τ_0. The case for the spherical model is denoted by 'SS', while the case for the plane parallel model is denoted by 'PP'. The parameters of the models are $T_{\rm eff}$ = 2800 K, $\log g$ = 0.0, $V_{\rm micro}$ = 3.0 km s^{-1}, C/O = 1.1, and 2 $M_\odot$ (for the spherical model)

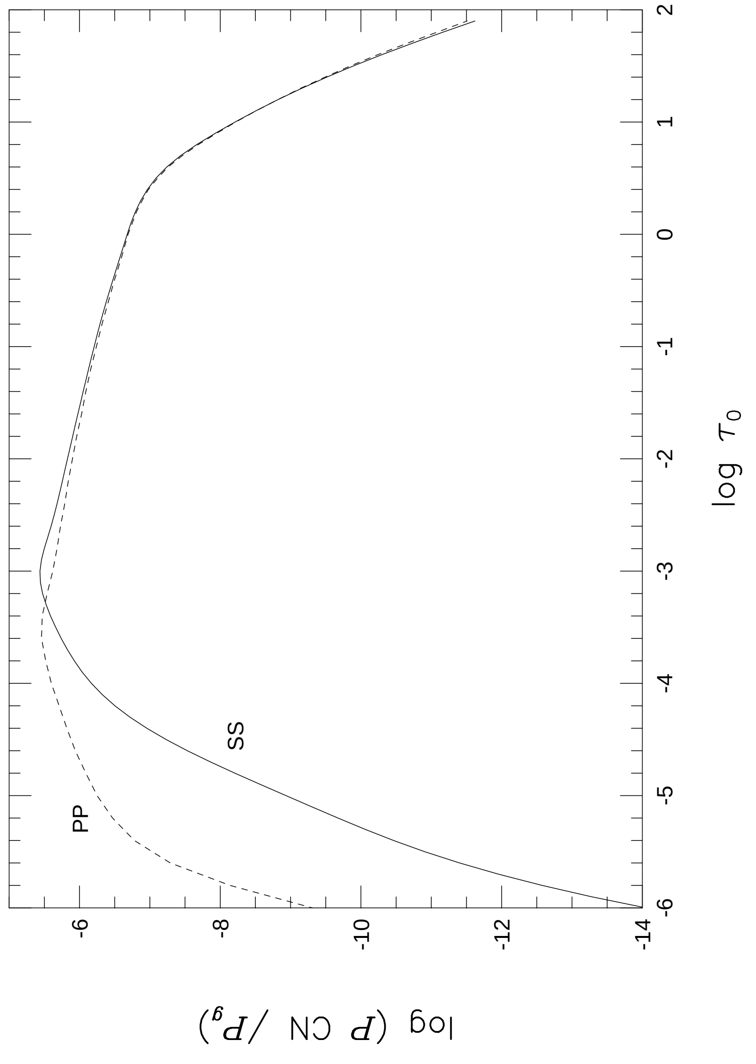

Fig. 4.8. The depth dependence of partial pressure of CN in the spherical and plane parallel models. The partial pressure is normalized by the gas pressure. The parameters of the models are $T_{\rm eff}$ = 2800 K, $\log g = 0.0$, $V_{\rm micro} = 3.0$ km s^{-1}, C/O = 1.1, and 2 $M_\odot$ (for the spherical model). See also the legend to Fig. 4.7

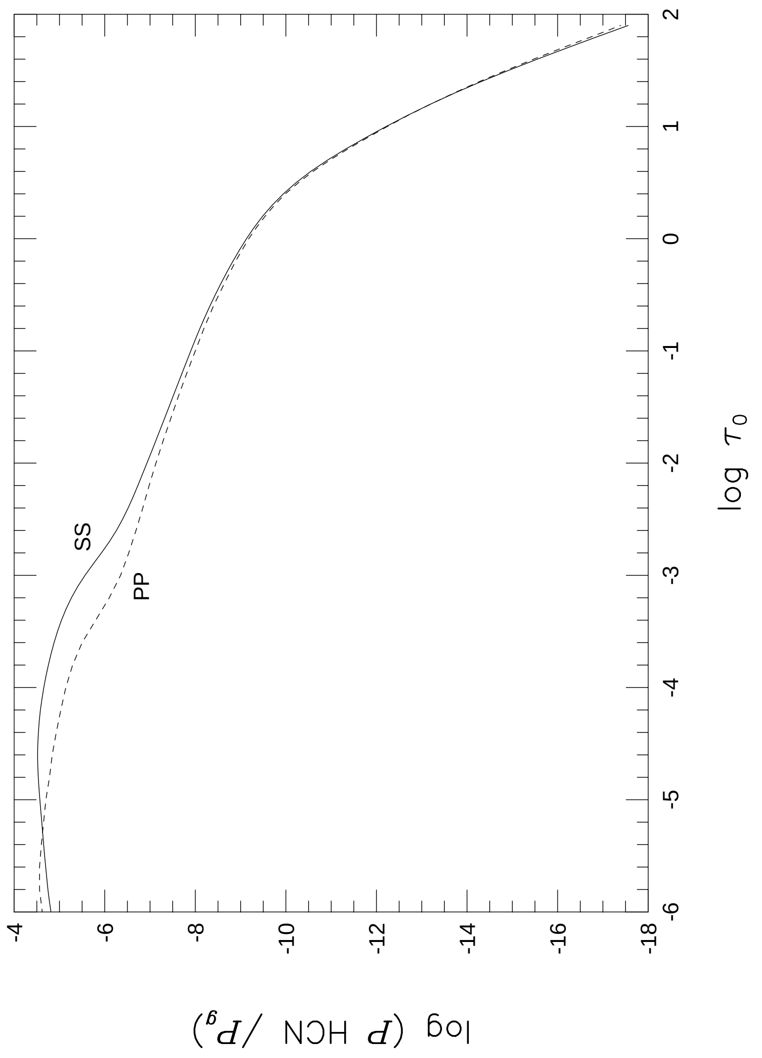

Fig. 4.9. The depth dependence of partial pressure of HCN in the spherical and plane parallel models. The partial pressure is normalized by the gas pressure. The parameters of the models are $T_{\rm eff}$ = 2800 K, $\log g$ = 0.0, $V_{\rm micro}$ = 3.0 km s^{-1}, C/O = 1.1, and 2 $M_\odot$ (for the spherical model). See also the legend to Fig. 4.7

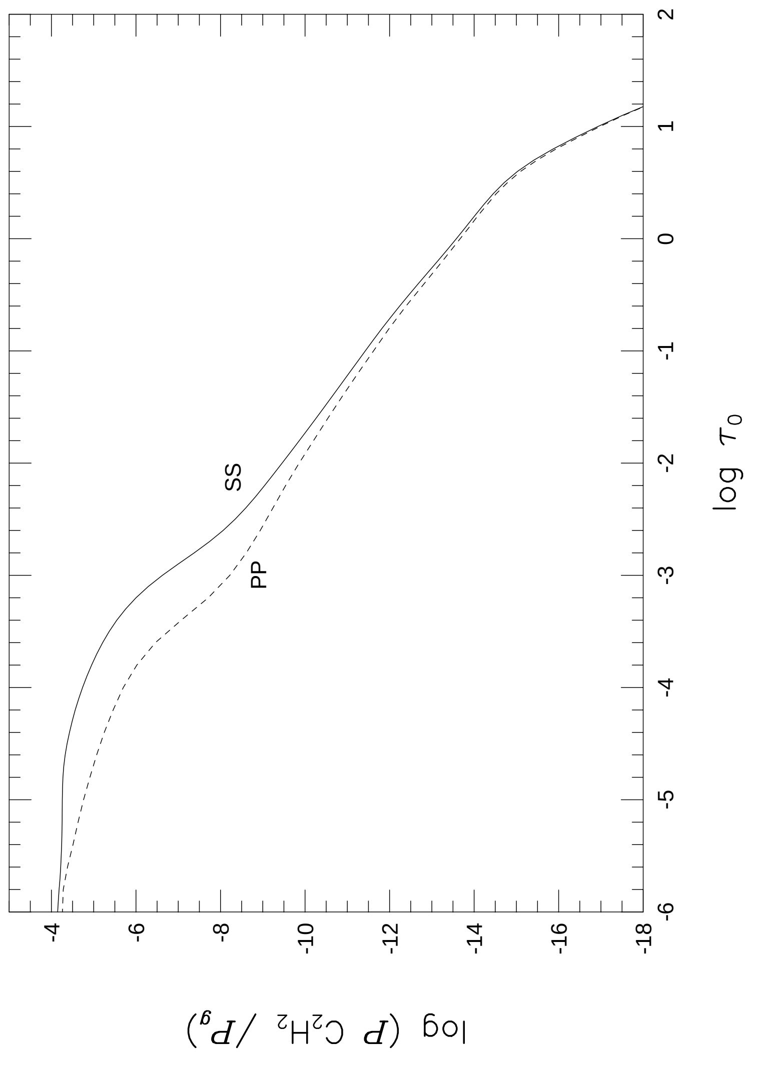

Fig. 4.10. The depth dependence of partial pressure of C_2H_2 in the spherical and plane parallel models. The partial pressure is normalized by the gas pressure. The parameters of the models are $T_{\rm eff}$ = 2800 K, $\log g = 0.0$, $V_{\rm micro}$ = 3.0 km s^{-1}, C/O = 1.1, and 2 $M_\odot$ (for the spherical model). See also the legend to Fig. 4.7

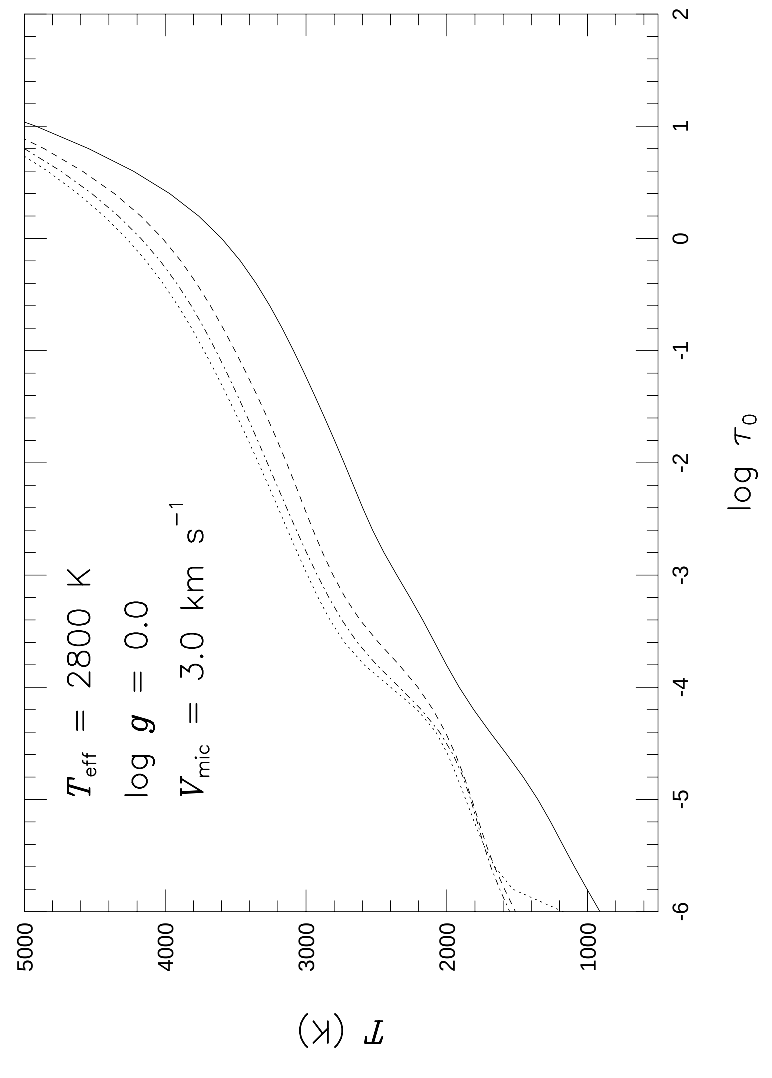

Fig. 4.11. The temperature stratifications of models with different C/O ratios. The parameters are $T_{\rm eff}$ = 2800 K, $\log g$ = 0.0, $V_{\rm micro}$ = 3.0 km s^{-1}, $\log \varepsilon(\mathrm{O}) = -3.07$, and $M = 2\ M_{\odot}$. Solid line: C/O = 1.1, dashed line: C/O = 2.0, dash-dotted line: C/O = 3.0, dotted line: C/O = 4.0

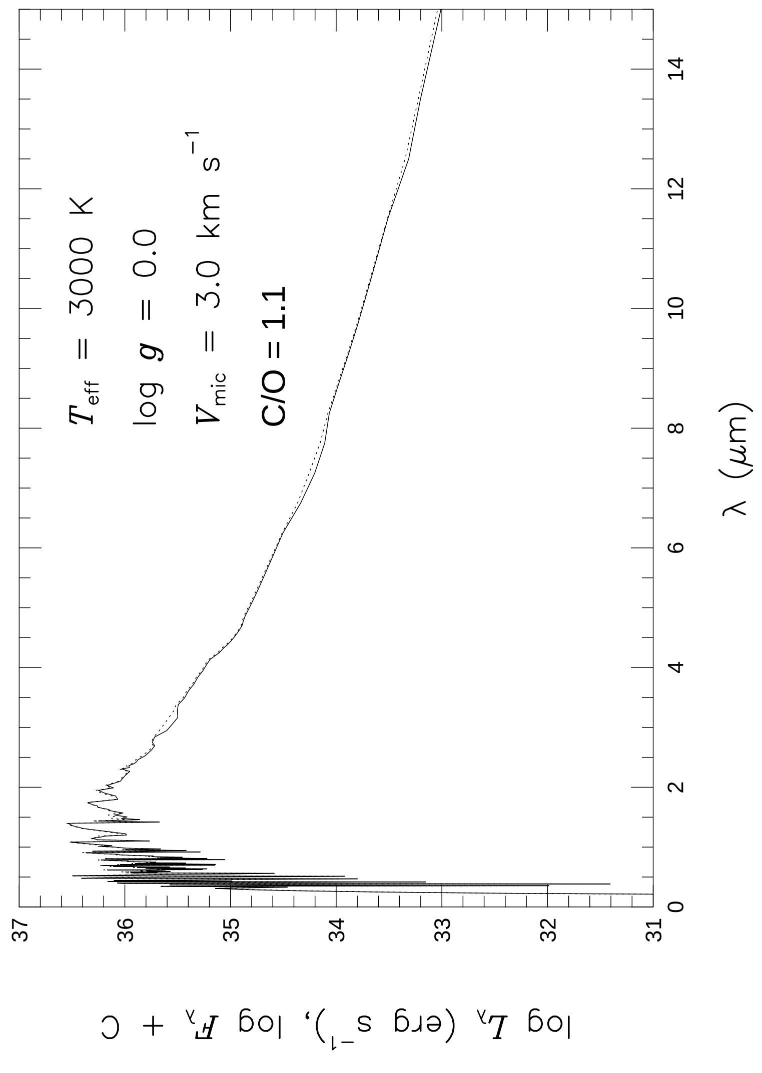

Fig. 4.12. Spectral energy distribution of a spherical model (solid line) is compared with that of its plane parallel counterpart (dotted line). The parameters are $T_{\rm eff} = 3000$ K, $\log g = 0.0$, C/O = 1.1, $V_{\rm micro} = 3.0$ km s^{-1}, and $M = 2\ M_\odot$

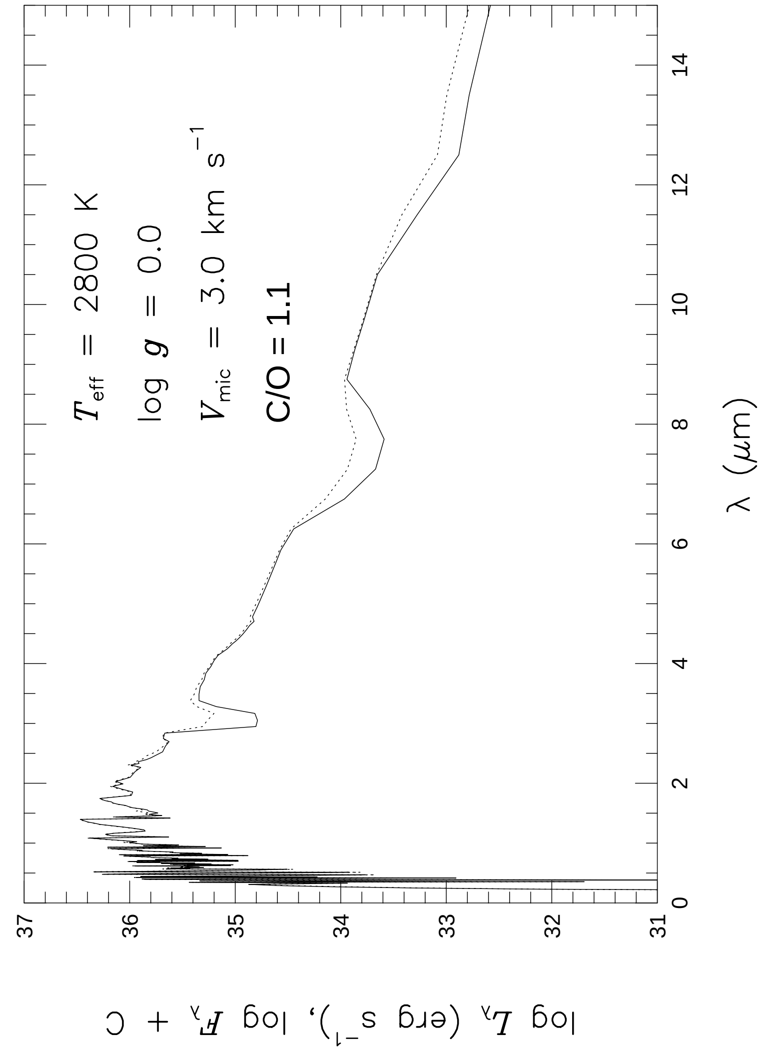

Fig. 4.13. Spectral energy distribution of a spherical model (solid line) is compared with that of its plane parallel counterpart (dotted line). The parameters are $T_{\rm eff} = 2800$ K, $\log g = 0.0$, C/O = 1.1, $V_{\rm micro} = 3.0$ km s^{-1}, and $M = 2\ M_\odot$

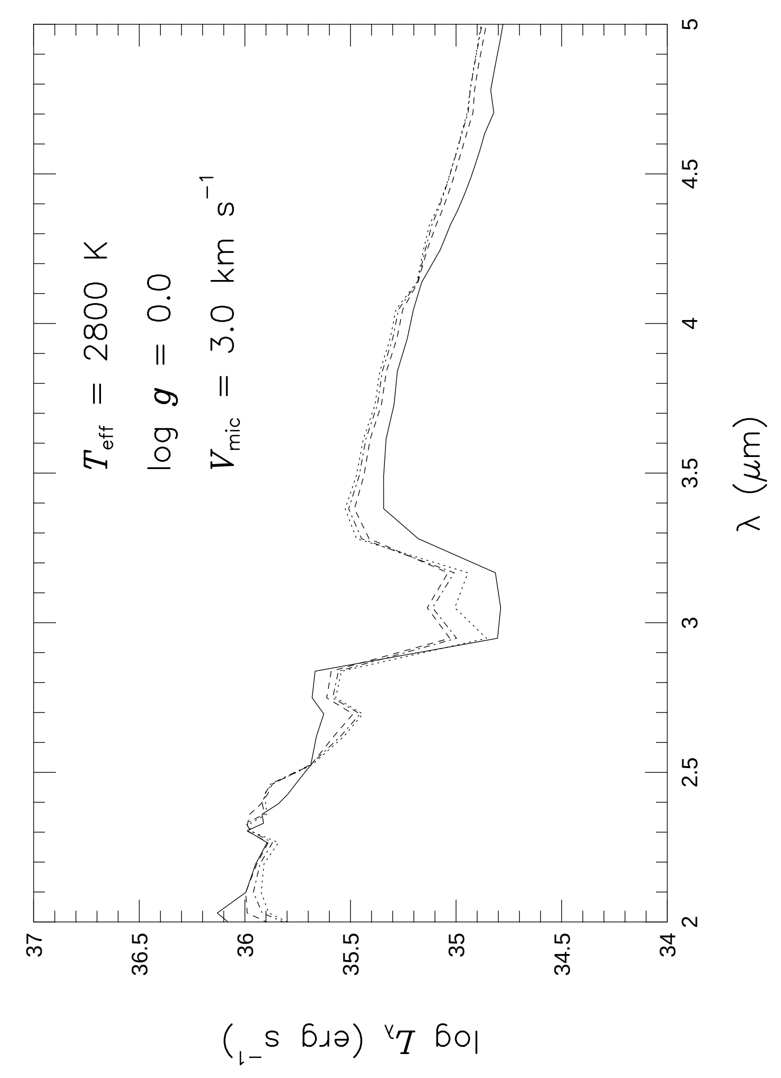

Fig. 4.14. Spectral energy distributions of spherical models with different C/O ratios. The parameters are $T_{\rm eff}$ = 2800 K, $\log g$ = 0.0, $V_{\rm micro}$ = 3.0 km s^{-1}, and M = 2 $M_\odot$. Solid line: C/O = 1.1, dashed line: C/O = 2.0, dash-dotted line: C/O = 3.0, dotted line: C/O = 4.0

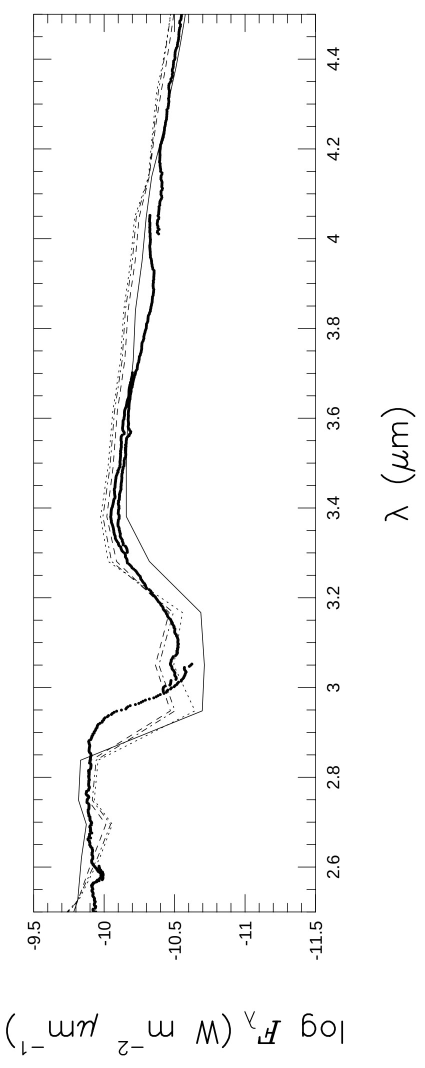

Fig. 4.15. The spectrum of SS Vir observed by the ISO SWS (filled circles) is compared with the SED's of 2800 K models with different C/O ratios. Other parameters are $\log g = 0.0$, $V_{\rm micro} = 3.0$ km s^{-1}, and $M = 2\ M_{\odot}$. solid line: C/O = 1.1, dashed line: C/O = 2.0, dash-dotted line: C/O = 3.0, dotted line: C/O = 4.0

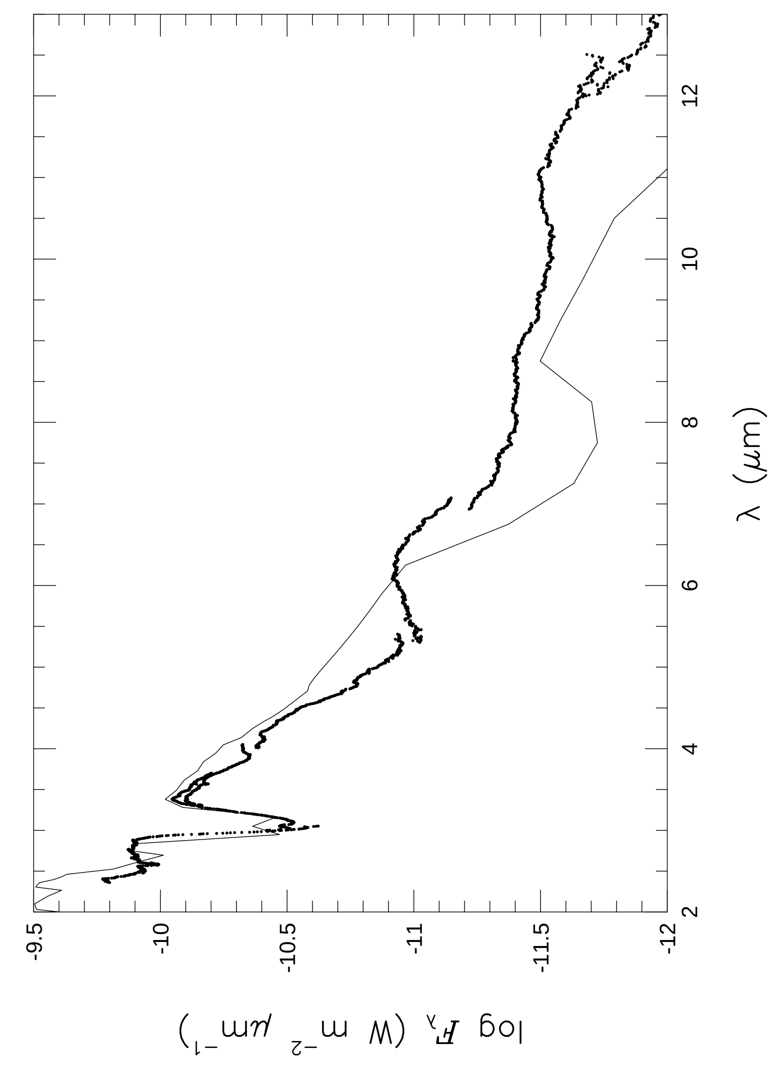

Fig. 4.16. The observed spectrum of SS Vir from 2 to 13 μm (filled circles) is compared with the SED of the model with $T_{\rm eff}$ = 2800 K, $\log g$ = 0.0, C/O = 2.0, $V_{\rm micro}$ = 3.0 km s^{-1}, and M = 2 $M_\odot$(solid line)

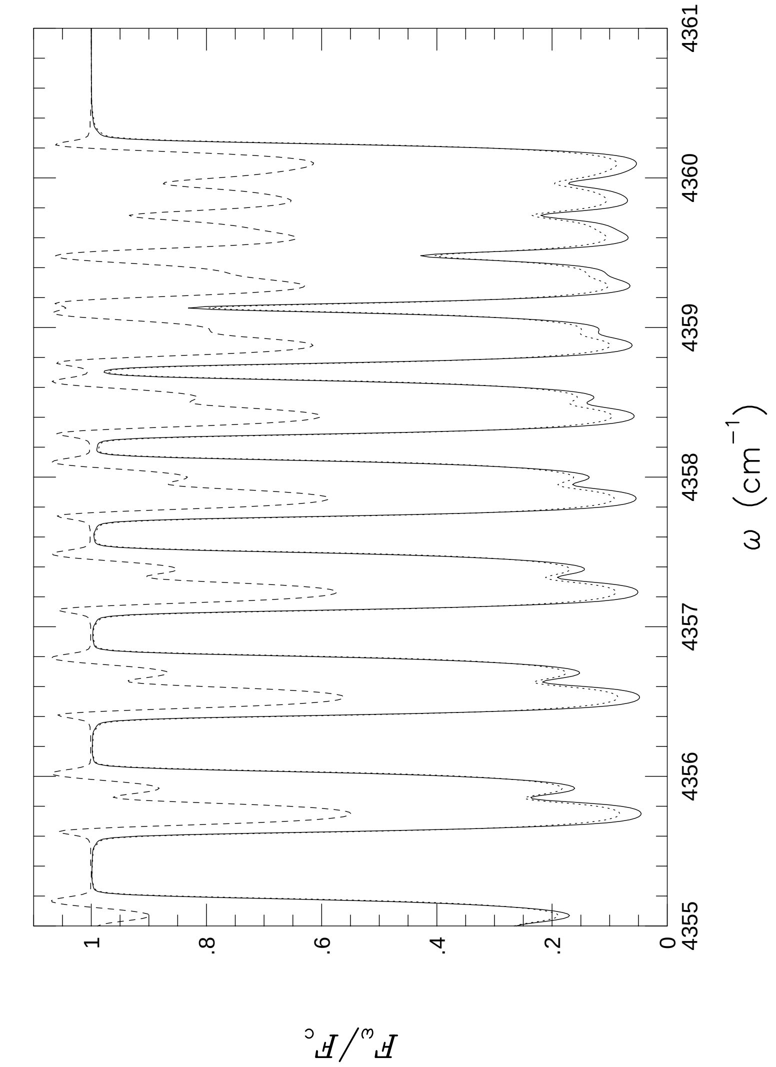

Fig. 4.17. Synthetic spectrum calculated by the spherical radiative transfer code and the temperature stratification of the spherical model is represented by the solid line. The corresponding spectrum in the case of plane parallel geometry is represented by the dotted line. The ratio between the two spectra is represented by the dashed line. The parameters of the models are $T_{\rm eff}$ = 2800 K, $\log g = 0.0$, $V_{\rm micro} = 3.0$ km s^{-1}, $\log \varepsilon({\rm O}) = -3.27$, C/O = 1.1, M = 2 $M_\odot$ (for the spherical model)

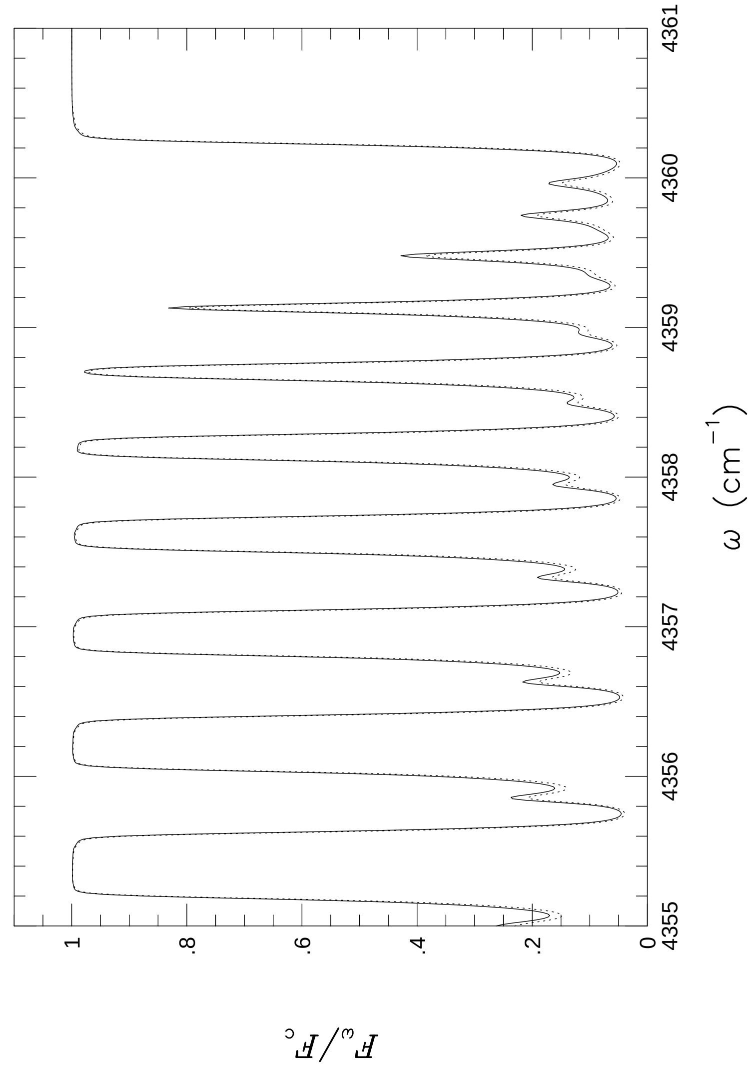

Fig. 4.18. The solid line is the synthetic spectrum calculated by the spherical radiative transfer code based on the temperature stratification of the spherical model. The dashed line is the synthetic spectrum calculated by the plane parallel radiative transfer code based on the temperature stratification of the identical spherical model. The parameters of the models are given in the legend to Fig 4.17

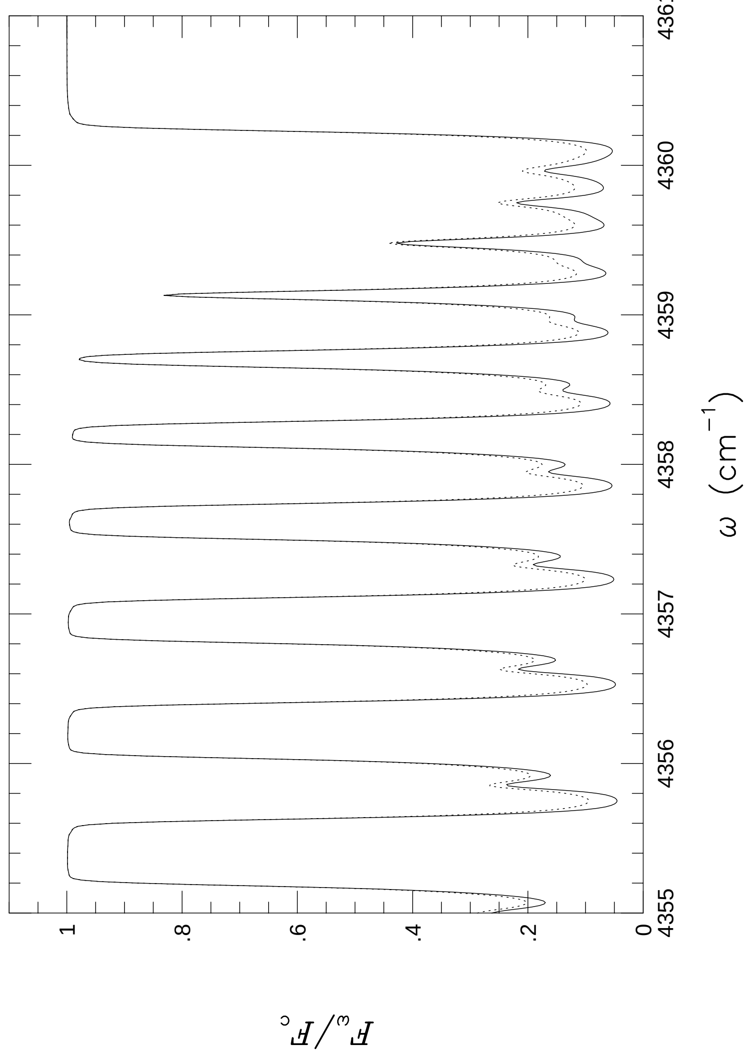

Fig. 4.19. The solid line is the synthetic spectrum calculated by the spherical radiative transfer code and the temperature stratification of the spherical model. The dotted line represents the synthetic spectrum calculated by the spherical radiative transfer code based on the temperature stratification of the plane parallel model. The parameters of the models are given in the legend to Fig 4.17

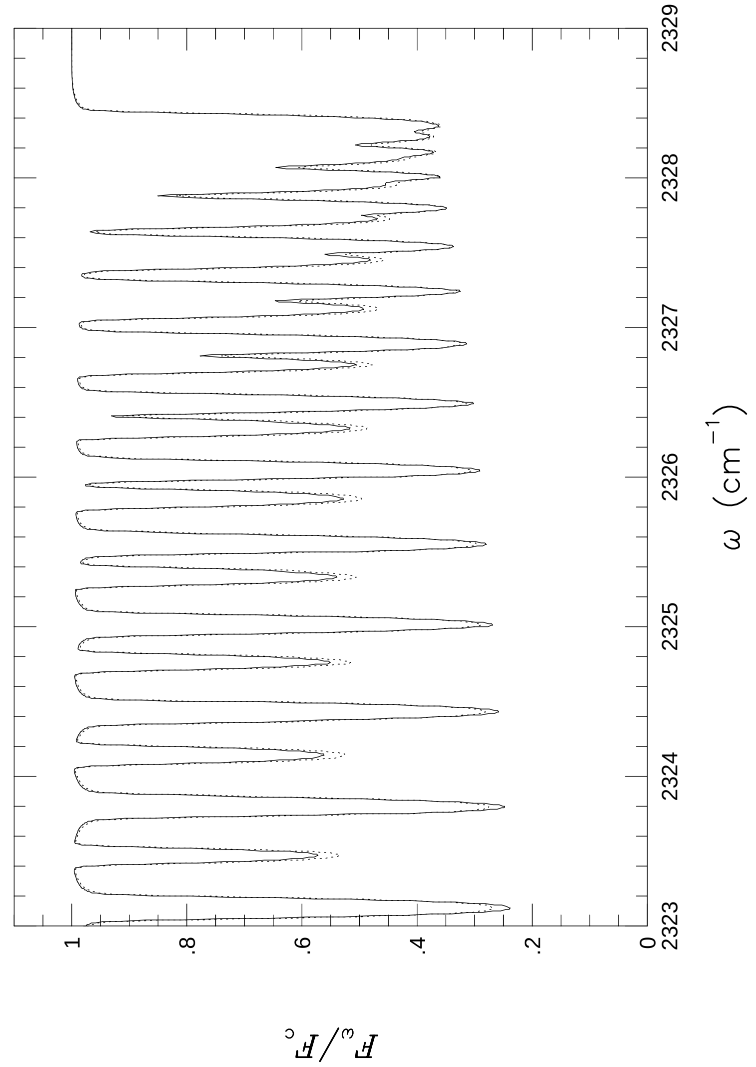

Fig. 4.20. The synthetic spectra of the CO fundamental band (1,0). The solid line corresponds to the case of spherical symmetry, while the dotted line to the case of plane parallel geometry. The parameters of the models are given in the legend to Fig 4.17

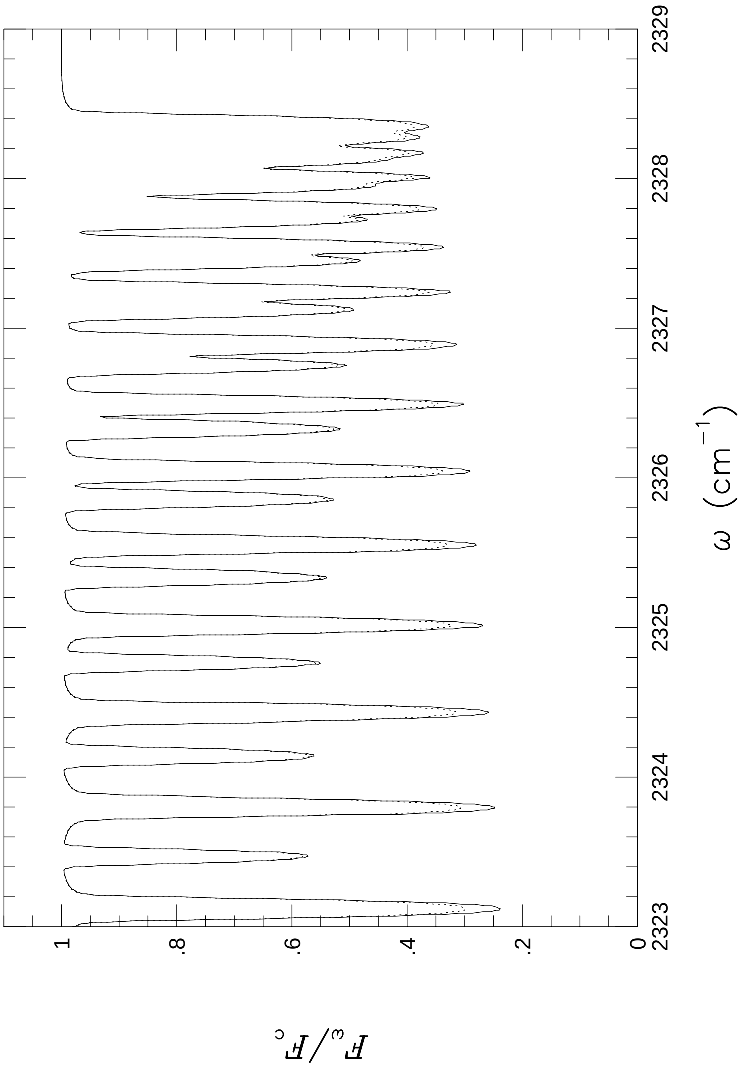

Fig. 4.21. The solid line represents the synthetic spectrum calculated by the spherical radiative transfer code and the temperature stratification of the spherical model. The dotted line is calculated by the spherical radiative transfer code, but based on the temperature stratification of the corresponding plane parallel model. The parameters of the models are given in the legend to Fig 4.17

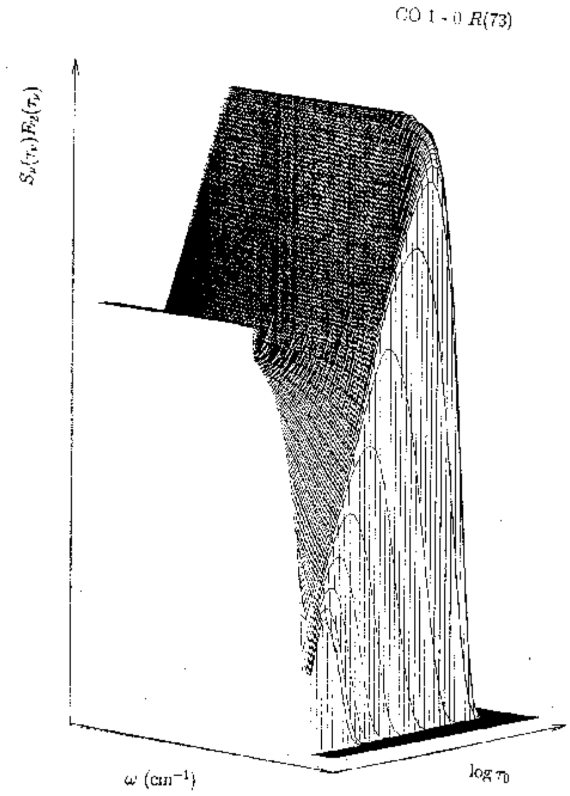

Fig. 4.22. Contribution function of CO $1-0$ $R(73)$ is plotted as a function of wavenumber ω and the depth $\log\tau_0$

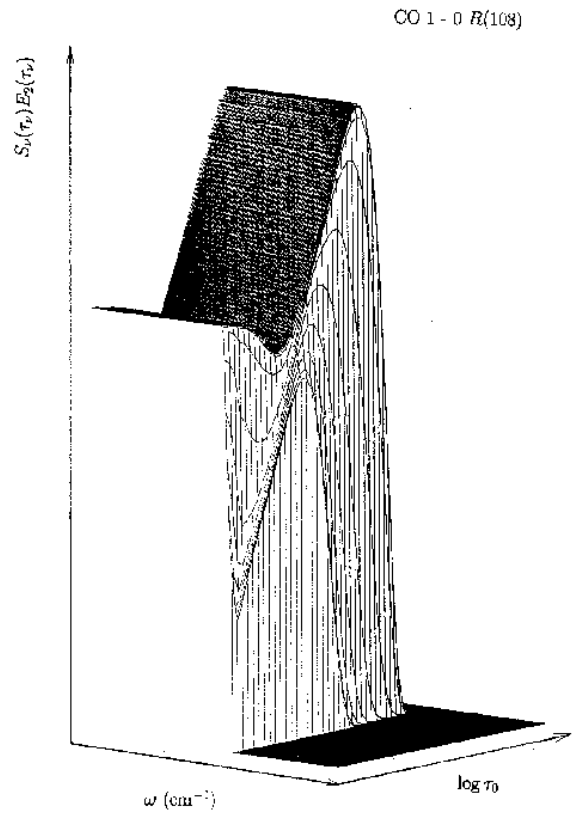

Fig. 4.23. Contribution function of CO $1-0$ $R(108)$ is plotted as a function of wavenumber ω and the depth $\log \tau_0$

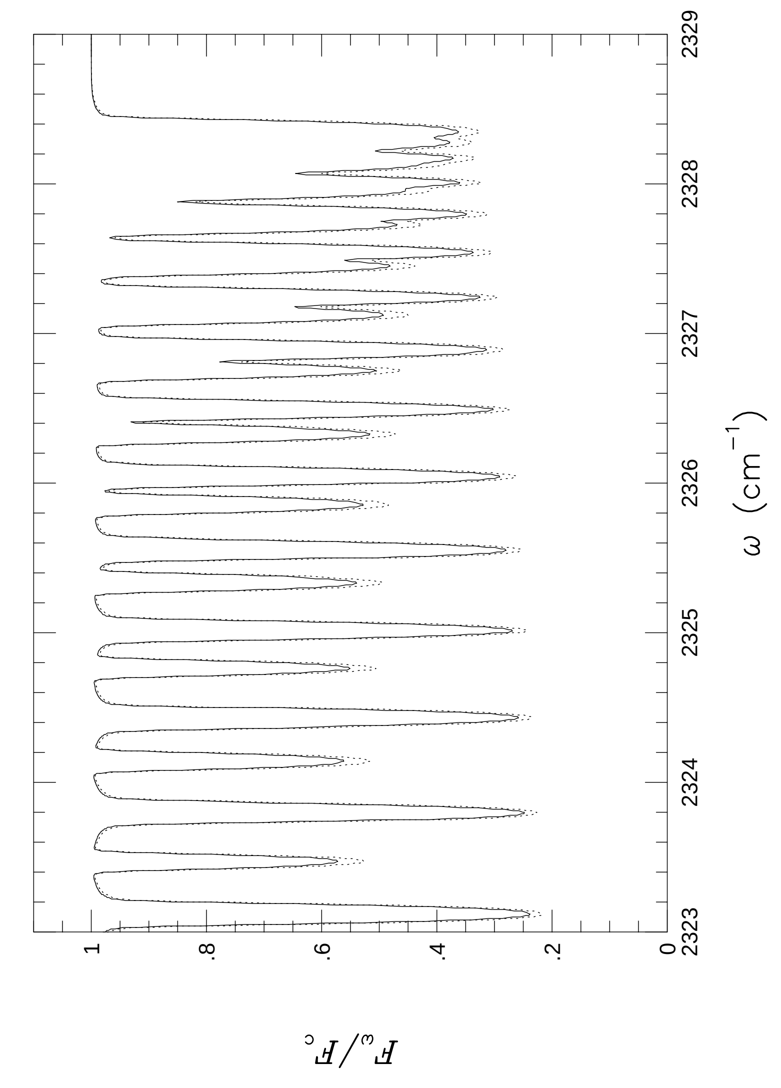

Fig. 4.24. The solid line is calculated by the spherical radiative transfer code, while the dotted line is calculated by the plane parallel code. Both spectra are calculated based on the temperature stratification of the spherical model. The parameters of the models are given in the legend to Fig 4.17

Chapter 5

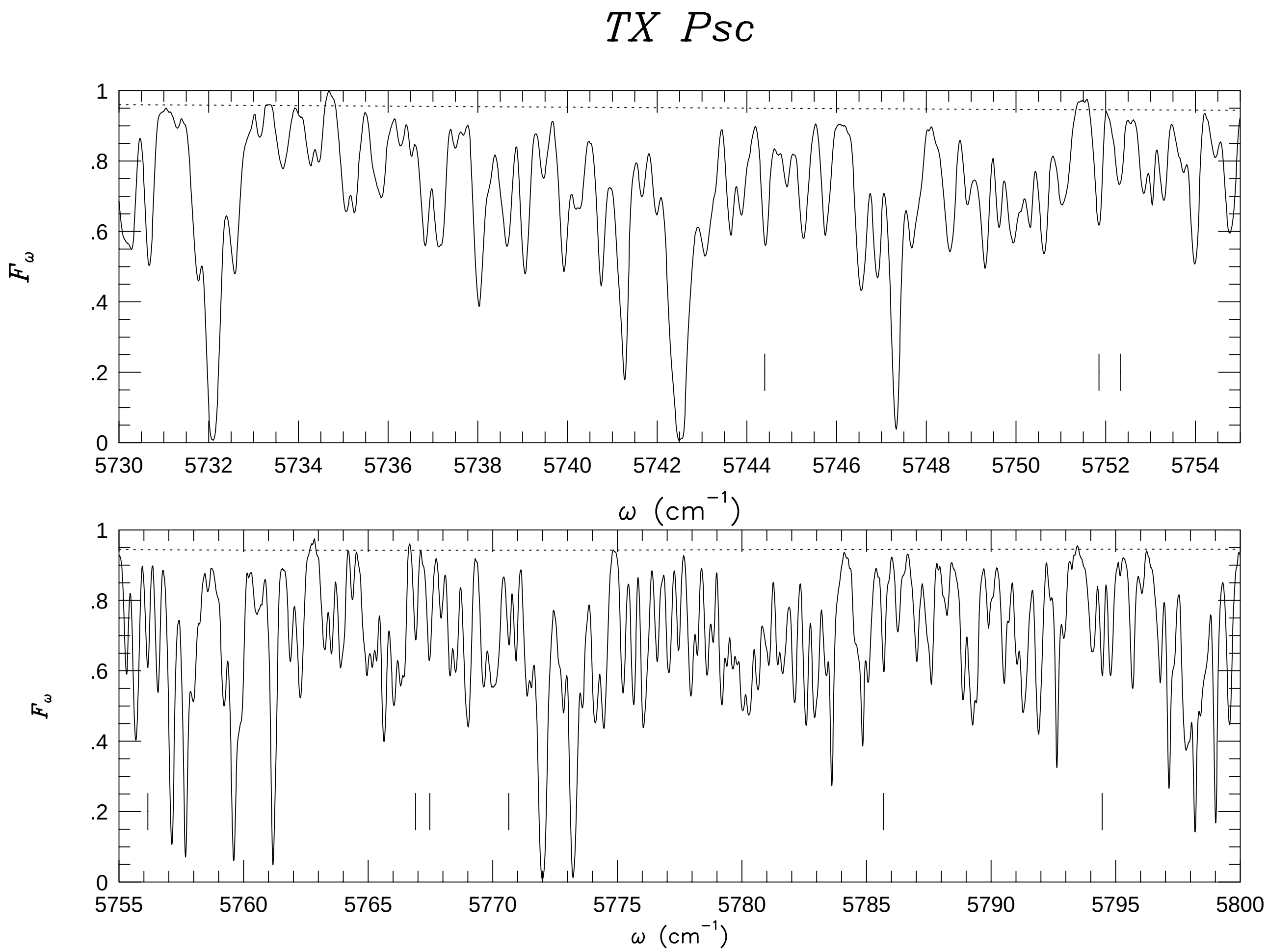

Fig. 5.1. A portion of the observed *H*-band spectrum of TX Psc. The ticks indicate the ^{12}CO lines used in the analysis

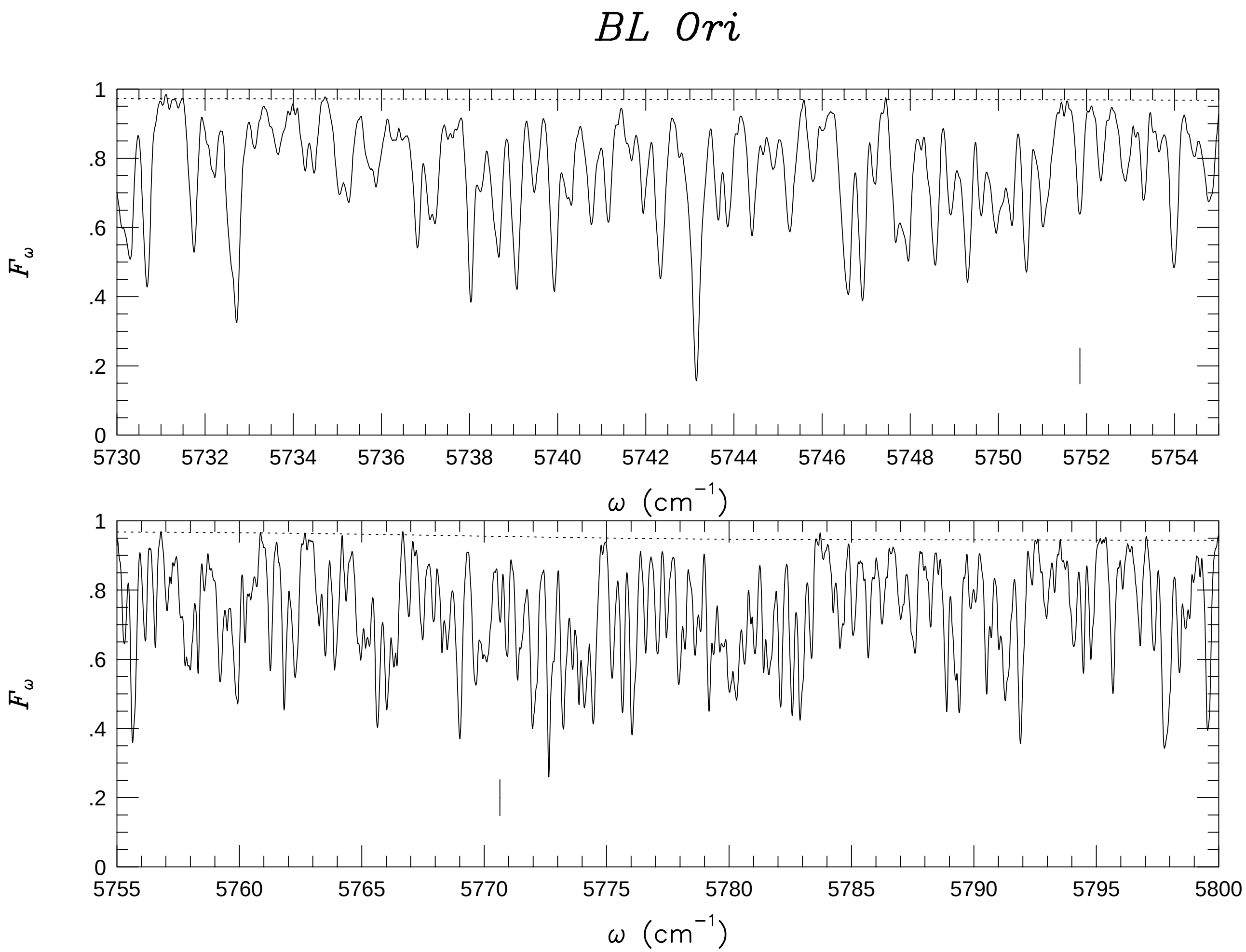

Fig. 5.2. A portion of the observed H-band spectrum of BL Ori. The ticks indicate the ^{12}CO lines used in the analysis

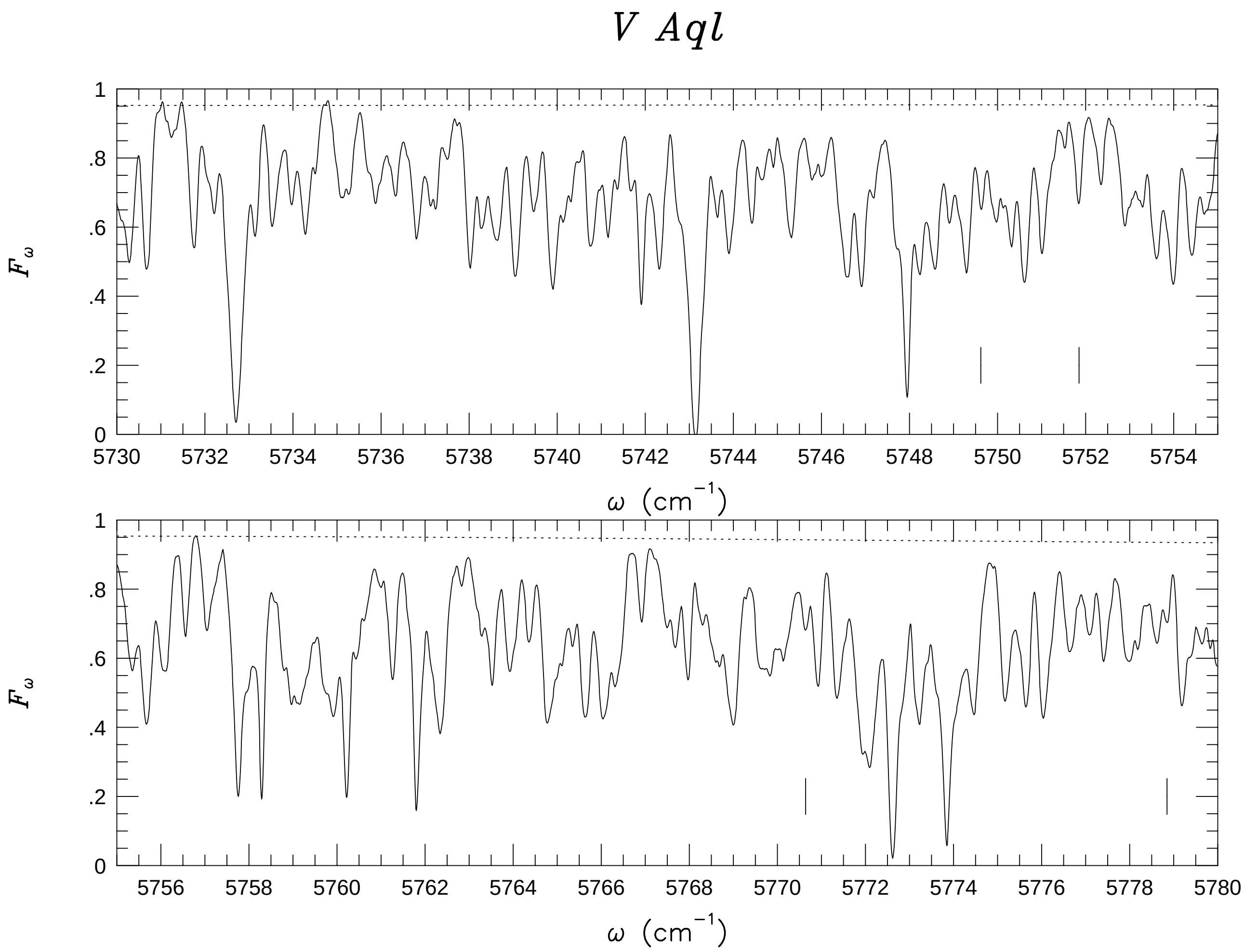

Fig. 5.3. A portion of the observed *H*-band spectrum of V Aql. The ticks indicate the ^{12}CO lines used in the analysis

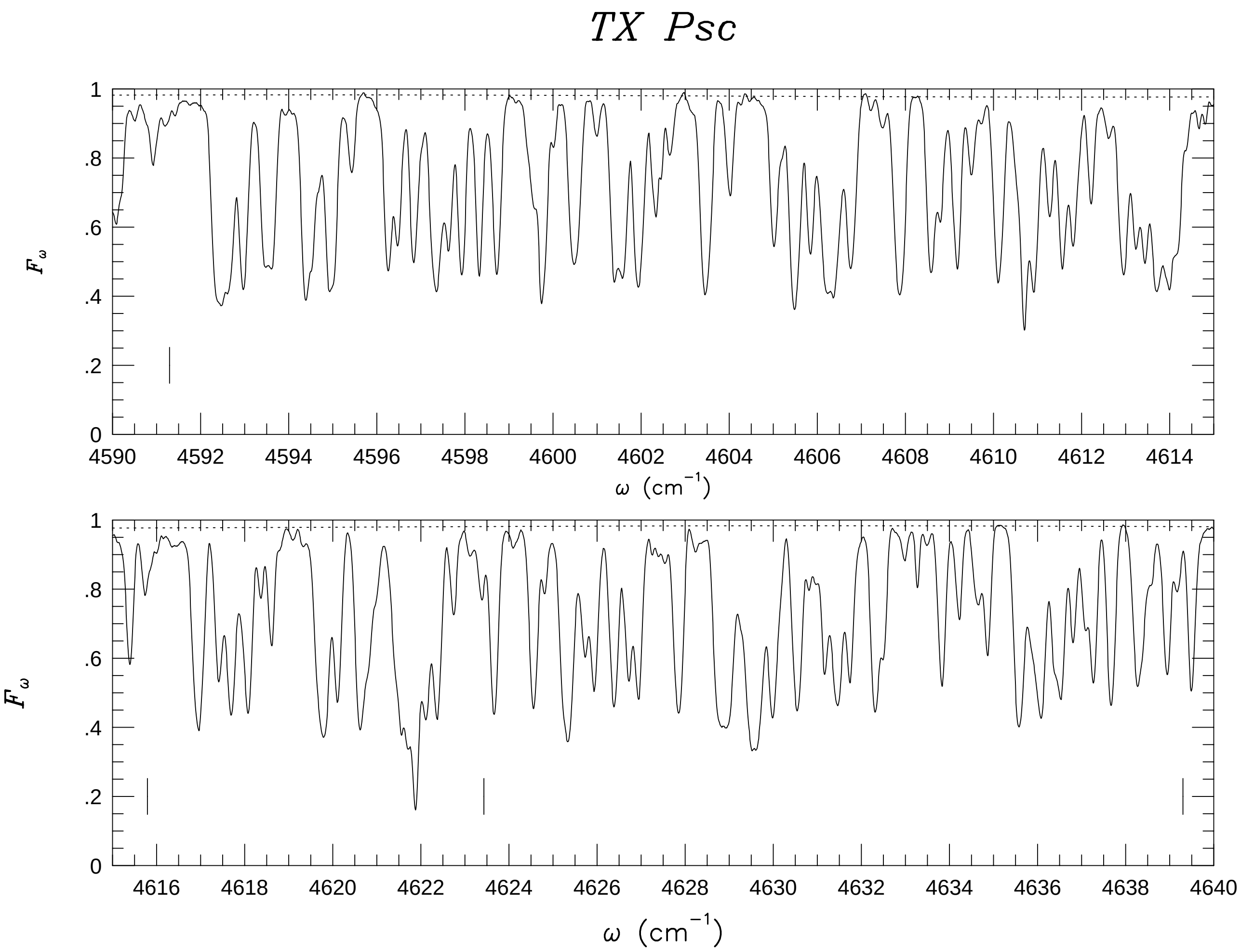

Fig. 5.4. A portion of the observed K-band spectrum of TX Psc. The ticks indicate the C_2 Phillips system lines used in the analysis

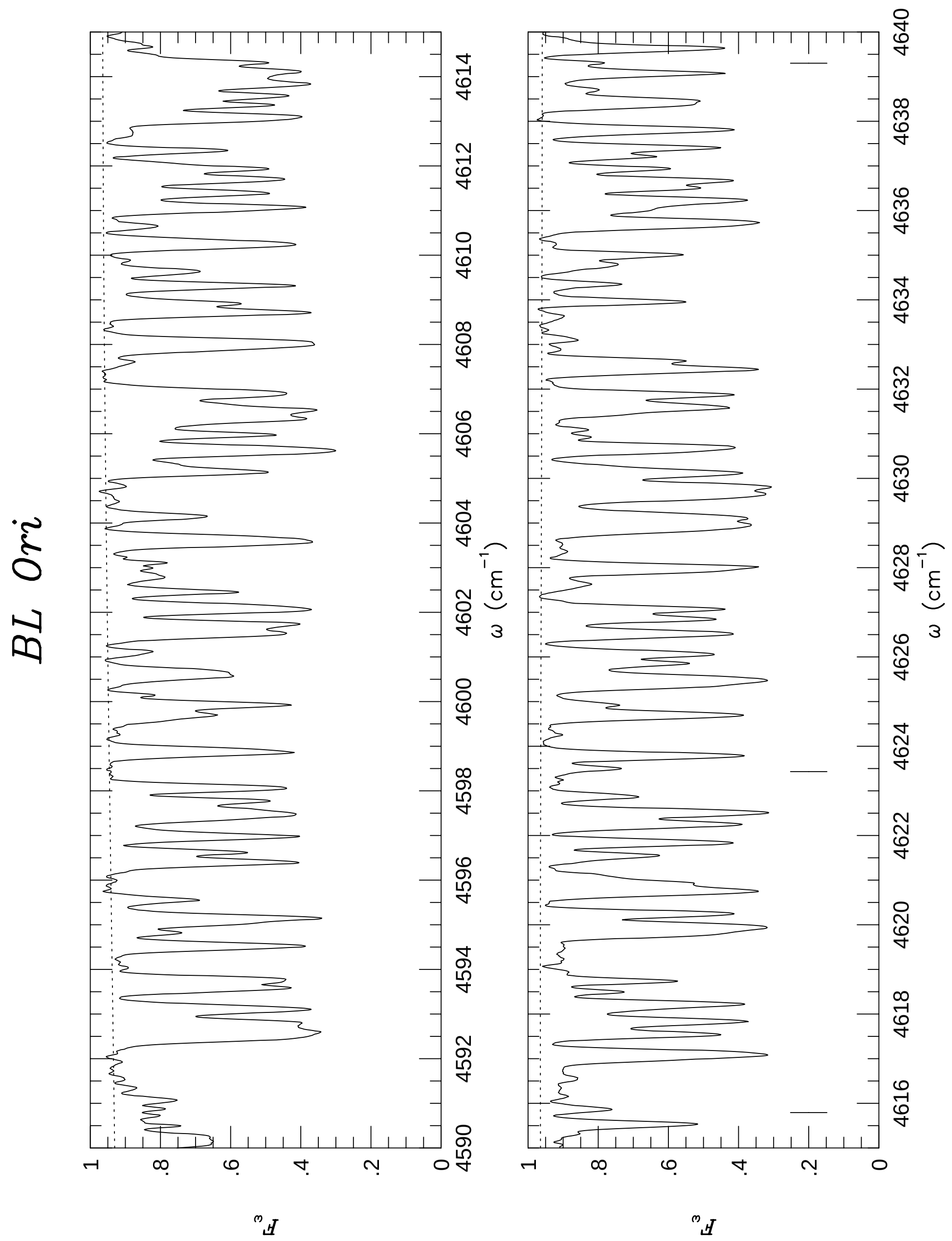

Fig. 5.5. A portion of the observed K-band spectrum of BL Ori. The ticks indicate the C_2 Phillips system lines used in the analysis

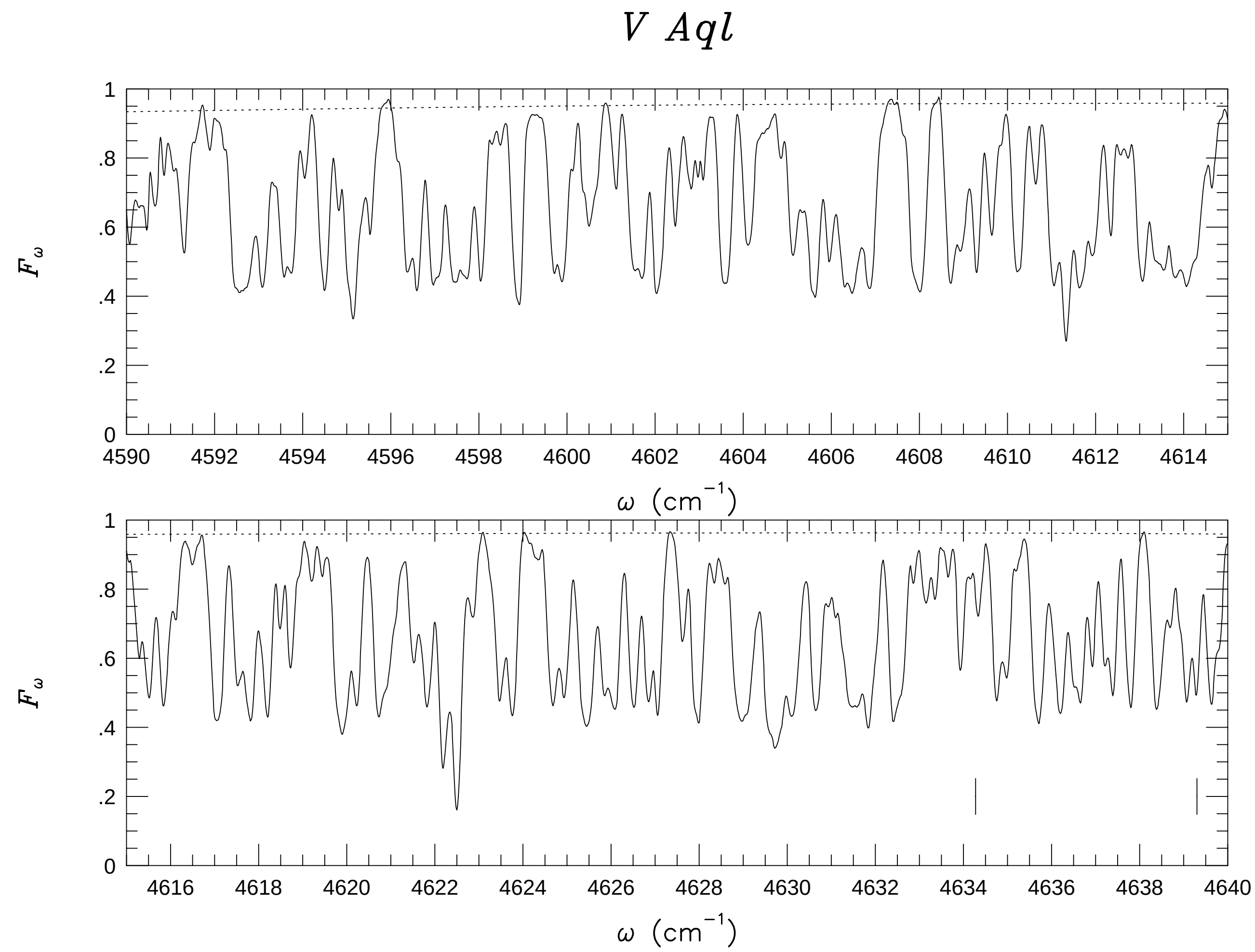

Fig. 5.6. A portion of the observed K-band spectrum of V Aql. The ticks indicate the C_2 Phillips system lines used in the analysis

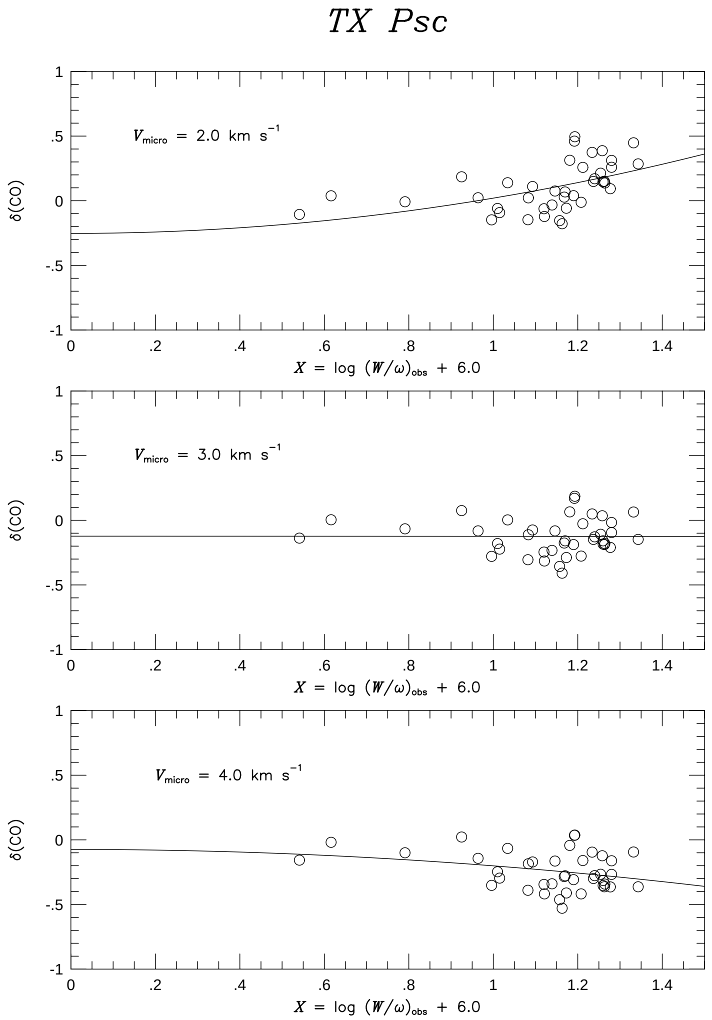

Fig. 5.7. An example of the standard analysis of the CO second overtone lines in TX Psc. The corrections to the molecular abundance are calculated based on a plane parallel model with $T_{\rm eff}$ = 3000 K, $\log g = 0.0$, $V_{\rm micro} = 3.0$ km s^{-1}, $\log \varepsilon(\rm O) = -3.07$, C/O = 1.1

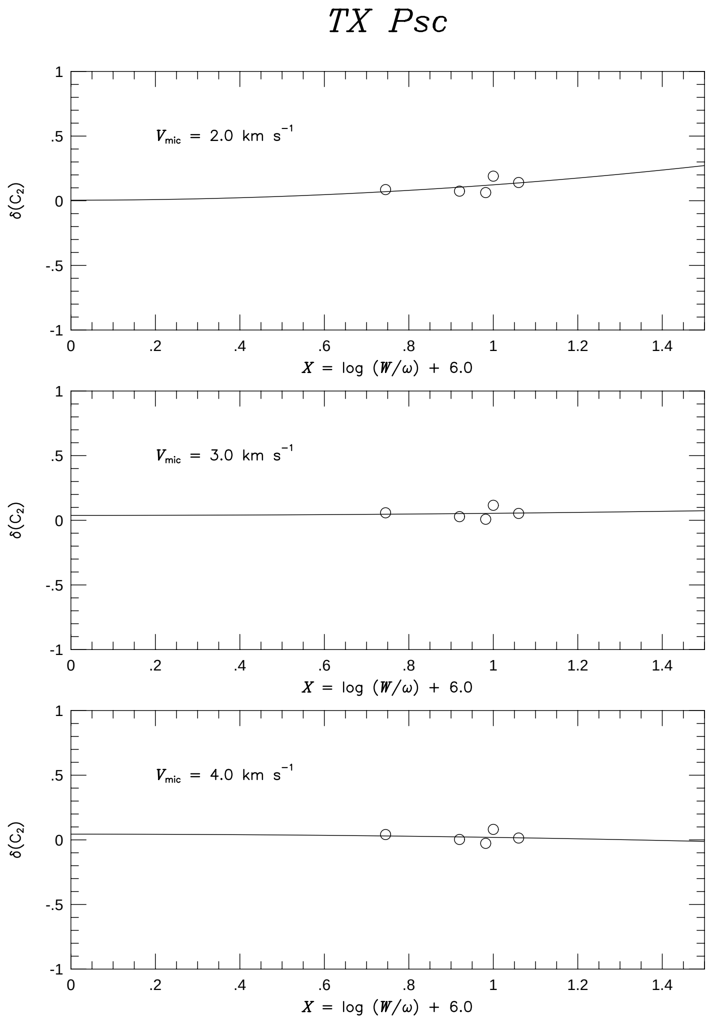

Fig. 5.8. An example of the standard analysis of the C_2 Phillips system lines in TX Psc. The parameters of the model atmosphere used are given in the legend to Fig. 5.7

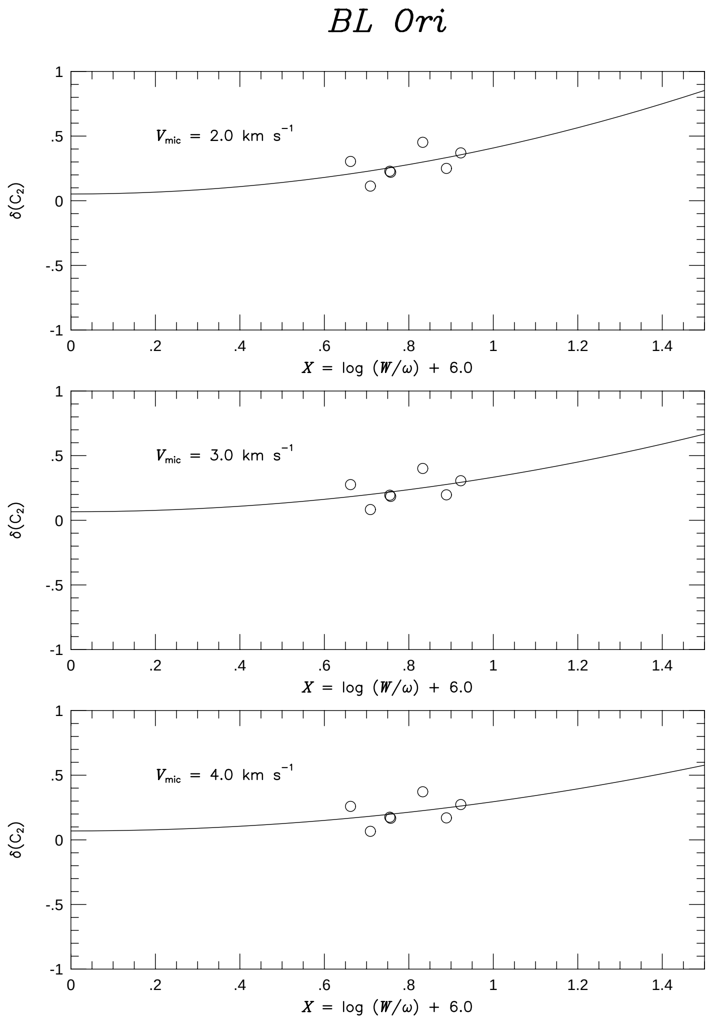

Fig. 5.9. An example of the standard analysis of the C_2 Phillips system lines in BL Ori. The corrections to the molecular abundance are calculated based on a plane parallel model with $T_{\rm eff} = 3200$ K, $\log g = 0.0$, $V_{\rm micro} = 3.0$ km s^{-1}, $\log \varepsilon(\rm O) = -3.07$, C/O = 1.1

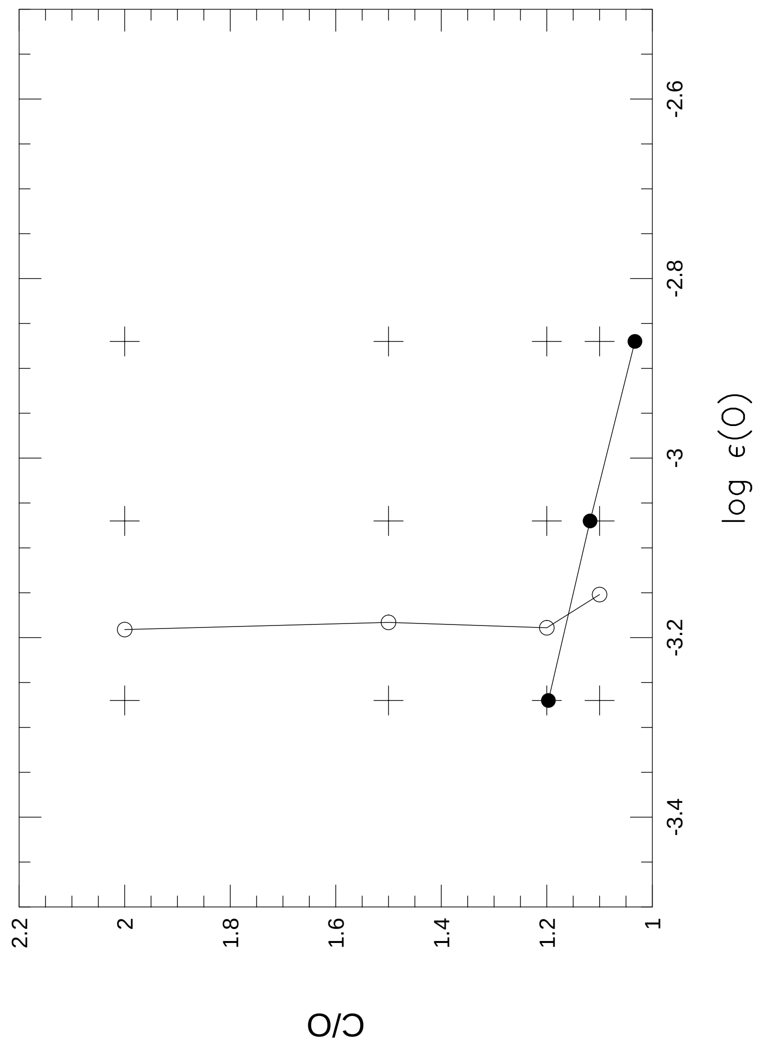

Fig. 5.10. Self-consistent analysis for TX Psc. The open circles represent the points where $\delta(\mathrm{CO}) = 0$, while the filled circles represent the points where $\delta(\mathrm{C_2}) = 0$. The intersection of the two lines gives the set of ($\log\varepsilon(\mathrm{O})$,C/O) where both of $\delta(\mathrm{CO})$ and $\delta(\mathrm{C_2})$ are zero. The crosses represent the grid points of model atmospheres

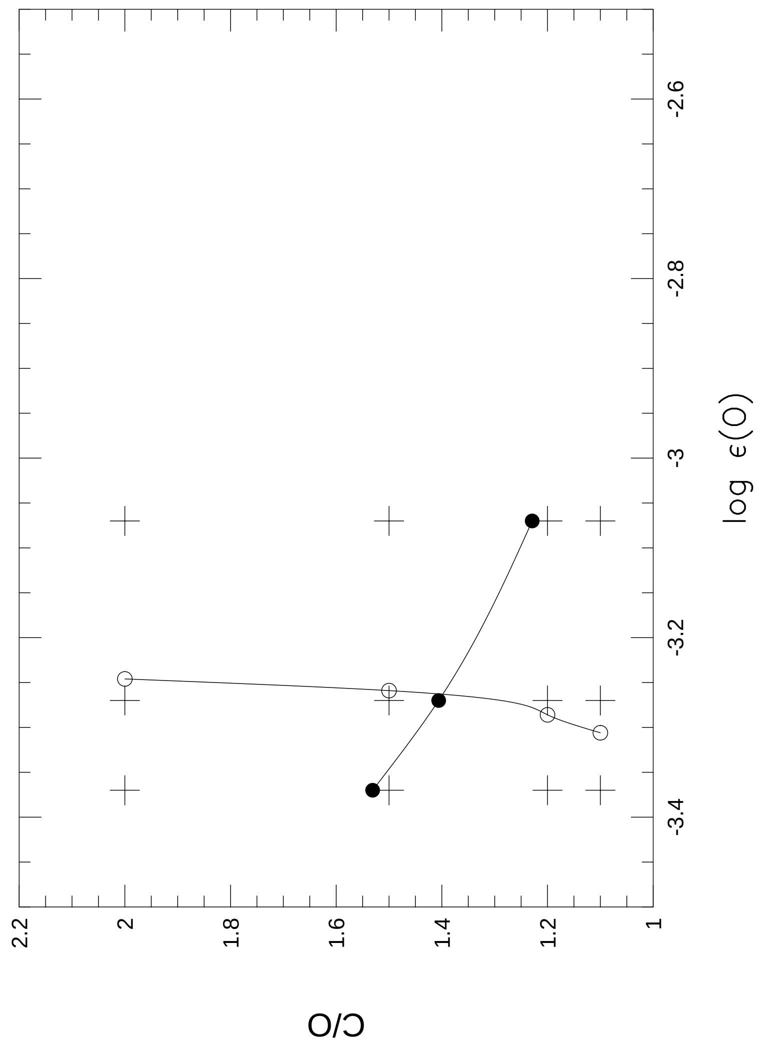

Fig. 5.11. Self-consistent analysis for BL Ori. See also the legend to Fig. 5.10

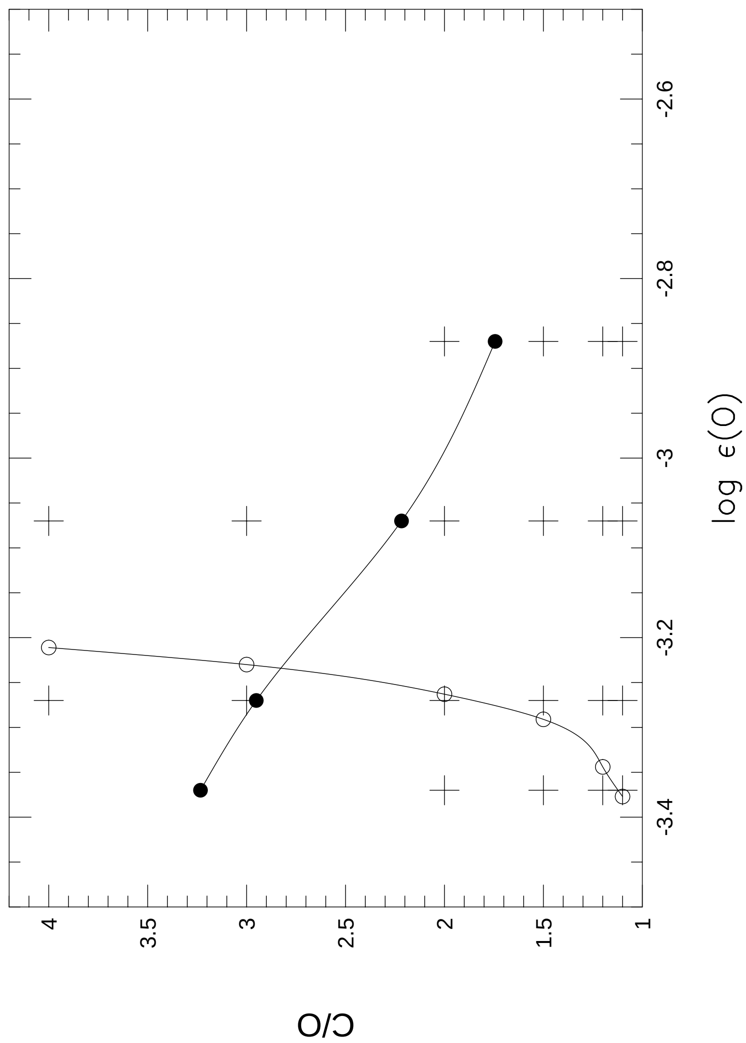

Fig. 5.12. Self-consistent analysis for V Aql. See also the legend to Fig. 5.10

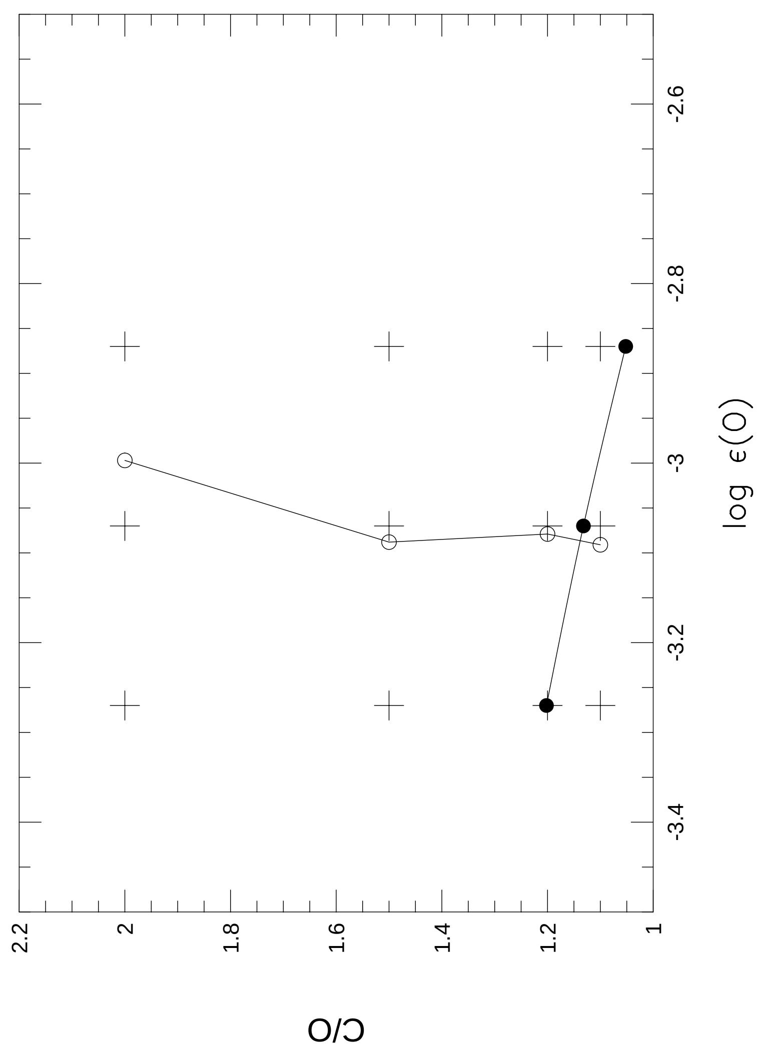

Fig. 5.13. Self-consistent analysis with the spherical models for TX Psc. See also the legend to Fig. 5.10

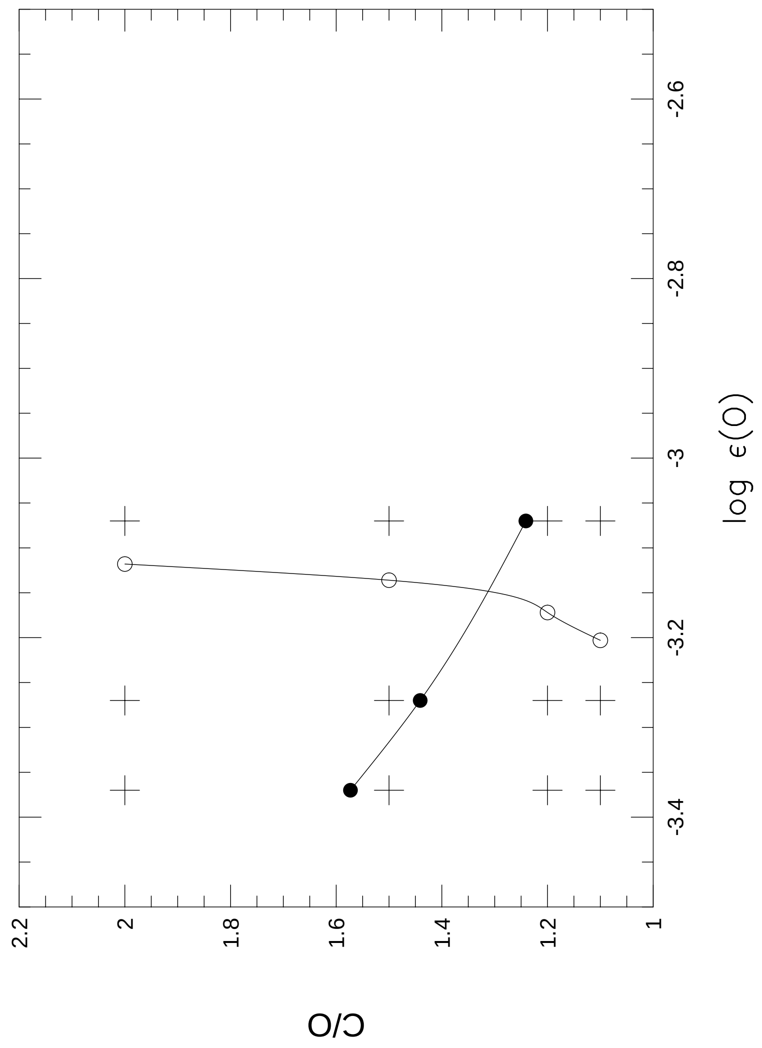

Fig. 5.14. Self-consistent analysis with spherical models for BL Ori. See also the legend to Fig. 5.10

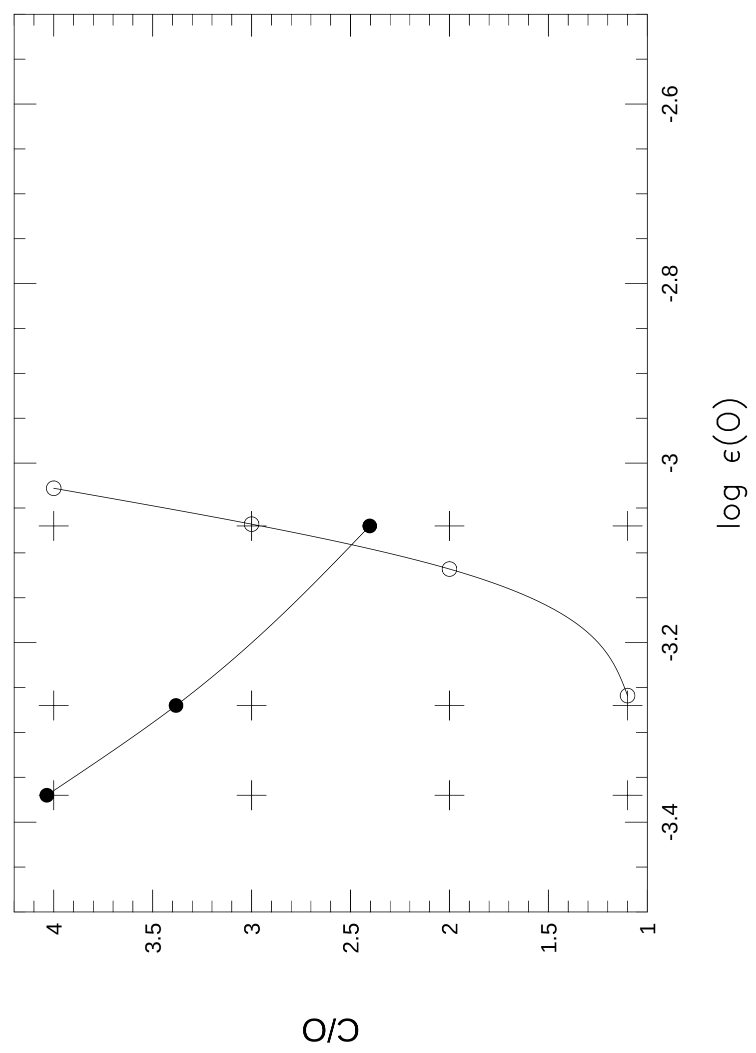

Fig. 5.15. Self consistent analysis with the spherical models for V Aql. See also the legend to Fig. 5.10

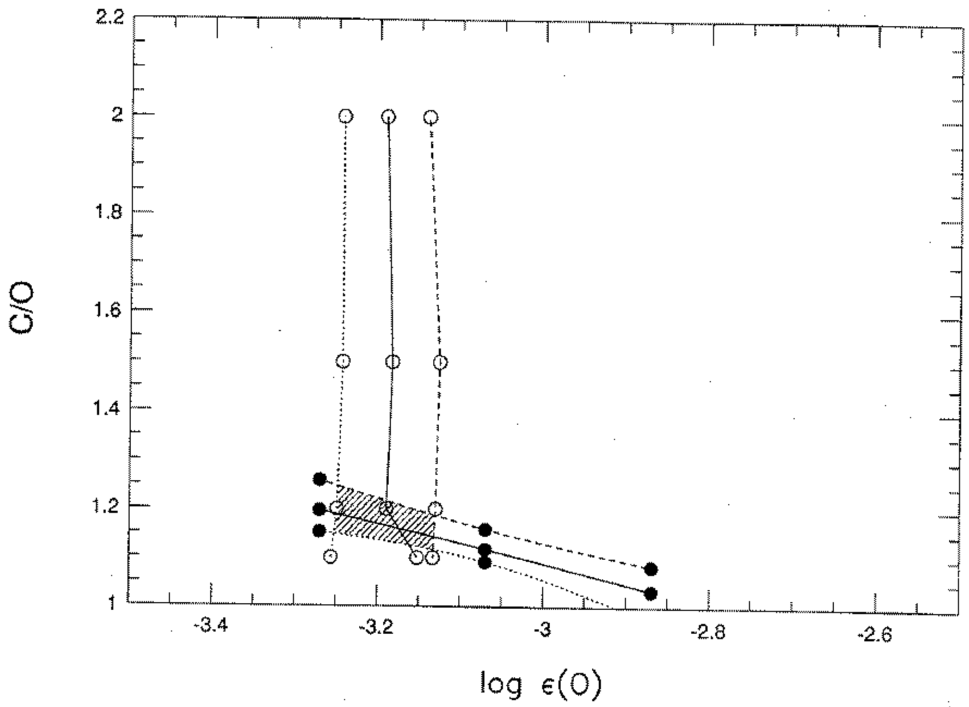

Fig. 5.16. The analysis of the uncertainties of determination of $\log \varepsilon(\mathrm{O})$ and C/O ratio for TX Psc. The dashed lines are drawn by taking the upper limits of $\delta(\mathrm{CO})$ and $\delta(\mathrm{C_2})$ at each grid point. The dotted lines represent the cases where the lower limits of $\delta(\mathrm{CO})$ and $\delta(\mathrm{C_2})$ are taken

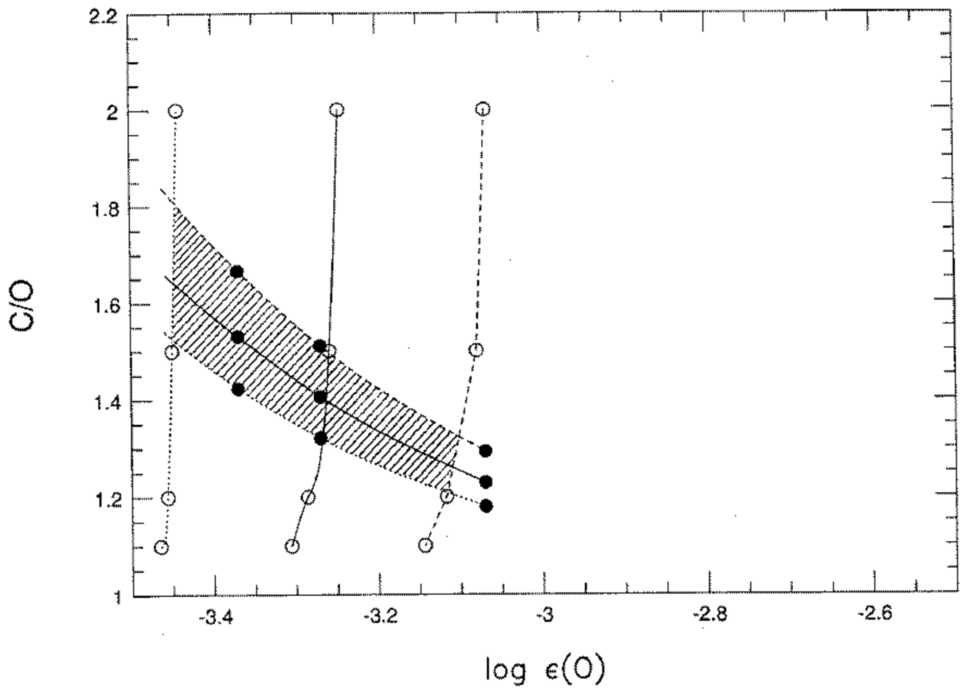

Fig. 5.17. The analysis of the uncertainties of determination of $\log \varepsilon(\mathrm{O})$ and C/O ratios for BL Ori. See also the legend to Fig. 5.16

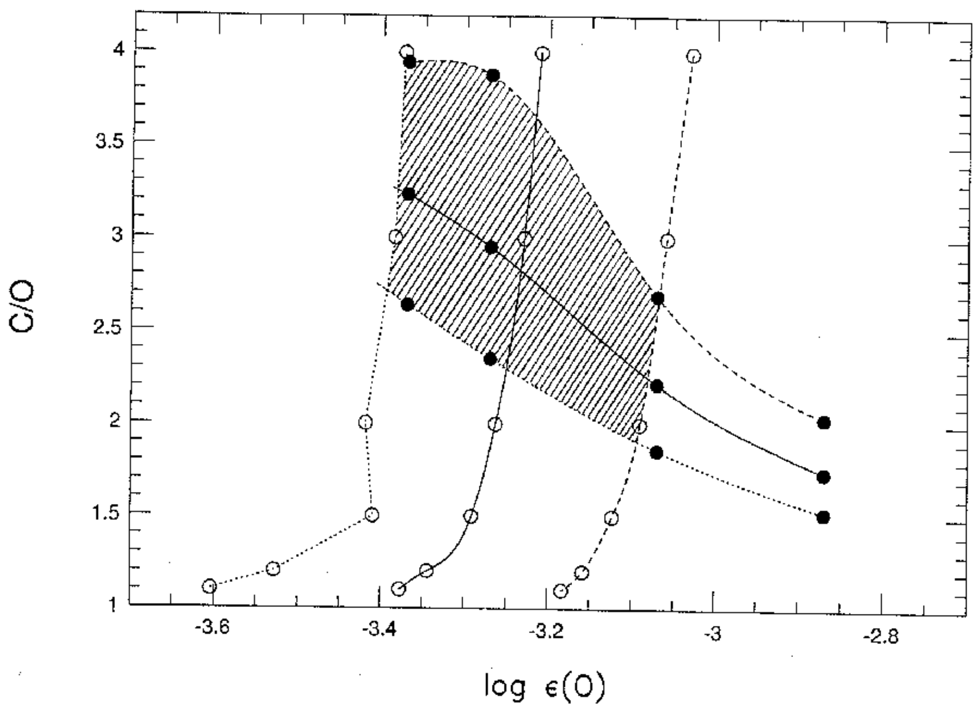

Fig. 5.18. The analysis of the uncertainties of determination of $\log\varepsilon(\mathrm{O})$ and C/O ratios for V Aql. See also the legend to Fig. 5.16

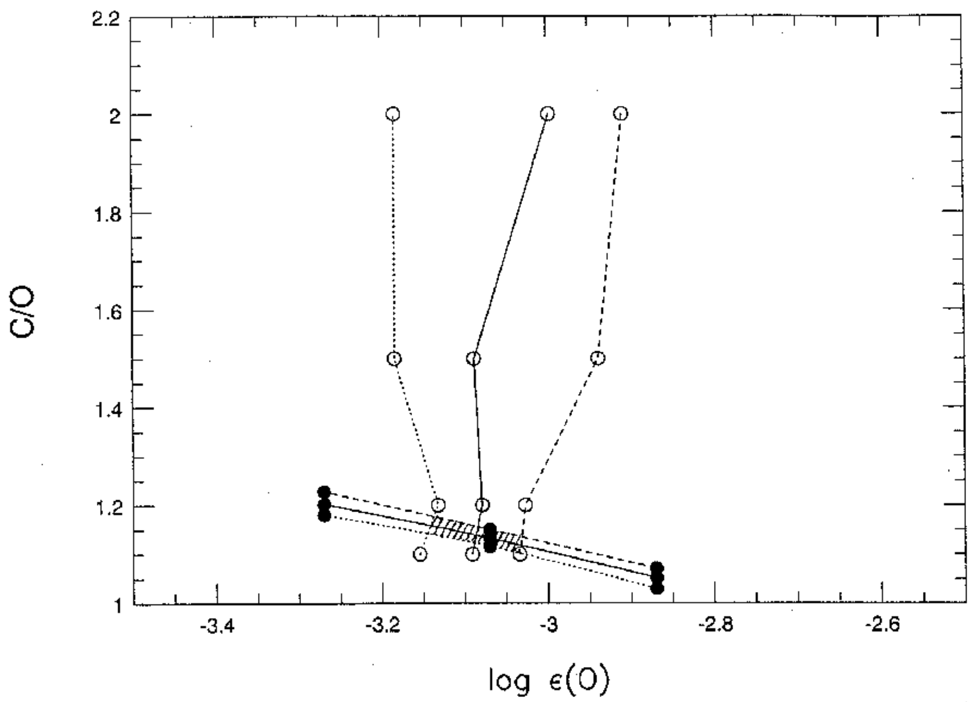

Fig. 5.19. The analysis of the uncertainties of determination of $\log \varepsilon(\mathrm{O})$ and C/O ratios for TX Psc in the case where the spherical models are used. See also the legend to Fig. 5.16

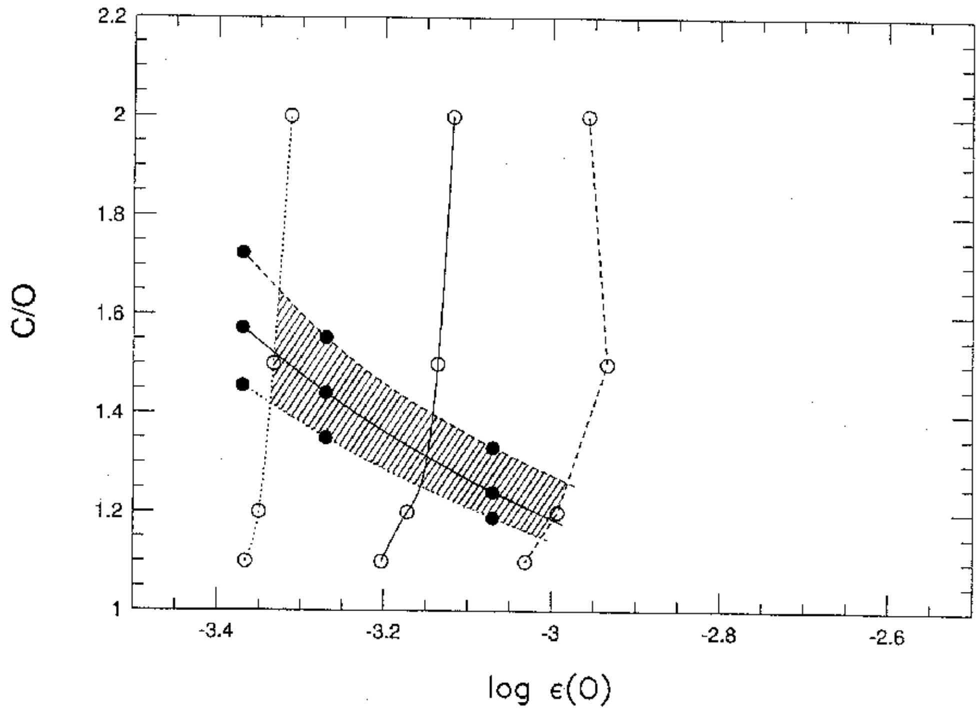

Fig. 5.20. The analysis of the uncertainties of determination of $\log \varepsilon(\mathrm{O})$ and C/O ratios for BL Ori in the case where the spherical models are used. See also the legend to Fig. 5.16

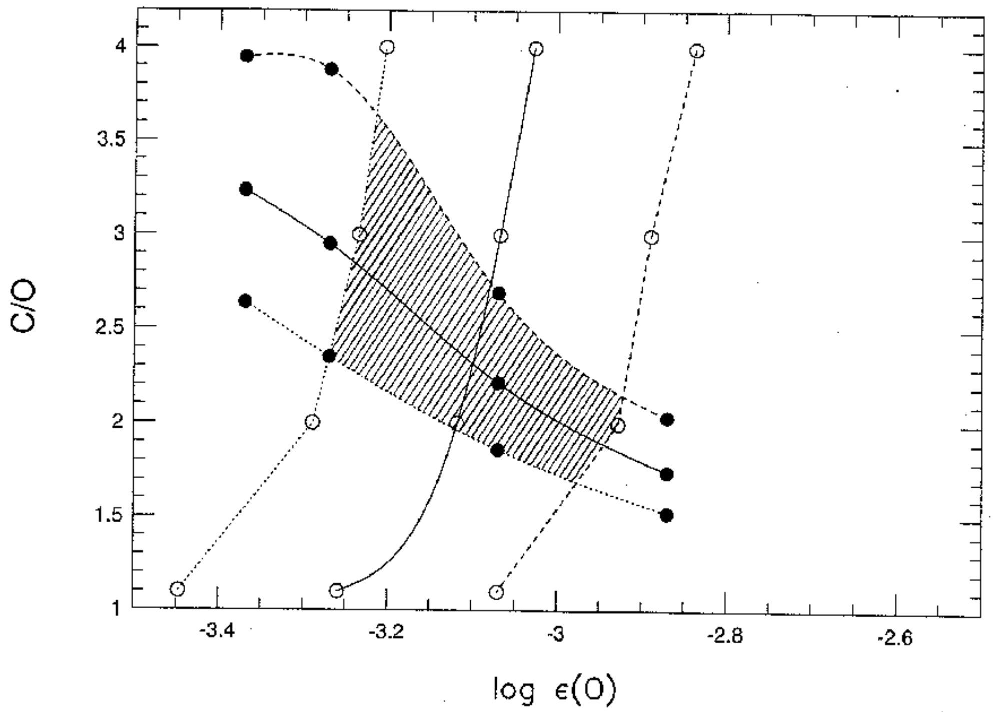

Fig. 5.21. The analysis of the uncertainties of determination of $\log \varepsilon(\mathrm{O})$ and C/O ratios for V Aql in the case where the spherical models are used. See also the legend to Fig. 5.16

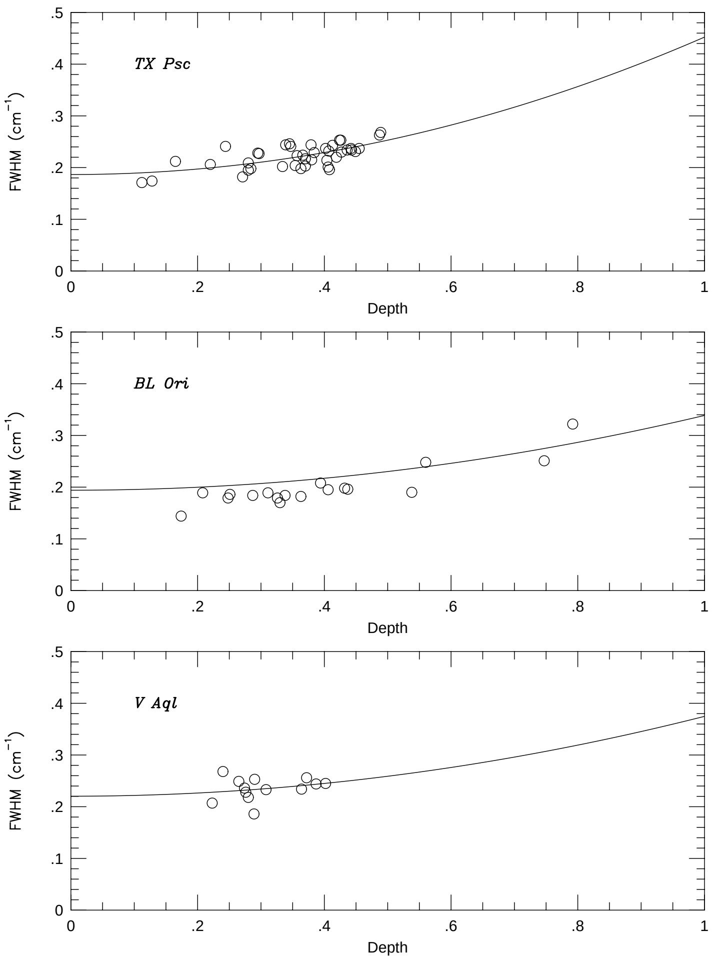

Fig. 5.22. The full widths at half maximum are plotted against the central depths for the lines of the CO second overtone bands

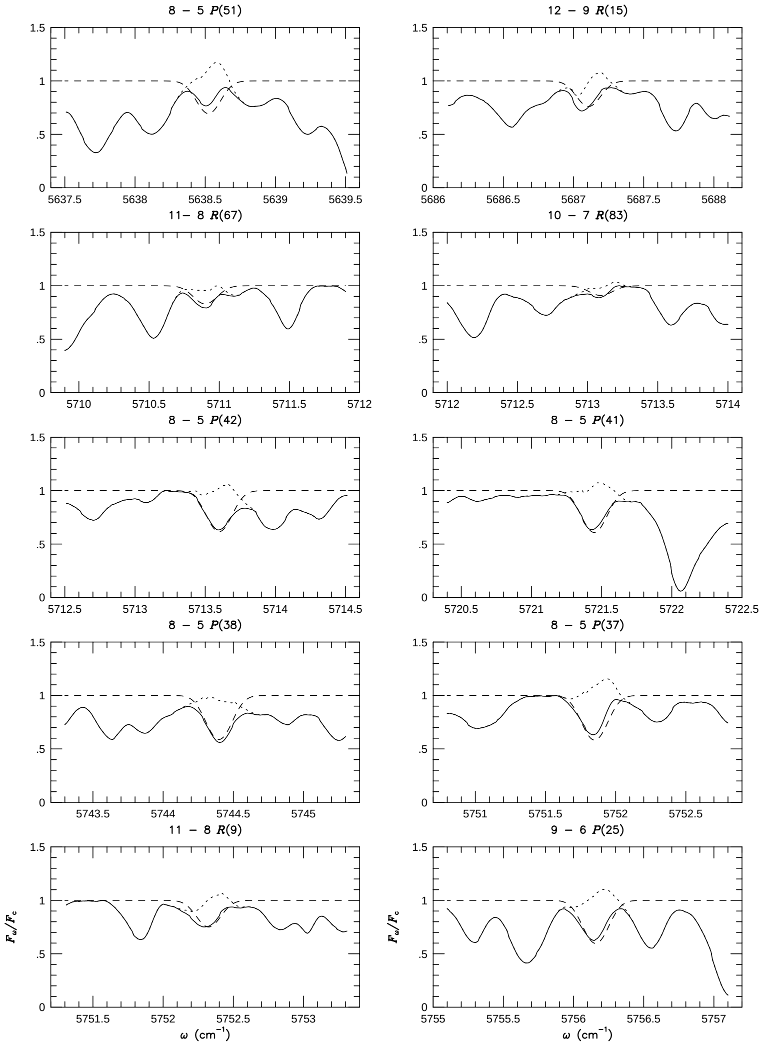

Fig. 5.23. Synthetic spectrum for each CO second overtone line used in the analysis of TX Psc. The solid lines represent the observed spectra, the dashed lines represent the synthetic spectra, and the dotted lines represent the ratios between the observed and the predicted spectra

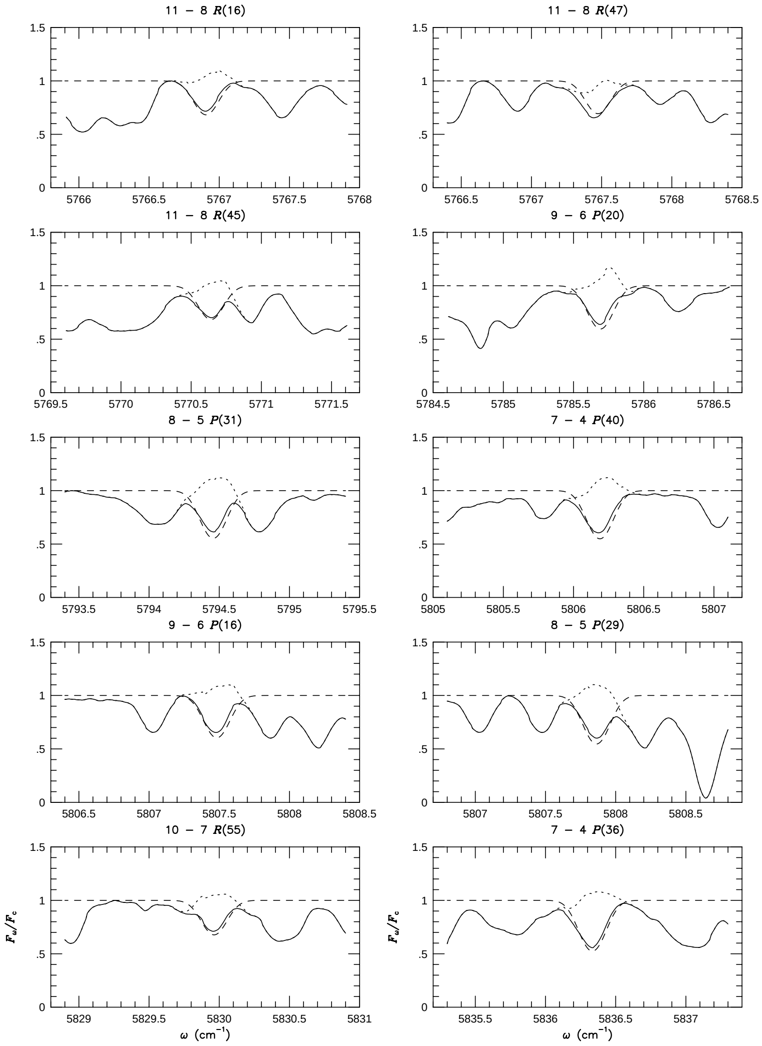

Fig. 5.23. — Continued

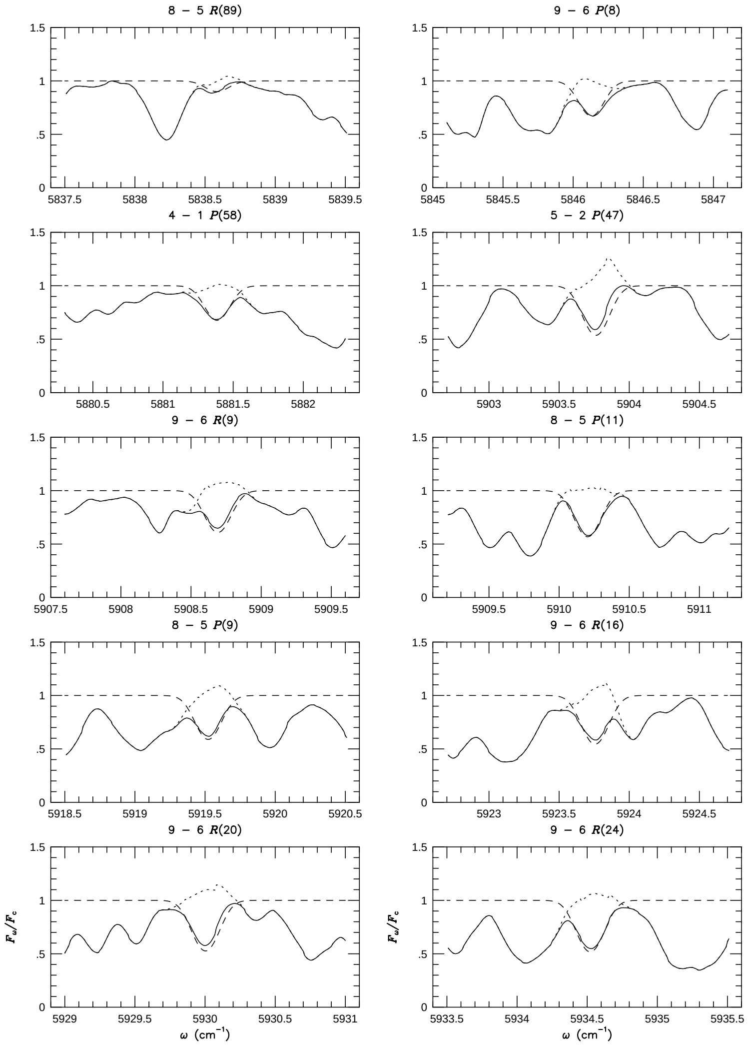

Fig. 5.23. — Continued

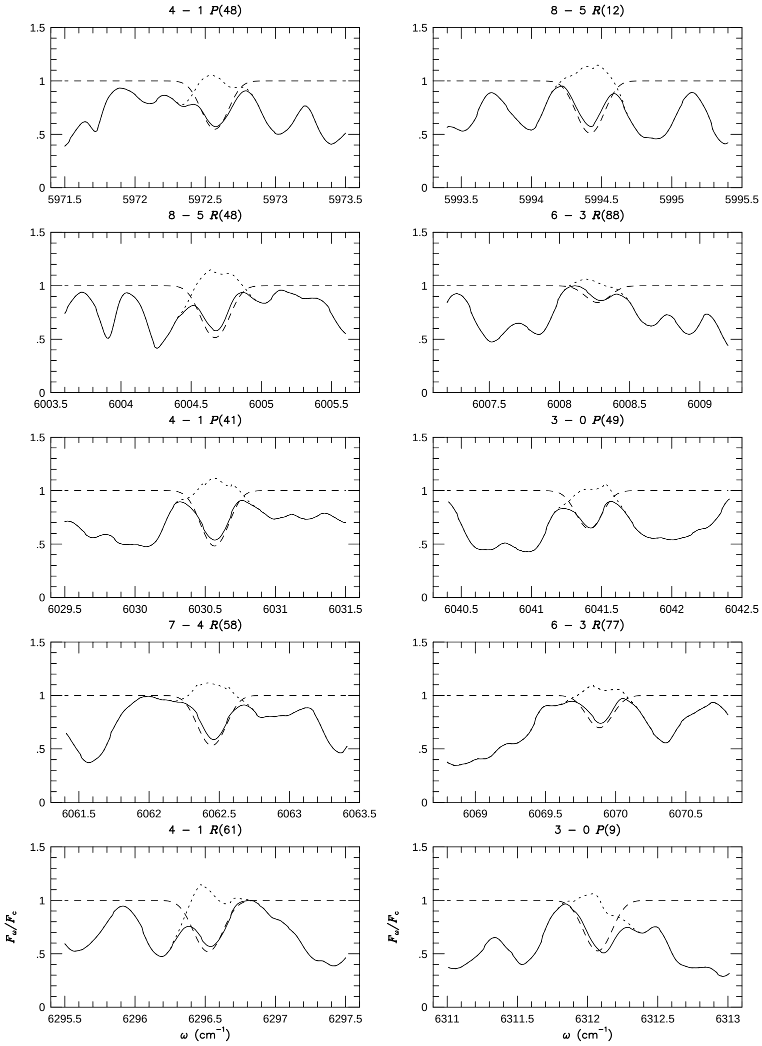

Fig. 5.23. — Continued

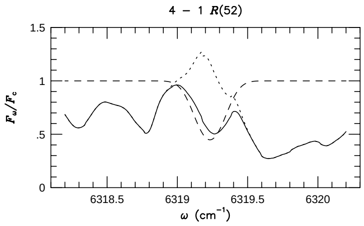

Fig. 5.23. — Continued

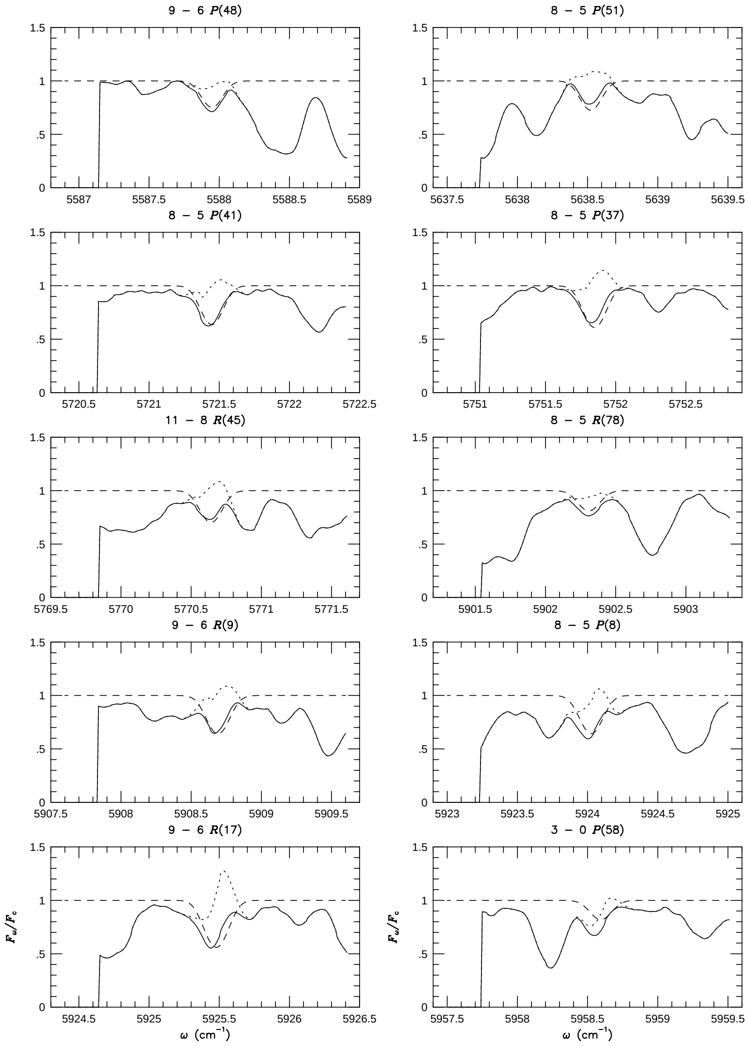

Fig. 5.24. Synthetic spectrum for each CO second overtone line used in the analysis of BL Ori. See also the legend to Fig. 5.23

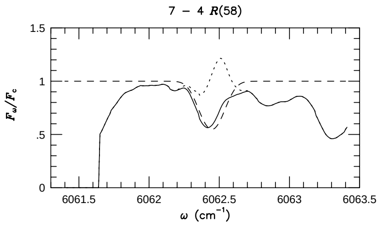

Fig. 5.24. — Continued

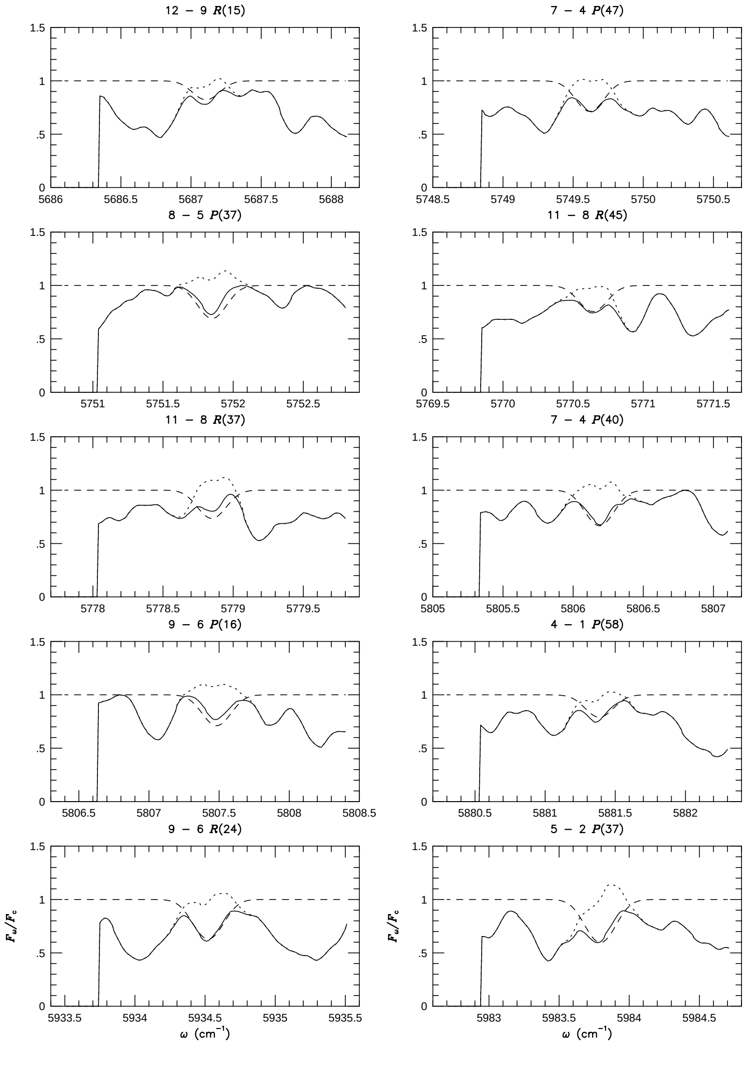

Fig. 5.25. Synthetic spectrum for each CO second overtone line used in the analysis of V Aql. See also the legend to Fig. 5.23

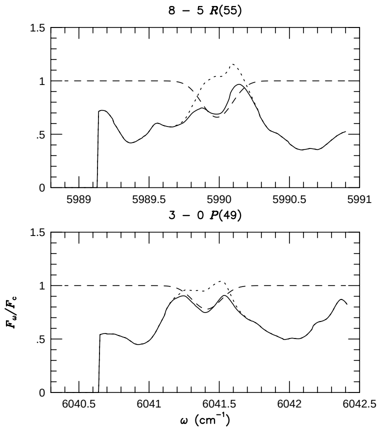

Fig. 5.25. — Continued

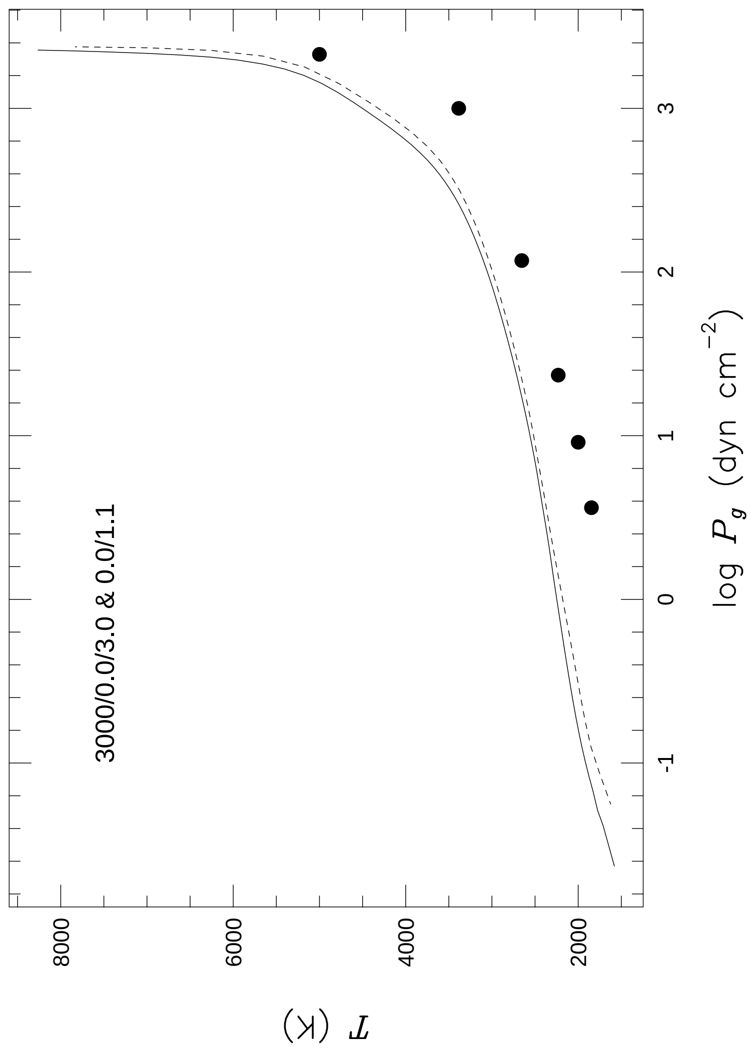

Fig. 5.26. The model atmospheres used in the present work is compared with that of Lambert et al. (1986). The solid line represents the temperature stratification of a model with the effect of turbulent pressure included. The dotted line represent a model without the effect of turbulent pressure. The filled circles represent a model used in the analysis by Lambert et al. (1986). The three models are calculated with $T_{\rm eff} = 3000$, $\log g = 0.0$, and C/O $= 1.1$ in plane parallel geometry

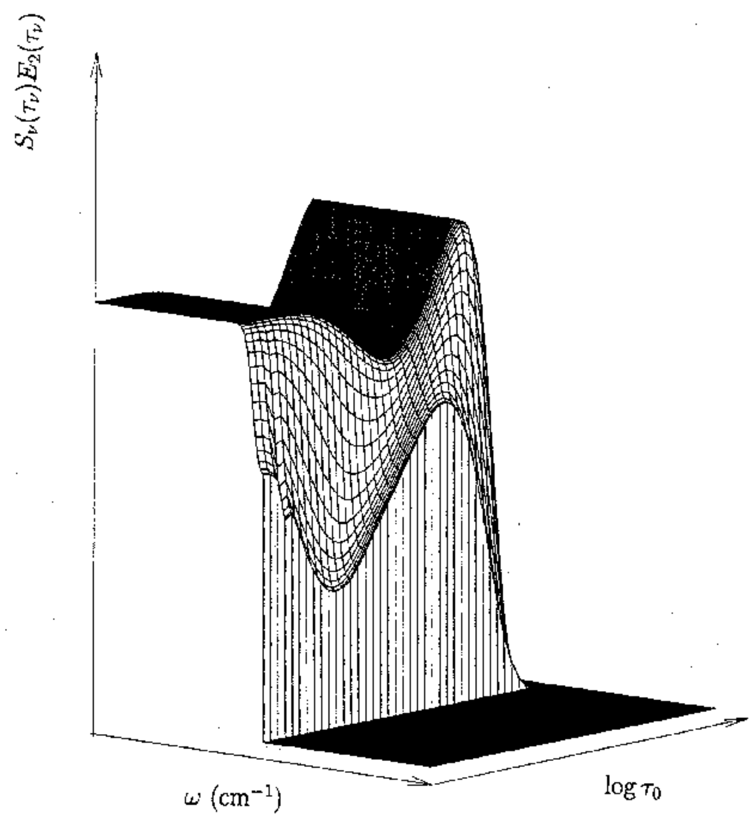

Fig. 5.27. Contribution function for a CO second overtone line, 12 - 9 $R(15)$ is plotted as a function of wavenumber and depth $\log \tau_0$

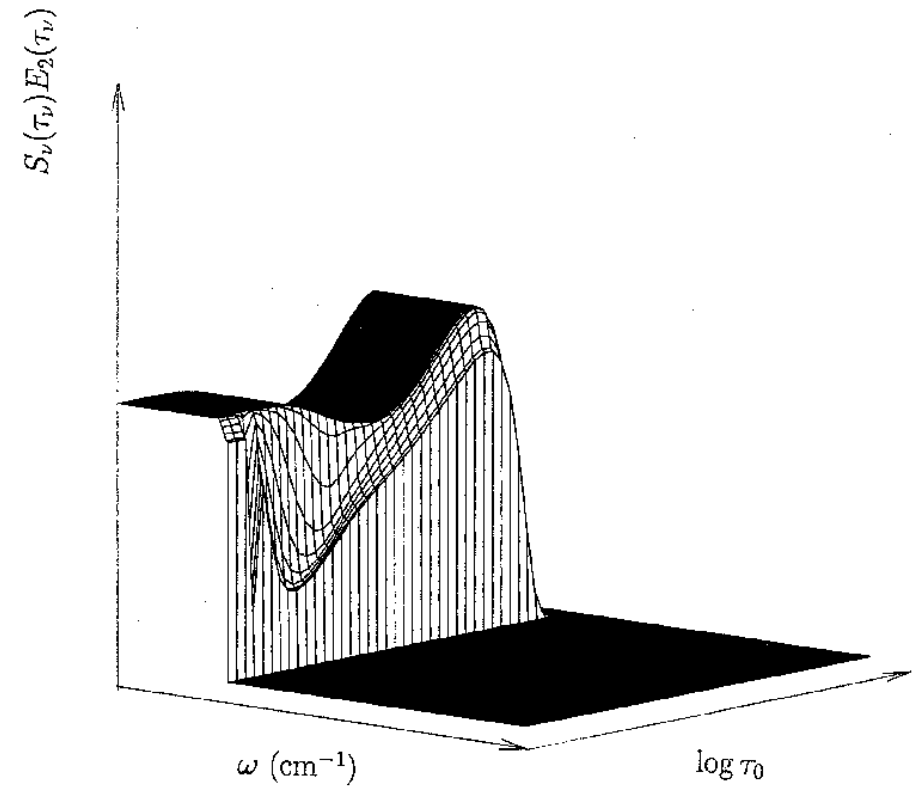

Fig. 5.28. Contribution function for a C_2 Phillips system line, 0 - 2 $P(2)$ is plotted as a function of wavenumber and depth $\log \tau_0$

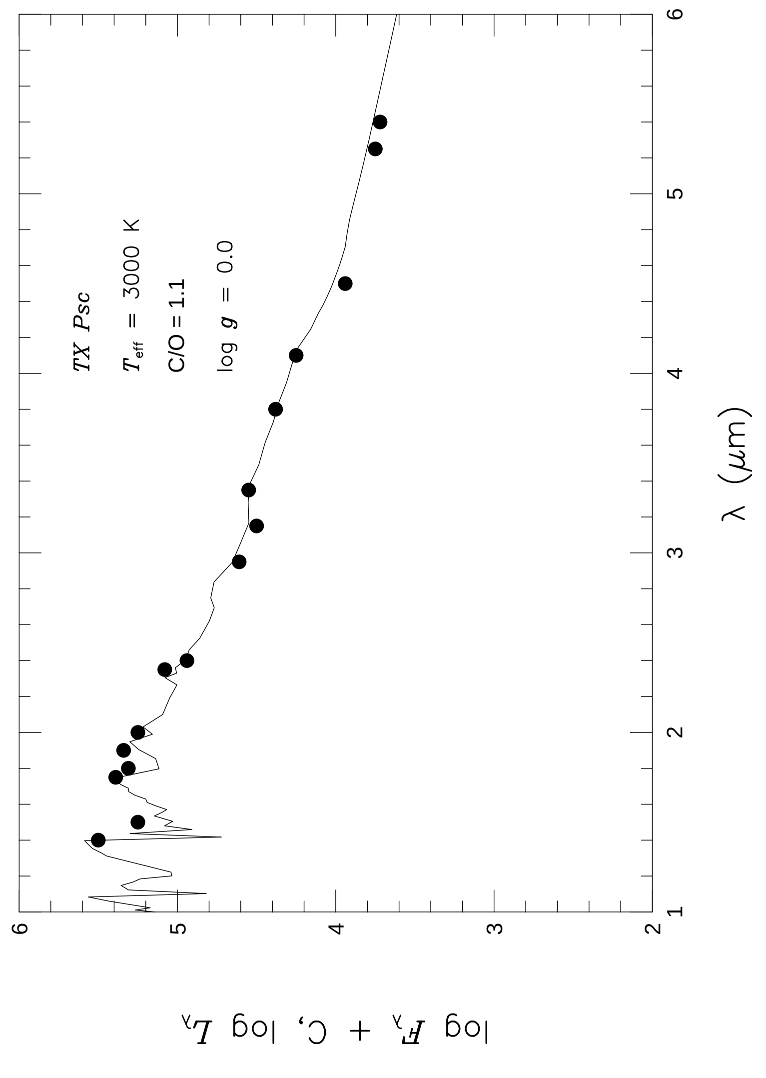

Fig. 5.29. Comparison between the observed flux of TX Psc and the emergent flux from the final model. The observed flux was read from Johnson et al. (1985)

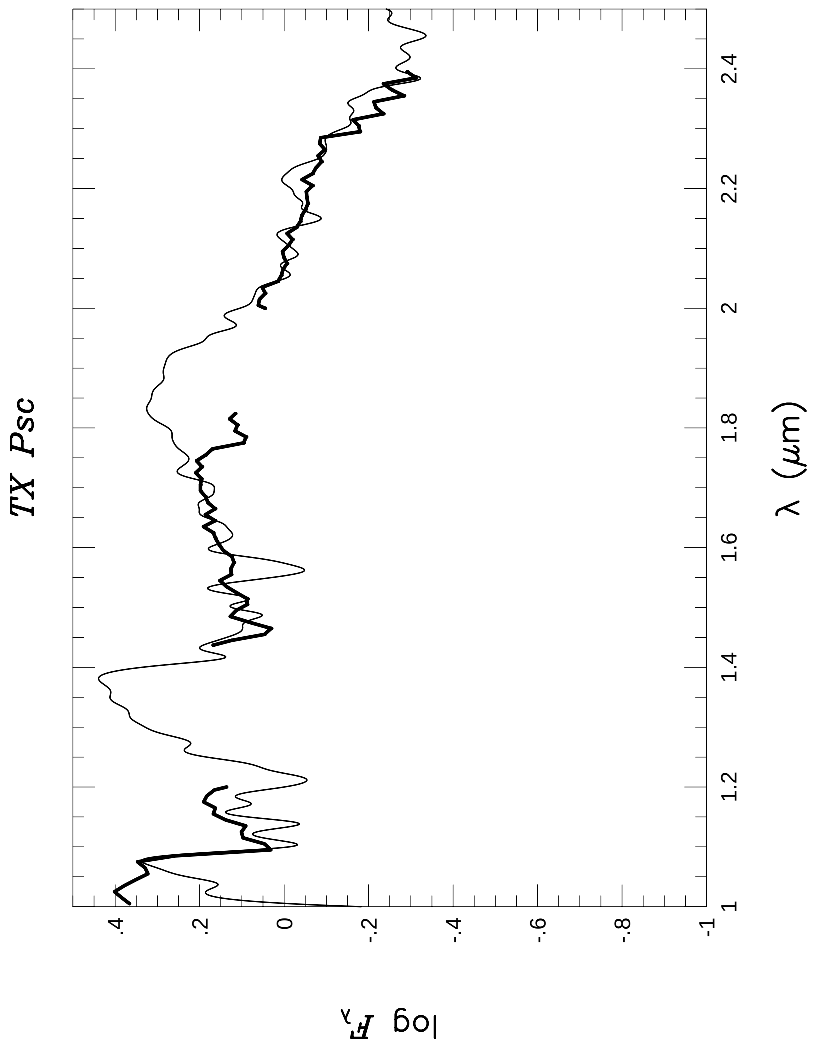

Fig. 5.30. Synthetic spectrum for TX Psc (thin line) is compared with the spectrophotometric observation (thick line) by Lazáro et al. (1994)

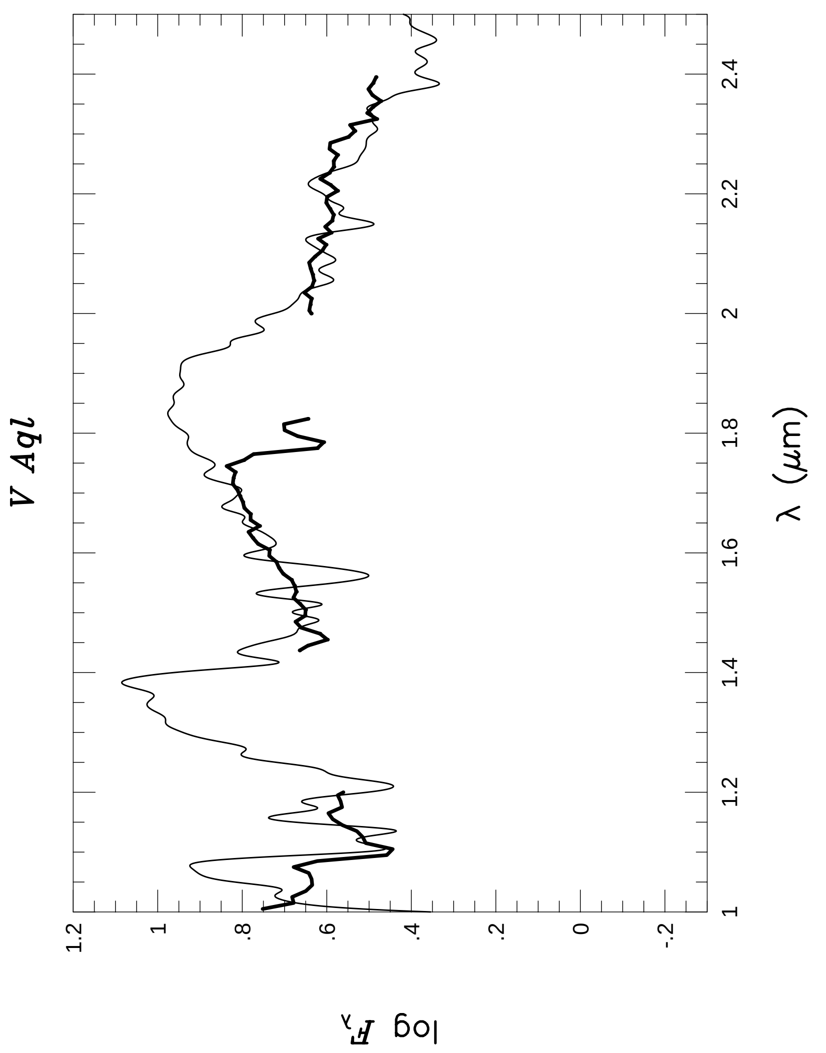

Fig. 5.31. Synthetic spectrum for V Aql (thin line) is compared with the spectrophotometric observation (thick line) by Lazáro et al. (1994)

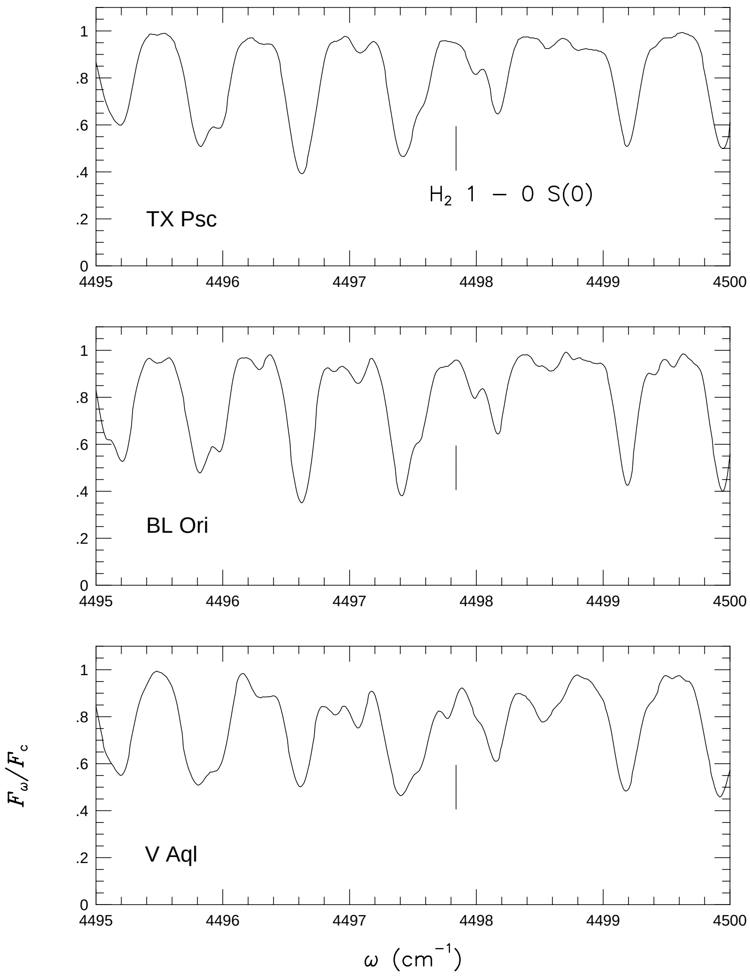

Fig. 5.32. A portion of spectra around H_2 $1-0$ $S(0)$ line for TX Psc, BL Ori, and V Aql

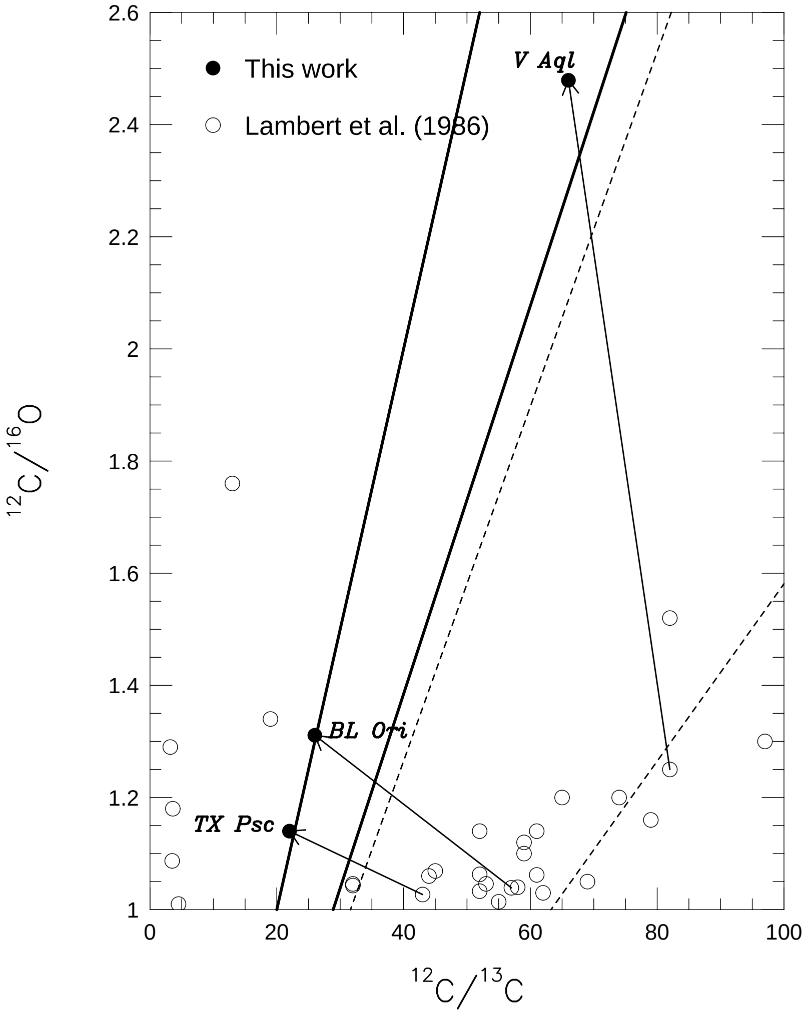

Fig. 5.33. C/O ratio is plotted against $^{12}C/^{13}C$ ratio for each program star. The filled circles represent the results by the present work, while the open circles represent those by Lambert et al. (1986). The solid lines are the relation between $^{12}C/^{13}C$ ratio and C/O ratio predicted by the addition of ^{12}C to the atmosphere of K and M giants. The left solid line is drawn with the assumption of the Case d, while the right one with the assumption of the Case b in Table 21. The dashed lines are predictions adopted by Lambert et al. (1986)

Chapter 6

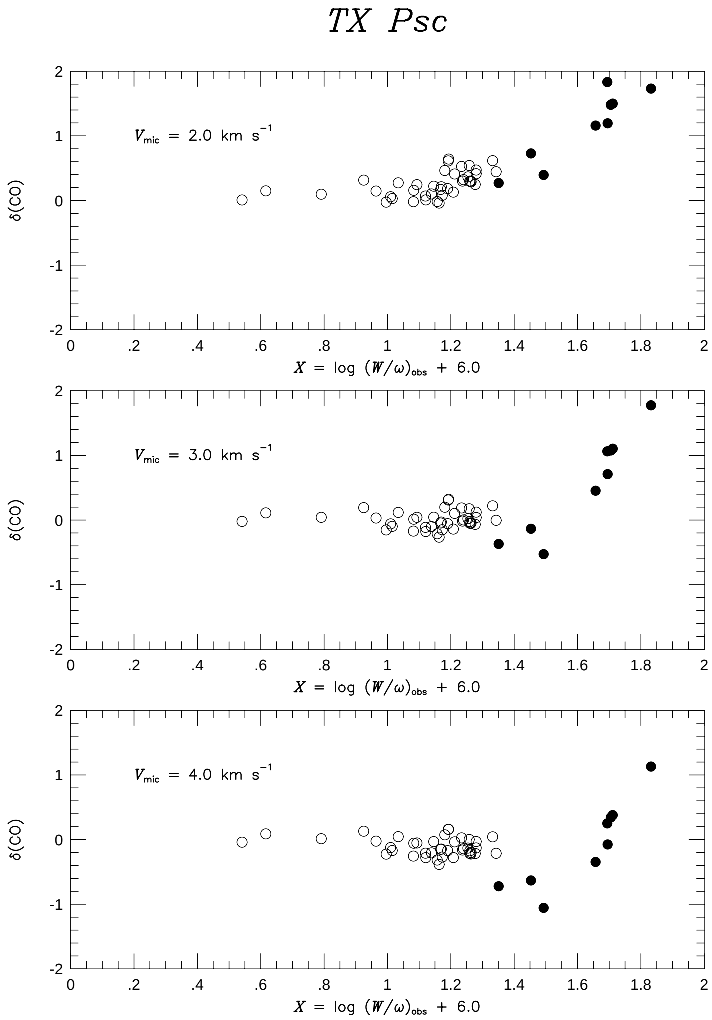

Fig. 6.1. The standard analysis is applied to lines of the CO first and second overtone bands for TX Psc. The open circles represent the second overtone lines, while the filled circles represent the first overtone lines

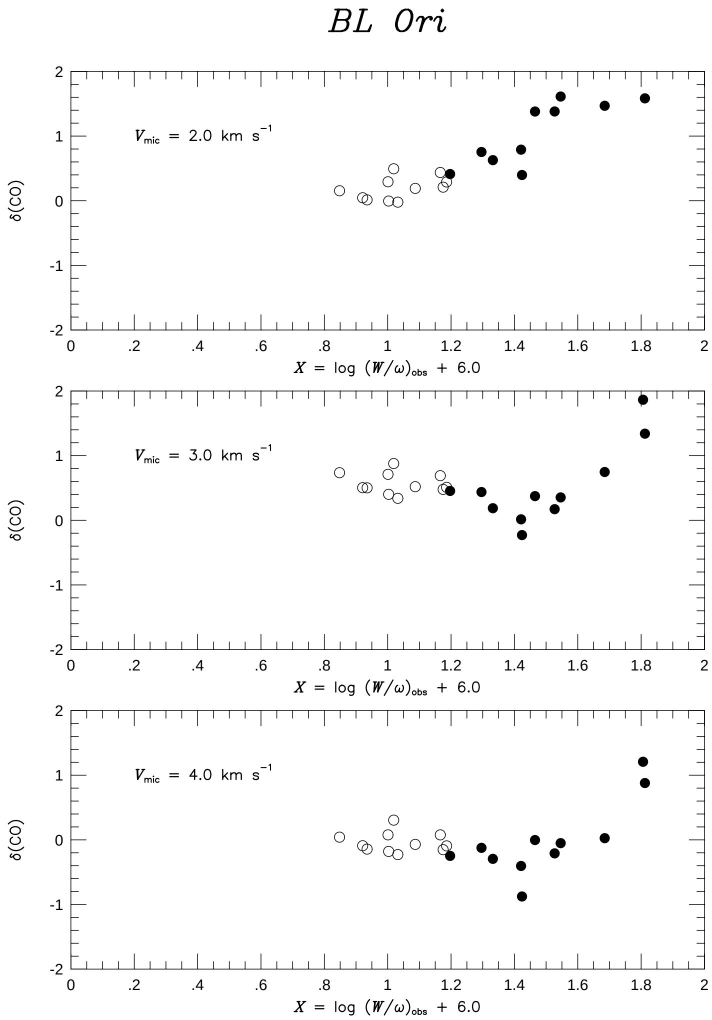

Fig. 6.2. The standard analysis is applied to lines of the CO first and second overtone bands for BL Ori. The symbols have the same meanings as in Fig. 6.1

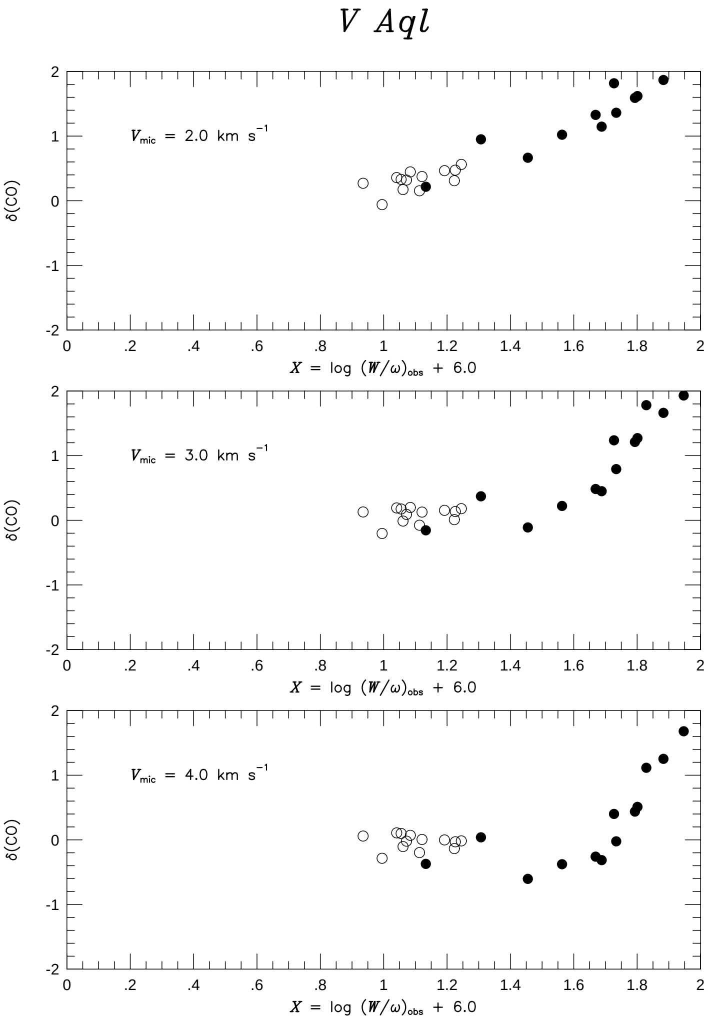

Fig. 6.3. The standard analysis is applied to lines of the CO first and second overtone bands for V Aql. The symbols have the same meanings as in Fig. 6.1

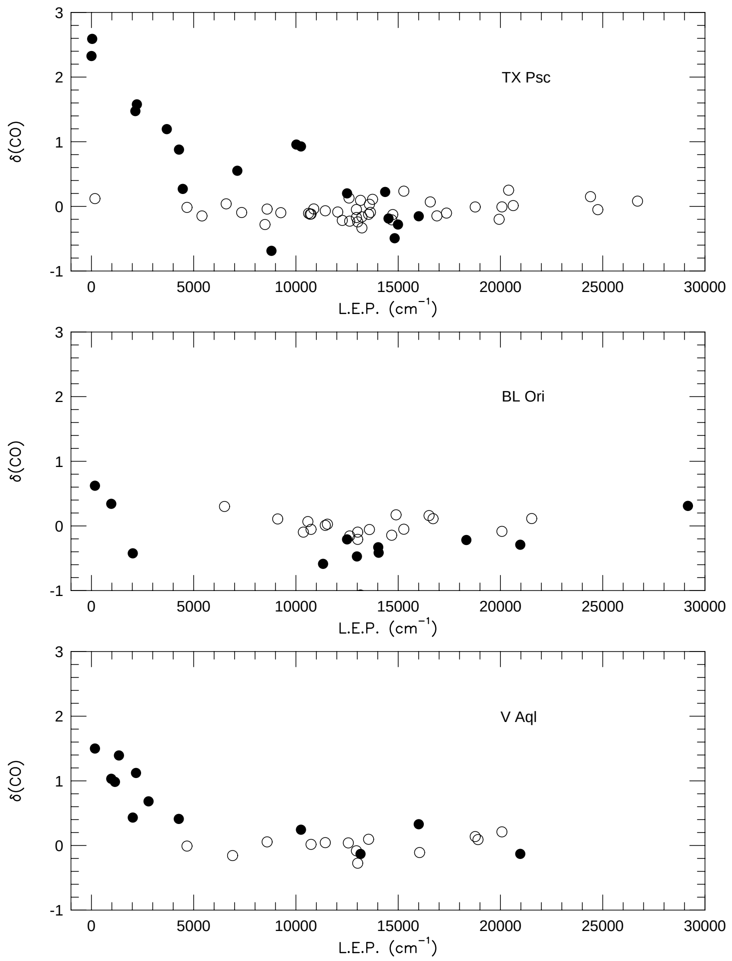

Fig. 6.4. The correction to the abundance of CO, δ(CO), for each line is plotted against lower excitation potential (L.E.P.) of the line. The open circles represent the second overtone lines, while the filled circles represent the first overtone lines. Low excitation lines of the first overtone show marked deviation as compared with high excitation lines in TX Psc and V Aql

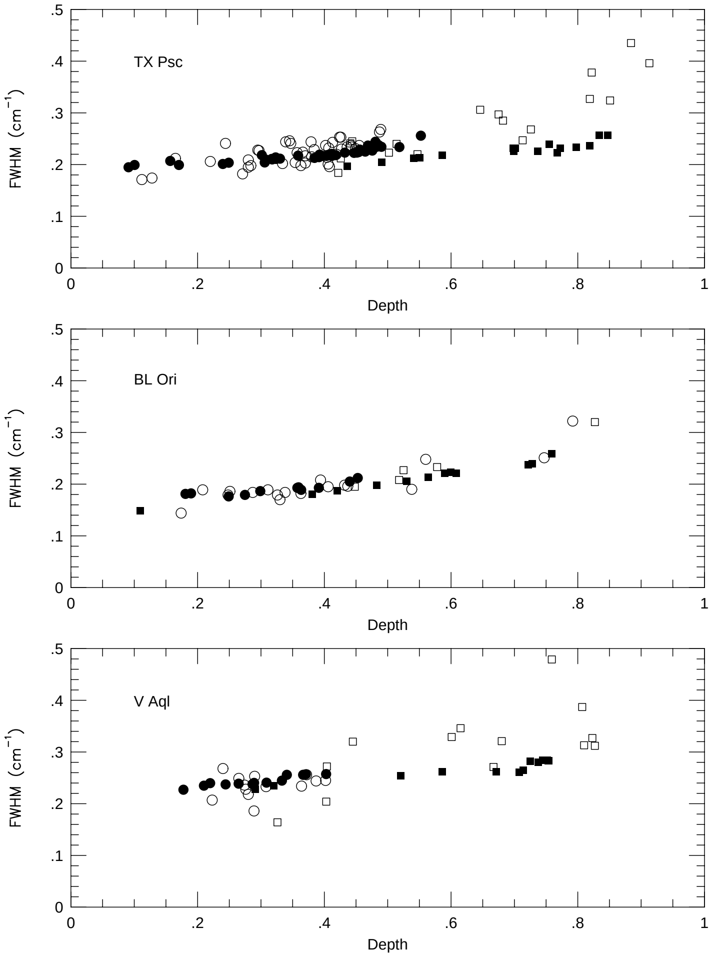

Fig. 6.5. The full widths at half maximum are plotted against the central depths of the lines of the CO second and first overtone. The open circles represent the observations for the second overtone lines, while the open squares represent the observation for the first overtone lines. The predictions by the models are represented by the filled circles for the second overtone lines and by the filled squares for the first overtone lines

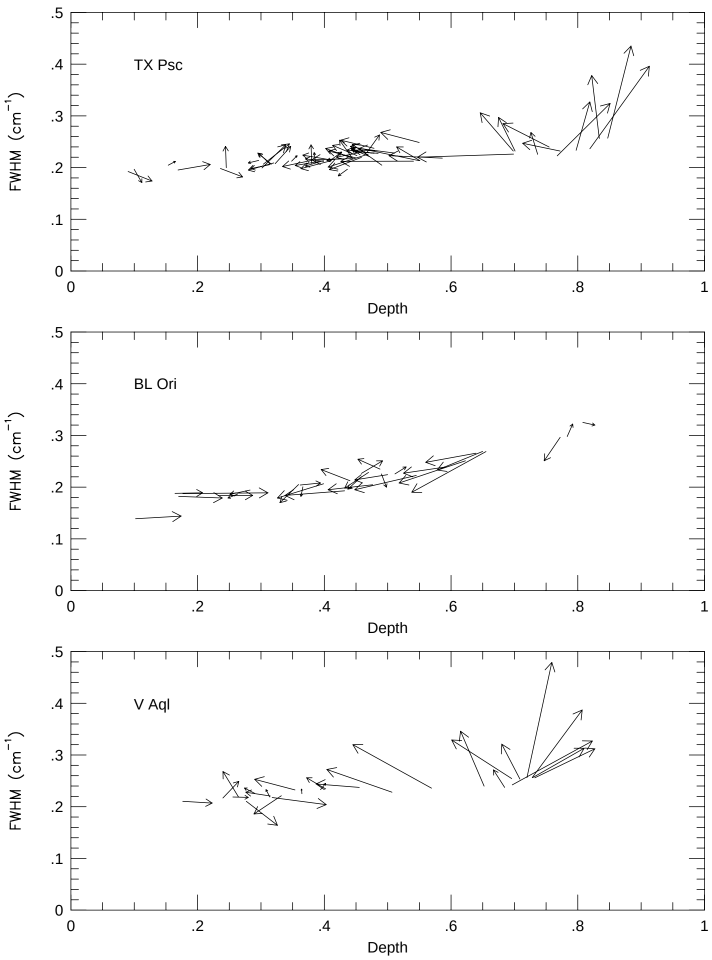

Fig. 6.6. The difference of the observations and the predictions are shown by vectors with their tails at the points of the predictions

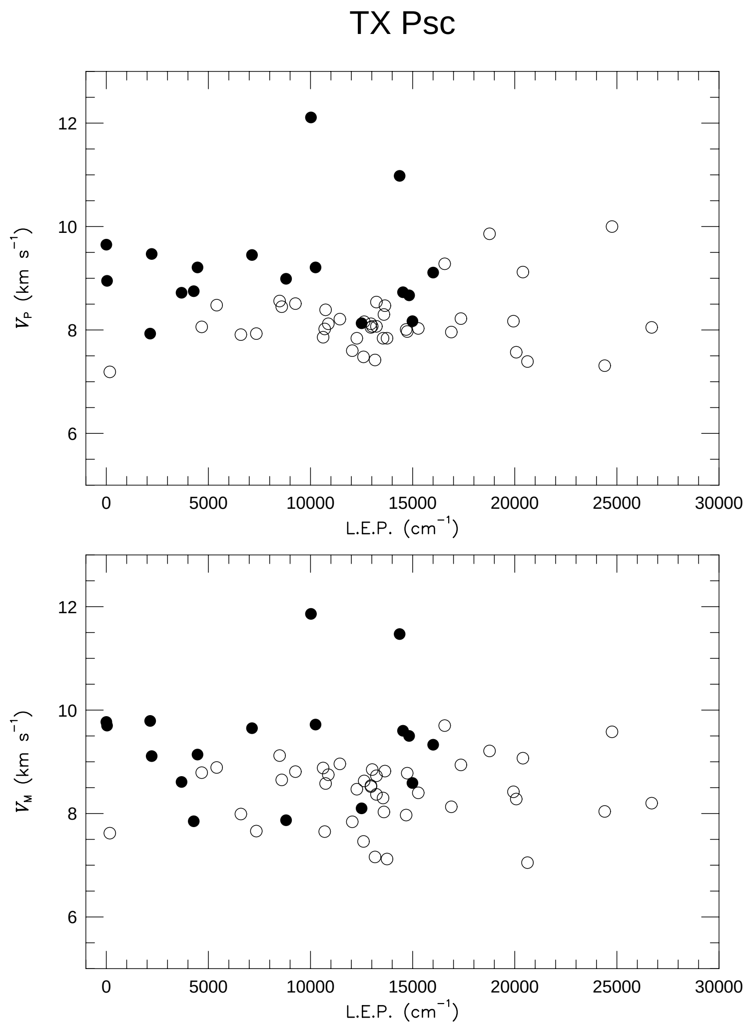

Fig. 6.7. The radial velocities of the CO second and first overtone lines are plotted against the lower excitation potentials of the lines for TX Psc. The radial velocity measured at the peak is denoted by $V_{\rm P}$, while that measured at the midpoint of the FWHM is denoted by $V_{\rm M}$. The second overtone lines are represented by the open circles and the first overtone lines are represented by the filled circles in both panels

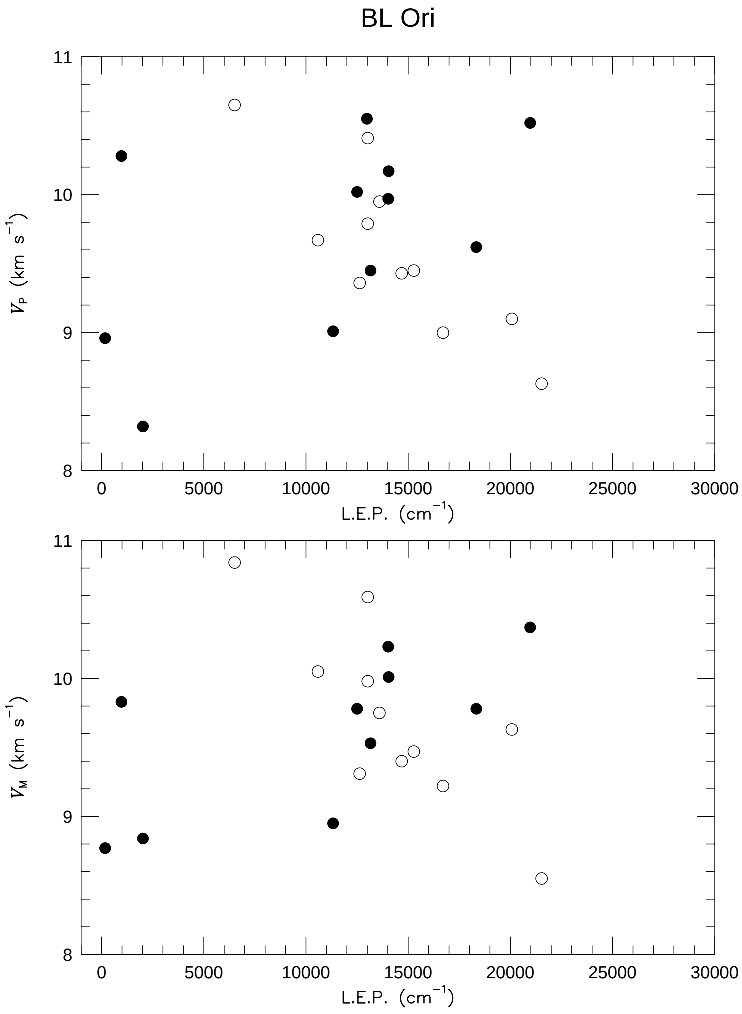

Fig. 6.8. The radial velocities of the CO second and first overtone lines are plotted against the lower excitation potentials of the lines for BL Ori. See also the legend to Fig 6.7

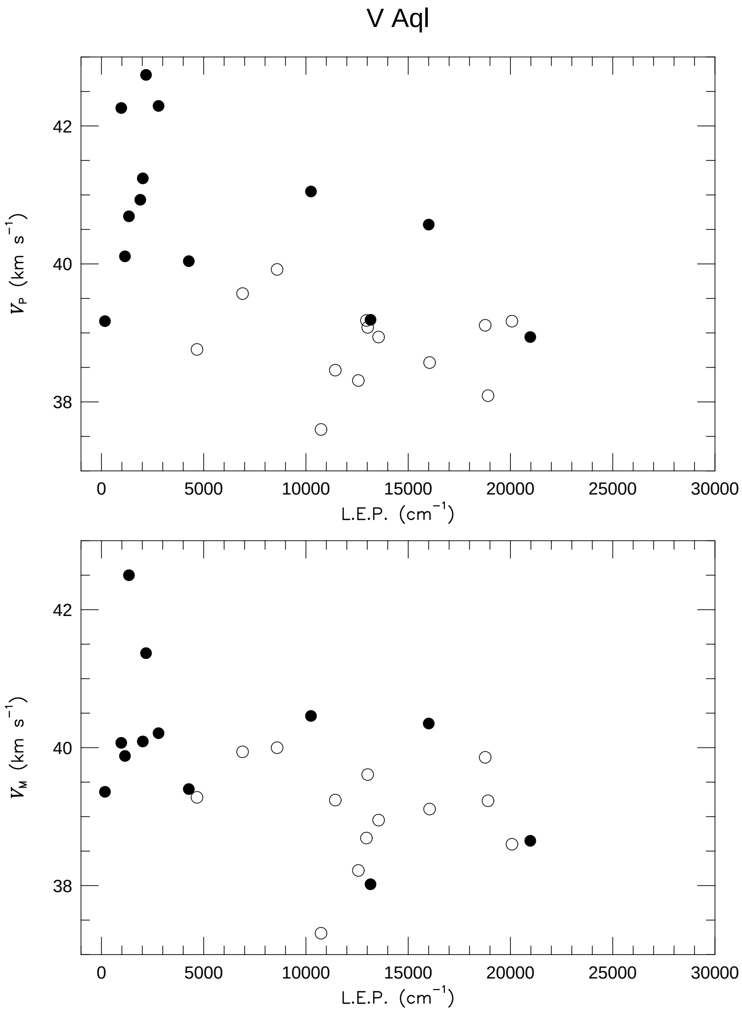

Fig. 6.9. The radial velocities of the CO second and first overtone lines are plotted against the lower excitation potentials of the lines for V Aql. See also the legend to Fig 6.7

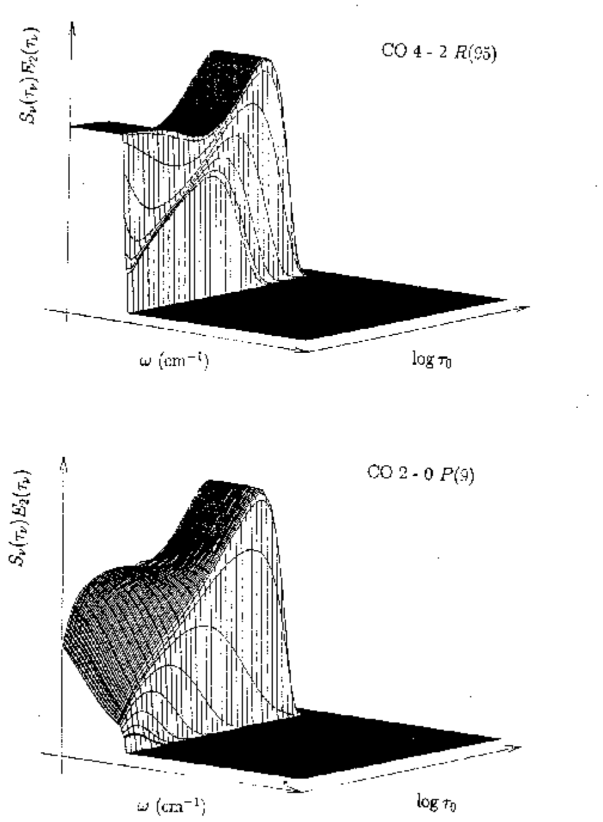

Fig. 6.10. Contribution functions for a high excitation line $4-2$ $R(95)$ and for a low excitation line $2-0$ $P(9)$ are plotted as functions of wavenumber and depth

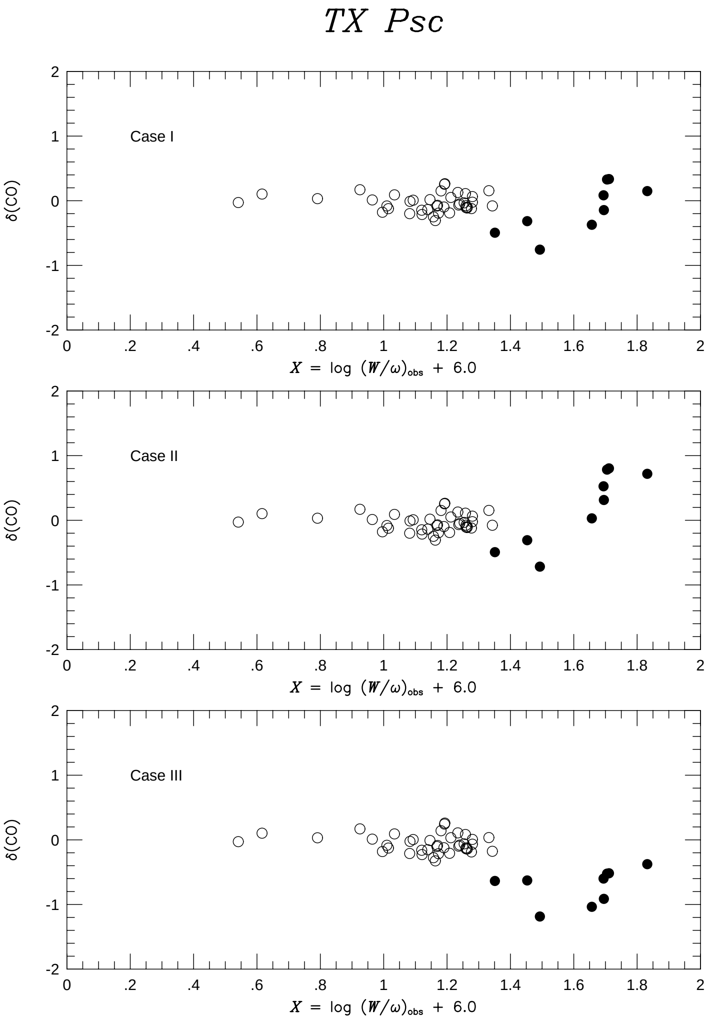

Fig. 6.11. The corrections to the CO abundance are plotted against $X = \log(W/\omega) + 6$ for the CO first and second overtone lines with different depth-dependencies of micro-turbulent velocity for TX Psc. The open circles represent the second overtone lines, while the filled circles represent the first overtone lines

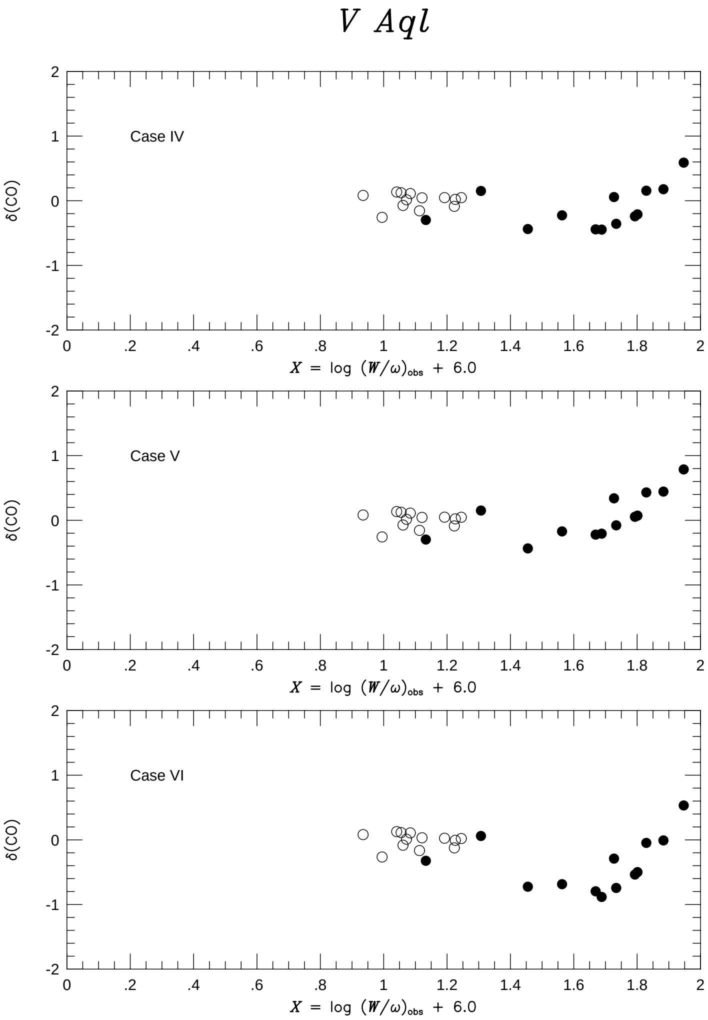

Fig. 6.12. The corrections to the CO abundance are plotted against $X = \log(W/\omega) + 6$ for the CO first and second overtone lines with different depth-dependencies of micro-turbulent velocity for V Aql. The symbols have the same meanings as in Fig. 6.11

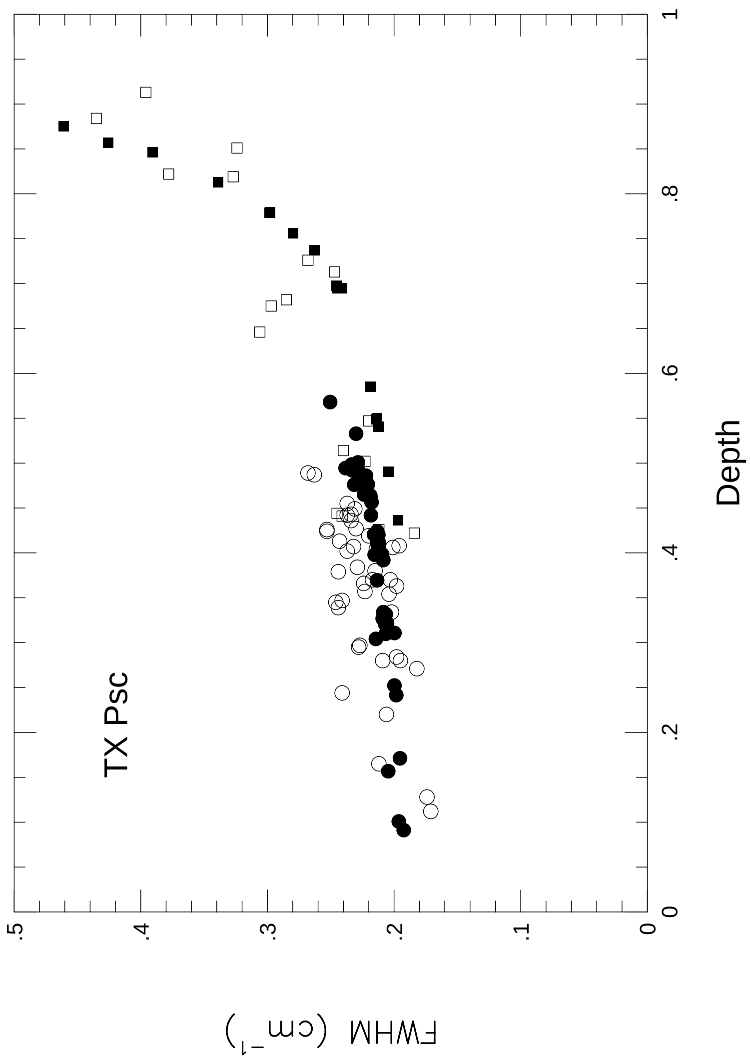

Fig. 6.13. The full widths at half maximum are plotted against the central depths for TX Psc with the depth dependency of micro-turbulent velocity given in Case I. The open circles represent the observations of the second overtone lines, while the open squares represent the observations of the first overtone lines. The predictions are represented by the filled circles for the second overtone lines and by the filled squares for the first overtone lines

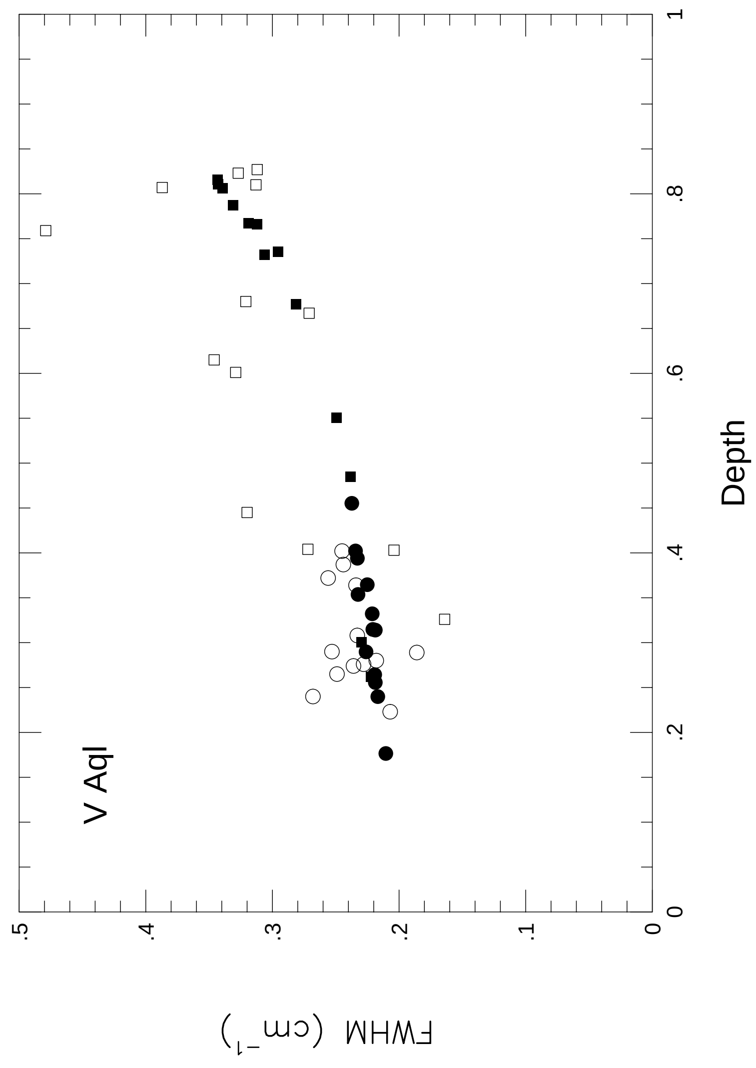

Fig. 6.14. The full widths at half maximum are plotted against the central depths for V Aql with the depth dependency of micro-turbulent velocity given in Case IV. The open circles represent the observations of the second overtone lines, while the open squares represent the observations of the first overtone lines. The predictions are represented by the filled circles for the second overtone lines and by the filled squares for the first overtone lines

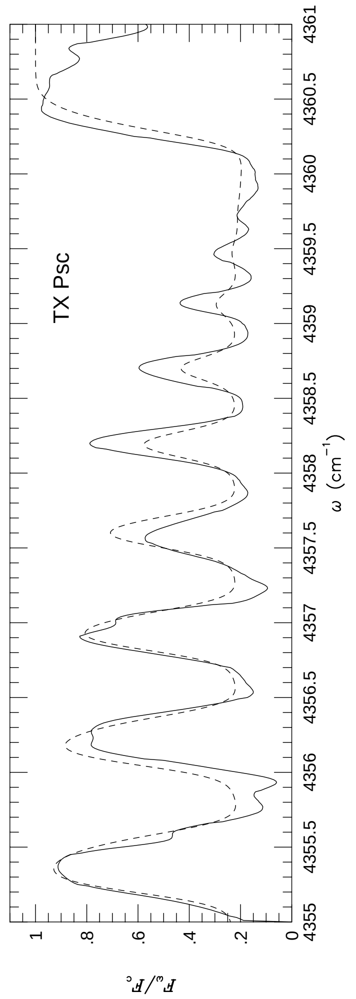

Fig. 6.15. Comparison between the observed and synthetic spectra around the (2,0) bandhead of CO for TX Psc. The solid line represents the observed spectrum for TX Psc. The synthetic spectrum calculated with the depth-dependency of the Case I is represented by the dashed line

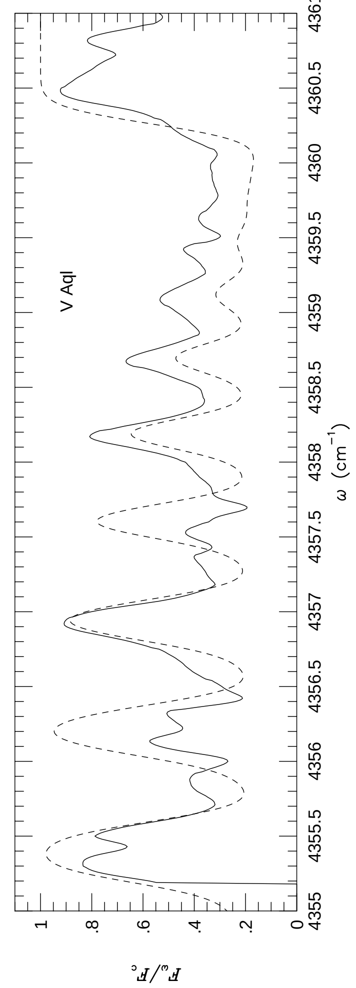

Fig. 6.16. Comparison between the observed and synthetic spectra around the (2,0) bandhead of CO for V Aql. The solid line represents the observed spectrum for V Aql. The synthetic spectrum calculated with the depth-dependency of the Case IV is represented by the dashed line

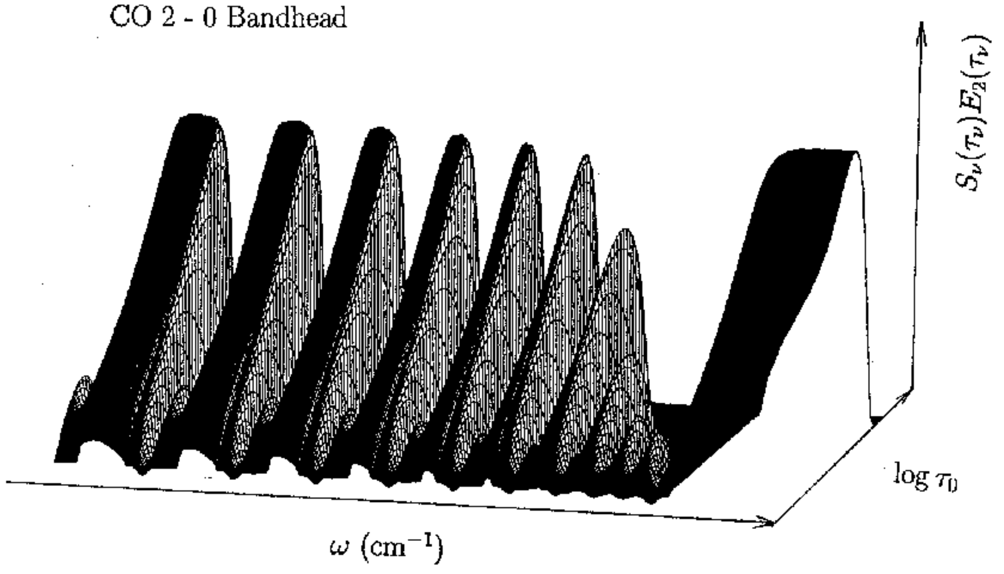

Fig. 6.17. Contribution function for the lines near the CO (2,0) bandhead is plotted as a function of wavenumber and depth $\log \tau_0$

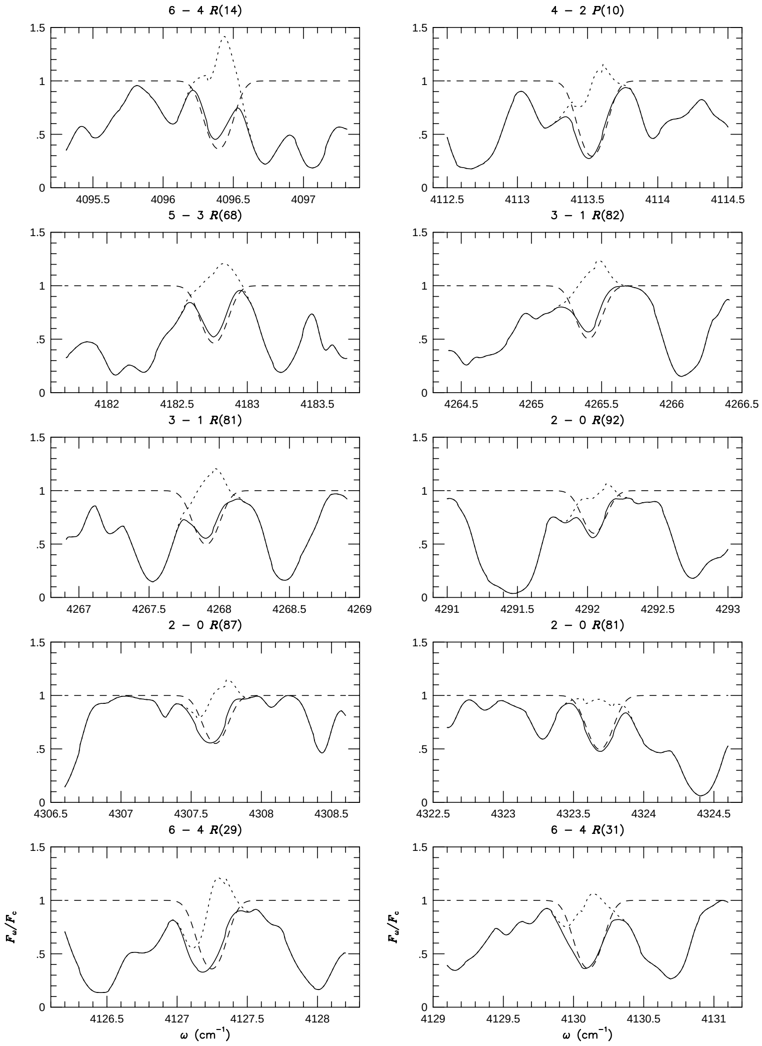

Fig. 6.18. Synthetic spectra for the CO first overtone lines used in the analysis for TX Psc are represented by dashed lines. The observed spectra are represented by the solid lines. The dotted lines represent the ratioed spectra. that is, the observed spectra divided by the synthetic spectra

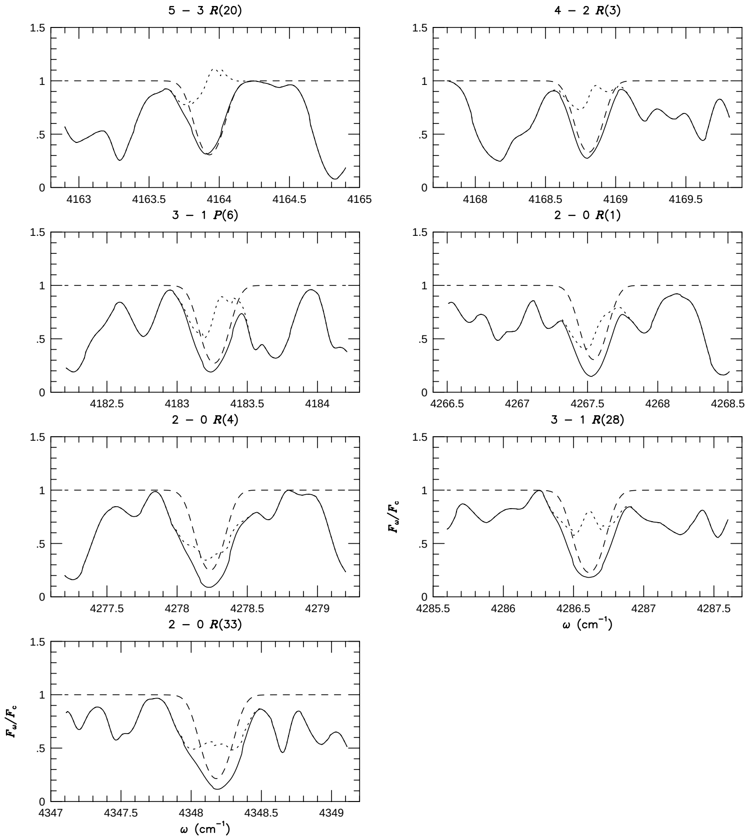

Fig. 6.18. — Continued

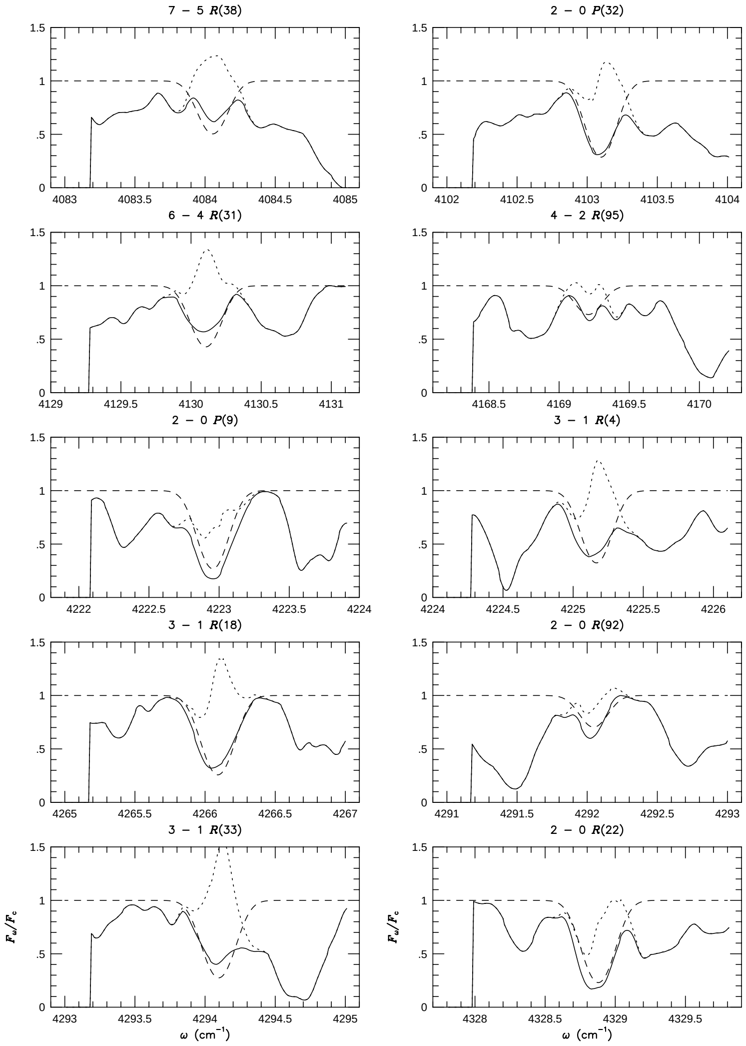

Fig. 6.19. Synthetic spectra for the CO first overtone lines used in the analysis for V Aql are represented by dashed lines. The observed spectra are represented by the solid lines. The dotted lines represent the ratioed spectra. that is, the observed spectra divided by the synthetic spectra

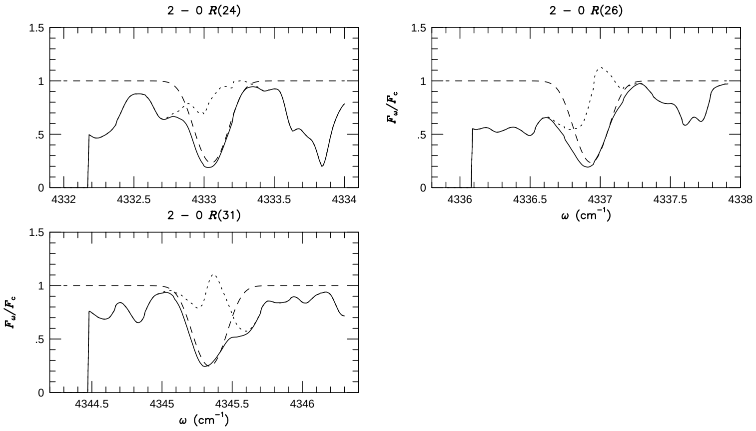

Fig. 6.19. — Continued

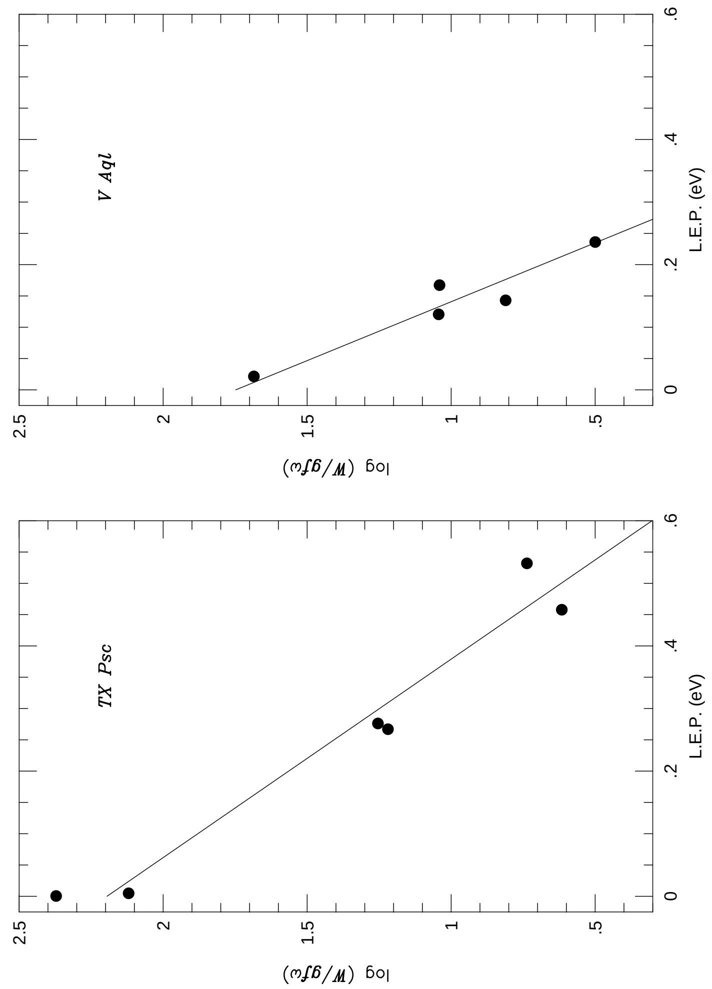

Fig. 6.20. The determination of excitation temperature for the absorption excesses in TX Psc and V Aql. The gradients of the plots give $\theta_{\mathrm{ex}} = 5040/T_{\mathrm{ex}}$

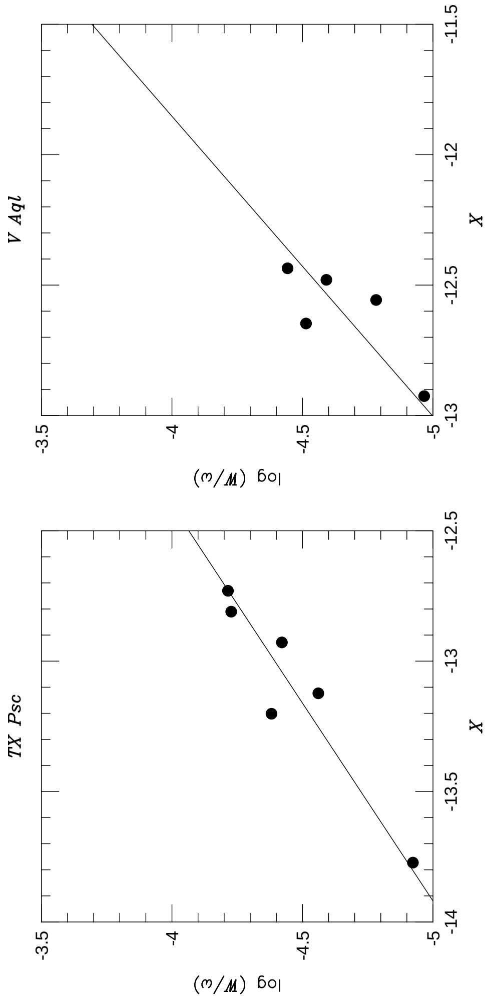

Fig. 6.21. The empirical curves-of-growth for the absorption excesses in TX Psc and V Aql

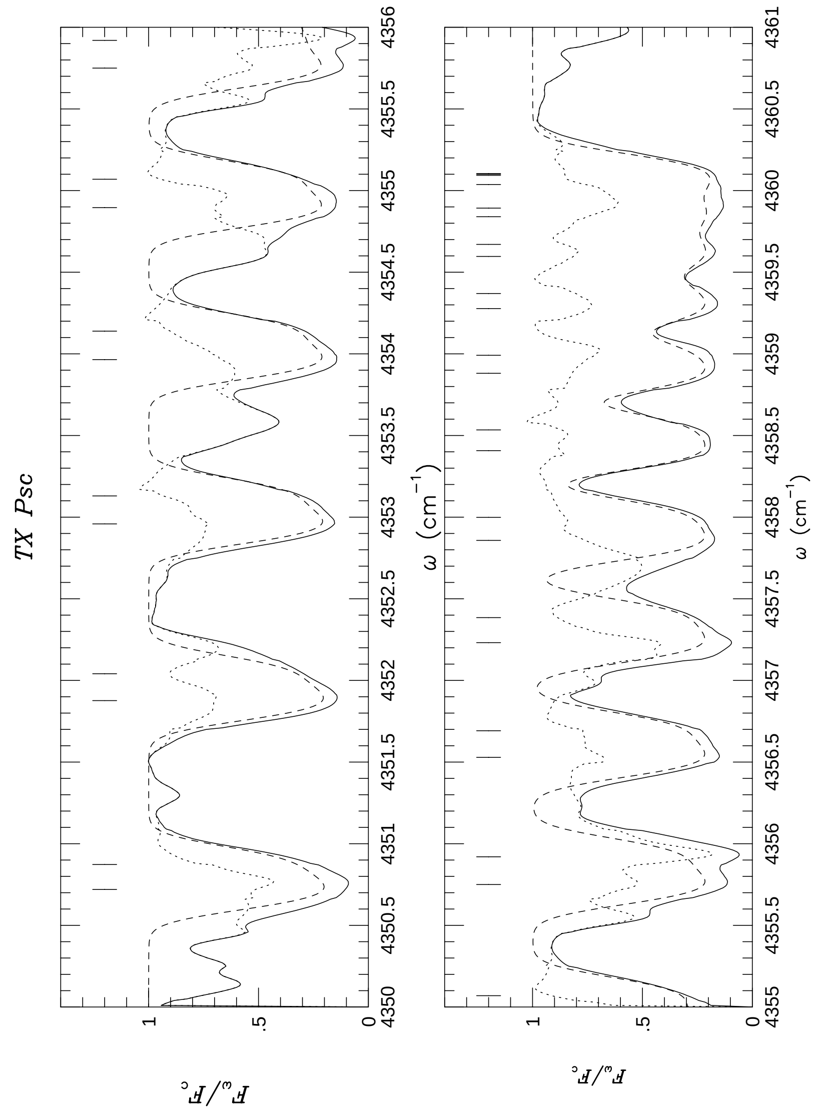

Fig. 6.22. The synthetic spectrum around the CO (2,0) bandhead is compared with the observed spectrum for TX Psc. The solid line represents the observed spectrum, and the dashed line represent the synthetic spectrum. The ratio between the observed and synthetic spectra is represented by the dotted line

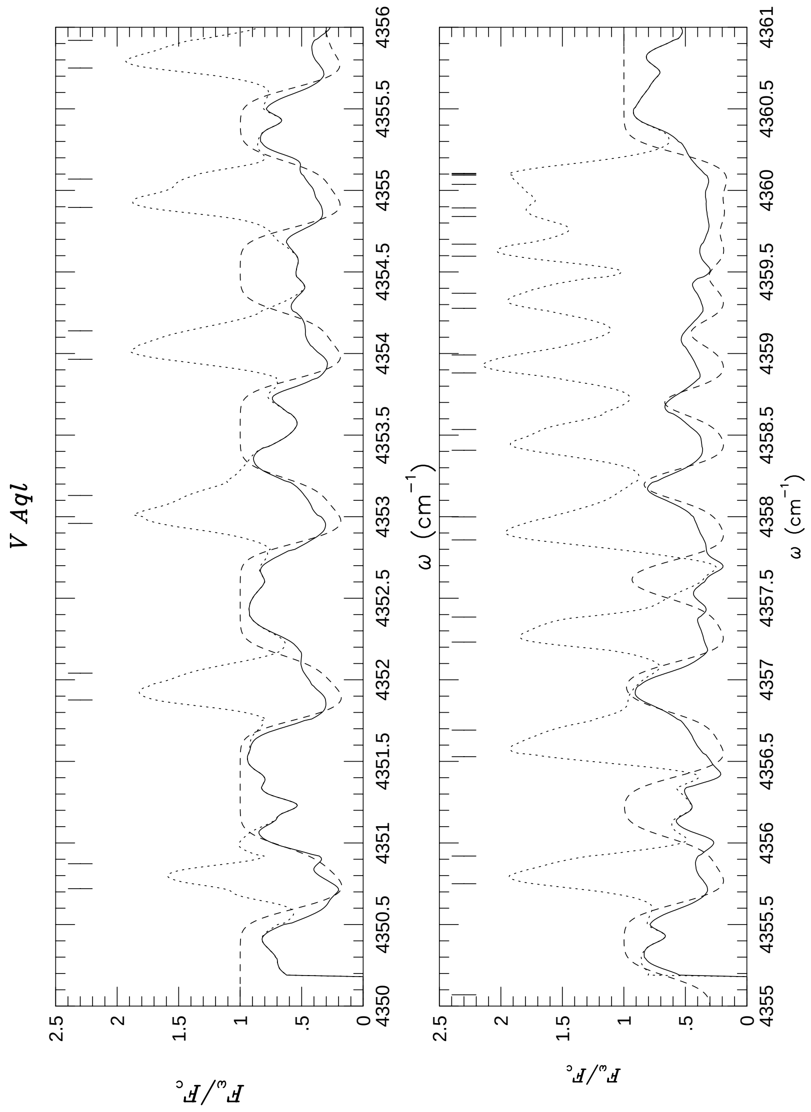

Fig. 6.23. The synthetic spectrum around the CO (2,0) bandhead is compared with the observed spectrum for V Aql. The solid line represents the observed spectrum, and the dashed line represent the synthetic spectrum. The ratio between the observed and synthetic spectra is represented by the dotted line